Effective Date: July 31, 2011
Revision -

GSFC JPSS CMO
October 21, 2011
Released

Joint Polar Satellite System (JPSS) Ground Project
Code 474
474-00032

Joint Polar Satellite System (JPSS) Cross Track Infrared Sounder (CrIS) Sensor Data Records (SDR) Algorithm theoretical Basis Document (ATBD)

For Public Release

The information provided herein does not contain technical data as defined in the International Traffic in Arms Regulations (ITAR) 22 CFC 120.10.
This document has been approved For Public Release.

Goddard Space Flight Center
Greenbelt, Maryland

National Aeronautics and
Space Administration

Check the JPSS MIS Server at https://jpssmis.gsfc.nasa.gov/frontmenu_dsp.cfm to verify that this is the correct version prior to use.

This page intentionally left blank.

Joint Polar Satellite System (JPSS) Cross Track Infrared Sounder (CrIS) Sensor Data Records (SDR) Algorithm theoretical Basis Document (ATBD)

JPSS Electronic Signature Page

Prepared By:

Neal Baker
JPSS Data Products and Algorithms, Senior Engineering Advisor
(Electronic Approvals available online at https://jpssmis.gsfc.nasa.gov/mainmenu_dsp.cfm)

Approved By:

Heather Kilcoyne
DPA Manager
(Electronic Approvals available online at https://jpssmis.gsfc.nasa.gov/mainmenu_dsp.cfm)

Goddard Space Flight Center
Greenbelt, Maryland

Check the JPSS MIS Server at https://jpssmis.gsfc.nasa.gov/frontmenu_dsp.cfm to verify that this is the correct version prior to use.

This page intentionally left blank.

Check the JPSS MIS Server at https://jpssmis.gsfc.nasa.gov/frontmenu_dsp.cfm to verify that this is the correct version prior to use.

Preface

This document is under JPSS Ground AERB configuration control. Once this document is approved, JPSS approved changes are handled in accordance with Class I and Class II change control requirements as described in the JPSS Configuration Management Procedures, and changes to this document shall be made by complete revision.

Any questions should be addressed to:

JPSS Ground Project Configuration Management Office
NASA/GSFC
Code 474
Greenbelt, MD 20771

Check the JPSS MIS Server at https://jpssmis.gsfc.nasa.gov/frontmenu_dsp.cfm to verify that this is the correct version prior to use.

This page intentionally left blank.

Check the JPSS MIS Server at https://jpssmis.gsfc.nasa.gov/frontmenu_dsp.cfm to verify that this is the correct version prior to use.

Change History Log

Revision	Effective Date	Description of Changes (Reference the CCR & CCB/ERB Approve Date)
Original	July 31, 2011	**474-CCR-11-0047:** This version baselines D43773, VIIRS Cross Track Infrared Sounder (CrIS) Sensor Data Records (SDR) Algorithm Theoretical Basis Document ATDB (REF: BOM-CrIS-0067/ITT8180004), Rev D, dated 09/17/2009, as a JPSS document, version Rev –. This is the version that was approved for NPP launch. Per NPOESS CDFCB - External, Volume V – Metadata, doc number D34862-05, this has been approved for Public Release into CLASS. This CCR was approved by the JPSS Algorithm ERB on July 31, 2011.

Check the JPSS MIS Server at https://jpssmis.gsfc.nasa.gov/frontmenu_dsp.cfm to verify that this is the correct version prior to use.

This page intentionally left blank.

Check the JPSS MIS Server at https://jpssmis.gsfc.nasa.gov/frontmenu_dsp.cfm to verify that this is the correct version prior to use.

Northrop Grumman Space & Mission Systems Corp.
Space Technology
One Space Park
Redondo Beach, CA 90278

Engineering & Manufacturing Development (EMD) Phase
Acquisition & Operations Contract

CAGE NO. 11982

Cross Track Infrared Sounder (CrIS) Sensor Data Records (SDR)

Algorithm theoretical Basis Document ATBD

(ref BOM-CrIS-0067/ITT8180004)

Document Number: D43773

Document Date: 9-17-2009 **Revision: D**

CDRL A032

Point of Contact: _____
Xia-lin Ma, Algorithms and Calibration/Validation

ELECTRONIC APPROVAL SIGNATURES:

_____ _____
Bruce Hauss, Algorithms & Calibration/Validation Lead

Prepared by
Northrop Grumman Space Technology
One Space Park
Redondo Beach, CA 90278

Under
Contract No. F04701-02-C-0502

Prepared for
Department of the Air Force
NPOESS Integrated Program Office
C/O SMC/CIK
2420 Vela Way, Suite 1467-A8
Los Angeles AFB, CA 90245-4659

DISTRIBUTION STATEMENT F: Distribution statement "F" signifies that further dissemination should only be made as directed by the controlling DoD Office (NPOESS IPO). Ref DODD 5230.24.

Northrop Grumman Space & Mission Systems Corp.
Space Technology
One Space Park
Redondo Beach, CA 90278

NORTHROP GRUMMAN

Raytheon

Revision/Change Record

Document Number D43773

Revision	Document Date	Revision/Change Description	Pages Affected
-	02/06/2007	Initial PCIM Release to bring document into Matrix Accountability. Reference original document number: BOM-CrIS-0067/ITT8180004 delivered in 2004	All
A	03/21/2008	Revised PCIM Release to bring document into Matrix Accountability. Reference document number: BOM-CrIS-0067/ITT8180004 delivered in 2008 rev E	All
B	4/15/2009	Remove ITAR; Incorporate ITT Document Rev E. Rev ECR A-230	All
C	5/13/2009	Add CDRL markings to Cover Sheet, including Dist Stament F. Ref ECR A-238	
D	9/17/2009	Ref ECR A-255. The major updates are the ICT environmental model and non-linearity correction. Details follow.	All

Northrop Grumman Space & Mission Systems Corp.
Space Technology
One Space Park
Redondo Beach, CA 90278

NORTHROP GRUMMAN

Raytheon

Revision/Change Record

Document Number D43773

Revision	Document Date	Revision/Change Description	Pages Affected
D	9/17/2009	Section 2.4.4 Change to need non-linearity correction. Section 2.6.2 Update to Equation 8. Section 3.3.3 Update FCE count (h becomes h current) in Equations 19 to 20. Section 3.3.3 Equation 19 updated showing the floor() operator instead of truncation. Section 3.3.3 Update to Figure 21. Section 3.3.3 Add paragraph on ICT-DS synchronization. Section 3.5 Update Equation 23d.. Section 3.5 Update Equation 23 showing the correct subscript of the function F. Section 3.7.2 Update Equation 58 to include the array truncation (subsetting) operator after transformation by the CMO operator. Update subsequent paragraphs. Section 3.8 Update Equation 60a that now includes the array truncation operator (or subsetting) after the CMO transformation. Update subsequent paragraphs. Section 5.2 Update to Equation 66 showing the correct parentheses. Section 5.3 Modify calibration equations to include frequency shift. Section 5.4 Update Figure 41. Section 6.3 Clarify the time bias is relative to null position instead of Nadir position. Also in section 6.6 Section 6.4 Update to bullet 1 citing that the raw servo errors are in count that are subsequently linearly transformed into micro radians prior to further processing. Section 6.4.1 Update citing the use of angle offset. Section 7.3.2 Update Figure 62 and subsequent description replacing H^x with H^{cur}. Figure 63 Update showing the correct conversion of the laser wavelength tolerance (division by 1 million added). Section 7.4.1 Update the Neon wavelength value to 703.4524 nm. Section 7.5.3.1 Add wording about truncating the output radiance array to the EDR user's grid.	

ITT SPACE SYSTEMS DIVISION

Document No. 8180004 (Vol 1) Rev. E

CrIS

Cross-track Infrared Sounder

Algorithm Theoretical Basis Document for the Cross Track Infrared Sounder (CrIS)

Sensor Data Records (SDR)

ITT SSD Document 8180004 (Volume 1)

Release Authority: See Document Change Record

Program: CrIS	Contract Number: 63882DGM2S
Responsible Engineer J. Predina	Chief Engineer R. Glumb
System Test N/A	Project Engineer K. Reemmer
Data Analysis R. Frain / L. Suwinski	Contamination & Safety Engineer(s) N/A
Systems Engineer M. Cromp	PRB Chairman K. Reemmer
Test Software T. Dukes	Program Manager D. Gray

Product Assurance	D. Orr	Release Date	2/20/09

TABLE OF CONTENTS

1. INTRODUCTION 1
1.1 Purpose of Document 1
1.2 Scope 1
1.3 Document Overview 2
1.4 Reference Documents 2
1.5 Acronyms 5
1.6 Notation and Symbols 9
1.6.1 Notation and Operators 9
1.6.2 Predefined Functions and Operators 9
1.6.3 List of Symbols Used 9
1.6.4 Identifiers Notation 10
1.6.5 Mathematical Definitions 12
2. SDR ALGORITHMS PRINCIPLES 13
2.1 Objective of the SDR Algorithms 14
2.2 Space Segment Signal Processing 15
2.2.1 Spikes Detection/Correction 16
2.2.2 Filtering and Decimation 17
2.2.3 Bit Trimming 21
2.2.4 Packet Encoding 22
2.3 Ground Segment Processing 24
2.4 Interferometer Model 25
2.4.1 Instrument Phase 25
2.4.2 Other Signal Contributors 27
2.4.3 Instrument Line Shape 27
2.4.4 Other Types of Errors 27
2.4.5 Interferometer Modeling Equations 29
2.5 CrIS Characteristics 31
2.5.1 Double-Sided Interferogram Measurements 31
2.5.2 CrIS Spectral Bands 32
2.5.3 CrIS Field of Regard 33
2.5.4 CrIS Measurement Sequence 34
2.5.5 CrIS Signal Processing 35
2.6 Signal Representation 36
2.6.1 Array Dimensions 37
2.6.2 Data Ordering 40
3. SPECIAL CONSIDERATIONS 41
3.1 Non-linearity Correction 41
3.2 Scan Mirror Polarization Compensation 44
3.3 Fringe Count Error Handling 46
3.3.1 Phase Analysis 46
3.3.2 Spectrum Based Detection and Correction 46
3.3.3 FCE Detection 48
3.3.4 FCE Correction 54
3.4 LUNAR INTRUSION Handling 59
3.4.1 Lunar Intrusion Detection 59
3.4.2 Lunar Intrusion Processing 60
3.5 Alignment of Data to a Common Spectral Grid. 61

3.6 ILS Correction 65
3.6.1 Introduction 65
3.6.2 CrIS Off-Axis Self Apodization 69
3.6.3 Self-Apodization Removal 70
3.6.4 Residual Term 76
3.6.5 Guard Band Damping 77
3.6.6 ILS Retrieval 78
3.7 Signal Apodization 80
3.7.1 Unapodized Channel Response Function 80
3.7.2 Hamming's Filter Function 82
3.7.3 Blackman-Harris's Apodization Function 84
3.8 CMO UPDATES 87
4. SPECTRAL CALIBRATION 90
4.1 Neon-lamp as a Spectral Reference 91
4.1.1 Wavelength Calculation 91
4.1.2 Calculation of Laser Metrology Wavelength 92
4.1.3 Rejecting Bad Neon Count Measurements (Quality Control) 93
4.2 Metrology Wavelength Monitoring 93
5. RADIOMETRIC CALIBRATION 94
5.1 Basic Radiometric Relations 95
5.2 General Calibration Equation 96
5.3 CrIS Specific Calibration Equation 97
5.4 ICT Radiometric Model 99
5.4.1 Radiometric Error 100
5.4.2 Radiometric Model Formulation 100
5.5 ICT Temperature Computation 104
5.6 Signal Coaddition 106
5.6.1 Moving Average 106
5.6.2 Impact of Temperature Drift 107
5.6.3 Throughput Delay 109
6. GEOMETRIC CALIBRATION 112
6.1 Coordinate Systems 114
6.1.1 Coordinate System Definition 115
6.1.2 Interferometer Optical Axis Reference (IOAR) 115
6.1.3 Rotating Mirror Frame (RMF) 115
6.1.4 Scene Selection Mirror Mounting Feet Frame (SSMF) 115
6.1.5 Scene Selection Module Reference (SSMR) 116
6.1.6 Instrument Alignment Reference (IAR) 116
6.1.7 Spacecraft Body Frame (SBF) 116
6.1.8 Orbital Coordinate System (OCS) 116
6.1.9 Earth Centered Inertial (ECI) 116
6.1.10 Earth Centered Earth Fixed (ECEF) or Earth Centered Rotating (ECR) 117
6.1.11 World Geodetic System 1984 (WGS84) 118
6.1.12 Topocentric-Horizon Coordinate System (THCS) 118
6.2 Coordinate System Transformations 119
6.3 Algorithm Partitioning 120
6.4 Sensor Specific Algorithm 121
6.4.1 CrIS FOV LOS in SSMF Coordinate System 121
6.4.2 SSMF to SBF Transformation Operator 122
6.4.3 CrIS FOV LOS in SBF Coordinate System 122

6.5 Spacecraft Level Algorithm 125
6.6 Timing Conventions 125
7. MODULES DEFINITION 126
7.1 Initialization 128
7.2 Input Data Handling 141
7.3 Preprocessing 144
7.3.1 Interferogram to Spectrum Transformation 144
7.3.2 Moving Average Handling 146
7.4 Spectral Calibration 149
7.4.1 Laser Wavelength Calibration from Neon Lamp Data 149
7.4.2 Laser Wavelength Drift Monitoring 153
7.4.3 Spectral Axis Labeling and Alias Unfolding 155
7.5 Radiometric Calibration 157
7.5.1 Radiometric Complex Calibration 157
7.5.2 ICT Radiance Calculation 160
7.5.3 Spectrum Correction 162
7.5.4 Non-linearity Correction 165
7.6 Quality Control 170
7.6.1 NEdN Estimation 170
7.6.2 Fringe Count Error Handling 172
7.6.3 Fringe Count Error Detection 172
7.6.4 Fringe Count Error Correction 177
7.6.5 Data Quality Indicators 180
7.7 Post-Processing 181
7.7.1 User Required Spectral Bins Selection 181
7.7.2 SDR Data Formatting 181
7.8 Output Data Handling 181
8. CONCLUSION 182
9. APPENDICES 184
9.1 Fast Fourier transforms 184
9.1.1 Comments on Various Algorithms 185
9.1.2 Data translation and centering 186
9.1.3 Prime Factor Algorithm Fast Fourier Transform 187
9.2 Alias unfolding 188
9.3 Linear fitting 190
9.3.1 Implementation of the linear interpolation 191
9.4 Numerical Integration 192
9.5 Determination of the goodness of fit 193
9.6 Definitions 195
9.6.1 Sensor Calibration 195
9.6.2 Raw Data Record (RDR) 195
9.6.3 Sensor Data Record (SDR) 195
9.6.4 Environmental Data Record (EDR) 196
9.6.5 Data product Levels 196
9.6.6 Measured Data 196
9.6.7 Auxiliary Data 197
9.6.8 Ancillary Data 198
9.6.9 Other Instrument Specific Terms and Definitions 198

LIST OF FIGURES

Figure 1: CrIS System Segments 13
Figure 2: Data processing flow at various levels....13
Figure 3: Space Segment Processing of the CrIS Sensor....15
Figure 4: In-space interferogram processing for one of the nine FOV's 16
Figure 5: Interferogram spike....16
Figure 6: Parks-McClellan FIR Band pass Filter for CrIS (LW)....18
Figure 7: Parks-McClellan FIR Band pass Filter for CrIS (MW)....19
Figure 8: Parks-McClellan FIR Band pass Filter for CrIS (SW) 19
Figure 9: Interferogram numerical processing 20
Figure 10: Interferogram envelope for a 17-bit word (each I & Q) 22
Figure 11: Ground Processing Data Flowchart....24
Figure 12: Phase dependencies in an interferometer....29
Figure 13: Double-sided versus single-sided interferograms....31
Figure 14: Long, Mid, and Short Wave IR bands....33
Figure 15: Field of Regard definition....33
Figure 16: CrIS Measurement Sequence 35
Figure 17: Numerical vectors data ordering....40
Figure 18: Spectral Distortion Due to Square Law Nonlinearity (courtesy of University of Wisconsin) 42
Figure 19: Barrel-roll scanner type....45
Figure 20: FCE detection scheme 48
Figure 21: FCE Detection Flow and Flags....52
Figure 22: FCE Correction Flow and Quality Flags 56
Figure 23: DS and ICT Synchronization Flow....58
Figure 24: Effect of the $\mathbf{F}$-matrix viewed in the interferogram domain 62
Figure 25: Instrument function contributors 66
Figure 26: Off-axis geometry and rays....66
Figure 27: Self-apodization due to beam divergence in the interferometer 68
Figure 28: Self-apodization function for the three basic pixel geometries 69
Figure 29: Off-axis geometry 71
Figure 30: Self-apodization effects and correction....74
Figure 31: Errors due to non-precise characterization....75
Figure 32: Post calibration filter for the LW band....78
Figure 33: ILS Retrieval Procedure....79
Figure 34: Boxcar apodization function and its sinc Fourier transform....81
Figure 35: Hamming apodization function and its Fourier transform 83
Figure 36: Blackman-Harris 3-terms apodization function and its Fourier transform....85
Figure 37: Flow Diagram for Updating CMO....88
Figure 38: Spectral Calibration Parameter diagram....90
Figure 39: Neon calibration scheme using fringe count interpolation approach 92
Figure 40: Radiometric Calibration Parameter Diagram....94
Figure 41: Radiometric model when the scene is the ICT 99
Figure 42: Interpolated Temperature Corrections for SSM Baffle (notional)....104
Figure 43: Moving average window updating (example case N^{ma} = 5)....107
Figure 44: Relative error causes by combining many blackbodies (N=30)....108
Figure 45: Relative error caused by combining many blackbodies (N=8) 109
Figure 46: Throughput delay in measurement sequence with $N^{ma}=30$ 110

Figure 47: Geometry of the detector field of view and Earth ellipsoid intersection 112
Figure 48: Sensor Algorithm Level Coordinate Systems 113
Figure 49: Geometric Calibration Parameter Diagram....114
Figure 50: Coordinate System Defined By Reference Cube 115
Figure 51: Orbital Coordinate System (OCS) 116
Figure 52: Earth Centered Inertial (ECI) 117
Figure 53: Earth Centered Earth Fixed (ECEF) or Earth Centered Rotating (ECR)....117
Figure 54: World Geodetic System 1984 (WGS84)....118
Figure 55: Topocentric-Horizon Coordinate System (THCS)....118
Figure 56: Roll, Pitch and Yaw Rotations 119
Figure 57: Geometric Calibration Algorithm Partitioning....120
Figure 58: Sample of CrIS FOVs Footprint on a Perfect Plane 124
Figure 59: General flow diagram for the radiometric and spectral calibration....127
Figure 60: Input Data Handling Flow Chart....141
Figure 61: Compute Spectrum Flowchart 143
Figure 62: Moving Average Flowchart 147
Figure 63: Laser Diode Wavelength Calibration Flowchart....150
Figure 64: LWIR Laser Diode Wavelength Monitoring Flowchart 153
Figure 65: Spectral Axis Labeling and Alias Unfolding Flowchart....155
Figure 66: Radiometric Complex Calibration Flowchart....157
Figure 67: ICT Radiance Calculation 160
Figure 68: Spectral Correction Flowchart 162
Figure 69: Self-Apodization Matrix Operator Computation 163
Figure 70: Non-linearity Correction Flowchart 166
Figure 71: NEdN Estimation Flowchart....170
Figure 72: Fringe Count Error Computation Flowchart....175
Figure 73: Interferogram decimation and alias unfolding....189

LIST OF TABLES

Table 1: Description of various global identifiers 11
Table 2: CrIS specifications 32
Table 3: FOV shape characteristics 34
Table 4: CrIS signal dimensions 35
Table 5: Long Wave array dimensions 37
Table 6: Middle Wave array dimensions 38
Table 7: Short Wave array dimensions 38
Table 8: Array dimensions and computing times (PII, 350 MHz) 39
Table 9: Resampling parameters for each band 61
Table 10: Error evaluation due to Dirac's delta approximation 73
Table 11: Summary of standard deviation error [%] 75
Table 12: Parameters for the post calibration filter $f_b[k]$ 77
Table 13: Blackman-Harris coefficients 85
Table 14: Symbols description for the ICT radiometric model 101
Table 15: Fraction of View from ICT Bottom Surface to Each Environment Surface (notional) 102
Table 16: SSM Baffle Temperature Offset Correction versus Orbit Position (notional) 103
Table 17: Tunable Parameters Reported via the Four Minute Engineering Telemetry RDR 128
Table 18: Tunable Parameters Provided via Configuration Files 131
Table 19: Parameters Monitored via the Eight Second Science Telemetry RDR 142
Table 20: Parameters Continuously Monitored via the Four Minute Engineering Packet RDR 143
Table 21: RDR Quality Flags in RDR Status Word 178
Table 22: SDR Quality Flags 179
Table 23: CrIS Product Levels Classification 196

DOCUMENT CHANGE RECORD

Issue	Rev.	Date	Chapter/Paragraph Number, Change Description (and Reasons)
ABB Draft	–	26 February 1999	Draft of document
ABB	–	26 March 1999	First release of document
ABB	A	21 April 1999	PDR release. Small modifications according to comments and baseline changes.
ABB 1	B	27 April 2001	Post DDR release. Updated ICT radiometric model, radiometric calibration and ILS correction schemes. Updated sampling wavelength and array size. Clarified explanations about fringe count error handling.
ABB 2	-	25 May 2001	Revised post DDR release. High level architecture of processing algorithm follows specification. Minor corrections to reflect updated CrIS instrument baseline.
ABB 2	A	15 February 2002	Post CDR release. Many updates. More accurate ICT radiometric model with respect to SSM. More details about NEdN estimates. More accurate description of FFT algorithm (PFBA) used. Modified modular decomposition of algorithm implemented by the new Science Code architectural design. More details about laser diode calibration and monitoring in Modules Definition section.
ABB 2	B	27 February 2003	Updated figures and tables with updated instrument design parameters. The following figures of the current document have been updated/added: 3, 4, 6, 7, 8, 10, 14, 15, and 34. The following table has been added: 3. The following sections of the current document have been updated/improved: 2.1, 3.3, and 4.1. A new section (3.5.6) has been added to outline an ILS retrieval algorithm.
ITT	A	20 October 2003	The geometric calibration section (6) has been completely revised. A table summarizing quality controls has been added to section 7.7.5.
ITT	B	30 June 2004	NGST rev D SPCR ALG00000456 Update CrIS SDR – J. Done Reference Sec 2.1.1.1 in [RD 34] for algorithm changes added to Sec 2.5.4, 2.6.1, 5.3, 6.5, 7, 7.5,.1, 7.7.2, & 7.7.5. [RD 34] add to Sec 1.4

ITT	C	2007-2008	Sec 1.4: Added [RD 34 through 52] Sec 2.5.4 update as per Sec, 2.1.1.1 in [RD 35] Sec 3: added a new sub-section, section 3.4, to explain lunar intrusion Sec 3 format change: As a result of the above the original section 3.4 is changed to 3.5, all following Section 3 subsections changed accordingly. Sec 3.3.3 Added detail and references for FCE detection derivation for equation 14. Updated equation 15 to include 2pi phase unwrap function that is described in text below equation. Substantial text added to this section to describe FCE detection methodology and changes to make FCE detection more reliable for cold earth scenes. Figure 19a, 19b and 19c added that describes FCE processing flow. Corrected typo in equation 22……added missing "n" term to match equation in Section 7.3.2 Sec 3.4: (Format change to 3.5) Equation (25) updated to match with latest ABB analysis. Sec. 3.5.3: (Format change to 3.6.3) Equation (37) added to reflect the robust implementation of the ILS equation (34). Sec. 3.5.5: (Format change to 3.6.5) Updated LW and SW post calibration filter coefficients in Table 12. Sec. 3.5.6: (Format change to 3.6.6) ILS retrieval section re-written to match with ITT retrieval process. Sec 3.7.1: Improved numerical precision of equation (51) to 5 decimal places. Sec 4.1 Fixed missing lines in Figure 34 and fixed wrong subscript (typo) on one parameter. Sec. 4.2: Updated to reflect the algorithm update that minimizes the false alarms by averaging of the laser diode temperature and current telemetry across the 4-minute moving average window. Also added wording to describe how and when monitored laser wavelength is used to update CMO. Sec 5.3: Equations 70 through 73 altered to reflect how SDR Algorithm actually computes radiometric calibration and to show how F_{int} operator cancels out and is not needed. Sec 5.4: Corrected subscripts in equation (74a) to distinguish between effective ICT emissivity and surface ICT emissivity. Added equation (74b) describing relationship between surface and effective emissivity. Added text to clarify new equation. Added variable definitions. Made subscripts of variables consistent throughout section.

ITT	C	2007-2008	(Continued) Sec 5.5: Added an outline of ICT temperature readout algorithm based on [RD 36]. Added the new reference [RD 36] to Sec. 1.4 Sec 6.3: Updated the 'Engineering Data' part of the section, to incorporate use 30 cross-track locations and 30 in-track offsets derived from test data. Sec. 7: Format change – bullets 19 through 27 changed to 1 through 9. Updated Figure 53 – added Lunar Intrusion block. Sec. 7.3.2: Updated Figure 56 to include averaging of laser diode telemetry parameters – Laser Diode Temperature and Current. Sec. 7.4.2: Updated laser diode drift monitoring outline to comply with the calculations using the windowed average. Flow chart in Figure 58 is also updated accordingly. Sec. 7.7.2: Revised the section to reflect to match with the C++ implementation of the Fringe Count Error Handling. algorithm Sec 8: Mentioned in the summary paragraph about ITT implementation of the SDR algorithm in C++ code. Revised the paragraphs on Scientific Code and Final Word to reflect latest status on SDR Scientific Code.

ITT	C	2007-2008	Sec 6.5: Most contents of this section deleted since this is now responsibility of S/C contractor Sec 7: Geolocation subparagraph changed to reflect ITT responsibility…..LOS calculation relative to S/C body Sec 7.1: Added table defining contents of engineering packet used for initialization. Added table of configuration file contents used for initialization. Sec 7.2: Added table showing contents of 8 second science telemetry used for calibration maintenance. Added table showing parameters in engineering packet continuously monitored for spectral calibration maintenance. Sec 7.4.2: Updated Figure 58 to indicate laser diode current and temperature are averaged Sec 7.5.1: Updated radiometric calibration equation in Figure 60 to match equation (72) of Sec 5.3. Added definition for cold target radiance. Sec 7.5.2.1: added note on how ICT surface emissivity calculated Sec. 7.7.1 and sub-section 7.7.1.1: Revised the sections to match the description with the new NEdN Estimation algorithm based on ICT measurements. Sec. 3.3 and sub-sections 3.3.1 through 3.3.4: Updated and added clarity to the Fringe Count Error Handling descriptions by providing details and block diagrams to explain the FCE detection and correction process Sec 7.7.2, 7.7.3, 7.7.4 and the sub-sections: Updated and added clarity to the material on Fringe Count Error Handling, Fringe Count Error Detection and Fringe Count Error Correction. Sec 7.7.5: Added two tables defining quality flags at SDR output Sec 1.6.4 Update FOR index definition for nadir and SSM slew

ITT	D	2008	Entire document: Fix print problem for equation numbers so that equation number prints same as viewed on screen.
ITT	D	2008	Section 5.4, Updated the ICT Environmental Model
ITT	D	2008	Section 3, Added section on non-linearity correction. Non-linearly corrected spectra will be underlined and spectra which have undergone non-linearity correction will not be underlined.
ITT	D	2008	Section 7, Updated figure 53 to include non-linearity correction
ITT	D	2008	Section 7.4.2 Updated radiometric section to reflect revised ICT environmental model
ITT	D	2008	Section 7.4.4 Updated Non-linearity correction module
ITT	D	2008	Section 1.4 Added references 53 through 55 to list
ITT	E	2009	Reordered paragraphs in Section 3.3.1 and deleted question
ITT	E	2009	Added section 3.8 describing how CMO is calculated and when it is updated
ITT	E	2009	Added Figure 37 illustrating processing flow in updating CMO from engineering packet
ITT	E	2009	Modified Section 4.2 & Section 7.4.2 to describe laser wavelength monitoring as quality control only. Eliminated references of laser monitoring triggering a CMO update. Updated Figure 65 equations
ITT	E	2009	Made table numbers, figure numbers and references to figures and tables consistent throughout document and index. All figures were renumbered to be consecutive.
ITT	E	2009	Updated Table 18 to show all engineering packet parameter categories (New….ECM model, nonlinearity, band specific neon wavelength & truncated ICT emissivity spectral range in tables for in-band emissivity only)
ITT	E	2009	Updated Table 19 to show all configuration file parameters used by SDR Algorithm and to better describe what these parameters are.
ITT	E	2009	Updated Table 3 with latest FOV dimensions
ITT	E	2009	Updated labels in Tables 4, 5, 6 & 7
ITT	E	2009	Fixed text reference for Eq. 8i & Eq 8j
ITT	E	2009	Update syntax for Eq 20, 21 23a, 23b, 23c.
ITT	E	2009	Changed subscript to indicate band on Eq 47
ITT	E	2009	Eq 63 updated to match SDR code and added i subscript
ITT	E	2009	Section 3.5 Updated wording to relate λ^{CMO} to spectral resampling. Clarification that laser does not drift. Section 3.6.6

ITT	E	2009	Added notes about gas ILS testing used to fine tune spectral correction during TVAC testing
ITT	E	2009	Section 4.1.2 Added comment on metrology laser wavelength being tailored specific to band.
ITT	E	2009	Added Section 3.8 describing how and when CMO is recalculated
ITT	E	2009	Clarified wording in Section 5.4 that explained how new ICT radiance model for environment worked.
ITT	E	2009	Section 5.4.1 Deleted contents of entire section containing radiometric error analysis and replaced with reference to ITT's radiometric uncertainty compliance document
ITT	E	2009	Section 5.4.2 Updated all equations (75 to 78C) for new ICT environmental model and revised Table 15 with parameter descriptions for new model
ITT	E	2009	Section 5.4.2.1 Edited section describing SSM scan baffle temperature compensation for clarity
ITT	E	2009	Table 15 was updated to define parameters of environmental model
ITT	E	2009	Section 7.3.1 Changes include all subsections. Interferogram to spectral conversion technical description was updated to match SDR code implementation.
ITT	E	2009	Figure 63 Equations updated to match SDR code implementation and added missing equations from previous version of ATBD
ITT	E	2009	Section 7.3.2 Changes include all subsections. Moving window averaging updated to match SDR code implementation. Better captures how FCE correction is applied in moving window. Better description of parameters used in equations.
ITT	E	2009	Figure 64 Updated moving window equations, input & output defined to match SDR code implementation. Added missing equations from prior version of ATBD. Added FCE correction to moving window
ITT	E	2009	Section 7.4.1 Neon calibration description updated for 3 metrology wavelengths calculated, one for each band. Explain exception handling.
ITT	E	2009	Section 7.4.2 Added cautions on wavelength monitoring function
ITT	E	2009	Figure 66 equations on wavelength monitoring were clarified
ITT	E	2009	Section 7.4.3 Spectral axis labeling updated to match SDR code implementation and better explain parameters used.
ITT	E	2009	Figure 67 Equations describing conversion of interferogram to spectra updated to match SDR code implementation and show more detail

ITT	E	2009	Section 7.5.1 Radiometric calibration description updated for clarity, better parameter descriptions and explain exception handling.
ITT	E	2009	Figure 68 Radiometric equations updated to show more detail
ITT	E	2009	Section 7.5.2 Updated with more clear description of ICT radiance calculation and new environmental model.
ITT	E	2009	Figure 69 Equations updated to describe current ICT environment radiance model.
ITT	E	2009	Section 7.5.3 Spectral correction using CMO updated for clarity.
ITT	E	2009	Figure 70 Updated to be consistent with SDR code.
ITT	E	2009	Section 7.5.3.2 CMO computation updated to reflect SDR code and for clarity. Better description of equation parameters.
ITT	E	2009	Figure 72 Equations describing CMO computation updated to reflect SDR code and for clarity. Equations now more detailed on CMO formulation.
ITT	E	2009	Section 7.5.4 Nonlinearity updated to reflect SDR code and for clarity and exception handling. Better description of all parameters used in nonlinearity correction
ITT	E	2009	Figure 73 Nonlinearity correction equations updated to reflect SDR code implementation
ITT	E	2009	Section 7.6 NEdN estimator descriptions enhanced to describe computation better and output reporting properties. Better describe parameters used in equations.
ITT	E	2009	Figure 74 updated with better equation detail
ITT	E	2009	Section 7.6.3 now indicated FCE uses LWIR only. More detail given in equations 100 through 103.
ITT	E	2009	Figure 75 equations updated, added missing equations, flag computation described and output descriptions
ITT	E	2009	Section 7.6.5 Data quality indicators for RDR and SDR updated to match current SDR code implementation. Tables 22 and 23 updated to match current implementation.
ITT	E	2009	Section 8.0 Removed obsolete wording and added wording about version 2.18 SDR code
ITT	E	2009	Removed proprietary markings from cover sheet & changed titles
ITT	E	2009	Reformatted header to indicate ITT document number and ITT logo and added ITAR statement to footer
ITT	E	2009	Removed ABB cover sheet & sign off authority
ITT	E	2009	Removed hidden text.

1. INTRODUCTION

1.1 PURPOSE OF DOCUMENT

The purpose of this document is to define the SDR Level 1B algorithms needed on ground in order to produce meaningful data meeting all the requirements of the CrIS instrument. Level 1B data is made of geolocated, radiometrically and spectrally (spatial frequency) calibrated spectra with annotated quality indicators.

The Cross-track Infrared Sounder (CrIS) is a part of the National Polar-orbiting Operational Environmental Satellite System (NPOESS) series of polar-orbiting spacecrafts. The CrIS *sensor* forms a key component of the larger Cross-track Infrared/Microwave Sounding Suite (CrIMSS) and is intended to operate within the context of the CrIMSS architecture. It also provides supporting measurements for a variety of other geophysical parameters.

The CrIS instrument is a Michelson interferometer infrared sounder covering the spectral range of approximately 3.9 to 15.4 microns. CrIS provides cross-track measurements of scene radiance to allow the calculation of temperature and moisture vertical distributions in the Earth's atmosphere.

1.2 SCOPE

This document presents the theoretical basis of the CrIS SDR Algorithms. This document takes precedence over prior versions of this document as well as prior presentation material from DDR and CDR on the CrIS program since the SDR algorithm has evolved over time. The functional flow of algorithms required to transform Raw Data Record (RDR) coming from the satellite into Sensor Data Record (SDR) are described. These SDR are then transformed into Environmental Data Record (EDR). Physical retrievals of atmospheric parameters from infrared spectra are computed by accurate radiative transfer models, known as forward models, relating the atmospheric parameters to the observed channel radiances. The CrIS forward model is described in another document and is not presented here.

This document describes the CrIS SDR Algorithms specific processing required at the ground segment. It covers the processing needs for all data being sent to ground when the instrument is operational, including observational and calibration data, for all measurements performed by the instrument. The algorithms for decoding and calibrating the calibration data (e.g. generation of ICT radiance) are also covered here.

However, the present document does not cover the data manipulation related to all instruments of the NPOESS platform. In other words, it is assumed that the data entering the SDR algorithm processing chain is identical to the CCSDS formatted data leaving the instrument on board. The processing of the data produced when the instrument is under test or characterization, e.g. during the Commissioning Phase, is excluded. The operational and processing steps required during the Commissioning Phase will be addressed in the CrIS Calibration/Validation Master Plan (ITT document #8180003). This will identify how CrIS is to be calibrated, what the baseline operational scenario is, how this scenario can be verified, etc.

The government considers the SDR and EDR algorithms adopted, adapted, or developed by the CrIS contractor to be scientific, rather than operational, algorithms. The CrIS contractor is not responsible for identifying or developing operational SDR and EDR algorithms for the CrIS.

1.3 DOCUMENT OVERVIEW

This document contains the SDR definitions for all the data processing algorithms. Chapter 1 serves as an introduction for the definition of various terms and concepts related to the CrIS instrument and data. Chapter 2 presents the SDR Algorithms principles and CrIS instrument characteristics. Chapter 3 describes special critical considerations for the SDR Algorithms design. Chapter 4, 5, and 6 discuss the spectral, radiometric, and geometric calibration respectively. Finally Chapter 7 gives a description of specific modules and functions and gives detailed information about the way that they should be applied. Assumptions, trade studies, alternatives, and justifications are given to highlight the choice of particular algorithms.

1.4 REFERENCE DOCUMENTS

No. **Reference and Title**

[RD 1] CCSDS 701.0-B.2, CCSDS Recommendations for Space Data, System Standards Telecomm and Part 3: Data Management, Service, Architectural Definition, Issue 1, Jan 87.

[RD 2] J. R. Birch and F. J. J. Clarke, “Fifty categories of ordinate error in Fourier transform spectroscopy” Spectroscopy Europe 7/4, 16 – 22, 1995.

[RD 3] H. E. Revercomb, H. Buijs, H. B. Howell, D. D. Laporte, W. L. Smith, and L. A. Sromovsky, “Radiometric calibration of IR Fourier transform spectrometers: solution to a problem with the High-Resolution Interferometer Sounder”, Appl. Opt., Vol. 27, No 15, pp. 3210–3218, Aug. 1988.

[RD 4] James W. Brault, “Fourier Transform Spectrometry”, National Solar Observatory, Tucson, Arizona, 1984.

[RD 5] C. Temperton, “Implementation of a self-sorting in-place prime factor FFT algorithm”, Journal of Computational Physics, Vol. 58, pp. 283–299, 1985.

[RD 6] C. Temperton, “A new set of minimum-add rotated DFT modules”, Journal of Computational Physics, Vol. 75, pp. 190–198, 1988.

[RD 7] CrIS Engineering Demonstration Model (EDM) Test Results: Technical interchange Meeting (TIM) at Bomem, 5 – 6 October 1998.

[RD 8] ”Correction of the non-linearity of FT remote sensing instruments”, Richard L. Lachance, André Villemaire, and Luc Rochette, Third Workshop on Infrared Emission Measurements by FTIR, Quebec, Feb. 4 – 6 1998.

[RD 9] “Spectral line-shape distortions in Michelson interferometers due to off-focus radiation source”, Pekka Saarinen and Jyrki Kauppinen, Appl. Opt., Vol. 31, No. 13, May 1992, pp. 2353 – 2359.

[RD 10] C.D. Barnet, J.M. Blaisdell and J. Susskind, "An analytical transformation for use in computation of interferometric spectra for remote sensing applications", IEEE Trans. Geosci. Remote Sens. Vol. 38, pp. 169–183, 2000.

[RD 11] E. O. Brigham, “The Fast Fourier Transform”, Prentice hall, Englewood Cliffs, New Jersey, 1974.

[RD 12] F. J. Harris, *Proceedings of the IEEE*, Vol. 66, (1978) 51.

[RD 13] Neon Wavelength Measurement System, System Description, ITT-BOM-014/97, Issue 1, Nov 7, 1997.

[RD 14] C. Weddigen et al., “Phase corrections for the emission sounder MIPAS-FT”, Appl. Opt. 32, 4586–4589, 1993.

[RD 15] E. E. Bell, “The use of asymmetric interferograms in transmittance measurements”, *J. Physique Colloq.* No. 2, 28, 18 – 25, 1967.

[RD 16] J. R. Birch, “Imperfect optical figure in Fourier transform spectroscopy”, *Infrared Physics*, 30, 155 – 159, 1990.

[RD 17] “Clouds and the Earth’s Radiant Energy System (CERES) ATBD”, Volume II – Geolocation, Calibration, and ERBE-Like Analyses (Subsystems 1-3), CERES Science Team, NASA Langley Research Center, Hampton, Virginia.

[RD 18] M. Frigo and S. G. Johnson, “The Fastest Fourier Transform in the West”, Massachusetts Institute of Technology, http://www.fftw.org.

[RD 19] W. H. Press, S. A. Teukolsky, W. T. Vetterling, and B. P. Flannery, *Numerical Recipes in C: The art of scientific computing*, Second Ed., Cambridge University Press, 994 p., 1992.

[RD 20] R. L. Burden and J. D. Faires, “Numerical Analysis”, Fourth Ed. PWS-KENT Publishing Company, Boston, 1988. [RD 20]A. Chedin, N. A. Scott, C. Wahicle, and P. Moulinier, 1985: “Contribution to the development of radiative transfer models for high spectral resolution observations in the infrared”. *J. Quant. Spectrosc. Radiat. Transfer*, Vol. 53, No. 6, pp. 597–611. (TIGR)

[RD 21] P. R. Bevington and D. K. Robinson, *Data reduction and error analysis for the physical sciences*, Second Edition, McGraw-Hill, Inc., New York, 328 p., 1992.

[RD 22] J. F. Hair, Jr., R. E. Anderson, R. L. Tatham, *Multivariate Data Analysis*, with readings", Second Ed., Macmillan Publishing Company, London, 449 p., 1987.

[RD 23] Erwin Kreyszig, *Advanced Engineering Mathematics,* Seventh Ed., John Wiley & Sons, Inc., New York, 1400 p., 1993.

[RD 24] CrIS SDR Document, Appendix A: Definition/Glossary of Terms, Revision 1998-04-17, R. J. Hertel, editor.

[RD 25] IPO CrIS Sensor Requirements Document (SRD), Revision 4/2/98

[RD 26] MIPAS, Michelson Interferometer for Passive Atmospheric Sounding, ESA ENVISAT-1 Instrument. http://envisat.estec.eas.nl/instruments/mipas,

[RD 27] IASI, Infrared Atmospheric Sounder Instrument, Alcatel.

[RD 28] SDR Scientific Code Description for the Cross Track Infrared Sounder (CrIS), BOM-CrIS-0084.

[RD 29] SDR Algorithms Requirements, ITT A/CD Document 8192900.

[RD 30] Architectural Design Document (ADD) for the CrIS Scientific Code, Volume 1, Sensor Data Records (SDR), BOM-CrIS-0078, Issue 2, 12 October 2001.

[RD 31] Joe Predina et al., Use of Apodization to Improve Quality of Radiometric Measurements from Interferometric Sounders, ITSC-12 Conference, February 2002

[RD 32] CrIS Calibration/Validation Master Plan, ITT doc #8180003

[RD 33] H. Goldstein, *Classical Mechanics*, Second Ed., Addison-Wesley, 1980.

[RD 34] M. Cromp, Operational Algorithm Description Document for the CrIS SDR Software, NGST D39132, 30 June 2004.

[RD 35] NPOESS Operational Algorithm Description Document for Cross-track Infrared Sounder (CrIS) Sensor Data Record (SDR), SDRL No. S 141, Raytheon, D39132 Rev A, 01 March 2006.

[RD 36] CrIS ICT Temperature Readout Algorithm, Version 6a, 8 May 2007

[RD 37] CrIS SDR Algorithms Detailed Design Review (DDR), 27 March, 2001 (NPOESS internal presentation package)

[RD 38] CrIS SDR Algorithms Critical Design Review (CDR), 22-23 January 2002, (NPOESS internal presentation package)

[RD 39] SDR Algorithm & ILS TIM, ITT Review with NGST, IPO NASA, 15 May, 2007, (NPOESS internal presentation package)

[RD 40] SDR Algorithm & ILS 'delta' TIM, ITT Review with NGST, IPO NASA, 19 September, 2007, (NPOESS internal presentation package)

[RD 41] SDR Algorithm Updates (version 2.13), 16 January, 2008, (NPOESS internal presentation package)

[RD 42] SDR Algorithm Updates (ICT Radiance Model, TLM Robustness, Nonlinearity), 7 February, 2008, (NPOESS internal presentation package)

[RD 43] BOM-CrIS-1005%20Draft-Derivation of the Spectra Resampling Matrix.pdf, 25 October 2006

[RD 44] Radiometry in Line Shape Modeling of Fourier Transform Spectrometers, Applied Optics 41(7), 1424 – 1432, 1 March 2002

[RD 45] Instrument Line Shape of Fourier Transform Spectrometers: analytic solutions for nonuniformly illuminated off-axis detectors, Applied Optics, Vol 38, No. 25, 1 September 1999

[RD 46] Derivation of Phase Extraction Function for Fringe Count Error Detection on Earth Scenes, ITT technical memo, 21 March 2008

[RD 47] Analysis to Determine Deep Space Envelope Threshold to Avoid Incorrect FCE Detection and Correction, 1 October 2007, ITT internal tech memo

[RD 48] Robust Implementation of self apodization equation, ITT internal technical memo

[RD 49] ILS Decomposition Software v2.3, Final Report, Telops, 24 October 2003

[RD 50] ILS Viewer Software, ATBD, Telops, 11 October 2002

[RD 51] BOM-CrIS-0108 ICT Radiometric Analysis, 14 April 2004, p24-25

[RD 52] Geolocation Baseline Letter (NGST & ITT partitioning of geolocation function, 18 July 2003

[RD 53] Correction of Instrument Line Shape in Fourier Transform Spectrometers Using Matrix Inversion / Applied Optics / Vol. 45, No. 21 / 20 July, 2006

[RD 54] Radiometry in Line Shape Modeling of Fourier Transform Spectrometers / Applied Optics / Vol. 41, No. 7 / March 2002

[RD 55] Matrix Form of the Instrument Line Shape in Fourier Transform Spectroscopy Using Matrix Inversion / Applied Optics / 45 (3), 2006

1.5 ACRONYMS

ADC	Analog to Digital Converted
AER	Atmospheric and Environmental Research Incorporated
ATBD	Algorithm Theoretical Basis Document
BB	Black Body
BS	BeamSplitter
CCSDS	Consultative Committee for Space Data Systems
CMO	Correction Matrix Operator
CPU	Central Processing Unit
CrIS	Cross-track Infrared Sounder
CrIMSS	Cross-track Infrared/Microwave Sounding Suite
DA	Dynamic Alignment
DFT	Discrete Fourier Transform
DOD	Department of Defense
DS	Deep Space
DSP	Digital Signal Processor
ECEF	Earth Centered Earth Fixed
ECI	Earth Centered Inertial
ECR	Earth Centered Rotating
ECT	External Calibration Target
EQM	Engineering and Qualification Model
EDR	Environmental Data Record
EMI	Electro-Magnetic Interference
EOS	End of Scan
ES	Earth Scene
ESA	European Space Agency
ET	Elapsed Time
FCE	Fringe Count Error
FFT	Fast Fourier Transform
FIR	Finite Impulse Response
FLOP	Floating Point Operation
FOR	Field of Regard
FOV	Field of View
FTS	Fourier Transform Spectrometer
FWHM	Full Width at Half Maximum
GEO	Geosynchronous Earth Orbit
GST	Greenwich Sidereal Time
HgCdTe	Mercury-Cadmium-Telluride
IAR	Instrument Alignment Reference
IBR	Instrument Bench Reference
ICS	Instrument Coordinate System

ICT	Internal Calibration Target
IF	Intermediate Frequency
IDPS	Interface Data Processing Segment
IERS	International Earth Rotation Service
IFFT	Inverse Fast Fourier Transform
IGM	Interferogram
ILS	Instrument Line Shape
IMC	Image Motion Compensator
INT	Interferometer
IOA	Interferometer Optical Axis
IPO	Integrated Program Office
IR	Infra Red
LOS	Line Of Sight
LWIR	Long Wavelength InfraRed
MCT	Mercury Cadmium Telluride
MPD	Maximum Path Difference
MFLOP	Million FLOP
MWIR	Mid Wavelength InfraRed
NEdN	Noise Equivalent Differential Radiance
NEdT	Noise Equivalent Differential Temperature
NIST	National Institute of Standards and Technology
NL	Non-Linear
NLS	Natural Line Shape
NOAA	National Oceanic and Atmospheric Administration
NPOESS	National Polar-orbiting Operational Environmental Satellite System
OCS	Orbital Coordinate System
OBT	On Board Time
OPD	Optical Path Difference
P/S	PorchSwing
PC	Photo-Conductive
PDR	Preliminary Design Review
PFA	Prime Factor Algorithm
PFBA	Prime Factor Based Algorithm
ppm	Part Per Million
PRT	Platinum Resistance Thermometer
PV	Photo-Voltaic
RDR	Raw Data Record
RMF	Rotating Mirror Frame
RMS	Root Mean Square
RSS	Root Sum Squared
S/C	Spacecraft
SADR	Spacecraft Attitude Determination Reference

SBF	Spacecraft Body Frame
SBT	Satellite Binary Time
SCS	Spacecraft Coordinate System
SDR	Sensor Data Record
SEU	Single Event Upset
SFR	System Functional Review
SNR	Signal-to-Noise Ratio
SPC	Spectrum
SRD	Sensor Requirement Document
SSMF	Scene Selection Mirror mounting feet Frame
SSMR	Scene Selection Module Reference
SSPR	Spacecraft System Performance Responsible
SWIR	Short Wavelength Infrared
SZA	Solar Zenith Angle
TDI	Time Delay and Integration
TE	Thermo-Electric
THCS	Topocentric-Horizon Coordinate System
TIGR	TOVS Initial Guess Retrieval
TIM	Technical Interchange Meeting
TIROS	Television InfraRed Observational Satellite
TLM	Telemetry
TOA	Top Of Atmosphere
TOVS	TIROS-N Operational Vertical Sounder
TSPR	Total System Performance Responsible
UT	Universal Time
UT1	Universal Time with 1/1/2000 noon epoch
UTC	Universal Time Coordinated
WGS84	World Geodetic System 1984
ZPD	Zero Path Difference
N/A	Not applicable, none
TBC	To Be Confirmed
TBD	To Be Determined
TBR	To Be Reviewed
TBS	To Be Supplied

Units

cm	centimeter
cm^{-1}	wavenumber
count	count
day	day, Julian day
deg	degree

h	hour
K	Kelvin
μm	micrometer, micron
nm	nanometer
rad	radian
sec	second
sr	steradian
[a.u.]	Arbitrary units
[d.u.]	Digitalization units (ADC or digital counts)
[n.u.]	No units (also called *dl* for “dimensionless”)
[r.u.]	Radiance units: $\frac{mW}{\mathrm{m}^2\,\mathrm{sr}\,\mathrm{cm}^{-1}}$

1.6 NOTATION AND SYMBOLS

This section gives the general description of all the notation conventions and mathematical symbols used throughout this document.

1.6.1 Notation and Operators

$\{\ \}$	Routine or process arguments, e.g. $\mathsf{F}\{x\}$
$(\ )$	Mathematical function argument, e.g. $\cos(\alpha)$, and also
	Range of mathematical vectors, e.g. $I(x)$, $S(\sigma)$
$[\ ]$	Index of numerical discrete arrays, e.g. $I[n]$, $S[m]$
$\langle\ \rangle$	Mean value, e.g. $\langle T \rangle$

1.6.2 Predefined Functions and Operators

$\widetilde{Q}$	Complex quantity, as opposed to real quantity noted without tilde ($\sim$)
$\mathrm{Re}\{\ \}$	Real part of a complex argument
$\mathrm{Im}\{\ \}$	Imaginary part of a complex argument
$\mathsf{F}\{\ \}$	Direct Fourier transform operator
$\mathsf{F}^{-1}\{\ \}$	Inverse Fourier transform operator
$\mathrm{FFT}\{\ \}$	Numerical discrete Fast Fourier Transform
F_{INT}	Instrument effect operator

1.6.3 List of Symbols Used

i	Complex unit: $i^2 = -1$	
λ_L	Laser diode wavelength [cm]	(e.g. 1550×10^{-7} cm)
λ_S	Sampling wavelength [cm]	(e.g. $\lambda_S = \lambda_L/2$, 775×10^{-7} cm)
x	Optical path difference [cm]	
σ	Wavenumber [cm^{-1}]	
σ_s	Sampling frequency of the reference metrology [cm^{-1}] ($=1/\lambda_S$)	
σ_{Max}	Spectral range maximum frequency [cm^{-1}] ($=\sigma_s/2$)	
Δx	Sampling interval [cm]	
$\Delta\sigma$	Spectral interval, also called wavenumber spacing [cm^{-1}]	
ϕ	Phase function ($\widetilde{S}(\sigma) = A(\sigma)\, e^{i\phi(\sigma)}$) [rad]	
φ	Linear phase dependency [rad]	
θ	CrIS Scan Mirror Angle [deg]	
Γ	Slant path viewing angle (Local sea level FOV center elevation angle to spacecraft)	

Φ_C	Geocentric latitude [deg], range [–90..90]
Φ_G	Geodetic latitude [deg], range [–90..90]
Λ_C	Earth fixed longitude [deg], range [–180, +180], Geocentric or Geodetic
α	Azimuth angle [deg]; angle of incidence of off-axis rays in interferometer
β	Elevation angle [deg]
T	Temperature [K]
N	Number of points in numerical arrays
n, m	Interferogram and spectrum data points indices $[0,\ldots,N\text{-}1]$
h	Fringe count error shift (integer)
$\otimes$	Convolution operator ($\oplus$ is the Correlation operator)

1.6.4 Identifiers Notation

Symbol convention:

$\widetilde{I}(x)$	Interferogram (IGM), (complex function), digitalization units [d.u.]
$I(x)$	Interferogram (IGM), (real function), digitalization units [d.u.]
$\widetilde{S}(\sigma)$	Measured raw spectrum (SPC), (complex function), arbitrary units [a.u.], corrected for non-linearity
$\underline{\widetilde{S}}(\sigma)$	Measured raw spectrum (SPC), (complex function), arbitrary units [a.u.], NOT corrected for non-linearity
$L(\sigma)$	Radiance, radiance units [r.u.]
$BB(\sigma, T)$	Planck function, radiance units [r.u.]
$A(\sigma)$	Signal amplitude ($\widetilde{S}(\sigma) = A(\sigma)\, e^{i\phi(\sigma)}$) [a.u.]
$\widetilde{O}(\sigma)$	Instrument Offset, (complex function), (see expression in Section 5.2)
$\widetilde{G}(\sigma)$	Instrument Gain, (complex function), (see expression in Section 5.2)

General superscripts referring to generic calibration:

X^C	Cold calibration reference measurement
X^H	Hot calibration reference measurement
X^S	Scene measurement

Equivalent superscripts referring to actual CrIS measurements:

X^{ds}	Deep Space measurement ($\equiv X^C$)
X^{ict}	Internal Calibration Target measurement ($\equiv X^H$)
X^{es}	Earth Scene; atmospheric measurement ($\equiv X^S$)

in Contribution from the interior of the interferometer, not coming from the FOV.

ext Contribution from the outside of the interferometer, as viewed through the FOV.

Complexity operator:

$O(\ )$ "Complexity" of an algorithm, standing for *of the order of*. The number of operations (or the time of computation) for the specified algorithm is proportional to the argument given.

Table 1: Description of various global identifiers

$$I^{type}_{b,p,d,i}[index]$$

Variable	Descriptive name	Details
superscript	*Type of signal*	
ds	Deep Space	
ict	Internal Calibration Target	
es	Earth Scene	
subscript	*Signal identification*	
b	Band index	1 = LW, 2 = MW, 3 = SW
p	FOV number	1 – 9
d	IGM sweep direction index	0 = forward, 1 = reverse
i	FOR index	Earth Scene $1 \le i \le 30$, ICT i=0, DS i=31, Nadir i=33, SSM slew/nonstandard = 32
$index$	*Element indices*	
m	Interferogram spatial index	$0 \le m \le N_b - 1$
n	Spectrum frequency index	$0 \le n \le N_b - 1$

Note: On all equations, the *prime* identification (e.g. $I'^{ds}_{b,p,d}$) refers to a transformed signal.

In the following processing, all numerical arrays are treated with origin zero.

1.6.5 Mathematical Definitions

Fourier Transform:

Continuous domain:

$$S(\sigma) = \int_{-\infty}^{\infty} I(x)\, e^{-2\pi i \sigma x} dx$$
$$I(x) = \int_{-\infty}^{\infty} S(\sigma)\, e^{+2\pi i \sigma x} d\sigma \qquad (1)$$

Discrete domain:

$$S[n] = \Delta x \sum_{m=0}^{N-1} I[m]\, e^{-2\pi i m n / N}$$
$$I[m] = \Delta \sigma \sum_{n=0}^{N-1} S[n]\, e^{+2\pi i m n / N}$$

With the following notation indicating the relation between the two spaces (see Appendix 9.1 for more details):

$$S(\sigma) \leftrightarrow I(x)$$

Convolution:

$$\begin{aligned} h(\sigma) &= f(\sigma) \otimes g(\sigma) \\ &= \int_{-\infty}^{\infty} f(u)\, g(\sigma - u)\, du \\ &= \mathsf{F}^{-1}\{\mathsf{F}\{f(\sigma)\} \times \mathsf{F}\{g(\sigma)\}\} \end{aligned} \qquad (2)$$

Planck Function:

$$B(\sigma\ [\mathrm{cm}^{-1}], T\ [K]) = \frac{c_1 \sigma^3}{e^{(c_2 \sigma / T)} - 1}\ [\mathrm{r.u.}] \qquad (3)$$

with the radiation constants: $c_1 = 1.1910427 \times 10^{-5}\ \mathrm{cm}^3 \mathrm{mW}/(\mathrm{m}^2 \mathrm{cm}^{-1})$

$c_2 = 1.4387752\ \ K\,\mathrm{cm}$

Sinc Function:

$$\mathrm{sinc}(a\,x) \equiv \frac{\sin(\pi\, a\, x)}{\pi\, a\, x} \qquad (4)$$

Standard deviation:

$$\mathrm{Stdev}\{V\} = \sqrt{\frac{1}{N-1} \sum_{i=0}^{N-1} \left(V_i - \langle V \rangle\right)^2} \qquad (5)$$

where N is the length of the vector V

2. SDR ALGORITHMS PRINCIPLES

The CrIS system is defined as a space borne sensor and ground-based scientific algorithms. The development of scientific algorithms is necessary to define the methods for calibrating and co registering raw sensor data and for producing the environmental data required by the users. This data is delivered to the users in the form of Raw Data Records (RDRs), Sensor Data Records (SDRs), and Environmental Data Records (EDRs). Figure 1 below indicates the functional interdependence of these elements, and the bold lines and shaded modules reflect the elements specific to the SDR Algorithms presented in this document.

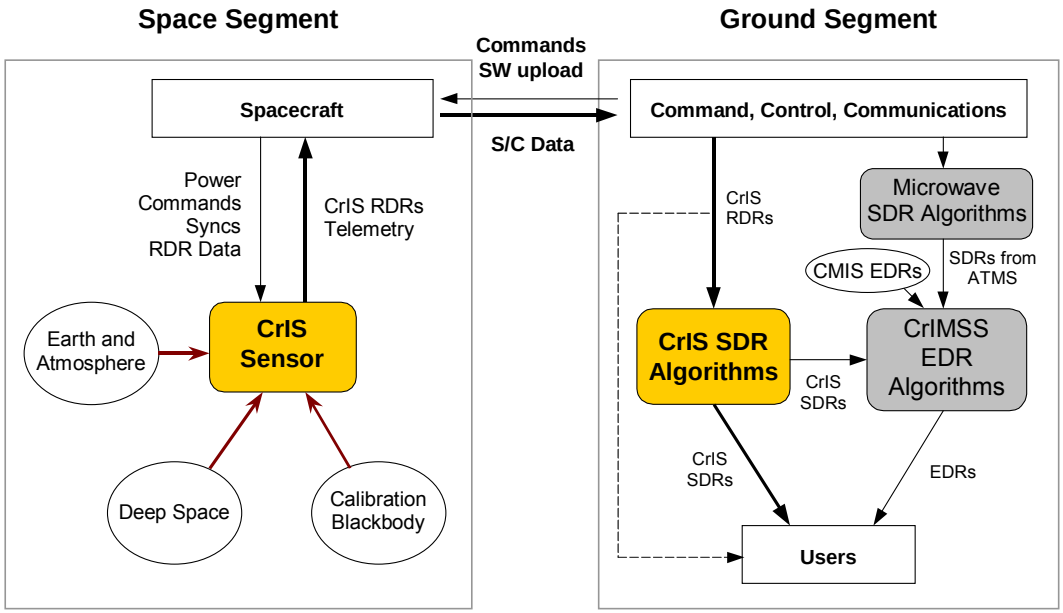

Figure 1: CrIS System Segments

Level 1B ground segment algorithms are required to transform raw instrument records (RDR) into sensor data records (SDR), which are essentially calibrated spectra. Auxiliary data will also be used in conjunction with several indicators to address the accuracy of the data. The SDRs are subsequently transformed into environmental data records (EDR) by another algorithm not presented in this document. Figure 2 shows the summary of the data processing flow between the measured radiance and the delivered EDR. All the needed functions are identified and described in this document, accompanied by all required major concepts and key equations.

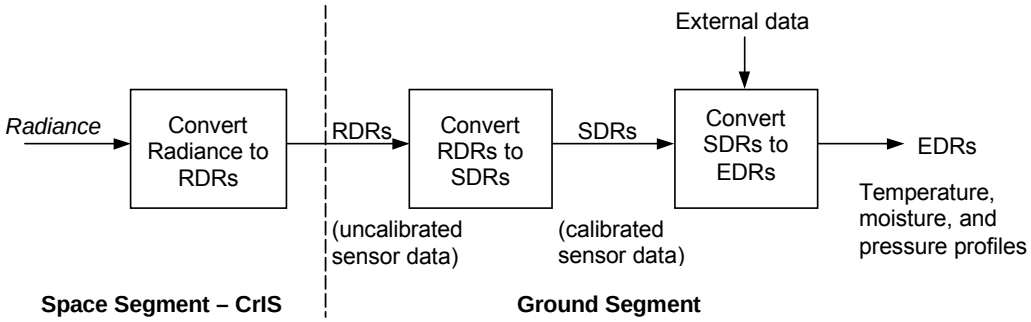

Figure 2: Data processing flow at various levels

2.1 OBJECTIVE OF THE SDR ALGORITHMS

Generally speaking, the SDR Algorithm system has to mathematically retransform the scene interferograms from the CrIS instrument into spectral information useful to scientists, considering all relevant data from characterization and calibration measurements in order to yield fully calibrated spectra. All this information will enable atmospheric key parameter retrieval.

The functions described in this section are to be implemented in the Ground Segment for processing of the CrIS scene and calibration data.

The incoming data may be acquired during deep space, internal calibration blackbody, and scene atmospheric measurements of the CrIS sensor. Each of these three types of incoming data therefore needs to be processed differently. Once combined together they will ultimately generate calibrated spectra with small residual errors.

The main objectives of the SDR Algorithms are:

Pre-process incoming data packets

Load and sort data

Convert interferograms to spectra

Convert scene measurements into calibrated spectra

Compute *spectral calibration*, using metrology wavelength measurements

- » Characterize metrology using neon lamp reference measurements
- » Monitor metrology drift using laser diode parameters measurements
- » Perform alias unfolding and spectral labeling
- » Map spectral channels to a fixed wavenumber grid

Compute *radiometric calibration*, using reference calibration measurements

- » Average warm calibration target data, average cold calibration target data
- » Subtract sensor background radiance
- » Remove sensor induced phase dispersion
- » Correct for fringe count errors
- » Perform non-linearity correction
- » Correct for off-axis self-apodization on each FOV
- » Correct for polarization errors
- » Remove orthogonal noise components

Compute *geometric calibration*, using LOS position and ephemeris data

Evaluate the associated error

Check for data quality and maintain quality controls

Compute NEdN estimates

2.2 SPACE SEGMENT SIGNAL PROCESSING

This section discusses processing done at the instrument level, namely spikes detection/correction, filtering and decimation, bit trimming, and packet encoding. Figure 3 summarizes the CrIS instrument part of the NPOESS satellite, viewed at the processing level.

CrIS is a Michelson interferometer based on the principle of Fourier Transform and designed to measure with high resolution and high spectral accuracy the emission of infrared radiation from the atmosphere in three bands in the spectral range from 3.9 to 15.4 µm (650 – 2550 cm^{-1}). The core of the instrument is a Fourier transform spectrometer which measures in one sweep the spectral features of the atmosphere with high spectral resolution and throughput. The spectrometer transforms the incoming spectral radiance, i.e. the spectrum, into a modulated signal, the interferogram, where all infrared wavenumbers in the band of interest are present simultaneously. The output from the spectrometer consists of one such interferogram for each observed scene.

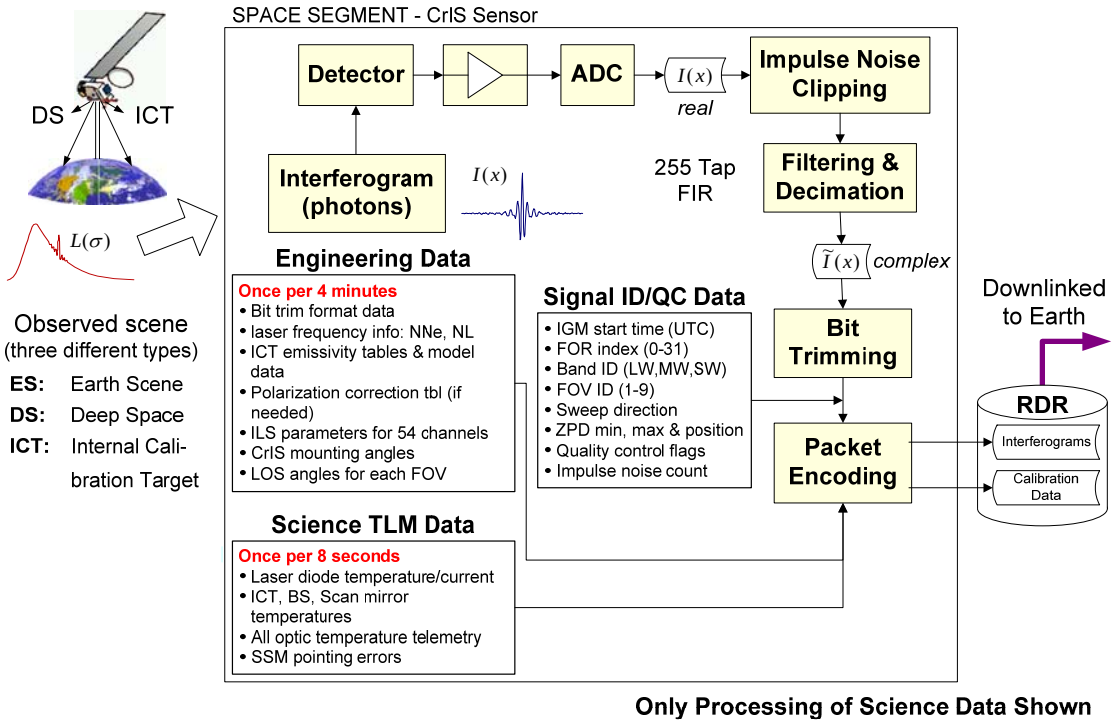

Figure 3: Space Segment Processing of the CrIS Sensor

Figure 4 depicts interferogram signal processing, showing filtering, decimation and data reduction.

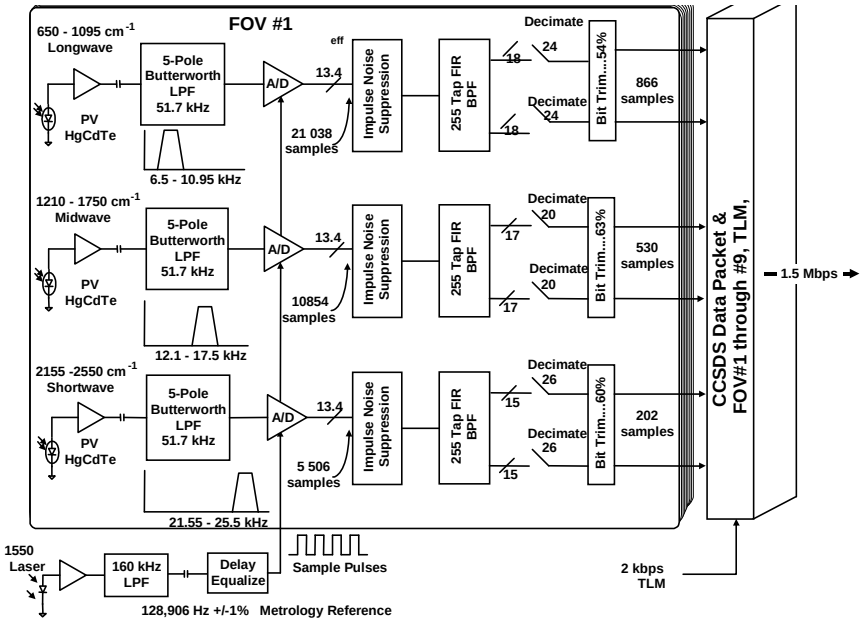

Figure 4: In-space interferogram processing for one of the nine FOV's

2.2.1 Spikes Detection/Correction

Noise spike detection and correction of raw interferogram data is accomplished by hardware and software on the CrIS sensor rather than by SDR Algorithms on the ground. This function is intended to suppress the effects of cosmic particle interaction with sensitive detector and associated electronics.

Detectors are subject to Impulse Noise due to direct bombardment of detector by high energy particles hitting spacecraft, and then emitting numerous X-rays that can excite detectors. The GOES satellite has shown to experience 2000 secondary X-rays events/cm^2/sec (60 KeV X-rays. The NPOESS orbit is under evaluation, but one can expect that the large area CrIS detectors (~870 μm diameter) be vulnerable to single event upset.

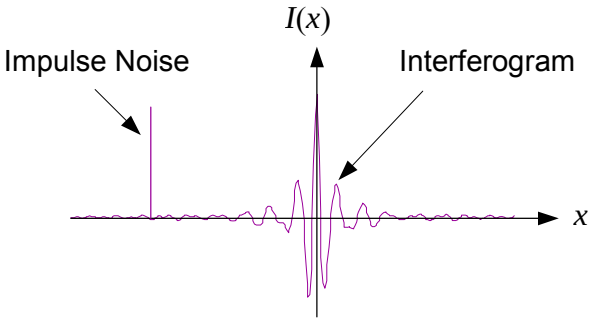

Figure 5: Interferogram spike

Spikes can be present anywhere in the interferogram, near or far the ZPD. Performing noise spike detection on raw interferograms and correction prior to filtering and decimation on the CrIS instrument is more effective than performing this same correction via software on the ground since the filtering and decimation process scrambles the data and makes the noise spike much less detectable/correctable. Thus, scientific code performing this function is not needed since it will be performed on the instrument instead.

Error detection and correction of transmission link errors from spacecraft to ground station are assumed to be the responsibility of the spacecraft integrator and operate outside the bounds of the SDR Algorithms. It is assumed that the transmission link will incorporate robust coding methods to make this source of bit errors negligible (remaining bit error rates are quite small: of the order of 10^{-9} – 10^{-10}).

As the processing will be performed in-space, the algorithm or detection and correction must be minimal in order to avoid the implementation of dedicated electronics and supplementary storage memory. More elaborate algorithms could be designed, but the current baseline is to go for a simple straightforward approach. Detection makes use of a predefined impulse noise mask, corresponding to an amplitude tight filtering window that will identify erroneous spikes. As a correction, each detected spike will be substituted by a zero count. This occurrence will be flagged for having been corrected for one or more spikes; the number of impulse noise hits is counted and reported for each interferogram via the telemetry data packets to aid in data quality assessment.

2.2.2 Filtering and Decimation

According to the current instrument design (and particularly the signal processor electronics), complex numerical filtering will be applied to the measurement data. The purpose of this section is to provide some theoretical background on this topic.

Neglecting the dispersion phenomenon inducing a non-null phase (see Section 2.3), an observed interferogram is basically a real and symmetrical function. The symmetry is about ZPD and, by extension about every multiple of MPD. The Fourier transform of such an interferogram is a real and symmetrical spectrum with symmetry about every multiple of the sampling frequency. We assume that the sampling frequency is chosen in order to meet the Nyquist criterion, i.e. there are no natural frequencies above half the sampling frequency. In other words, the full spectrum will show on one half the true physical spectrums and on the other half the image of this spectrum. Depending on the convention, this second half may be displayed as negative frequencies or as frequencies above half the sampling frequency (see Section 2.6).

A numerical filter with *real coefficients* shows the same symmetry as described above. The pass band defined by such a filter transmits both the desired physical band and its image. Under sampling this filtered spectrum is possible provided the following two conditions are met:

1– The decimation factor is not larger than $\sigma_s/2(\sigma_1-\sigma_0)$, where σ_s is the sampling frequency (or Nyquist frequency) and σ_0, σ_1 are the band limits.

2– There is no folding frequency within the pass band.

A *complex numerical filter* can be devised such that it has no image pass band, by defining its imaginary part anti-symmetrical such that it produces a compensating negative image (negative frequencies are filtered out). After such a filtering, the only under sampling condition is:

1– The decimation factor is not larger than $\sigma_s/(\sigma_1-\sigma_0)$, where σ_S is the sampling frequency.

Thus, the decimation factor can be two times larger after complex filtering than the best case with real filtering. On the other hand, the generated spectrum produced by the numerical filtering is complex (composed of a real and an imaginary part).

Since the folding frequencies are not restricted to be out of the band of interest, there is not this additional restriction on the decimation factor. It is then possible to better optimize the decimation factor. This is where a gain can be made with respect to data reduction.

Figure 6, Figure 7 and Figure 8 present the 255 taps band pass filter for the LW, MW and SW bands, exhibiting a ±2.37 dB in-band ripple and a 69 dB stop band. This numerical filter can be implemented with a low power ASIC electronic implementation. The predetection optical filter selectivity of the CrIS instrument is also shown overlaid on the numerical filter response.

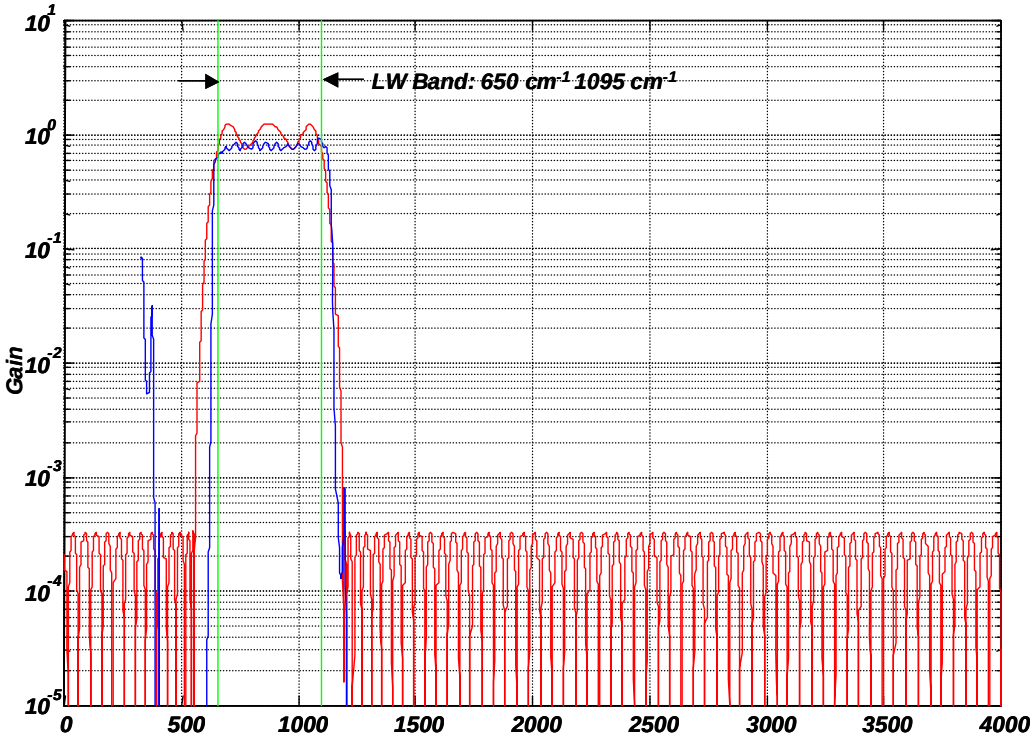

Figure 6: Parks-McClellan FIR Band pass Filter for CrIS (LW)

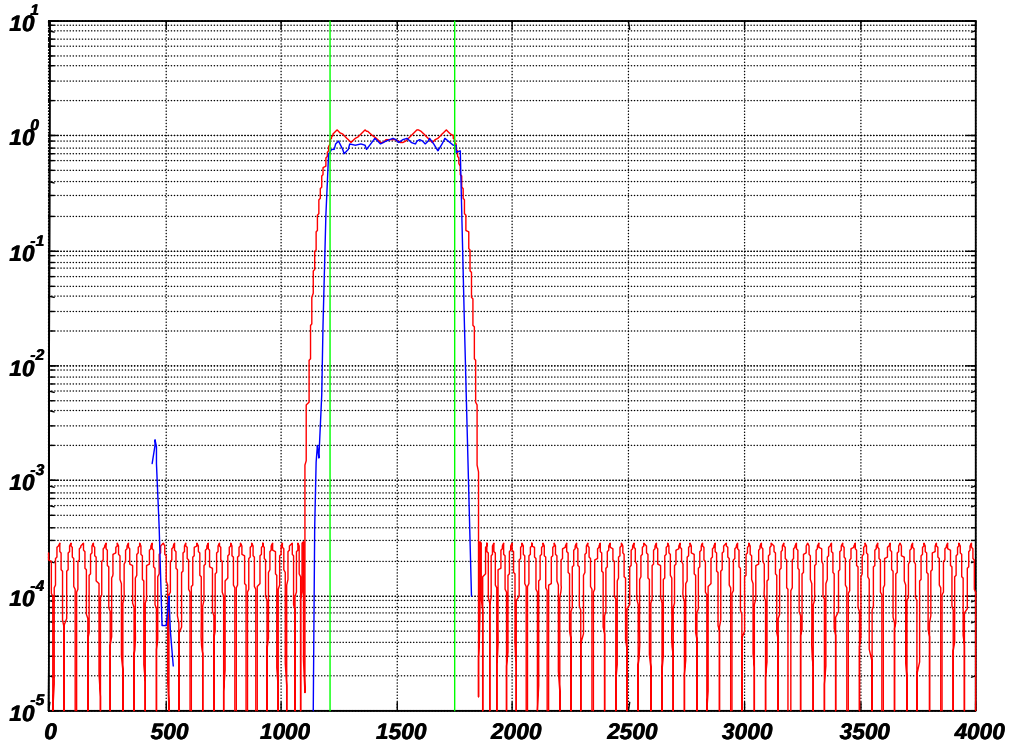

Figure 7: Parks-McClellan FIR Band pass Filter for CrIS (MW)

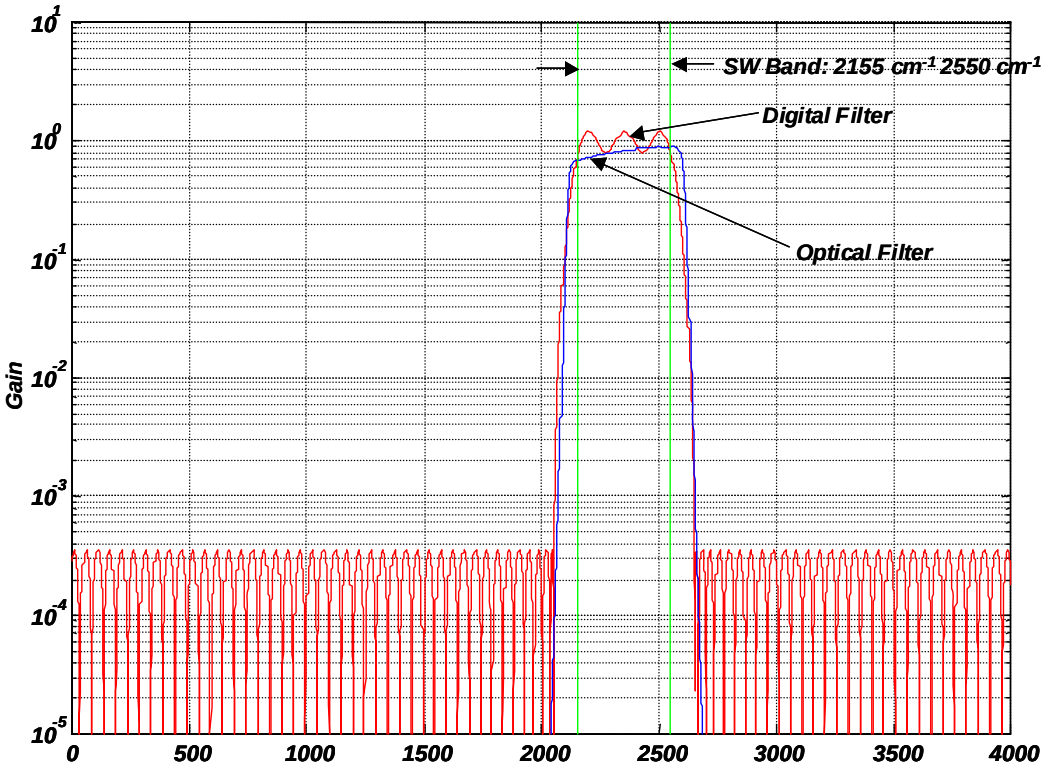

Figure 8: Parks-McClellan FIR Band pass Filter for CrIS (SW)

Figure 9 summarizes the interferogram numerical acquisition process and Figure 73 summarizes the decimation and alias-folding process. The actual unfolding method processing needed for the proper recovery of the wavenumber axis is described in Section 9.2. This operation must be executed after the Fourier transform of every incoming filtered and decimated interferogram signal.

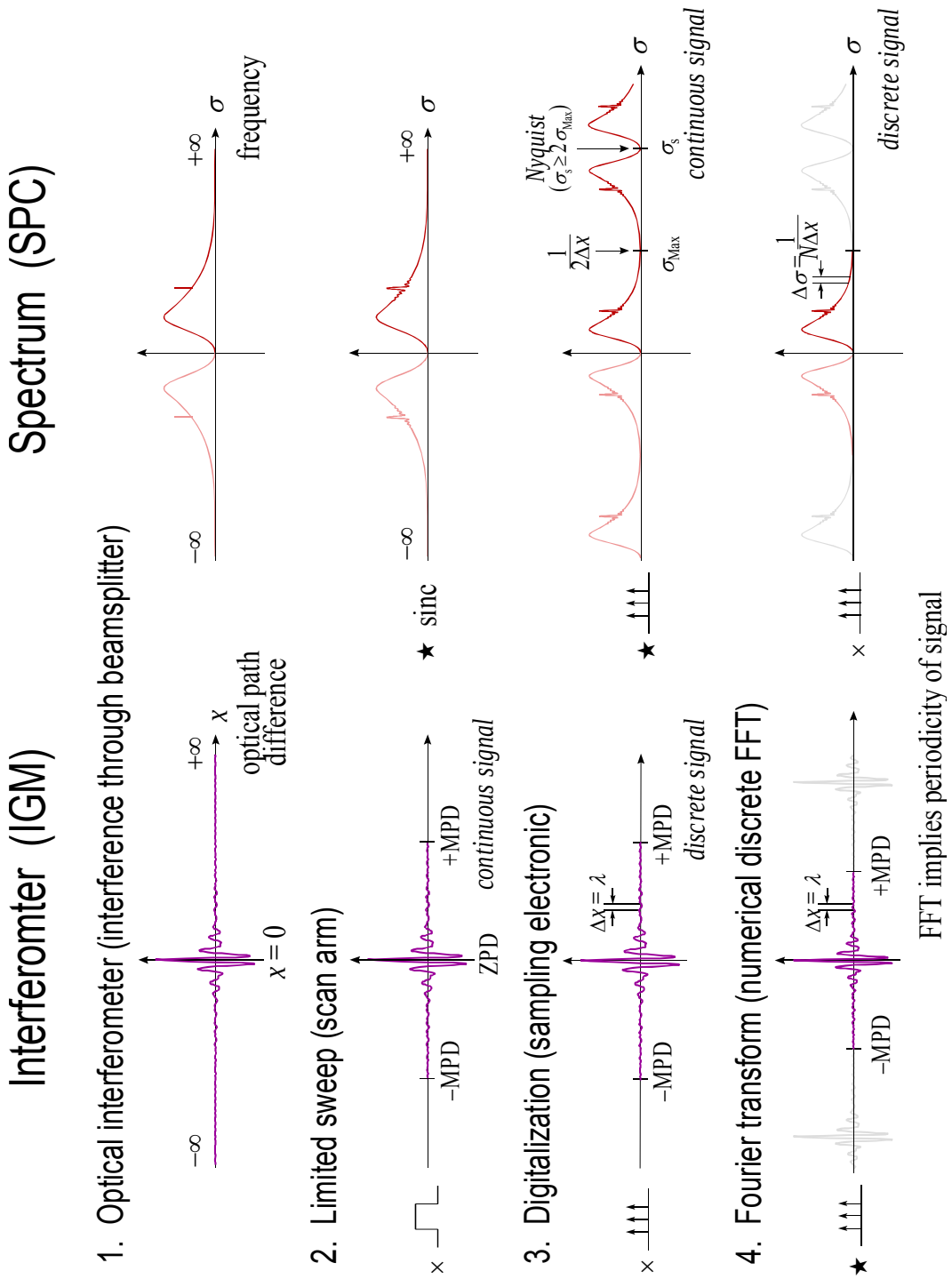

Figure 9: Interferogram numerical processing

2.2.3 Bit Trimming

In an effort to further compress the generated raw data rates to help meeting the available data transfer channels, bit truncation, or bit-trimming, is used to reduce the amount of data without losing information.

After performing filtering and decimation, the size of resulting interferograms can be reduced further by taking advantage of the characteristic distribution of the interferogram intensities. Intensities found away from the ZPD position are typically a few orders of magnitude lower than the intensity at the ZPD itself. The exact ratio depends primarily on the spectral content of the scene and other sources of radiation seen by the detector and on the bandwidth of the detector with its optical filters. To a lesser degree, it also depends on the recorded noise which can be important compared to the intensities in the interferogram ends. Collecting the interferogram while keeping a constant gain forces the digitalization range to be set by the ZPD intensity. For the points away from the ZPD this results in an under utilization of the digitized words. One can take advantage of this under utilization by omitting unused bits in a word (the most significant bits) and therefore contribute to data reduction. If the data values of the signal under consideration were more randomly distributed, as in spectral data, this method would not be appropriate as the range of points with important weights would become significant. This method is referred to here as bit trimming since the high order bits are trimmed from blocks of small valued data.

This bit trimming scheme is most useful for high resolution measurements where the ZPD region is narrow with respect to the full extent of the IGM. The full resolution sweeps benefit from extended truncation on a greater portion of its blocks than lower resolution sweeps. Bit truncation is most efficient when used with short block size. Compression rates on typical atmospheric spectra can range from 10 up to 40% reduction. Figure 10 shows an example of the ADC bit-trimming mask, for the long wave band if the word width at ZPD is 17 bits. The CrIS bit-trimming masks enable a data rate reduction of 37% in the LW, 27% in the MW, and 38% in the SW.

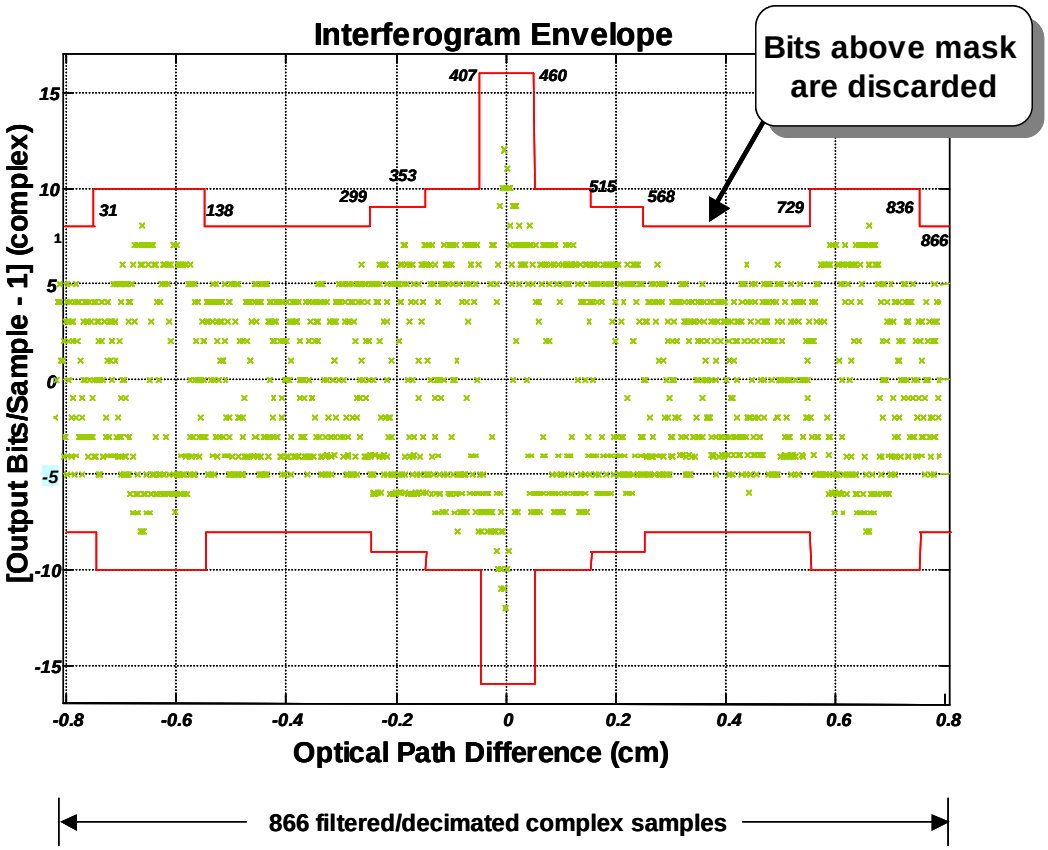

Figure 10: Interferogram envelope for a 17-bit word (each I & Q)

2.2.4 Packet Encoding

All the data coming directly from the instrument are formatted into source packets. The data packets generated by the CrIS conform to the Consultative Committee for Space Data Systems (CCSDS) packetization per the real-time interface specification and the stored data interface specification. Details about the size, content and organization of data in the source packets as well as the data rate corresponding to the transfer of source packets to the ground processor can be found in [RD 1].

The data formatting and transmission will be performed as follows:

CCSDS Encoded Data Organized in Packets

- 27 interferogram packets per Field of Regard (FOR), 918 interferogram packets every 8 seconds
- One housekeeping telemetry packet every second (rotation of 8 per frame)
- One science telemetry packet every 8 seconds
- One engineering data packet every 4 minutes
- Diagnostic data by command (as needed)

Upload to CrIS Sensor

- Commands
- Software uploads

Spacecraft Generated CCSDS Packets

Spacecraft orbit position, orbit rate vector, roll, pitch, yaw & UTC time stamp

2.3 GROUND SEGMENT PROCESSING

The SDR Algorithms can be viewed as two main modules being processed separately. Radiometric and spectral calibration are interlinked within one another, while geometric can be done in parallel. Those processes are described respectively in Chapters 4, 5, and 6. Individual sub-modules defining these super-modules are described in Chapter 7.

The ground processing flow is illustrated by the data flowchart of Figure 11.

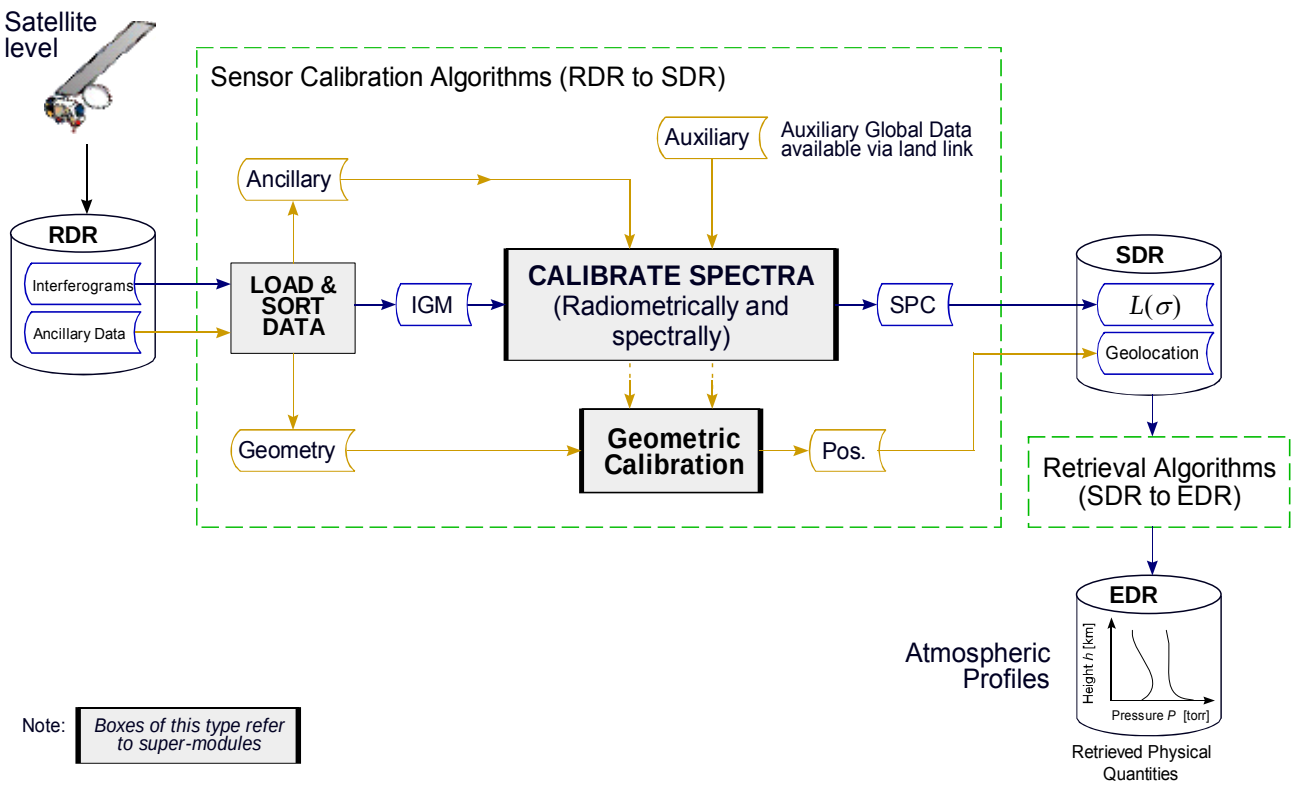

Figure 11: Ground Processing Data Flowchart

2.4 INTERFEROMETER MODEL

In this section we model a generic interferometer, with all relevant characteristics. The goal is to correctly describe the CrIS interferometer in order to define correctly the required ground segment SDR Algorithms.

If an interferometer was at a temperature of zero Kelvin, with perfectly symmetric (compensated) ports and with perfect electronics, particularly with perfect scanning speed then measured interferograms would be perfectly symmetric, resulting in a spectral signal with zero phase (real signal). Some of the real-life effects are hard to correct while some others are easier to avoid. Some effects can also be corrected by external complex calibration methods, like, for instance, the self-emission of the instrument.

The following sections present a comprehensive and logically ordered list of categories of the most significant ordinate errors that are found in conventional Fourier Transforms Spectroscopy (FTS). Each item in the list contains a brief description giving causes and consequences [RD 2].

Only the intrinsic errors caused by the instrument, technique or sample, are covered. Extrinsic errors induced by human actions are not considered. This discussion does not deal with error types that can be considered as “manipulation errors”, or “setup errors”, that can be avoided, like for example inappropriate sampling of the interferogram leading to spectral aliasing from above the Nyquist limit.

Knowledge of these error sources and their consequences is an essential pre-requisite for developing adequate calibration algorithms.

2.4.1 Instrument Phase

The reason for getting a non-zero imaginary component out of the FT is that the FT interferogram is not mirror-symmetrical about the ZPD point ($x = 0$). The asymmetry originates from two different sources, either extrinsic or intrinsic. Extrinsic sources may arise from sampling errors. Intrinsic asymmetry may be due to wavenumber-dependent phase delays of either the optics or the electronics. Instrument phase, sometimes called “phase error” is more of a characteristic than an error as such.

Extrinsic

Electronic dispersion in the signal processing electronics (Sampling effects)

1– None of the IGM sampling positions coincides exactly with the proper position of zero path difference. This is generally the case and causes a phase linear in σ. This effect is easily corrected by calibration, if it remains constant during calibration and scene measurements. This incorrect location of center sample may be due to a poor algorithm or inadequate set of sample used for this (use of a reference white light).

2– If *fringe counts* are lost during the sweep, the effect is more dramatic and constitutes a phase errors. If fringe count errors occur at turn-around, corrective linear phase shifts can be applied to re-align measurements on the same reference. If a fringe count error occurs “in-sweep”, the last part of the interferogram will be shifted with respect to the first part of that interferogram. This effect results in a distortion of the current measurement that is very difficult to recover.

3– Also, reference metrology interferogram sampling may be different from infrared signal. This may cause *fractional FCE*, if for example metrology optical path changes slightly and suffers different

temperature drifts not seen by IR optical path. This fact motivates the use of a coaxial IR and reference laser is baselined in the CrIS sensor.

4– There are *sampling fluctuations* between each digitized point. Sampling jitter can be caused by metrology laser wavelength and/or amplitude fluctuations. Sweep speed may vary causing effective sampling jitter in systems where there exist delays between the IR signal and the metrology trigger signal. These errors result in instrument noise.

5– Shift between the up zero crossing and the down zero crossing of the metrology laser analog signal will generate a correlated sampling jitter, when up and down sampling is used. These errors can result in instrument noise, which in the CrIS instrument fall out of the band and are removed via filtering.

6– Errors due to differences between the optical paths in the interferometer used by the IR measuring beam and those used by the metrology laser radiation for monitoring the sampling of the interferogram.

It cannot be taken for granted that the monitoring beam optical surfaces are coplanar with the corresponding ones for the measuring radiation, as inserted elements and/or different coatings were involved. This type of error introduces constant phase shifts.

The electronics transfer function may be different for metrology laser and IR signal channels. This causes mismatch delays between IR electrical response and the ADC trigger signal.

7– Errors in the servo drive mechanism for OPD measurement. This can pertain to S/N ratio of the post detected metrology signals or their delay variation under various operating conditions

8– IR channel electronics introduce delays that vary with frequency (wavenumber).

Intrinsic

Optical dispersion in the beamsplitter-compensator subassembly

Because the overwhelming majority of BS coating materials is placed at one side of a dispersive substrate, the index of refraction of the substrate affects each wavelength in a different way. The ZPD of each monochromatic interferogram is at a different spatial location. This is the most common and better known source of phase error.

The role of the compensator plate is to attempt to compensate the dispersion effect of the beamsplitter. Its presence helps to compensate most of the phase errors introduced at the beamsplitter. The level of compensation depends on thickness matching.

Misalignments

Shear, Systematic IR misalignment, Interferometer divergence, Systematic OPD measuring Laser misalignment, Blur, Aberrations introduced by the interferometer collimator mirror can all contribute to the instrument phase error. If these effects remain constant between calibration and measurement, they will be cancelled out.

2.4.2 Other Signal Contributors

It is important to take into account other-than-scene contributors to the measured signal, mainly the instrument self-emission, also called self-radiance.

Beamsplitter

The *self-emission* constitutes an additional signal contribution to the observed scene. As it will be shown in Section 2.4.5, for any arbitrary measurement, the recorded interferogram is the sum of the interferogram of the viewed scene and the interferogram corresponding to the self-emission of the instrument. This last one is emitted principally by the beamsplitter, which undergoes phase shift different from the emission from the scene which goes through the whole optical chain of the interferometer [RD 3].

This effect is strongly temperature dependent. The out-of-phase contribution will depend on coatings.

Second port contribution

The second optical port of the interferometer is 180° out of phase with respect to the first port. The detected signal is the sum of the contribution from the two ports. For a perfectly compensated interferometer with a second port at 0 K, the observed signal would correspond to the pure scene, but in practice, the term corresponding to the instrument self-emission is not null. This explains IGM reversal when scene becomes colder than the terminator of the second port (complex calibration takes care of this effect).

Other parts of the instrument contributions

Can be grouped together, as long as they remain constant.

2.4.3 Instrument Line Shape

Traditionally, the spectrum $S(\sigma)$ of a finite interferogram was obtained by convolving the true spectrum with the “instrumental line shape” (ILS) function. This enabled a clear description of a measured line shape in terms of a natural line shape (NLS) due to physical line-broadening, the ILS representing the contribution of instrumental finite resolution and all other contributors like instrument misalignments, shear, blur, etc. Due to an ILS that depends significantly on wavenumbers, this approach is no longer valid for CrIS. A new approach is presented later in this document.

2.4.4 Other Types of Errors

Includes non-uniform sampling intervals: two cases are possible:

1. repeatable, causing artifacts,
2. non-repeatable, causing noise.

Non-linearity

The detector, its analogue circuit or its ADC can suffer from non-linearity. This can result for example in a transfer function that can saturate with incoming flux. Non-linearity induces a global scaling and the apparition of spectral artifacts in the spectral domain. The CrIS instrument uses PV IR detector technology expected to produce nonlinearity of 0.13% or less. This magnitude of error is large enough to require the need to perform linearity correction upon data.

Channel spectrum

Channel spectrum results from multiple reflections of the IR beam between the plane surfaces in the IR beam of spectrometer's optical path. Parasite reflections from the beamsplitter and compensator substrate surfaces produce satellite interferograms, which may overlap the sampled region of the main interferogram. Inter-reflection effects such as the plane parallel sample itself or a liquid-cell window can induce the formation of resolvable interference fringes (channel fringes). These results in "ghost" interferograms or "echo peak" offset from the center burst.

The CrIS instrument optical design minimizes this effect by using wedged optics that prevent reflected wave fronts from combining in a way that generates channel spectrum.

Skew rays

Skew rays give a different wavenumber scale for each off-axis ray. However, this does not shift ZPD. The skew for each CrIS FOV is characterized and becomes part of the spectral correction performed by the SDR algorithm.

Polarization

The polarization of the light from the scene interacts with the polarization bias of the instrument and can cause radiometric errors. The polarization of the instrument can also change as a function of scan angle. The CrIS design has minimized the scan induced instrument polarization change to less than 0.15%. There is a capability to correct radiance measurements for each scan position if polarization characterization of the instrument is made.

Summary:

One of the biggest challenges is to move the interferometer mirror along at *constant velocity*. In general, this does not happen to the degree desired. Analog electronics can be designed to minimize the interaction of non-constant sweep speed and filter response. But it also has severe limitations of dynamic range and non-idealities like harmonic distortion, drift, non-well-behaved combination of gain and phase versus frequency. The use of broadband electronics gives frequencies of interest a "small range" in the bandwidth. This requires significant digital oversampling. Digital processing can be done (in some cases) at high precision and dynamic range.

Another big challenge is to move the interferometer mirror without changing the modulation: i.e. maintain interferometric alignment over scan. The CrIS interferometer uses servo controlled feedback mechanisms to maintain the needed alignment.

Each of these problems, sometimes grouped together, will be associated with a clear solution throughout the document.

2.4.5 Interferometer Modeling Equations

According to the comments made in Section 2.4, the various instrument phase contributions can be grouped in given terms, and the interferometer system can finally be viewed as follows:

1. The equivalent phase dependency of the observed scene, corresponding to the incident photon flux through the FOV of the instrument: $e^{i\phi^{ext}}$. This term combines all the phase effects proportional to the amplitude of the measured signal.
2. The phase dependency on the instrument itself, corresponding to all the light *not* coming through the scanned FOV, like the thermal emissions of the various surrounding parts of the interferometer (instrument contribution), dispersion effects and thermal emission of the beamsplitter, electronics effects, etc.: $e^{i\phi^{in}}$ (*in* superscript for *in*side or *in*strument).

   Corresponds to the sum of all contributors, summed vectorially
3. Amplitude functions proportional to each observed scene: A^x (real functions)

This analysis properly accounts for the situation in which the phase response for radiance from the instrument itself differs from the one for radiance from an external source. This model also effectively takes care of the emission of the various parts of the interferometer. The main mechanism responsible for this dual phase interferometer response is emission from the beamsplitter [RD 3].

These terms indicate that the resulting phase of deep space, calibration BB, and scene measurements may vary substantially. Note: all these terms are functions of wavenumber. The following Figure 12 summarizes the situation:

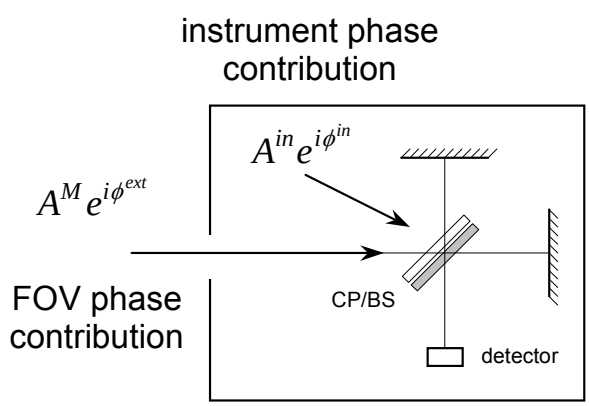

Figure 12: Phase dependencies in an interferometer

According to this model, and the notation given in Section 1.6, a given measurement can be described as follows:

$$\begin{aligned}\widetilde{S}^{M} &= \underbrace{A^{M}e^{i\phi^{ext}}}_{\text{scene contribution}} + \underbrace{A^{INT}e^{i(\phi^{INT}+\delta_1)} + A^{BS}e^{i(\phi^{BS}+\delta_2)}}_{\text{instrument contribution}} \\ &= A^{M}e^{i\phi^{ext}} + A^{in}e^{i\phi^{in}}\end{aligned} \tag{6}$$

where the complex raw spectrum $\widetilde{S}^M$ is built from the scene amplitude A^M affected by the sum of the various interferometer contributions $e^{i\phi^{ext}}$, on which the instrument contribution is added, composed the amplitude A^{INT} multiplied by phase $e^{i\phi^{INT}}$ plus the beamsplitter amplitude contribution A^{BS} multiplied by phase $e^{i\phi^{BS}}$. When the BS temperature remains constant (or negligible), the second and third term is combined vectorially and is considered together as $A^{in}e^{i\phi^{in}}$ to simplify analysis.

If the observed scene is much colder than the instrument ($T^C \ll T^{in}$ and sufficient high σ), then $A^C \ll A^{in}$, suggesting that this measurement can be considered as the instrument offset itself. $\widetilde{S}^C \approx A^C e^{i\phi^{ext}}$. This is true for space borne instrument looking at the deep space ($\approx 4\ K$) as the cold reference.

Following these assumptions, the three following basic measurements can be modeled as:

Cold reference: $\widetilde{S}^C = A^{in}e^{i\phi^{in}}$

Hot reference: $\widetilde{S}^H = A^H e^{i\phi^{ext}} + A^{in}e^{i\phi^{in}}$

Scene Measurement: $\widetilde{S}^S = A^S e^{i\phi^{ext}} + A^{in}e^{i\phi^{in}}$

2.5 CRIS CHARACTERISTICS

This section goes through some of CrIS characteristics related to the SDR Algorithms.

2.5.1 Double-Sided Interferogram Measurements

Interferograms can be recorded with the optical path difference x varying from a little less than 0 to +MPD (single-sided), or from –MPD to +MPD, as shown in Figure 13.

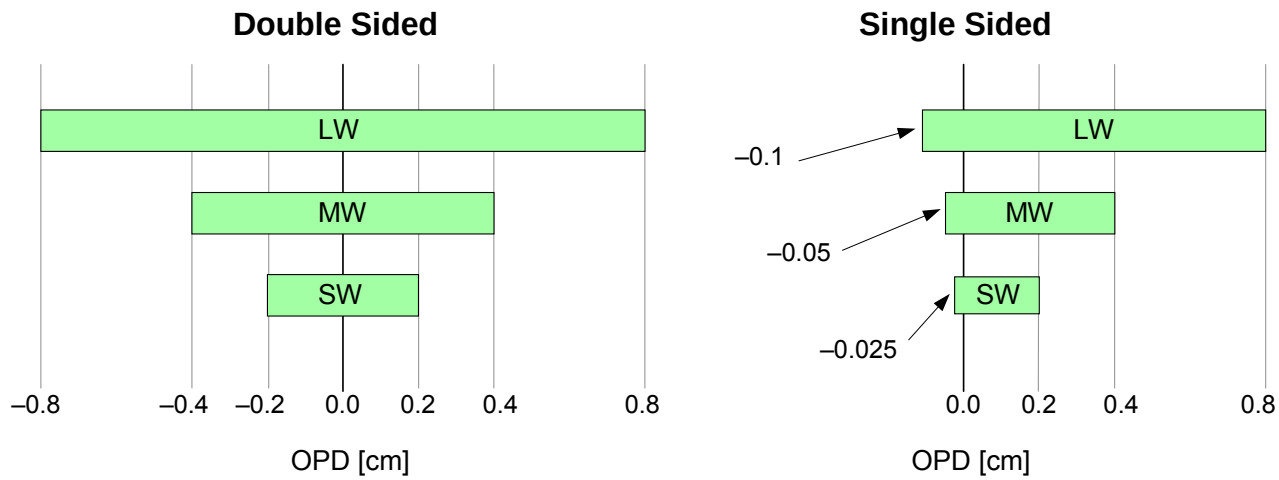

Figure 13: Double-sided versus single-sided interferograms

In theory, both halves of a sampled interferogram contain the same information, and if only a limited total path difference variation is mechanically available, only one half of the interferogram can be measured, yielding to a lower data rate. But there are in fact at least four major advantages to symmetric sampling of the interferogram [RD 4]:

1. The sensitivity of line positions to the accuracy of the phase correction is drastically reduced. For one-sided interferograms, the local instrument line shape has as its real part the usual $2MPD\ \mathrm{sinc}(2MPD\,\sigma)$; but unlike the symmetric interferogram it also has an equally large asymmetric imaginary part $2MPD\ \sin(2\pi\ MPD\,\sigma)\,\mathrm{sinc}(2MPD\,\sigma)$. Even a very small phase error is enough to rotate a portion of this imaginary part into the real plane, producing an asymmetric apparatus function in the final spectrum. Since the phase error is often a function of wavenumber, this produces a varying apparatus function and hence a variable wavenumber scale. With two-sided interferograms, the only imaginary part comes from any slight asymmetries in the interferogram itself, and these are normally very much smaller; the sensitivity to phase error is proportionally reduced.

2. Double-sided interferogram naturally reject the linear source intensity variations.

3. The source noise of the measurement is reduced because of the increasing the sampling frequency.

4. Double-sided interferograms have a major advantage over single-sided ones for an application like atmosphere emission measurements by the CrIS instrument. As opposed to sun occultation measurements for example, emission measurements generate larger ZPD regions that are harder to represent in single-sided mode. Double-sided interferograms are

more appropriate as they offer better phase definition, since the information is spread equally on each side of the ZPD. There can be a better control on the quality of the phase correction without any hypothesis on the ZPD neighborhood. It assures that the phase correction will be correctly performed, even taking care of slight asymmetries.

5. All path differences are sampled symmetrically about a common mean time, so that, to first order, all frequencies components refer to the same mean epoch. This results in considerably more accurate line profiles in many situations where there is a monotonic variation in source intensity during an observation. Examples of such sources include astronomical sources near the time of rising or setting (i.e. rapidly changing air mass).

The following discussions in the present document make the assumption that interferograms will be recorded double-sided, and the algorithms will process them in full width.

Characteristics

Both the single-sided and the double-sided approaches have same spectral resolution for a fixed MPD,

Single-sided has lower data rate (5/8 of baseline double-sided),

Both have the same NEdN if sweep time remains the same,

→ Double-sided provides better phase calibration of instrument.

→ Double-sided is less sensitive to sweep asymmetries of hardware.

→ With double-sided interferograms, the sensitivity of line positions to the accuracy of the phase correction is drastically reduced.

2.5.2 CrIS Spectral Bands

There are three infrared spectral bands defined for the CrIS sensor: the Long Wave (LW), the Middle Wave (MW), and the Short Wave (SW). The sampling interval is defined by the 1550 nm laser metrology wavelength using up/down zero crossing for an effective sampling interval of 775 nm. The spectral limits corresponding to these bands and the required on-axis unapodized spectral resolution $(1/(2\,MPD))$ in each CrIS band are given in Table 2 (SRD 3.2.1.4). The CrIS interferometer MPD is 0.8 cm. This results in the basic resolution of 0.625 cm^{-1}. The other 1.25 and 2.5 cm^{-1} resolution are simply obtained by sampling a smaller number of points along this same optical path, resulting in effective MPDs of 0.4 and 0.2 cm for MW and SW bands respectively.

Table 2: CrIS specifications

Band	Spectral range [cm^{-1}]	Spectral range [μm]	Band width [cm^{-1}]	Resolution $\Delta\sigma$ [cm^{-1}]	MPD [cm]
LW	650 – 1095	15.4 – 9.1	445	0.625	0.8
MW	1210 – 1750	8.3 – 5.7	540	1.25	0.4
SW	2155 – 2550	4.6 – 3.9	395	2.5	0.2

Figure 14 presents each band with their array constituents. 127 oversample points are used to fill 255 tap FIR pipeline (see Section 2.2.2). The OPD lengths are fixed to accommodate the Prime Factor FFT with decimated complex data (see Section 2.6.1). Two spare decimated samples are kept to accommodate ZPD uncertainty.

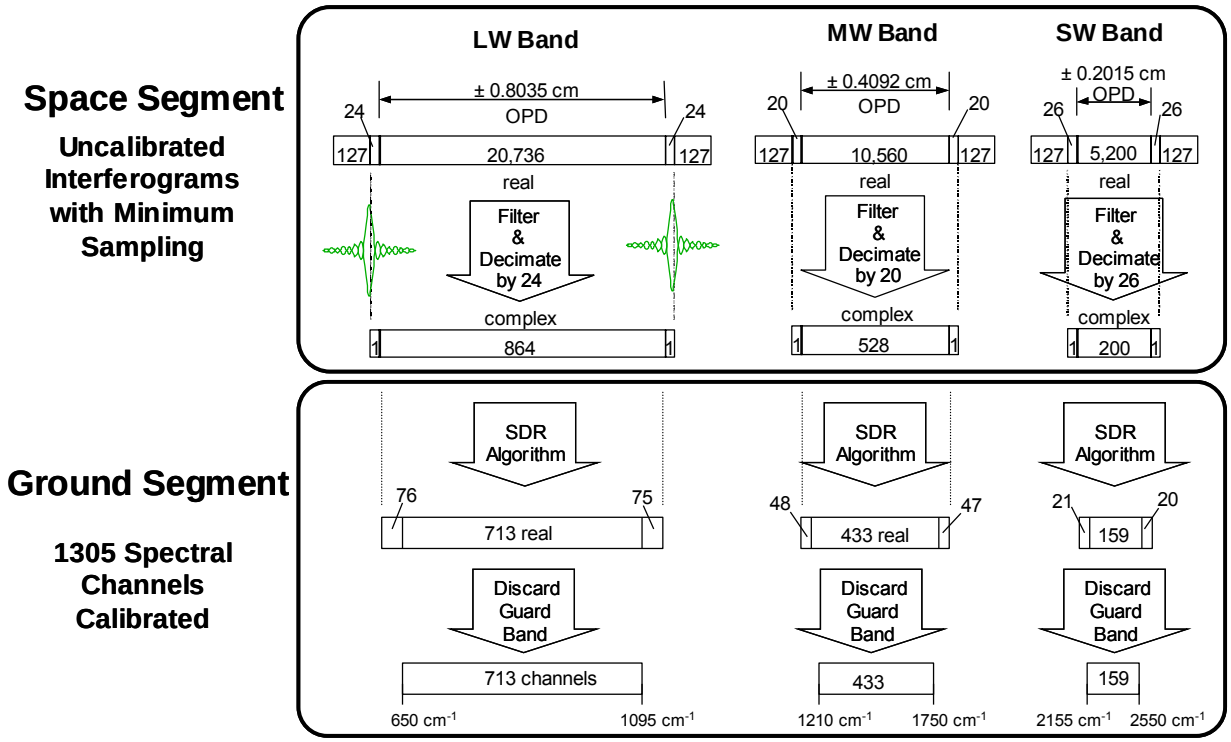

Figure 14: Long, Mid, and Short Wave IR bands

2.5.3 CrIS Field of Regard

The CrIS instrument is designed to observe the ground with an instantaneous field of view which maps to a nadir footprint of 14 km on the ground from an altitude of 833 km (corresponding to a FOV = 16.8 mrad). Figure 15 shows the Field of Regard definition and Table 3 shows FOV's shape characteristics.

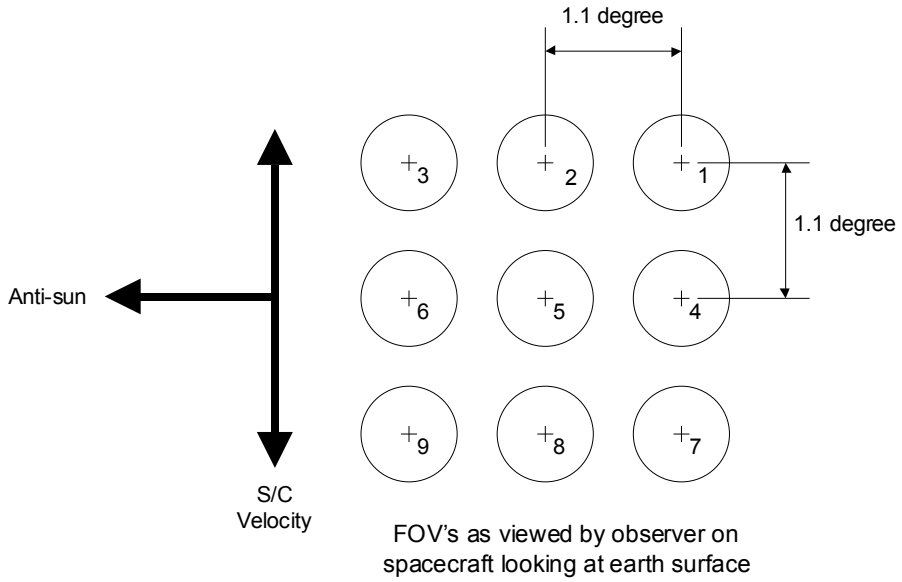

Figure 15: Field of Regard definition

Table 3: FOV shape characteristics

	FOV Shape (degrees, Cross Track)	FOV Shape (degrees, In Track)	FOV Matching Band-to-Band, In-track and Cross-track (degrees)
70% of Peak Response Width	> 0.8735	> 0.8735	+/- 0.0206
50% of Peak Response Width	0.942	0.942	+/- 0.0137
10% of Peak Response Width	< 1.100	< 1.100	+/- 0.0206
3% of Peak Response Width	< 1.238	< 1.238	N/A

2.5.4 CrIS Measurement Sequence

In order to properly calibrate the radiometric output from the instrument, it is also necessary to acquire regularly, during the course of the mission, two additional types of measurements of well-defined targets. The first one is done with an internal high-precision calibration blackbody, the internal Calibration Target (ICT). For the second measurement, the instrument is simply looking at the deep space (DS) that represents a source of low (negligible) IR radiance where the measured interferogram is related to self-emission of the instrument. This offset will be subtracted from scene measurements during on-ground data processing. These two calibration measurements will be performed once every 8 seconds in order to account for changing self-emission of the instrument due to temperature variations in the orbit.

A typical measurement scan sequence consists of 34 interferometer sweeps (see Figure 16), including 30 earth scenes plus 2 deep space and 2 ICT measurements (these numbers include both forward and reverse sweeps). One scan of the CrIS sensor will take about 8 seconds.

- They are 40 intervals of 200 ms comprising an 8 second scan
  - 1 rapid movement from ICT to Earth Scene 1 x 600 ms = 0.6 s
  - 30 Earth scenes x 200 ms = 6.0 s
  - 1 rapid movement to space location x 200 ms = 0.2 s
  - 2 deep space sweep x 200 ms = 0.4 s
  - 1 rapid slew to ICT target x 400 ms = 0.4 s
  - 2 ICT scans x 200 ms = 0.4 s
- The instrument can perform a new measurement (sweep) every 200 ms:
  33 ms for repositioning, up to 167 ms for data acquisition
- Each 8 seconds scan is comprised of 918 interferograms
  34 data collection sweeps × 3 bands × 9 FOV

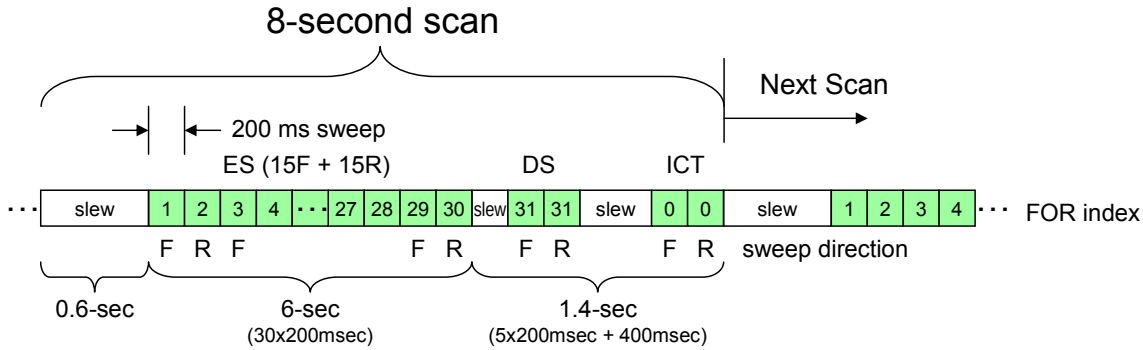

Figure 16: CrIS Measurement Sequence

The in-track sensor scan angle will be adjustable during a cross track scan sequence in order to compensate for the in-track spacecraft motion. This is accomplished by a scan mirror that moves backward so that the FOV footprint on the earth surface begins at the beginning of the sweep (saw teeth motion). See Sec. 2.1.1.1 [RD34] for update.

2.5.5 CrIS Signal Processing

At the satellite level, or space segment, the observed radiance is transformed into a modulated signal by the interferometer. This IR signal is detected by an HgCdTe detector and sampled with an effective metrology wavelength of 775 nm. This electrical signal is then amplified and converted to a digital signal by an ADC. Taking into account guard bands, the total number of measured sampling pulses per sweep is given in the second column of Table 4, while the third columns lists the number of points strictly corresponding to the OPD sweep. Measured raw data points are then filtered and decimated to limit the band pass in order to lower the transfer data rate. The decimation factor used in each band depends on its bandwidth. The fourth and fifth column of Table 4 list the decimation factor that can be used in each channel (see Section 2.2.2) and the resulting number of points.

The SDR Algorithms will provide a set of nominal retrieval spectral channel wavenumbers as an output. Radiance data from all detectors will be interpolated to this standard set of spectral channel wavenumbers for retrieval studies and other EDR validations (SRD 3.2.1.21-1). The sixth column of Table 4 gives the number of bins delivered to the EDR algorithms.

Table 4: CrIS signal dimensions

Band	Total sampling pulses per sweep	Samples Spanning 2MPD	Decimation factor DF_b	Decimated points N_b*	Output bins
LW	21 038	20 736	24	864	713
MW	10 854	10 560	20	528	433
SW	5 506	5 200	26	200	159

* These numbers do not include an additional 2 over scan points

2.6 SIGNAL REPRESENTATION

All signals are composed of their ordinate data point's array, in conjugation with a definition for their associate abscissa, together with additional relevant parameters. All spectral vector signals start at 0.0 cm^{-1}.

For example, the numerical signal of a given band is composed of:

IGM:

$I_b^X[m]$	ordinate data points array.
m	spatial index, range $0 \le m \le N_b^X - 1$
N_b^X	total number of points of the array.
Δx_b^X	sampling interval, or spacing between spatial points of the array
$flags$	various flags representing the integrity of the signal

SPC:

$\widetilde{S}_b^X[n]$	ordinate data points array.
n	spectral index, range $0 \le n \le N_b^X - 1$
N_b^X	total number of points in the array.
$\sigma_b[0]$	spectral range lower limit (wavenumber origin) of the array.
$\Delta\sigma_b^X$	spectral interval, or spacing between spectral points of the array.
$flags$	various flags representing the integrity of the signal

2.6.1 Array Dimensions

It has been chosen to process signals at *full resolution* (lengths non powers of 2) with *no zero padding* for the following reasons:

1. Incoming signals have small dimensions (less than 1000 points)

   Dimensions can be adjusted to match lengths that are factor of small prime numbers. Thus, the processing of the Fourier transform can be executed on these signals by fast algorithms (FFT) faster than the corresponding zero-padded case.

   Working with coarse resolution (smaller dimensions than the nominal array dimensions) would attain no real gain in speed, and the increase of processing complexity would waste the advantage.

2. Second, the processing at the original signal dimension without zero-padding is easier since:

   It limits spectral bin mixing and avoids introducing correlation between spectral points that could be detrimental to the Level 2 algorithms, since the noise of each bin is spread around neighbors by the interpolation done by zero-padding. The effect of zero-padding causes the covariance matrix in the calibrated scene spectra to have non-zero off-diagonal elements. Otherwise the covariance matrix would have to be evaluated so that the EDR algorithms could use the information.

   Border effects are reduced.

   No constant DC offset removal is required to match the zero-offset of the padding in order to avoid discontinuities in the interferogram signal.

In order to compute the SDR Algorithms ground processing as fast as possible, the Prime Factors Based Algorithm (PFBA) FFTW [RD 5, RD 6 and RD 18] is suggested for the computation of Fast Fourier Transforms with non powers of 2 array dimensions. See Table 8.

Array dimensions that are multiple of small prime factors can be processed very rapidly by the FFTW, even faster than optimized standard powers of 2 FFTs, for dimensions smaller than the next power of 2 available (see Appendix 9.1.2). For example, a FFT of 560 points can be processed 60% faster by the FFTW, compared with a traditional optimized FFT on a vector of 1024 points, that is the next power of 2 larger than 560.

According to the latest official specifications for the CrIS instrument, the Data Rate Budget for two-sided interferogram is summarized in Table 5 through Table 7 with respect to the number of samples transmitted to ground. The values of N_{LW} = **864**, N_{MW} = **528**, and N_{SW} = **200** seem to be good choices, as they can be executed quite fast and still remain very compatible with the presently defined band widths. With this particular choice of prime factor dimensions, we get 0.52 ms with the FFTW algorithm compared to the 0.87 ms obtained with optimized routines for powers of 2 algorithms, meaning that we can save 40% of processing time by using prime factor algorithm with this particular array dimension choice.

Table 5: Long Wave array dimensions

CrIS Data Rate Budget	LW band

	min max
Wavenumber	650 1095
Effective MPD [cm] (radiometric)	±0.8035
Sampling interval (metrology laser $\lambda/2$)	775 nm
Sampler per IGM over OPD interval	20736
Total measured samples per IGM	21038
Decimation factor DF_b	24
Samples per IGM / DF_b = dimension (2^5x3^3)	**864**
SDR output spectral bins	713
Percentage of used band	82.3%

Table 6: Middle Wave array dimensions

CrIS Data Rate Budget	**MW band** **min max**
Wavenumber	1210 1750
Effective MPD [cm] (radiometric)	±0.4092
Sampling interval (metrology laser $\lambda/2$)	775 nm
Sampler per IGM over OPD interval	10560
Total measured samples per IGM	10854
Decimation factor DF_b	20
Samples per IGM / DF_b = dimension ($2^4 \times 3 \times 11$)	**528**
SDR output spectral bins	433
Percentage of used band	81.7%

Table 7: Short Wave array dimensions

CrIS Data Rate Budget	**SW band** **Min max**
Wavenumber	2155 2550
Effective MPD [cm] (radiometric)	±0.2015
Sampling interval (metrology laser $\lambda/2$)	775 nm
Sampler per IGM over OPD interval	5200
Total measured samples per IGM	5506
Decimation factor DF_b	26
Samples per IGM / DF_b = dimension (2^3x5^2)	**200**
SDR output spectral bins	159
Percentage of used band	78.7%

With the attainable execution speeds, the FFT computation is not really a bottleneck for the SDR Algorithms. More complex operations influence the total computation time, like convolution operations required for the self-apodization removal or matrix multiplication for the self-apodization removal. This means that with fast C language algorithms, the need to execute the FFTs with the help of DSPs does not seem to be a necessity at the current time of algorithm development. This fact, together with

the simplifications obtained with the use of non-powers of 2 array dimensions, significantly simplifies the SDR Algorithms. This simplified processing increases computing speed and avoids the introduction of supplementary errors. Table 8 gives the processing times for four of the fastest FFT routines described in Section 9.1.3.

Table 8: Array dimensions and computing times (PII, 350 MHz)[1]

FFT Points	Prime Factors Decomposition	Execution time [ms]			
		Routine 1	Routine 2	Routine 3	Routine 4
189	$3^3 \times 7$		0.27	0.26	0.09
190	$2 \times 5 \times 19$		0.36	0.33	0.23
192	$2^6 \times 3$		0.21	0.15	0.09
195	$3 \times 5 \times 13$	0.06	0.34	0.31	0.11
196	$2^2 \times 7^2$		0.29	0.26	0.14
198	$2 \times 3^2 \times 11$	0.06	0.29	0.28	0.11
200	$2^3 \times 5^2$		0.30	0.21	**0.09**
203	7×29		0.42	0.49	0.34
204	$2^2 \times 3 \times 17$		0.31	0.33	0.29
207	$3^2 \times 23$		0.34	0.42	0.26
208	$2^4 \times 13$	0.06	0.29	0.27	0.11
518	$2 \times 7 \times 37$		1.18	1.54	0.89
520	$2^3 \times 5 \times 13$	0.16	0.92	0.80	0.40
522	$2 \times 3^2 \times 29$		1.01	1.28	0.83
525	$3 \times 5^2 \times 7$		1.08	0.81	0.34
527	17×31		1.25	1.61	1.12
528	$2^4 \times 3 \times 11$	0.13	0.77	0.71	**0.26**
529	23^2		1.18	1.55	1.00
532	$2^2 \times 7 \times 19$		0.97	1.08	0.63
539	$7^2 \times 11$		1.07	1.02	0.31
540	$2^2 \times 3^3 \times 5$		0.79	0.69	0.29
544	$2^5 \times 17$		0.87	0.86	0.63
546	$2 \times 3 \times 7 \times 13$	0.18	0.99	1.00	0.29
840	2^3 x 3 x 5 x 7	0.23	2.00	1.23	0.46
845	5 x 13^2		2.31	1.86	0.91
847	7 x 11^2		2.46	1.82	0.86
850	2 x 5^2 x 17		2.11	1.76	1.03
855	3^2 x 5 x 19		2.17	1.97	1.06
858	2 x 3 x 11 x 13	0.33	2.39	1.85	0.86
864	2^5 x 3^3		1.71	1.03	**0.49**
867	3 x 17^2		2.50	2.19	1.54
870	2x 3 x 5 x 29		2.33	2.29	1.29
874	2 x 19 x 23		2.56	2.52	1.66
875	5^3 x 7		2.15	1.48	0.57
880	2^4 x 5 x 11	0.28	1.95	1.36	0.49

[1] The routine 4 is the FFTW algorithm implemented in Matlab R12. It has been tested on a PIII 500 and the results have been scaled up for comparison.

2.6.2 Data Ordering

For the storage of numerical signals, array data vectors are stored with *zero origin*, meaning that the points ordering is assumed “normal” (as opposed to the “bit reversed" sometimes seen), that is defined as follows:

If input data is a time series with linear time spacing Δx:

$$x_i = \Delta x[0..N-1] \tag{7}$$

Then the corresponding frequencies after execution of the FFT are:

$$\sigma_i = \Delta\sigma \times \left([0..N/2], -[N/2..0-1]\right) \tag{8}$$

i.e., the first half of the result corresponds to positive increasing frequencies; the second half of the result corresponds to negative frequencies (decreasing in absolute value). The zero-frequency ZPD point is at the beginning of the vector (zero index).

Even if this representation is a little less “visually” attractive than vectors with the origin at the center of the array (normal ordered vectors must be swapped before display of the whole range of negative and positive frequencies), it is more straightforward for numerical implementations, as it requires no extra processing only for display effects.

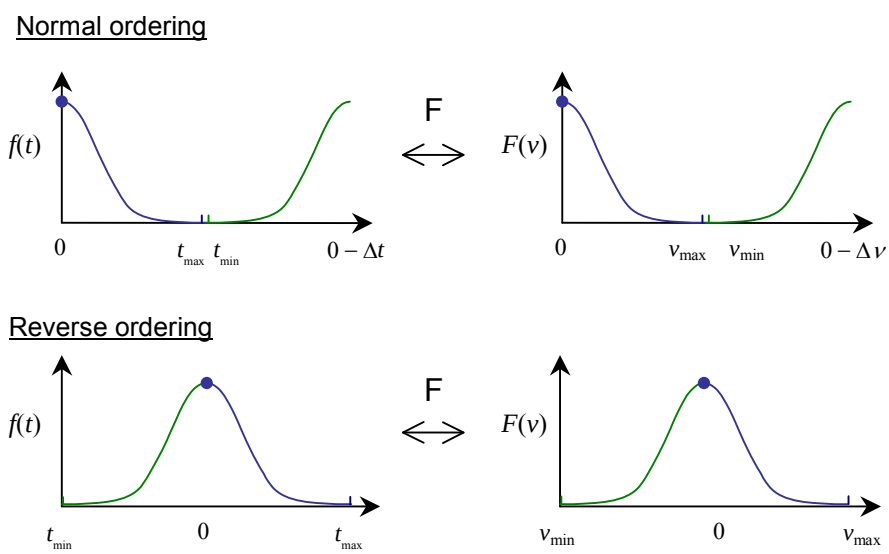

Figure 17: Numerical vectors data ordering

3. SPECIAL CONSIDERATIONS

This section presents the discussion of various effects that need to be corrected, namely channel nonlinearity, spurious interferogram spikes, fringe count errors, and lunar intrusion. The need to align data to a user's grid is also discussed.

3.1 NON-LINEARITY CORRECTION

Non-linearity levels in the LWIR and MWIR detectors are high enough to require application of a non-linearity correction to the uncalibrated spectra in order to reduce the radiometric error introduced by the detector non-linearity. An interferogram signal that has undergone nonlinear square law distortion will have the following properties:

a) Signal energy at second harmonic of spectrum will be produced

b) Signal energy at low frequency out-of-band will be produced

c) In-band signal magnitude will be reduced in magnitude linearly by the same factor for all in-band wavenumbers

d) A DC error signal will be produced

An example of these spectral properties and relationships is illustrated in Figure 18. The detector non-linearity illustrated in Figure 18 closely follows the following mathematical form.

$$Interferogram_{non-linear} = (Interferogram_{ideal} + V) - a_2 \cdot (Interferogram_{ideal} + V)^2 - \cdots \quad \text{(8a)}$$

3rd order and higher nonlinearity terms are not significant in the CrIS hardware and therefore have been ignored. The term V in equation 8a represents the DC voltage at the detector/preamp output which is produced solely from detector photo and dark currents. Thus, V does not include circuit DC offsets of the preamp. $Interferogram_{ideal}$ is the AC signal at detector/preamp output in volts corresponding to the desired ideal linear interferogram. $Interferogram_{non\text{-}linear}$ is the actual signal at detector/preamp output in volts which includes the non-linearity distortion.

Expanding the squared portion of Equation 8a and eliminating the DC terms produces:

$$Interferogram_{non-linear} = Interferogram_{ideal} - 2a_2 V \cdot Interferogram_{ideal} - a_2 \cdot Interferogram_{ideal}^2 \quad \text{(8b)}$$

Transforming into the spectral domain with a Fourier Transform and replacing multiplication in the interferogram domain with convolution in the spectral domain yields:

$$Spectrum_{non-linear} = (1 - 2a_2 V) \cdot Spectrum_{ideal} - a_2 \cdot (Spectrum_{ideal} \otimes Spectrum_{ideal}) \quad \text{(8c)}$$

where $\otimes$ indicates convolution.

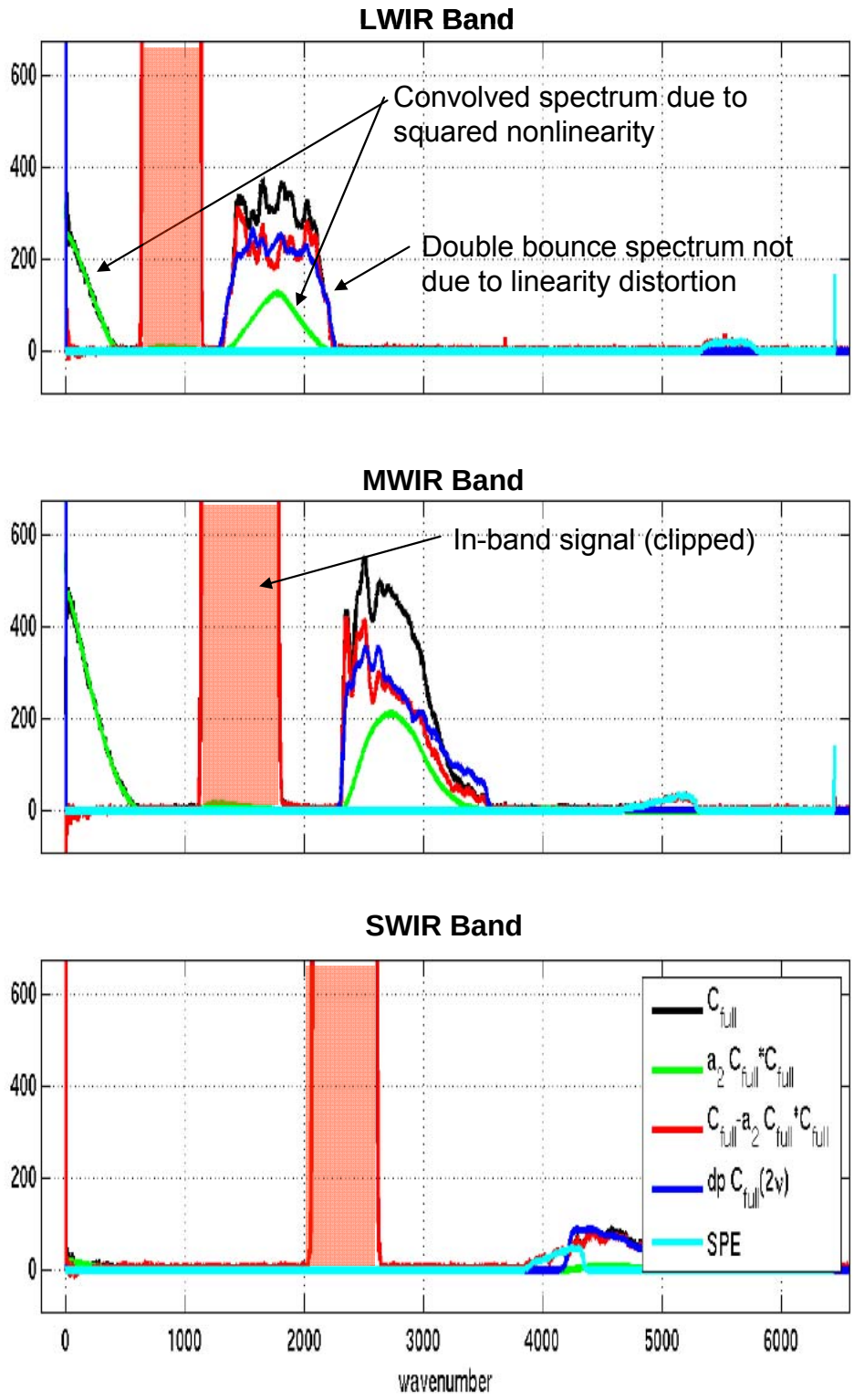

Figure 18: Spectral Distortion Due to Square Law Nonlinearity (courtesy of University of Wisconsin)

Examination of Figure 18 and Equation 8c shows that the in-band distortion caused by square law nonlinearity simply results in a scaling of the in-band spectrum by (1-2a_2V). Secondly, the out-of-band distortion caused by convolution of the spectrum with itself does not overlap the in-band spectrum. These out-of-band spectral artifacts can be used to estimate a value for a_2. Since the out-of-band artifact at the second harmonic can be contaminated with signal distortions not associated with non-linearity, then it is preferable to use the low frequency spectral artifact illustrated in Figure 18 for this purpose.

Equation 8c provides a mathematical basis for performing the non-linearity correction prior to radiometric calibration. Furthermore, from equation 8c we see that a_2 is simply the ratio given below in equation 8d; the observed non-linear spectrum divided by the ideal spectrum convolved with itself. This spectral ratio is evaluated in the wavenumber regions where the convolution produces low frequency out-of-band products in the range of 50 – 300 cm^{-1} (see Figure 18).

$$a_2(\sigma) = -Spectrum_{non-linear}(\sigma)/(Spectrum_{ideal}(\sigma) \otimes Spectrum_{ideal}(\sigma))_{\sigma=50\,to\,300\,cm^{-1}} \qquad (8d)$$

The ideal linear spectra are not available for this calculation. So a_2 must be estimated by using the observed non-linear spectra as shown in equation 8e. This approximation can be iterated for better a_2 accuracy by making an initial a_2 calculation per equation 8e, perform a linearity correction on the observed spectra and then using the more linear result to make a better estimate of a_2 using equation 8e again. However, this is not necessary when the nonlinearity to be corrected is very small. For example, the approximation in going from equation 8d to equation 8e results in only 2% error in the a_2 estimate when the observed non-linearity is 1%.

$$a_2(\sigma) \cong -Spectrum_{non-linear}(\sigma)/(Spectrum_{non-linear}(\sigma) \otimes Spectrum_{non-linear}(\sigma))_{\sigma=50\,to\,300\,cm^{-1}} \qquad (8e)$$

The non-linearity parameter a_2 can be referenced to either the output of the A/D converter in which case it is expressed in the units of $counts^{-1}$ or it can be referenced to the output of the detector preamplifier where it is expressed in the units of $volts^{-1}$. If the a_2 parameter is calculated to correspond to the A/D converter output, then it must be recalculated every time the CrIS IR channel PGA electrical gain changes. In order to avoid this difficulty, it is preferable to reference the a_2 characterization parameter to the detector/preamp output. The a_2 parameter corresponding to A/D converter output can be converted to an a_2 parameter corresponding to detector/preamplifier output by multiplying by the A/D gain ($G^{A/D}$) and PGA gain (G^{PGA}).

The nonlinear spectra can be corrected by inverting equation 8c and ignoring spectral terms that fall out-of-band.

$$Spectrum_{ideal} = Spectrum_{non-linear}/(1-2a_2V) \qquad (8g)$$

In order to complete the nonlinearity correction per Equation 8g, it is also necessary to make a calculation of the preamp DC voltage output "V" that is due to photon flux and detector dark current. This calculation must be performed for every interferogram collected. Since the a_2 parameter had been determined for a signal observed at the detector/preamp output, and then the V parameter must also be determined at that same node in the signal processing chain. Equations 8h through 8j show

how V is determined for each of three spectra needed to produce calibrated radiances for the CrIS sensor.

$$V_{b,p}^{ds_preamp} = V_{b,p}^{inst} \tag{8h}$$

$$V_{b,p}^{ict_preamp} = V_{b,p}^{inst} + \frac{1}{G_{b,p}^{\mathrm{mod}_eff} \cdot G_{b,p}^{PGA} \cdot G^{A/D} \cdot G_b^{DFT}} \cdot \sum_{n=0}^{N_b-1} \frac{\left| \underline{\widetilde{S}}_{b,p,d}^{ict}[n] - \left\langle \underline{\widetilde{S}}_{b,p,d}^{ds}[n] \right\rangle \right|}{G_b^{FIR}[n]} \tag{8i}$$

$$V_{b,p}^{es_preamp} = V_{b,p}^{inst} + \frac{1}{G_{b,p}^{\mathrm{mod}_eff} \cdot G_{b,p}^{PGA} \cdot G^{A/D} \cdot G_b^{DFT}} \cdot \sum_{n=0}^{N_b-1} \frac{\left| \underline{\widetilde{S}}_{b,p,d}^{es}[n] - \left\langle \underline{\widetilde{S}}_{b,p,d}^{ds}[n] \right\rangle \right|}{G_b^{FIR}[n]} \tag{8j}$$

where

$$V_{b,p}^{inst} = \left| V_{b,p}^{TLM_ds} - V_b^{CIRCUIT} \right| \tag{8k}$$

V^{inst} is the preamp output DC voltage produced by the *inst*rument background photon flux and detector dark current. Any DC voltage at preamp output that is due to circuit offsets does not get included in V^{inst}. Thus, V^{inst} is determined from an observation of the preamp DC output voltage available in the CrIS telemetry when viewing deep space and then differencing this observed value with the circuit offset $V^{CIRCUIT}$ corresponding to a detector current of zero. Since the instrument background photo flux depends upon the interferometer and aft optic temperatures, then V^{inst} must be re-established whenever those temperatures change significantly.

The second term in equations 8i and 8j represents the additional change of preamp output DC voltage as the instrument's view changes from Space to ICT or Earth. Equation 8i and 8j are evaluated for each ICT and earth scene spectrum. Dividing by the A/D, PGA, DFT and FIR filter gains allows the voltage change at the detector preamplifier output to be calculated from spectra that was observed at FIR filter output. The division by the modulation efficiency provides the conversion from the change in AC signal level provided by the normal mode spectra to the change in DC signal level that is required for the correction.

3.2 SCAN MIRROR POLARIZATION COMPENSATION

The CrIS scan mirror is used to select calibration and scene targets. Rotating the scan mirror does the selection. By design, the CrIS uses a barrel-roll scan mirror (see Figure 19), so the angle of reflection θ at the surface of the mirror remains constant for all types of viewed scenes.

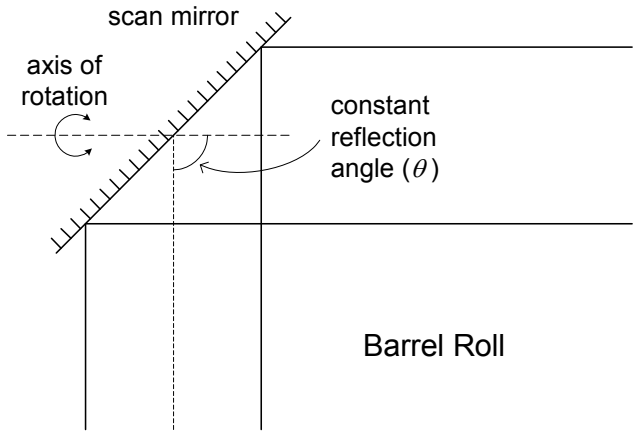

Figure 19: Barrel-roll scanner type

Reflection on an inclined surface always induces some polarization. Since the CrIS incident angle is constant, the polarization induce by the scan is constant too. However, its plane rotates with the barrel roll angle. Since the interferometer itself is expected to create a significant polarization, this will create a modulation of the signal as the scan mirror rotates. This effect will be corrected in the radiometric calibration equation by the introduction of a polarization operator. This operator is computed on ground from analysis and/or measurement during pre-flight characterization and testing. It is produced with the same spectral axes as the ones requested for the calibrated spectra in each band.

The CrIS engineering data packet can contain polarization correction data for each earth scene scan positions, DS and ICT. The correction is relative to the polarization at Nadir and ICT positions. There are 9 coefficients for each scan position (3 for LW, 3 for MW and three for SW). The three coefficients for each band allow a wavenumber dependence to be modeled and interpolated to each wavenumber channel. The polarization capability is only expected to be used if the CrIS has a polarization imbalance that changes more than 1% as a function of earth scene scan angle. There is no attempt to correct any polarization in the earth scene radiance.

3.3 FRINGE COUNT ERROR HANDLING

A fringe counting system using a reference laser source within the interferometer subsystem, determines the sampling. If, for any reason, a fringe is lost, then the current and the following interferograms are shifted with respect to previous ones. This means that the phase of subsequent measurements will be affected and if they are calibrated using a gain or offset measurement taken before the occurrence of the fringe loss, then errors will be introduced into the final spectrum. The method for detecting and correcting fringe losses is based on the analysis of the residual phase of spectra.

3.3.1 Phase Analysis

With an *unfiltered and undecimated interferogram*, the fringe count error detection could be done directly on the interferogram by looking at the position of the observed ZPD.

In the best cases, when the scene contains some sort of continuous background, the ZPD position can be easily determined (one just identifies the maximal IGM observation). However, if the scene is sensibly different from a blackbody distribution, containing only sparse spectral lines for example, the strong ZPD point is no longer an available reference. Moreover, if the signal suffers from strong phase dependencies to wavenumber (see Section 2.4.1); one could have a hard time trying to identify the true ZPD point as interferometric frequencies are spread around a larger area. Alternatively, FCE handling could be based on IGM center of gravity computation. This could be done with an auto-correlation to extract its ZPD position with sub-point precision. However, this approach is limited by the dispersion in the interferometer.

When the interferogram is *filtered and decimated*, as it is the case for CrIS, the ZPD region is further affected and the maximum intensity point can be difficult to identify. In addition, a shift by a number of points smaller than the decimation factor will produce only a small shift of the decimated interferogram. For example, the shift of a 20 times decimated interferogram will be 1/20 the effective sampling interval if the fringe error is one point. Therefore, the monitoring of the ZPD position of the decimated interferograms is not a sensitive approach to detect fringe count errors for CrIS.

An alternative method for FCE detection based on absolute position sensor is not accurate enough. The resulting accuracy only ties down the ZPD position to within the order of a hundred samples or so.

The approach selected for FCE detection consists of an analysis of the linear wavenumber-dependent residual phase that comes from comparing signals to each other (ES, ICT and DS). When the OPD axis definition of the actual measurement is the same as the current gain and offset used for radiometric calibration, then the residual phase should be zero. A shift in one of them with respect to the two others produces a phase error increasing linearly with wavenumber. This can be seen using the “shift theorem”. This is explained in further details in Section 3.3.3.

As the phase extraction process must mathematically be processed in the spectral domain, the FCE detection is performed on complex spectra. The correction is done by the multiplication with a linear shifting phase, enabling the correction of fractional point shifts in the corresponding interferograms.

3.3.2 Spectrum Based Detection and Correction

Fringe count errors (FCE) can occur anytime. First, they can occur at turnaround between successive IGMs: the effect of such FCEs is to shift all measurements following the error by h points. If this

remains uncorrected, problems will arise because all the measurements involved will not have the same sampling positions. A stable instrument is not expected to suffer from this type of error.

On the other hand, if a cosmic ray falls on the metrology system (detector, electronics, etc.), a spike could be induced and the metrology system could loose one or more fringes. This type of error can occur anywhere in the IGM. The effect of “in-sweep” fringe errors is twofold: first it shifts the last part of the interferogram in which the error occurs with respect to the first part. This effect results in a distortion of the current measurement that is very difficult to recover. The second effect is that all subsequent measurements will be shifted with respect to any previous measurements. This latter effect is the same as if the error would have been at the turn-around.

For all types of measurements, the fringe count reference is the *actual* Earth scene measurement. When a FCE occurs for a given sweep with respect to the previous sweep, the associated average ICT and DS need to be shifted to match the current fringe count position, in order to match all spectra that follow. This has the advantage that all subsequent measurements will need no correction. The fact of aligning moving averaged deep space (DS) and warm blackbody (ICT) references is easier and less error inducing because they essentially are smooth blackbody distributions. This limits the error accumulation on the scene.

The following summarizes the conditions under which the FCE handling will be performed:

Because the phase is not strictly the same for forward and reverse sweeps, the fringe count error detection and correction is done independently for the two sweep directions.

Because each detector measures signals from a common sweep, FCEs affects equally each pixel: However, the detection is performed on FOV1 in LW band (LW1) in a given FOR. If the LW1 detection validates, the required correction is calculated and applied to all FOVs in each band for the sweep direction. If LW1 does not detect/validate, the detection is done for LW2 and so on and so forth until a valid fringe count is detected or all FOVs in the LW band are exhausted. After a valid detection, FCE correction is applied to all pixels in each band.

The order of detection is LW1, LW2, and LW9. Any FOVs with missing data packets are skipped. MW and SW band FOVs are not used for FCE detection purposes. However, the same FCE correction is applied to all 27 detector FOVs in all 3 bands.

Since FCEs can occur in all types of measurements done by the CrIS instrument, the detection and correction approach is slightly different depending if the signal is a scene or a calibration measurement.

ZPD Synchronization

Each time the instrument is powered on or initialized; the interferogram sampling window position is re-established. This is done using a LED interrupter circuit mounted on the interferometer porch swing assembly. This ZPD position is initially used to mark the sampling window position. Following this “coarse” ZPD position determination, the CrIS sensor refines the ZPD centering of the sweep by detecting the maximum absolute value of interferogram sample while viewing the ICT target in the MW band.

ZPD centering is always maintained to within ±12 fringe counts of the center by the CrIS instrument to eliminate the need to send excess data. This shift of the sampling window is not critical since it can be considered as a fringe count error and is automatically detected and corrected during the radiometric characterization and radiometric calibration process. In principle the data can be used no matter where the sampling window position is, since extra samples are collected to assure that the full MPD of the interferometer is achieved for both ends of the sweep. The amount of drift can be almost arbitrary, as the IGM is sampled double-sided. Therefore, no special care has to be taken in order to avoid loosing the ZPD point, like it would be the case for single-sided IGMs for example.

3.3.3 FCE Detection

The shift theorem states that a shift of a in the interferogram domain corresponds to a linear phase in the spectrum domain:

$$I(x-a) \leftrightarrow \underline{S}[\sigma]e^{-2\pi i a \sigma} \tag{9}$$

In our case, a is an integer in the undecimated interferogram, and in the decimated interferogram, it is a multiple of the inverse of the decimation factor.

Based on this relation, the residual phase of a calibrated spectrum is the phase corresponding to the initial shift, all other phase contributors having been cancelled out by the calibration process itself (see Section 4.1.2). Therefore, a linear regression on the residual phase of the calibrated spectrum reveals the shift due to a fringe count error on the observed interferogram (see Figure 20).

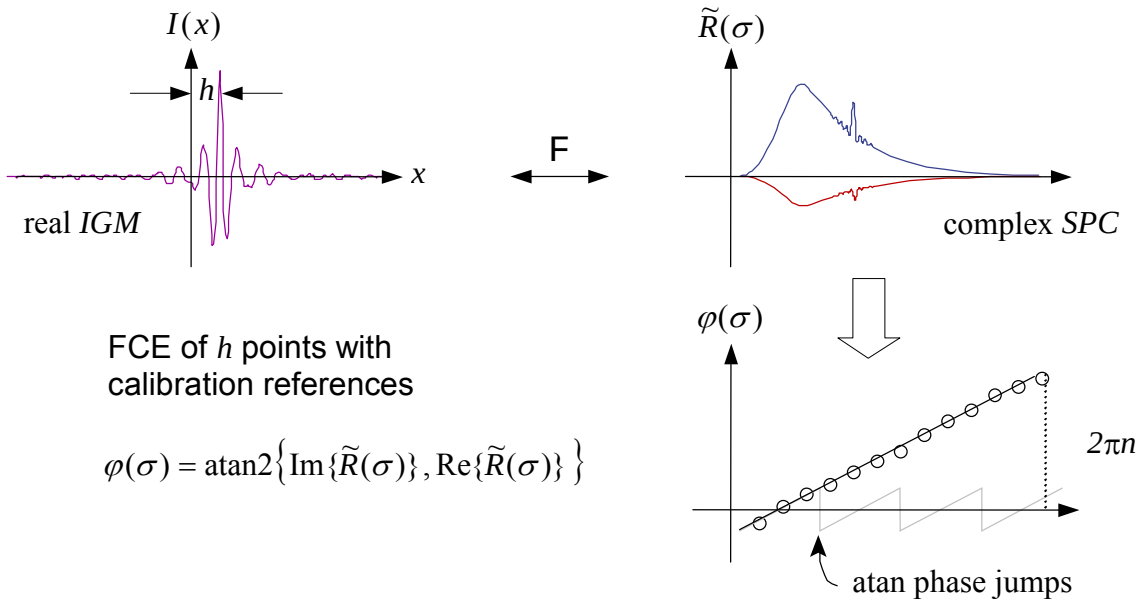

Figure 20: FCE detection scheme

In practice, this phase shift is not measured in absolute way but in a relative way to a reference spectrum because a part of the spectrum's phase is unknown. For reference calibration measurement, FCE detection is done with respect to the *previous equivalent mean* measurements. As the current and previous spectra are equivalent (always looking as the DS or at the same reference blackbody) the instrument phases are cancelled out, their ratio can be used to compute the phase extraction function $\widetilde{R}(\sigma)$ needed for linear phase extraction (here $\phi_h = -2\pi h \lambda_S$):

$$\widetilde{R}(\sigma) = \frac{\underline{\widetilde{S}}^C(\sigma)}{\left\langle \underline{\widetilde{S}}^C \right\rangle(\sigma)} = \frac{e^{i\phi_h}(A^C e^{i\phi^{ext}} + A^{in} e^{i\phi^{in}})}{A^C e^{i\phi^{ext}} + A^{in} e^{i\phi^{in}}} = \frac{e^{i\phi_h}(0 + A^{in} e^{i\phi^{in}})}{0 + A^{in} e^{i\phi^{in}}} = e^{i\phi_h}, \tag{10}$$

where $\underline{\widetilde{S}}^{C}(\sigma)$ is the cold reference spectrum, and the 0 in the last equation is there to indicate that the cold reference's radiance is negligible when compared to the instrument's contribution.

The same reasoning applies for the hot reference:

$$\widetilde{R}(\sigma) = \frac{\underline{\widetilde{S}}^{H}(\sigma)}{\left\langle \underline{\widetilde{S}}^{H} \right\rangle(\sigma)} = \frac{e^{i\phi_h}(A^H e^{i\phi^{ext}} + A^{in} e^{i\phi^{in}})}{A^H e^{i\phi^{ext}} + A^{in} e^{i\phi^{in}}} = e^{i\phi_h}, \tag{11}$$

where $\underline{\widetilde{S}}^{H}(\sigma)$ is the hot reference's spectrum.

Phase synchronization of the cold and hot reference spectra is performed by taking the ratio of the cold over the hot reference spectra. Since the cold reference spectrum has a phase shift of π with respect to the hot reference spectrum, the phase of the cold reference spectra is shifted by π prior to taking the ratio.

As the measured earth scenes are different one to another, the previous scene can not be used as a reference as it is done with calibration measurements. Earth scene measurements $\widetilde{S}^{S}(\sigma)$ must be processed in a particular way in order to isolate only the linear fringe count dependency. The following equations summarize the process.

Define $\widetilde{P}(\sigma)$ and $\widetilde{Q}(\sigma)$ as follows:

$$\begin{aligned} \widetilde{P}(\sigma) &= \frac{\underline{\widetilde{S}}^{S}}{\left\langle \underline{\widetilde{S}}^{H} \right\rangle - \left\langle \underline{\widetilde{S}}^{C} \right\rangle} = \frac{e^{i\phi_h}(A^S e^{i\phi^{ext}} + A^{in} e^{i\phi^{in}})}{(A^H e^{i\phi^{ext}} + A^{in} e^{i\phi^{in}}) - (A^C e^{i\phi^{ext}} + A^{in} e^{i\phi^{in}})} \\ &= e^{i\phi_h}\left[\frac{A^S}{A^H - A^C} + \frac{A^{in}}{A^H - A^C} e^{i(\phi^{in} - \phi^{ext})}\right] \end{aligned} \tag{12}$$

$$\widetilde{Q}(\sigma) = \frac{\left\langle \underline{\widetilde{S}}^{C} \right\rangle}{\left\langle \underline{\widetilde{S}}^{H} \right\rangle - \left\langle \underline{\widetilde{S}}^{C} \right\rangle} = \frac{A^{in}}{A^H - A^C} e^{i(\phi^{in} - \phi^{ext})} \tag{13}$$

It then becomes possible to solve for the linear phase shift versus wavenumber for any earth scene without knowledge of prior earth scenes [RD 46]. The phase extraction function for earth scenes is then given by

$$\widetilde{R}(\sigma) = \frac{\widetilde{P}(\sigma)}{\pm\sqrt{\left|\widetilde{P}(\sigma)\right|^2 - \mathrm{Im}\left\{\widetilde{Q}(\sigma)\right\}^2} + i\ \mathrm{Im}\left\{\widetilde{Q}(\sigma)\right\}} = e^{i\phi_h} \tag{14}$$

SDR algorithm uses only the positive square root term in the denominator of phase extraction function, equation (14), to implement FCE detection for earth scenes. This would be valid whenever earth scene radiance is larger than the instrument background radiance. The SDR algorithm code tests for this condition to assure that any spectral bin used in this calculation has radiance larger than the instrument background. Knowledge of the instrument background is maintained by space looks and performing a running average of the uncalibrated space look spectra.

Once the spectral phase extraction function $\widetilde{R}(\sigma)$ is known, its associated phase shift as a function of wavenumber can be computed with the following relation:

$$\varphi(\sigma) = Unwrap_{2\pi}[\mathrm{atan2}\left\{\mathrm{Im}\left\{\widetilde{R}(\sigma)\right\}, \mathrm{Re}\left\{\widetilde{R}(\sigma)\right\}\right\}] \tag{15}$$

In the presence of a FCE, substantial additional contribution from the signal appears in the imaginary part of $\widetilde{R}(\sigma)$. This contribution manifests itself in a signal phase increasing linearly as function of the spectral frequency (see Figure 20).

This calculation includes an "un-wrapping" of the phase in case it exceeds the range [$-\pi$, $+\pi$] (caused by the numerical $\mathrm{atan2}()$ function). Compensations of $\pm 2\pi$ are added to the phase where discontinuities (absolute difference greater than 2π) are noticed between two consecutive points.

The second step is a linear regression of the phase $\varphi(\sigma)$ versus the wavenumber σ.

$$\varphi_0, \delta\varphi = \mathrm{LinearFit}\left\{\varphi(\sigma), \sigma\right\} \tag{16}$$

The output consists of two values per band and sweep direction.

$\delta\varphi$ the slope

φ_0 the ordinate at origin

The linear fit is accomplished using data from one CrIS FOV in the LWIR band. The wavenumber range used to perform the linear fit is defined in the SDR configuration file (default range is FFT bins 314 to 603 corresponding to wavenumber range 800 cm^{-1} to 980 cm^{-1}). This wavenumber range was found to have best signal to noise ratio for FCE detection and also had highest likelihood of earth scene radiance exceeding the instrument background [RD 40].

The FFT bins used to perform the linear fit described in equation (16) must also exceed a minimum signal level to assure adequate signal to noise ratio for ICT and DS scenes and to assure that the earth scene radiance is larger than the instrument background radiance in each FFT bin for earth scenes [RD 40]. When processing ICT or DS spectrum, only FFT bins exceeding a specified minimum signal level relative to peak signal level in the spectrum can be used. This is described in more detail later in this section.

Consequently, any linear fit having too few data points after undergoing these previously described quality checks will be rejected due to insufficient number of data points to make a good estimate of FCE. The number of good data points p used to find the linear fit relative to the number of bins N available in the LWIR band (N = 864) is the quality measure computed. A flag is raised when the fractional number of bins used to fit data is less than a configurable parameter (typically 0.2). The Dimension Threshold Limit N^{thres} = 0.2 implies that at least 20% of the available 864 FFT bins must be of good quality and all of these bins must lie between 800 cm^{-1} to 980 cm^{-1}.

The validity of this linear fit using only high quality data points is further evaluated by a goodness of fit computation, evaluated by means of a squared standard deviation s^2 of the data points along the fitted straight line.

$$s^2 = \frac{1}{N-1}\sum_{p=0}^{N-1}\left(\varphi(\sigma_p) - (\delta\varphi \cdot \sigma_p + \varphi_0)\right)^2 \tag{17}$$

If the s^2 value is larger than a predetermined threshold, then the FCE detection can not be performed on this set of FOV data. This threshold limit is typically set so that s^{thres} = 0.004 rad^2 and translates into an equivalent 3.6º rms phase error of data points relative to straight line fit. This type of error performance typically requires a signal to noise ratio of better than 20 dB in all the FFT bins used for the curve fit.

Thus, these validity checks help to identify invalid linear phase estimates. For example,

if $s^2 > s^{thres}$ is true, then flag goodness of fit failure. (18a)

if $\frac{Length[p\}}{N} < N^{thres}$ is true, then flag Dimension Threshold failure (18b)

If either of these tests fail, then a new FOV is selected for evaluation and the process is repeated. If all 9 LWIR FOVs fail these criteria, then FCE detection can not be performed for the current earth scene and all spectra are processed with the assumption that there is no FCE.

If the quality checks of equations (18a) and (18b) are passed, then an estimate of FCE can be made if one exists. From the slope computed from equation (16), it then becomes possible to extract the interferogram displacement of a number of h current fringes, using the metrology sampling wavelength value λ_S:

$$h^{cur} = \frac{\delta\phi}{2\pi\ \lambda_S} \tag{18}$$

This number is expected to be an integer, since the FCE comes from a mismatch of the fringe count between two spectra. Numerical error in the fitting process might generate a number, which is not an integer, but close to an integer. So the value used for the correction is rounded toward the nearest integer using

$$h^{cur} = floor(\frac{\delta\phi}{2\pi\ \lambda_S} + \frac{1}{2}) \tag{19}$$

where the function floor() is used to indicate the truncation function.

The difference between these two values of h allows one to estimate how close the computed value is to an integer, and raise a flag if the difference is too great. The fractional part of the calculated FCE is subjected to a fractional threshold limit check (default h^{thres} = 0.1 typically). In addition, a flag is raised if the FCE magnitude is greater than the FCE maximum limit (h^{max} = 18 typically). Equations (20a) and (20b) summarize these quality control measures.

If $\left|h^{cur} - floor(h^{cur} + 0.5)\right| > h^{thres}$ is true, then flag fractional FCE threshold failure (20a)

If $|\ h^{cur}\ | > h^{\max}$ is true, then flag maximum FCE threshold failure (20b)

If either of these tests fail, then a new FOV is selected for evaluation and the process is repeated. If all 9 LWIR FOVs fail these criteria, then FCE detection can not be performed for the current earth scene and all spectra are processed with the assumption that there is no FCE.

The following flow diagram in Figure 21 illustrates the processing steps used to extract FCE from linear phase shift for each uncalibrated LWIR spectrum processed. The computed FCE is used for

correction only if it passes all four validation tests highlighted in yellow in Figure 21. If quality control measures are not passed in all 9 LWIR FOVs evaluated, then flags are assigned to all 27 spectrum (9 in each IR band) associated with the current CrIS Field of Regard (FOR).

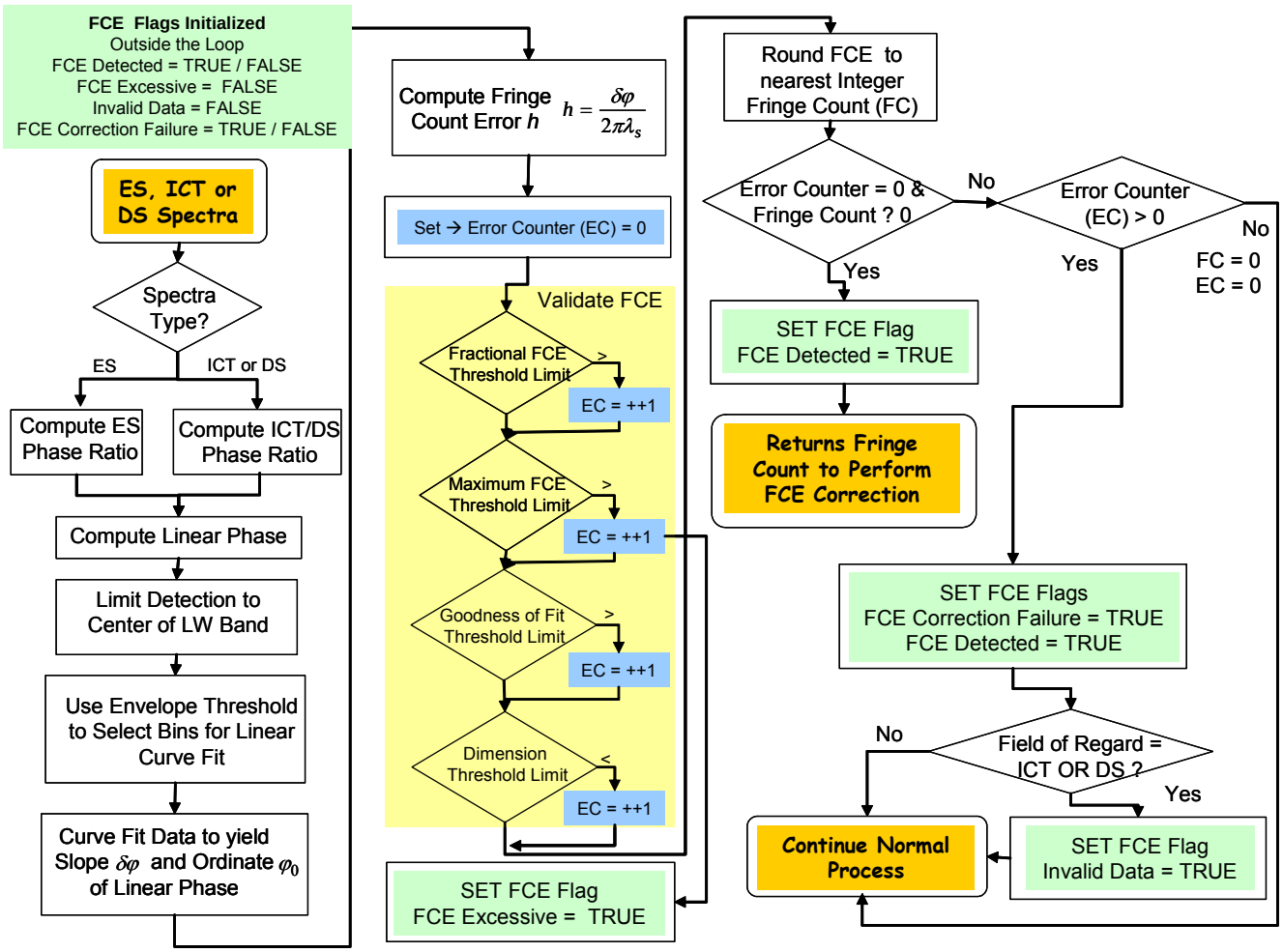

Figure 21: FCE Detection Flow and Flags

FCE Validation Summary

The SDR algorithm provides four quality measures to validate the detected Fringe Count Error (FCE). The FCE detection is considered valid if it passes all four of the following quality control measures.

- <u>Fractional FCE Threshold Limit:</u>

  The SDR algorithm generates a FCE integer value by rounding the computed value toward the nearest integer and then performs a quality check before using this integer for FCE correction. If the calculated fringe count error has a fractional part that exceeds the Fractional FCE Threshold Limit h^{thres}, then a flag is raised. Fractional FCE Threshold Limit h^{thres} is a configurable parameter in the SDR algorithm (typically 0.1)

- <u>Maximum FCE Threshold Limit:</u>

  The SDR algorithm provides a quality measure to reject fringe count values that are too high to be considered realistic. A flag is raised if the calculated FCE value exceeds the

Maximum FCE Threshold Limit h^{max}. Maximum FCE Threshold Limit h^{max} is a configurable parameter in the SDR algorithm (typically 18). *Note: The CrIS sensor hardware is designed to maintain FCE less than 12 via hardware resets.*

- Goodness of Linear Fit Threshold Limit:

  Validity of straight line fit is estimated by a goodness of fit criteria given by equation (17). A flag is raised to identify invalid measurements if s^2 value is too large, that is, greater than the Goodness of Linear Fitting Threshold Limit s^{thres}. s^{thres} is a configurable parameter in the SDR algorithm (typically 0.004)

- Dimension Threshold Limit:

  In order to improve fit accuracy when processing ICT or DS reference spectrum, only FFT bins with high SNR that exceed a pre-defined Amplitude Threshold Parameter Ref^{thres} are used (typically Ref^{thres} = 0.25). This threshold is set relative to the largest magnitude FFT bin in the current ICT or DS spectrum.

  In order to improve fit accuracy when processing earth scene spectrum, only FFT bins having signal magnitude that exceeds the instrument background can be used. A pre-defined Amplitude Threshold Parameter Cal^{thres} is used (typically Cal^{thres} = 1.05). This threshold is set relative to the running average DS spectrum magnitude. *Note: Depending upon the phase relationship between instrument background and earth scene spectrum in each FFT bin, a threshold of* Cal^{thres} *= 1.05 means the earth scene spectral magnitude can be anywhere from 1.05 times greater than the instrument background to 2.05 times greater than the instrument background.*

  Any fit having too few points indicates that the data is not suitable for FCE estimation. A flag is raised when the relative number of bins used to fit data is less than the Dimension Threshold Limit N^{thres}. N^{thres} is a configurable parameter in the SDR algorithm (typically 0.2). Note: Since there are 864 FFT bins available in the LWIR band, then a threshold of 0.2 implies that 173 FFT bins must be available for the calculation. All of these bins must also be within the 314 to 603 FFT bin range (800 cm^{-1} to 980 cm^{-1} spectral range approx.). Since there are only 290 FFT bins in this range, then only 117 of them (40%) can be lost.

Reliable FCE detection (cold earth scene exclusion)

The SDR algorithm has been implemented with only the positive square root term of equation (14), to extract phase of earth scene (ES) spectra. The correct sign of the square root term in the phase extraction function depends upon the magnitude and phase of the instrument background [RD 40], [RD 46] & [RD 47]:

If |ES radiance| > |Instrument Background *cos ($\phi_{Bg} - \phi_{ES}$)|, the square root term in equation (14) is positive and the SDR algorithm implementation correctly handles FCE detection. However, if |ES Radiance| < |Instrument Background *cos ($\phi_{Bg} - \phi_{ES}$)|, the square root term in equation (14) is negative and the SDR implementation for this case is invalid. Here ($\phi_{Bg} - \phi_{ES}$) is the phase shift between background and earth scene.

The on-orbit CrIS instrument will normally see earth scene radiance greater than the sensor background. The earth scene radiance levels in MW and SW band can go below sensor background when orbiting over poles or if the instrument is looking at a very cold and/or cloudy earth scene. In LW band, earth scene radiance levels between 800 cm^{-1} to 980 cm^{-1} should be above sensor background except in rare instances.

However, because FCE detection as implemented in the SDR algorithm can produce ambiguous results (i.e. A π shift in computed phase) whenever a spectral bin is dominated by instrument background instead of by the scene radiance, the SDR algorithm compares earth scene spectra to a running average of the instrument background (spectral bin by spectral bin). If a sufficient number of spectral bins cannot be found to perform a reliable FCE detection in any of the 9 FOVs available in LW band, then FCE detection/correction will not be attempted. FCE detection/correction will automatically resume when earth scene brightness temperature is sufficiently high to pass the Cal Threshold Parameter Cal^{thres} limit. Typical value of this parameter, Cal^{thres} = 1.05, sets the earth scene brightness to be 5% more than the instrument background when the earth scene spectrum is in phase with the instrument background (105% more than the instrument background when the earth scene spectrum is out-of-phase with the instrument background. Normally, the earth scene spectrum is out of phase with instrument background and considerable margin is provided by this thresholding method.

In order to further improve likelihood of a successful FCE detection/correction on as many earth scenes as possible, only LW band spectra in the wavenumber range 800 cm^{-1} to 980 cm^{-1} are used to perform FCE detection. The algorithm extracts interferogram displacement of *h* fringes from equation (19) over this spectral range to detect Fringe Count Error. This spectral range is absorption and emission line free (window channel region) thereby maintaining greatest margin of scene radiance above instrument background radiance over a wide spectral range. Best FCE determination can be made in this wavenumber range. However, these limits are configurable in the SDR algorithm.

3.3.4 FCE Correction

Once the OPD shift h^{cur} is known, the correction of a shifted *undecimated* interferogram is straightforward: you simply shift it back to its correct position. This is done by removing a number of points equal to the shift at on one end of the IGM, the one corresponding to the direction of the shift. These removed points are put at the other end of the IGM, using the implicit periodicity of the Fourier transform.

The correction of a shifted and *decimated* interferogram is more difficult. This is because the shift will not necessarily be an integer multiple of the decimation factor. Therefore, the decimated IGM would have to be shifted by a *fractional* number of points. This requires some sort of interpolation. The present approach is to compute in spectral domain a direct multiplication with the inverse phase function, as shown by Equation (21). As the new fringe alignment will remain present after the detection, the correction scheme brings previous signals back to this new fringe count. This explains the positive sign in the following equation, which *introduces* an equivalent FCE into the unaffected signals.

$$\underline{\tilde{S}}^{X}_{b,p,d}(\sigma) = \underline{\tilde{S}}^{X}_{b,p,d}(\sigma)\, e^{+2\pi\, i\, h^{cur}\ \lambda_S\ \sigma} \tag{20}$$

In the array representation of decimated signal this gives:

$$\underline{\tilde{S}}^{X}_{b,p,d}[n] = \underline{\tilde{S}}^{X}_{b,p,d}[n] \exp\left(+2\pi\, i \frac{h^{cur}}{N_b \cdot DF_b} \left(\frac{\sigma_b[0]}{\Delta\sigma_b} + n \right) \right) \tag{21}$$

The corrected signals are also properly flagged as having been shift-corrected.

The following flow diagram illustrates the FCE detection and correction process for earth scenes. If ICT and DS moving window averages are at least half full (i.e. at least 15 out of 30), with valid ICT and DS data, then the <u>earth scenes</u> processed with this calibration reference are not flagged invalid

(SDR Algorithm software version 2.13 and above). Also, the earth scenes processed are not flagged as invalid if FCE detection does not pass validation criteria (SDR Algorithm software version 2.13 and above). However, the invalid data flag is raised in the current FOR if FCE is detected and not successfully corrected. Figure 22 illustrates this logic as well as other quality flag settings related to FCE detection/correction.

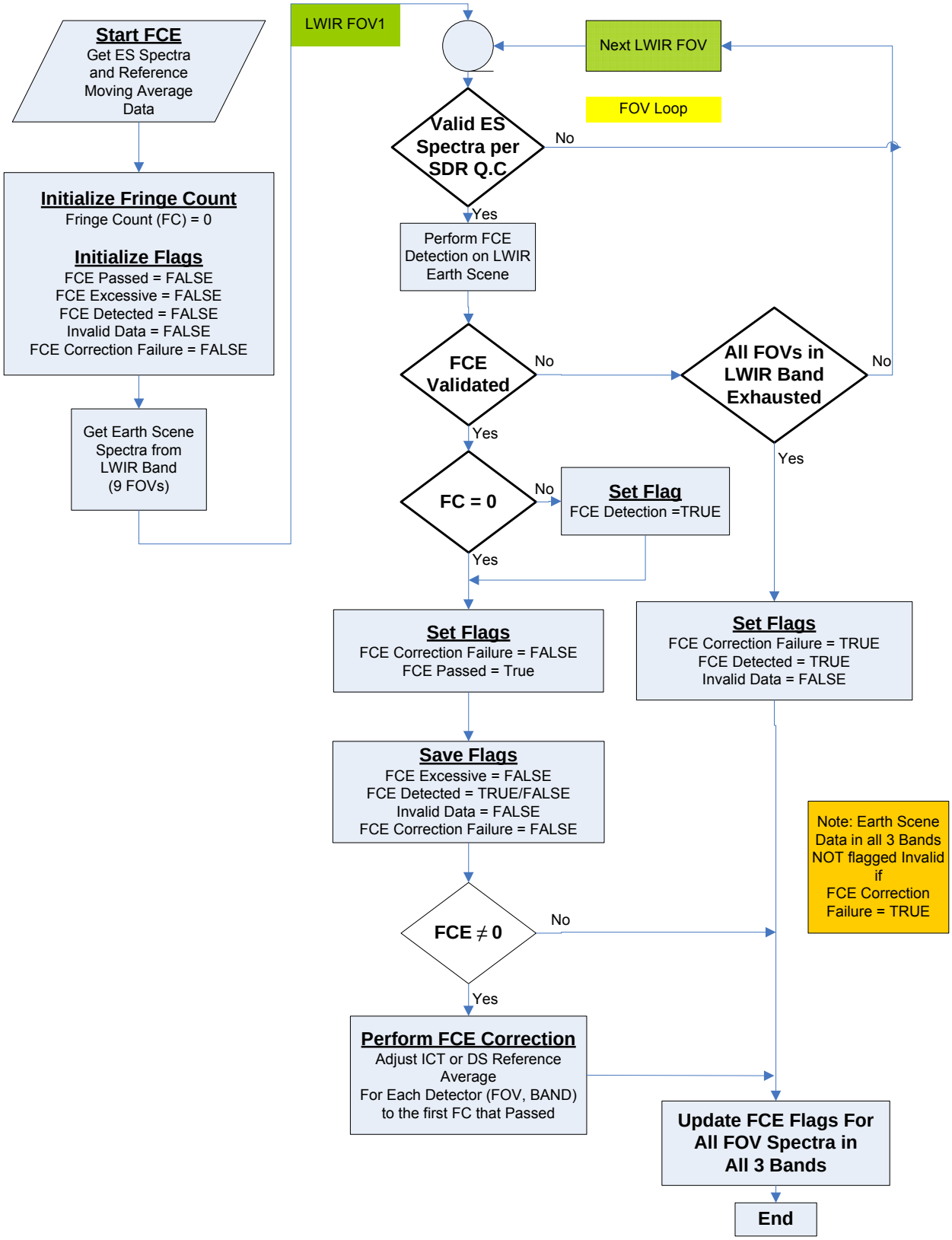

Figure 22: FCE Correction Flow and Quality Flags

FCE & Calibration Moving Window Average

Upon algorithm startup, all DS spectra within the moving window average are aligned to the phase of the first DS spectra by using equation (10) to detect any FCE in DS spectra which occurs after the collection of first DS spectra. Likewise upon algorithm startup, all ICT spectra within the moving window average are aligned to the phase of the first ICT spectra by using equation (11) to detect any FCE in ICT spectra which occurs after the first ICT spectra.

This process assures that all DS spectra in the moving window average are aligned with each other and also assures the same for the ICT spectra. However, this does not guarantee alignment between DS and ICT. It is possible that a FCE occurring between the first DS and the first ICT measurement can result in a relative offset between DS & ICT even though DS and ICT have been separately aligned.

DS and ICT Synchronization

It is important to make sure that ICT and DS fringe count is aligned to one another within the moving window average and that this is accomplished when processing the first earth scene. If there is a fringe count error between DS and ICT initially, then the FCE detection process on the first earth scene processed will fail to pass quality control tests described previously.

The phase of the DS average is then adjusted by +1 fringe count and the process repeated……then by -1 fringe, +2 fringe, -2 fringe, +3 fringe and -3 fringe until a successful FCE detection is made on the first earth scene. If synchronization is not achieved using the first earth scene, then a second earth scene and finally a third earth scene is tried. The synchronization is successful if the FC = 0, passes all the FCE validation tests, that is, no fractional FCE error, no maximum FCE error, no slope error, and no array dimension error. The DS and ICT moving window averages are thus synchronized before performing FCE detection on any subsequent earth scenes.

Currently, the DS to ICT synchronization is configured in the SDR Algorithm configuration file to cover a +/-3 count range in this DS to ICT synchronization process. This limit can be changed to a value other than +/-3 counts if desired. If the initial error between DS and ICT is larger than +/-3 fringes, then synchronization will fail and the SDR algorithm will need to be restarted using a better data set. In addition, if there is a FCE that occurs between the first ICT interferogram and the first earth scene interferogram, then synchronization will also fail to be achieved?

The +/-3 count search for DS and ICT synchronization requires at least one half of the moving window average to be populated with data. Since the nominal moving average window size for calibration is 30, then the average of 15 DS and 15 ICT spectra, plus an Earth scene measurement is initially used to resolve any FCE that may exist between DS and ICT.

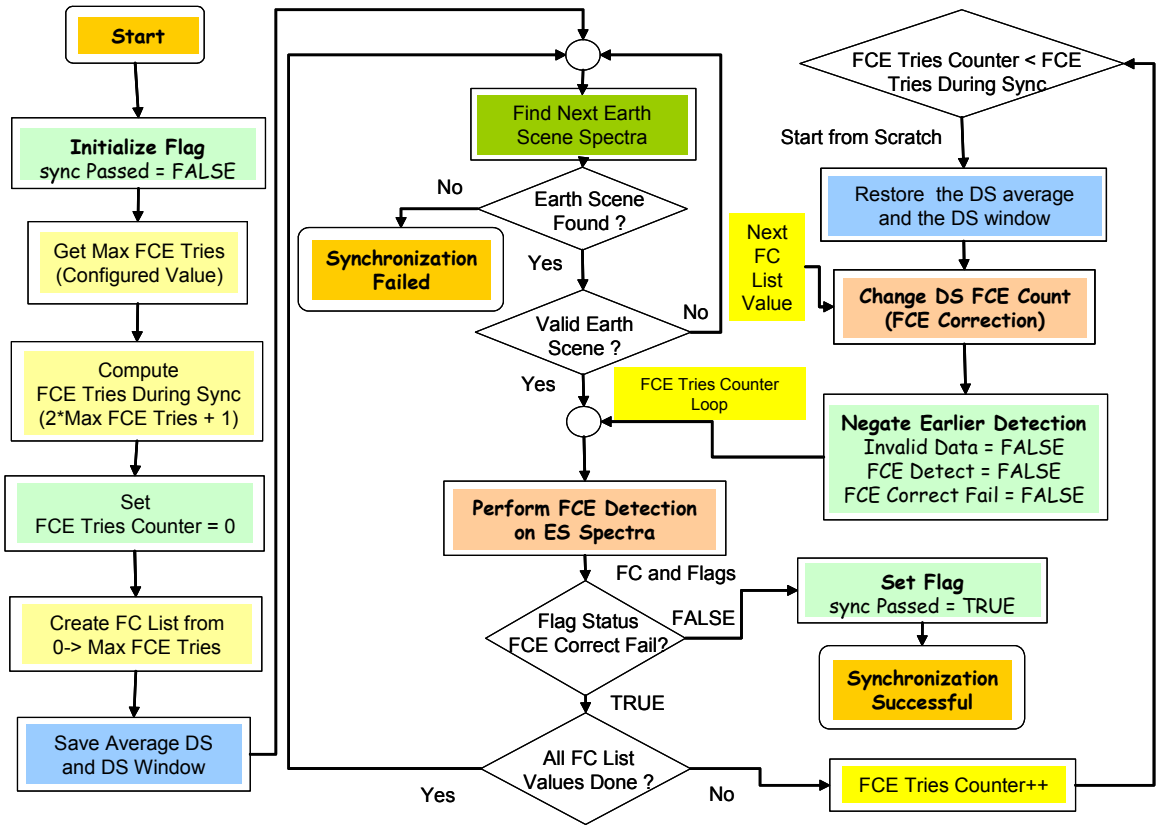

Figure 23: DS and ICT Synchronization Flow

FCE Detection/Correction (Normal Operation)

After DS to ICT synchronization is achieved, then FCE processing retains a normal flow as described in Figure 21 and Figure 22. All the DS and ICT of the current moving average are aligned to the fringe count phase of the currently observed earth scene. Therefore, when a fringe count error is detected on an earth scene (ES), the *current average* of the DS/ICT needs to be *shifted* to remove the fringe count mismatch. Thus, the current earth scene is always the master with regard to FCE alignment. The phase of the ICT and DS (15 prior and 15 after) are adjusted to match the earth scene phasing.

If FCE is first detected on a DS or ICT spectrum during normal operation, then that spectrum is immediately phase shifted to then align to the average of all prior spectra in the moving window average.

3.4 LUNAR INTRUSION HANDLING

It is possible that a regular space look data collect will occasionally coincide with a full or partial view of the moon. The space reference spectra that experience a lunar intrusion are detected and invalidated to prevent contamination of the DS moving window average. The detection is done separately for each FOV and for each sweep direction by using LWIR spectra. It is possible for some FOVs to experience lunar intrusion while others do not.

3.4.1 Lunar Intrusion Detection

On rare instances, the space look measurement used to calibrate the CrIS sensor background may encounter a view of the moon. Typically, this may only occur on one or two FOVs simultaneously and possibly on 2 to 3 successive space looks as the spacecraft orbit progresses past the view of the moon. When this happens, then it is necessary to detect this condition and exclude use of this contaminated space look data in the CrIS calibration.

Lunar intrusion is detected by comparing the average uncalibrated spectrum of any new deep space scene to the prior running average of the uncalibrated Deep Space spectrum. This is done independently on all 27 CrIS detector channels (9FOVs in 3 bands). The detection threshold is typically set to a 3% maximum allowable increase of the deep space spectral magnitude relative to ICT spectrum.

3% was chosen as the detection threshold since a single deep space reference having 3% error would only contaminate the 30 deep moving window average by 0.1%. Thus, the radiometric error for the CrIS system is also maintained less than 0.1% due to this effect. The 3% rejection threshold can be changed in the SDR algorithm configuration file to a smaller or larger percentage if desired.

The following steps are taken to detect a lunar intrusion:

1. Perform FCE handling on the new uncalibrated deep space spectrum in each band “b”, FOV “p” and sweep direction “d” $\underline{\widetilde{S}}^{ds}_{b,p,d}[n]$.

2. Subtract the averaged uncalibrated deep space spectrum from the newest deep space spectrum that was not included in the average,
$$\underline{\widetilde{R}}^{ds}_{b,p,d}[n] = \underline{\widetilde{S}}^{ds}_{b,p,d}[n] - \langle \underline{\widetilde{S}}^{ds}_{b,p,d}[n] \rangle \tag{23a}$$

3. Subtract the average uncalibrated DS spectrum from the average uncalibrated ICT spectrum,
$$\underline{\widetilde{R}}^{ict}_{b,p,d}[n] = \langle \underline{\widetilde{S}}^{ict}_{b,p,d}[n] \rangle - \langle \underline{\widetilde{S}}^{ds}_{b,p,d}[n] \rangle \tag{23b}$$

4. Compute real part of calibrated lunar spectrum in digital units [d.u.], averaged over the IR band and then compared with a configurable threshold (typically 3%),
$$\frac{\sum_{n=n_{\min}}^{n_{\max}} \mathrm{Re}\left(\frac{\underline{\widetilde{R}}^{ds}_{b,p,d}[n]}{\underline{\widetilde{R}}^{ict}_{b,p,d}[n]} \right)}{n_{\max} - n_{\min}} > \frac{LI_{\lim}}{100} \tag{23c}$$

   Here, $n_{\min}$, $n_{\max}$ define the wavenumber bins corresponding to lower and upper band edge respectively.

3.4.2 Lunar Intrusion Processing

If equation 23c is true for any specific FOV and sweep direction, then the new DS spectrum is marked as invalid only for the FOVs and sweep directions noted. Any deep space measurements marked invalid from this process are excluded from the Moving Window average. The lunar intrusion flag is also set. Earth scenes calibrated while lunar intrusion is present are also marked with lunar intrusion flag.

For SDR algorithm software versions 2.13 and above, the invalid DS spectrum no longer invalidates earth scene spectra processed while the invalid DS spectra is in the moving window.

The lunar intrusion detection feature should only be turned ON (enabled) for instrument data collects in the normal SSM scan mode. The feature is not compatible with scan interrupt mode where long data collects at one scan position are performed.

3.5 ALIGNMENT OF DATA TO A COMMON SPECTRAL GRID.

The channel centers defined for the EDR algorithm do not necessarily match the channel centers of the CrIS sensor. The wavenumber interval is fixed by the precise laser wavelength during measurements, does not correspond exactly to the output spectral grid, and may drift over time. Possible laser and optical alignment drifts will produce a different spectral grid on each measurement. The calibration software has thus to remap the sensor data onto a common reference grid to match the channel centers needed for the EDR algorithms. The new common resampling grid is called the "user's grid".

The total number of decimated points sent down by the instrument is given in Table 9. This number corresponds to the number of points sampled by the metrology laser, including guard bands on each side of the requested band limits. This number corresponds to a product of small prime factors, like discussed in Appendix 9.1.3. Processing will be done with this number of points. This table also gives the number of output bins in the SDR product (common user's grid dimension).

Table 9: Resampling parameters for each band

Band	OPD samples	Decimation factor DF_b	Decimated points N_b	Output bins	$2\,MPD_b^{req}$ [cm]	$\lambda_S^b\,(opt)$ [nm]
LW	20736	24	864	713	1.60000	771.60494
MW	10560	20	528	433	0.80000	757.57576
SW	5200	26	200	159	0.40000	769.23077

According to the sampling procedure in the interferometer, the spectra are aligned on a $n/(2\,MPD_b^s)$ spectral grid. Of course, $2\,MPD_b^s$ is dependent upon the actual metrology sampling interval used in band "b", λ_S^b, the decimation factor DF_b, and the number of points in the band, N_b, i.e.,

$$2 \cdot MPD_b^s = N_b \cdot DF_b \cdot \lambda_S^b \tag{23d}$$

Since the laser wavelength is likely to change during the mission, or not be at the exact specific value corresponding to the requested output grid, then the spectral grid and line shape due to interferogram truncation are not constant. In addition, Table 9 shows that the optimum metrology sampling interval $\lambda_S^b(opt)$ is different for each IR band. Thus, it is not possible to simultaneously satisfy all three conditions using a single laser metrology. We thus have to find a way to resample spectra in order to deliver them on a fixed, end-user defined, spectral grid with exactly the same $\mathrm{sinc}(2 \cdot MPD_b^{req})$ function on each bin within each band b. This must be accomplished no matter what the value of metrology sample interval λ_S^b. Fortunately, this is of no concern, as the $\mathbf{F}$-matrix operator to be discussed next corrects for this difference. The following spectral resampling relation is represented in matrix form:

$$L'_{b,p,d}[k] = \sum_{k'=0}^{N-1} F[k,k']\, L_{b,p,d}[k'] \tag{22}$$

with
$$\mathbf{F}_b[k,k'] = \frac{\Delta\sigma_b}{\Delta\sigma_b^{req}} \frac{\operatorname{sinc}\left(\frac{\sigma_{k'} - \sigma_k^{req}}{\Delta\sigma_b^{req}}\right)}{\operatorname{sinc}\left(\frac{1}{N_b}\left(\frac{\sigma_{k'} - \sigma_k^{req}}{\Delta\sigma_b}\right)\right)} \tag{23}$$

and where $\Delta\sigma_b$ is the spectral grid defined by $\lambda_S^{b_CMO}$, $\Delta\sigma_b^{req}$ is the user defined grid spacing, $\sigma_{k'}$ is the wavenumber for the bin k' on the grid $\Delta\sigma_b$, and σ_k^{req} is the wavenumber for the bin k on the user defined grid. At the limit of $\lambda_S^{b_CMO} \rightarrow \lambda_S^b(opt)$ from Table 9, then $\Delta\sigma_b \rightarrow \Delta\sigma_b^{req}$ and the correction matrix tends towards the identity matrix, as it should.

Equations 22 and 23 are referred to as the spectral re-sampling function and have been formally derived in [RD 43]. This operator permits the correction to any input spectra sampled at a given wavelength onto the requested output grid with a specific fixed sinc width in each band. This is also required for the application of the following self-apodization removal operation.

The $\mathbf{F}$-matrix is a matrix enabling the calculation of the corrected spectrum with a simple product between a correction matrix and the input spectrum vector. The application of the $\mathbf{F}$-matrix will transform the spectral grid of the input signal $\sigma_b[0]$, $\Delta\sigma_b$ into the requested user's grid defined by $\sigma_b^{req}[0]$ $\Delta\sigma_b^{req}$, while keeping the same number of signal points. The resulting inherent sinc width will be that of the requested band, for example 0.625 cm^{-1} for the LW, corresponding to the interpolated MPD width of exactly 0.8 cm in the interferogram domain, as displayed in Figure 24.

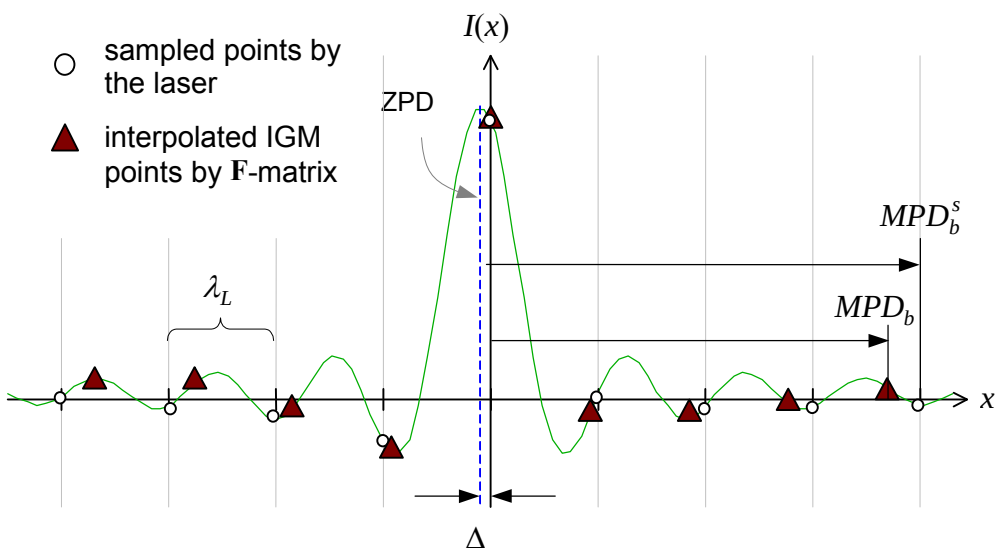

Figure 24: Effect of the $\mathbf{F}$-matrix viewed in the interferogram domain

Wavenumbers assigned to each spectral bin prior to resampling are based on the laser metrology sampling wavelength (see Section 4.1). The laser $\lambda_L^{b_CMO}$ value in band "b" is computed by the spectral calibration module and used to update the CMO (based on the calibration neon count). The laser wavelength is stabilized on the CrIS instrument (λ_L stable to within +/-0.4 ppm over one orbit). If

the laser has drifted more than a given value 2 ppm is current default), then a recomputation of the $\mathbf{F}$ matrix used in the CMO is required.

3.6 ILS CORRECTION

When the radiation source in a Michelson interferometer is located in front of or behind the focal plane of the collimator, distortion arises in the spectral line shape. For CrIS, this well-known self-apodization induced by the instrument (ILS is distorted from a pure sinc) shall be removed from the scene radiance in each channel before being handed off to the EDR algorithms. The present section discusses an algorithm for correcting the distorted interferogram or spectrum as described in [RD 44] and [RD 45].

The need for ILS correction is primarily driven by EDR cloud clearing algorithms, which require radiances measured in adjacent FOVs to be spectrally aligned onto the same channel center to possess the exact same ILS (here a pure sinc). Previous instruments, which used a single scanning FOV, did not experience these types of FOV to FOV distortion differences since the same sensor FOV was used for every measurement.

The assumption is made that the self-apodization will remain constant over the instrument lifetime. This ILS stability assumption is based on the presence of dynamic alignment (DA) in the instrument system design. No algorithmic provision is made with respect to scene self-apodization, i.e. ILS variation with scene content (e.g. with clouds in it).

3.6.1 Introduction

In Fourier transform spectroscopy, the radiation to be examined is made to interfere in a Michelson interferometer and the interference signal is registered. The spectrum is then computed as the Fourier transform of the signal. Strictly speaking, this is true only under the assumption of a perfect instrument measuring the radiance of a very distant source. When this is not the case, the different instrument function contributors affecting the spectral lines of a data-cube spectrum are due to effects inherent to the instrument as shown in Figure 25.

Starting from an elementary line contribution, e.g., emission from a single gas molecule, interactions between the molecules, expressed as temperature and pressure, produce a line broadening (C0 in Figure 25). This physical effect cannot be removed and reflects in fact some of the gas properties which we want to measure.

The first instrument contribution illustrated here (C1) is due to beam divergence which causes a self-apodization. As the emitted energy enters the interferometer, different angles for the different fields of view produce different apparent spectral frequencies. A monochromatic signal thus produces a continuum of frequencies. The shape of this continuum is a function of the pixel geometry, the pixel position with respect to the optical axis, and the spectral frequency of the signal. The corresponding line shape indicated by Beam Divergence is shown in Figure 25.

The second effect (C2) is due to perturbations like shear and tilt on the interfering beam which may fluctuate causing distortions on the measured lines. The corresponding line shape is indicated by Modulation Degradation in Figure 25.

The third contribution (C3) is due to acquisition of interferograms which are of finite length. This third effect introduces the Sinc “dressing”. The corresponding line shape is indicated by Sampling Window in Figure 25.

The mathematical operation for applying the contributions C2 and C3 to the gas line is expressed either by multiplication when considering the interferogram domain or by convolution when considering the spectral domain. However, the first contribution C1, i.e. self-apodization, can not be treated as a simple convolution in either domain since this effect is non-local in both domains. But its expression takes the well known form as the Volterra integral of the first kind.

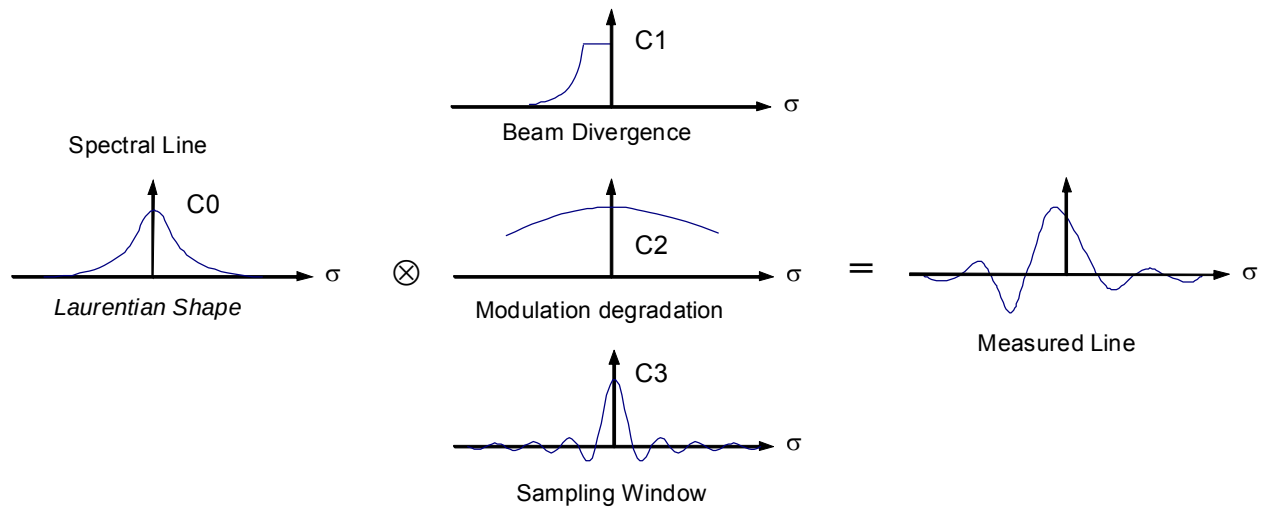

Figure 25: Instrument function contributors

To understand this self-apodization effect, consider that every monochromatic component of light traveling in the effective direction produces an interference signal that oscillates with the frequency corresponding to the correct wavenumber [RD 9]. However, as you may see from Figure 26, if the wave vector of a monochromatic plane wave component with wavenumber σ_0 makes an angle α with respect to the effective direction, its interference signal has a cosine dependence which oscillates at a frequency corresponding to the wavenumber $\sigma_0 \cos(\alpha)$. Thus, we shall call the line passing through the center of the collimator lens parallel to the effective direction the *effective* axis, as shown in Figure 26.

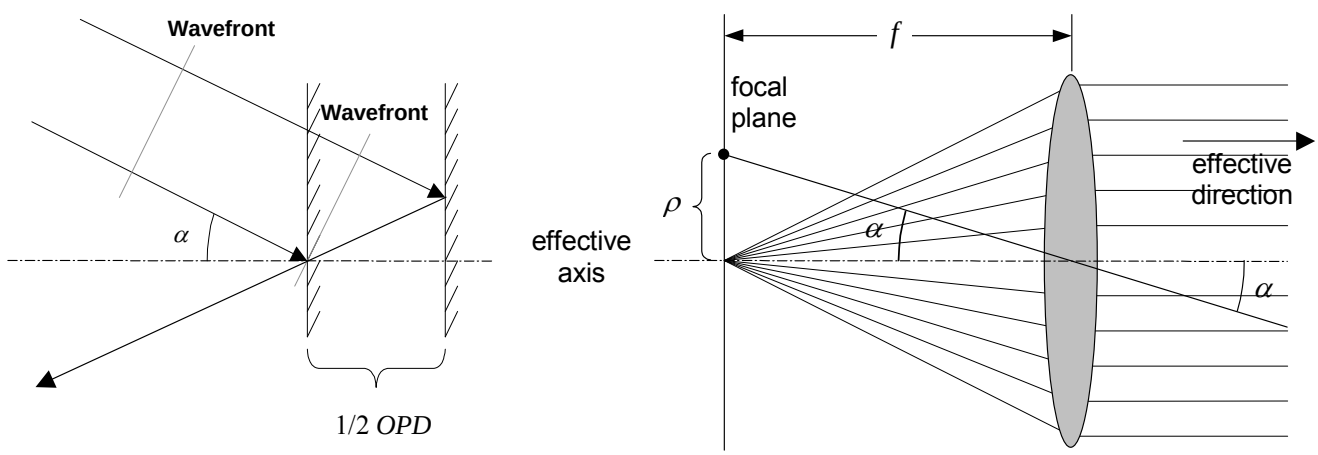

Figure 26: Off-axis geometry and rays

This figure identifies the point or the radiation source lying at the intersection of the focal plane and the effective axis. Any point in the focal plane aside from the effective axis gives a distorted spectrum, in which every wavenumber is multiplied by $\cos(\alpha)$. Therefore the presence of nonparallel light rays in the interferometer stretches the spectral lines toward the lower wavenumbers. This phenomenon is always present, unless we have a perfect point radiation source exactly at the point of the focal plane of the collimator lens (mirror), corresponding to the effective direction and an infinitely wide interferometer aperture, so that there are no diffraction effects. When the interferometer is perfectly

aligned, the effective axis passes through the center of the radiation source. If the radiation source is located exactly in the focal plane, the distance of its arbitrary point from the effective axis completely determines the angle α (see Figure 26), and thus determines the amount of spectral shift of the light emanating from that point. Let us now examine a monochromatic ($\sigma = \sigma_0$) point radiation source that is placed on a circle of radius ρ and centered on the effective axis, as in Figure 26.

The radiation is detected at the wavenumber:

$$\begin{aligned}\sigma(\rho) &= \sigma_0 \cos(\alpha) \\ &= \frac{\sigma_0}{\sqrt{1+(\rho/f)^2}}\end{aligned} \tag{24}$$

which further gives, under the paraxial approximation,

$$\sigma(\rho) \cong \sigma_0 \left(1 - \frac{\rho^2}{2f^2}\right) \tag{25}$$

One then sees that the line shape given by a round monochromatic radiation source which has a true line shape $E(\sigma) = \delta(\sigma - \sigma_0)$, a radius of R_0, and a shift of s from the effective axis is expressed as:

$$E(\sigma, s) = \begin{cases} \dfrac{2\pi}{\sigma} & s < R_0, \rho(\sigma) \le R_0 - s \\ \dfrac{2}{\sigma}\arccos\left(\dfrac{\rho(\sigma)^2 + s^2 - R_0^2}{2\rho(\sigma)s}\right) & \rho(\sigma) \in \left(|R_0 - s|, R_0 + s\right) \\ 0 & \text{elsewhere} \end{cases} \tag{26}$$

Here $\rho(\sigma)$ is the radius of the circle in the focal plane, whose radiation is detected at wavenumber σ, or according to Equation (25),

$$\rho(\sigma) = f\sqrt{2(1 - \sigma/\sigma_0)} \tag{27}$$

In the case of the shifts $s = 0$, we obtain the well-known result that a delta peak line is seen as a boxcar line shape with the width:

$$\begin{aligned}\Delta\sigma = \sigma(0) - \sigma(R_0) &= \sigma_0 - \sigma_0 \cos(\alpha) \\ &\approx \sigma_0 \frac{R_0^2}{2f^2}\end{aligned} \tag{28}$$

Figure 27 shows rays of the same wavelength (e.g. σ_0) forming different angles with respect to the optical axis and experience different effective OPDs.

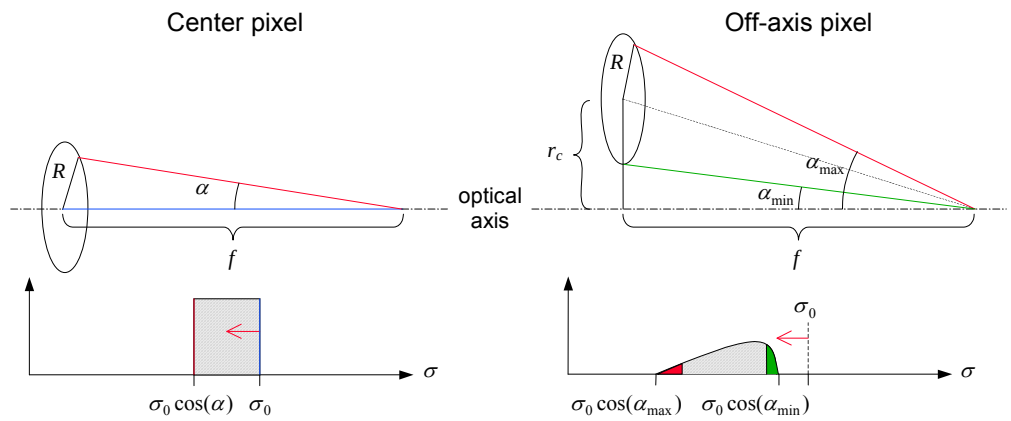

Figure 27: Self-apodization due to beam divergence in the interferometer

Self-Apodization: What it is...

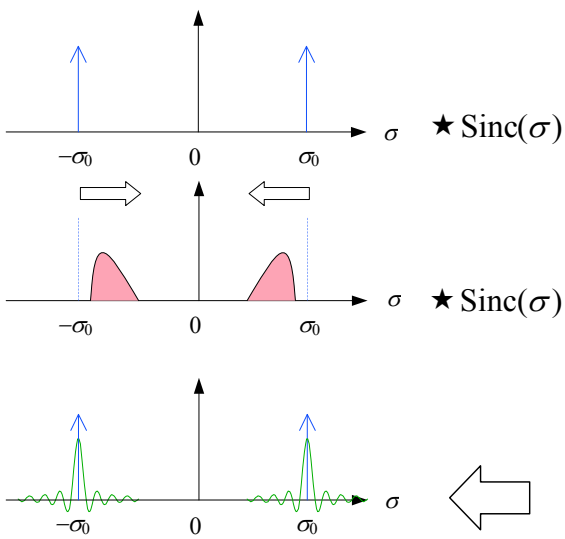

Beam divergence produces an effect corresponding to a *complex ILS*, dependent on *every* frequency contained in the incoming signal.

← Notice symmetric spectral stretching on both positive and negative frequencies

A good SA Removal algorithm should:

Remove the effects of frequency dependent line shape

Correct the stretching effect due to Self-Apodization

Provide output spectra with the same pure Sinc on each bin

Self-Apodization: What it isn't...

Not a simple convolution, nor a standard Sinc convolution by a frequency independent ILS

$$L(\sigma) = \int_{-MPD}^{+MPD} I(x)\, e^{-2i\pi x\sigma}\, dx$$

Not a simple modulation of the IGM

$$L(\sigma) = \mathrm{F}\{I(x) \cdot m(x)\}$$

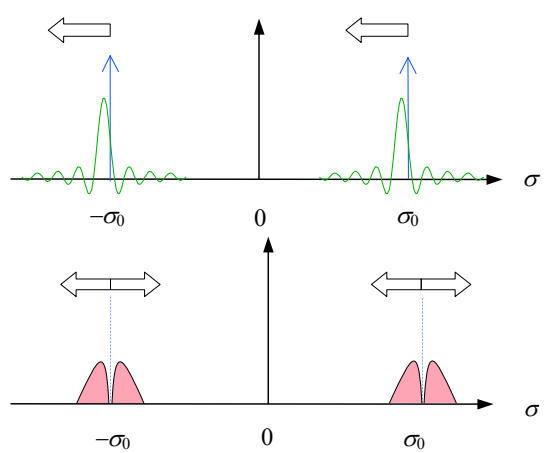

Self-Apodization is more complex than that, since it is not a local operator neither only in the IGM domain, nor only in the spectral domain, since it is expressed as a Volterra integral of the first kind.

3.6.2 CrIS Off-Axis Self Apodization

As stated before, beam divergence introduced by finite field of view (extended source) produces broadening of monochromatic spectral lines. Both the detector size and its position on the focal plane define the width and the shape of the spectral lines. Due to their position, each of the CrIS FOV pixels has its own line shape. Even though by symmetry there are only 3 basic different line shapes, one at the center, four on the diagonal corners and four at the mid-point of the array sides, the 9 are all independent due to the fact that the instrument is not perfect and that the array will never be perfectly aligned.

Furthermore, the ILS is wavenumber dependent, because of:

- finite aperture of the interferometer,
- off-axis position of the detector in the focal plane with respect to the center of the interference pattern (9 pixels for CrIS),
- various optical, mechanical, and electrical imperfections of the interferometer system during the sweep of the optical path difference.

Figure 27 illustrates the self-apodization function normalized to the frequency of the incoming light. Note that the functions plotted in the figure also have to be normalized to unit area. The final ILS for each FOV and for each frequency could then be obtained by doing a convolution of these functions with the ideal Sinc function corresponding to the Fourier Transform of the interferometer sampling window. It can be seen that the self-apodization functions also contains the spectral stretch inherent to off-axis detectors. This spectral stretching causes each off-axis FOV to be slightly shifted in wavenumber from the on-axis FOV in the center of the array.

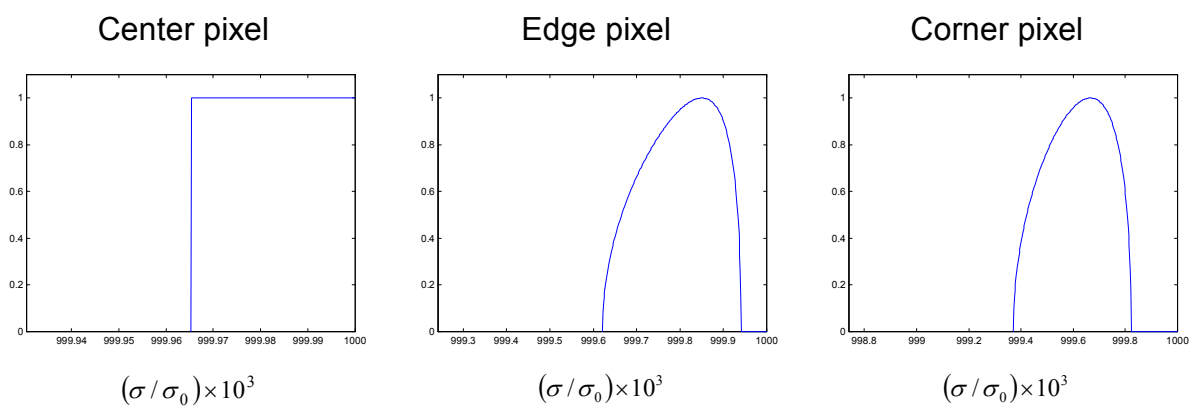

Figure 28: Self-apodization function for the three basic pixel geometries

Self-apodization within an interferometer depends upon the maximum OPD stroke, the FOV cone angle and the angular offset from the center FOV. For the results previously pictured the FOV footprint is 14 km yielding a FOV full cone angle of 0.96 degrees. The spacing between FOVs is 1.1 degree arranged in a 3 $\times$ 3 square pattern. The maximum OPD is 0.8, 0.4 and 0.2 cm for the LW, MW, and SW respectively. There is no telescope or other magnification in front of the interferometer to cause larger beam divergence which would worsen this self-apodization effect and make it harder to remove.

3.6.3 Self-Apodization Removal

It is possible to correct and eliminate this artifact by correcting the instrument spectra with these functions (basically applying the inverse of the self-apodization effect). However, the difficulty arises because the apodization is different for each wavenumber across the spectral band of interest.

It is interesting to note that self-apodization removal can be combined with the spectral resampling (Section 3.5) and the apodization (Hamming or Blackman, as described in Sections 3.7.2 and 3.7.3) so that the three can be done simultaneously.

The self-apodization functions plotted in Figure 27 are computed assuming a perfectly aligned instrument. During the actual CrIS instrument build and acceptance testing there will be measurements of the ILS for each FOV to capture the effects of misalignment. These measurements can then be compared to calculations, which take into account misalignment data that will be obtained during optical co registration tests. Each instrument is uniquely characterized in this regard so that this becomes part of the characterization database used by the SDR algorithm for that particular instrument.

Because of its position on the detector plane, each detector has its own beam divergence self-apodization. The correction is applied in the spectral domain by performing a kind of frequency-dependent convolution of the analytical signal by the inverse of the original correction matrix. This inverse matrix is tabulated for different pixel distance to the optical axis and spectral frequency. It can also include further physical instrument characteristics obtained at a future characterization stage. During correction of a vector the pixel distance to optical axis remains the same for a given pixel but the frequency does change. So, for a given channel, say channel k', the effect of self-apodization on the original spectrum $L_{b,p}[k]$ is given by

$$L'_{b,p}[k'] = \sum_{k=0}^{N-1}\left[\int_0^{\sigma_s} d\sigma \int_0^{\sigma_s} d\sigma' \, 2MPD \,\mathrm{Sinc}\big(2MPD(\sigma_{k'} - \sigma')\big)\, ILS(\sigma',\sigma)\, \mathrm{Sinc}\big(2MPD(\sigma_k - \sigma)\big)\right] L_{b,p}[k] \quad (29)$$

or in matrix form,

$$L'_{b,p} = \mathbf{SA} \cdot L_{b,p} \quad (30)$$

with $$\mathbf{SA}[k',k] = \int_0^{\sigma_s} d\sigma \int_0^{\sigma_s} d\sigma' \, 2MPD \,\mathrm{Sinc}\big(2MPD(\sigma_{k'} - \sigma')\big)\, ILS(\sigma',\sigma)\, \mathrm{Sinc}\big(2MPD(\sigma_k - \sigma)\big) \quad (31)$$

In this last equation, the self apodized instrument line shape distortion due to off axis geometry, $ILS(\sigma',\sigma)$ has received treatment in [RD 45] and resulted in the following equations (32), (33), (34), and (37). Thus, it has been shown that:

$$ILS(\sigma',\sigma) = \begin{cases} A & r_c < R_0, \quad \sigma\cos(\alpha_{\min}) \le \sigma' \le \sigma \\ \dfrac{A}{\pi}\arccos\left(\dfrac{\left(\dfrac{\sigma^2}{\sigma'^2} - 1\right) f^2 + r_c^{\,2} - R_0^2}{2 r_c f \sqrt{\left(\dfrac{\sigma^2}{\sigma'^2} - 1\right)}}\right) & \sigma\cos(\alpha_{\min}) < \sigma' \le \sigma\cos(\alpha_{\max}) \\ 0 & \text{elsewhere} \end{cases} \quad (32)$$

with $$\cos(\alpha_{\min}) = \frac{f}{\sqrt{f^2 + (r_c - R_0)^2}} \tag{33}$$

and $$\cos(\alpha_{\max}) = \frac{f}{\sqrt{f^2 + (r_c + R_0)^2}} \tag{34}$$

and $$r_c = \tan^{-1}\sqrt{\tan^2(IT_{FOV}) + \tan^2(CT_{FOV})} \tag{37}$$

where IT_{FOV} and CT_{FOV} are the individual FOV offset angles in the in-track and cross-track axis of the CrIS sensor. These offset angles are delivered in the CrIS engineering packet and have been measured from a ground ILS testing process.

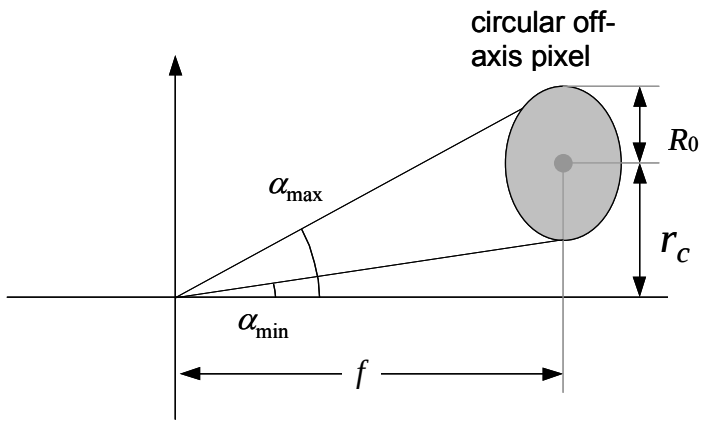

Figure 29: Off-axis geometry

and where the A in equation (32) is a normalization factor used to preserve energy such that

$$\int ILS(\sigma', \sigma)\, d\sigma' = 1. \tag{38}$$

Equations (32) through (38) result in the self apodization spreading of spectra depicted in Figure 28. Performing the integration in equation (31) then allows the ILS contribution at each channel center to be computed.

A mathematically equivalent and more robust form of equation (32) is shown in equation (39) [RD 48]. Equation (39) is preferred over equation (32) because the argument of the arccos function is better behaved using the “tan“ functions in its argument. The C++ implementation of the SDR algorithm uses equation (39) instead of equation (32).

$$ILS(\sigma',\sigma)=\begin{cases} A & r_c<R_0,\quad \sigma\cos(\alpha_{\max})\le\sigma'\le\sigma \\ \dfrac{A}{\pi}\arccos\left(\dfrac{\left(\dfrac{\sigma^2}{\sigma'^2}-1\right)+\tan(\alpha_{\min})\tan(\alpha_{\max})}{\left[\tan(\alpha_{\min})+\tan(\alpha_{\max})\right]\sqrt{\left(\dfrac{\sigma^2}{\sigma'^2}-1\right)}}\right) & \sigma\cos(\alpha_{\max})<\sigma'\le\sigma\cos(\alpha_{\min}) \\ 0 & \text{elsewhere} \end{cases} \tag{39}$$

The arccos argument of equation (39) is also tested to assure a value less than or equal to 1.0 prior to exection of the arccos function.

Numerical evaluation of the integral

Equation (31) needs to be evaluated numerically for each matrix element (k,k'). Though not complex, this numerical procedure remains tedious even when using Gauss-Legendre integration technique (see Section 9.4). However, an approximation can be made that greatly simplifies the computation of the matrix elements while keeping excellent accuracy. This approximation consists in replacing the Sinc function in the integration over σ by a Dirac's delta, i.e.

$$2MPD\,\mathrm{Sinc}\big(2MPD(\sigma_k-\sigma)\big)\approx\delta(\sigma_k-\sigma) \tag{40}$$

which leads to the simplified form:

$$\mathbf{SA}[k',k]\;\approx\int_0^{\sigma_S}d\sigma'\,\mathrm{Sinc}\big(2MPD(\sigma_{k'}-\sigma')\big)\,ILS(\sigma',\sigma_k)\,. \tag{41}$$

Equation (40) becomes exact as $2MPD$ tends toward infinity, i.e., when spectral resolution becomes infinite. One may analyze the limitations of this approximation within two conceptually related points of view.

First, if the signal in the interferogram is significantly high for OPDs larger than MPD, then in the incoming signal, high frequency structures are present that won't be correctly taken into account. The self-apodization effects are thus averaged over the spectral resolution size.

The second point of view considers that the self-apodization function, $ILS(\sigma',\sigma)$, does not strongly depends on the parametric frequency σ. Self-apodization is thus seen as a piecewise convolution over spectral section with size comparable to the spectral resolution.

But as seen in the following table, the error induced in the central point by the approximation of Equation (40) remains below 0.0035% for CrIS band definitions and pixels geometry.

Table 10: Error evaluation due to Dirac's delta approximation

Band	Error on Pixel in %		
	Center	Edge	Corner
LW	0.000390	–0.000012	–0.000007
MW	0.001360	–0.000270	–0.000012
SW	0.003441	–0.000600	–0.000600

Self-Apodization Removal

Since the effect of self-apodization may be included as the multiplication of the original spectrum by the self-apodization (SA) matrix, it can be as easily removed with a multiplication by the inverse of the SA matrix. The matrix

$$\mathbf{ISA} = \mathbf{SA}^{-1} \tag{42}$$

is thus the instrument line shape correction (not a simple deconvolution) matrix that takes as input the pixel geometry and which is pre-computed for each CrIS following ground characterization tests.

This matrix is compatible in size with the incoming spectrum $L_{b,p}$ that has been resampled by the previous $\mathbf{F}$-matrix operator (see Section 3.5) at the exact wavenumber values corresponding to σ_k and $\sigma_{k'}$ of the $\mathbf{SA}$ matrix.

Results

Equation (41) provides one way of adding the self-apodization effects to an initial, sampled, spectrum. But to validate this procedure, a brute force technique should be used to include self-apodization in the sampled interferogram of high resolution spectra. This is achieved by summing the IGM contributions of every frequency contained in the high resolution spectrum, i.e.

$$\begin{aligned} I\left(x_n^b\right) &= \int d\sigma \left(\int d\sigma' \, ILS(\sigma',\sigma) \, e^{2i\pi\sigma' x_n^b} \right) S(\sigma) \\ &\approx \sum_{\kappa} \left(\int d\sigma' \, ILS(\sigma',\sigma_\kappa) \, e^{2i\pi\sigma' x_n^b} \right) S(\sigma_\kappa) \Delta\sigma \end{aligned} \tag{43}$$

where $S(\sigma_k)$ is a typical Earth scene spectrum, e.g. here from TIGR database, with a resolution of 0.1 wavenumbers. The IGM sampling rate was chosen according to specifications of Table 4. Upper panel of Figure 30 shows the initial TIGR spectrum (dashed line) that has been filtered to isolate CrIS LW band, along with the FFT of the self-apodized IGM (dotted line) for the corner pixel geometry.

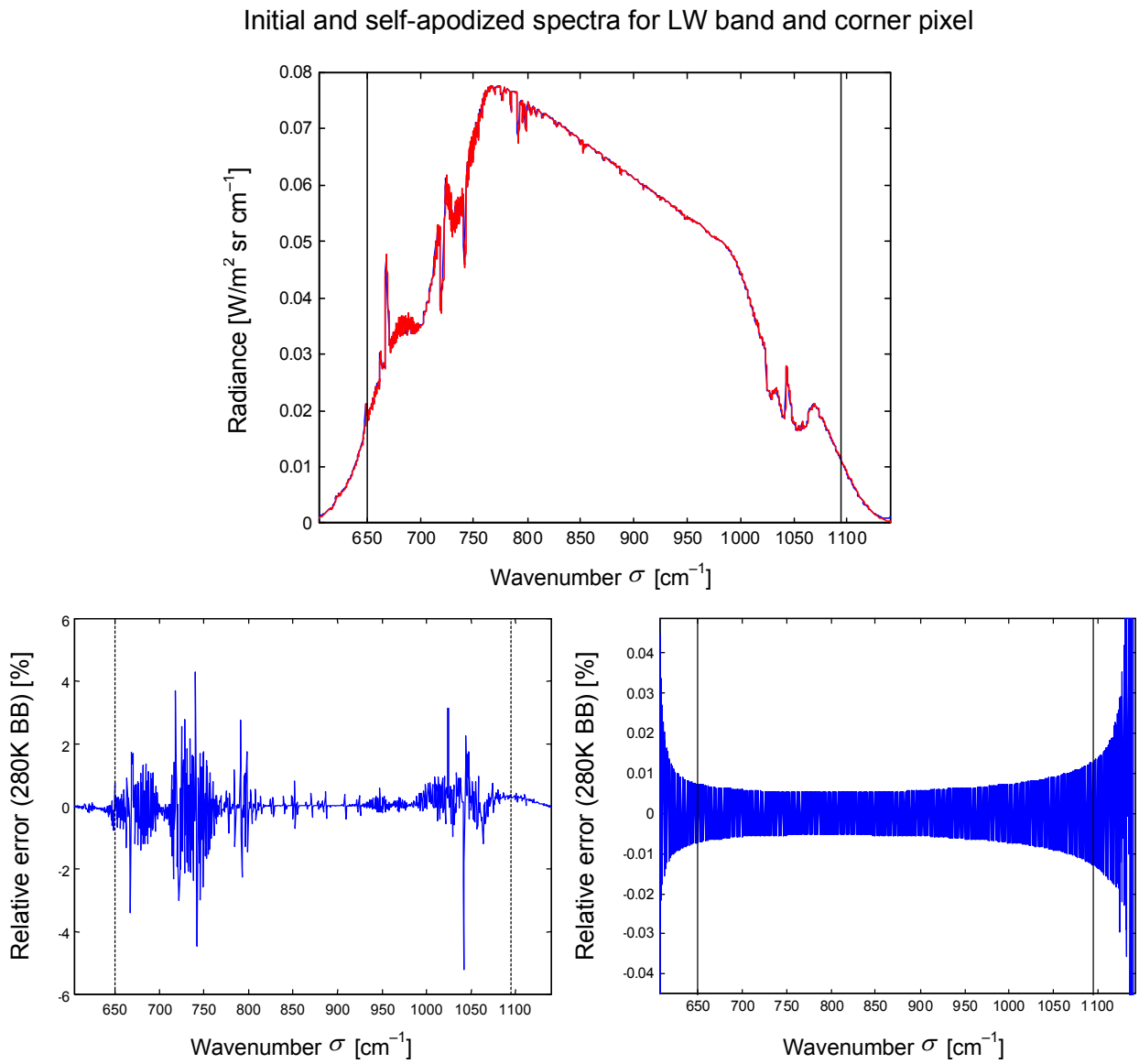

Figure 30: Self-apodization effects and correction

The radiometric errors (normalized relative to a 280K black body) that would be made if self-apodization was not corrected by SDR Algorithms are of the order of 1%, as presented in the lower left panel of Figure 30.

The corrected spectrum obtained by multiplying the self-apodized, sampled, spectrum by the inverse of the SA matrix of Equation (41) differs from the initial TIGR spectrum sampled at the same wavenumber values by only 0.01% (always normalized to a 280K black body) as can be seen in the lower right panel of Figure 30. This residual error shows that no spectral signature remains after the correction. Thus, the self-apodization removal procedure efficiently corrects the affected spectra provided that a good characterization of the instrument function, $ILS(\sigma',\sigma)$, is performed.

The impact of remaining errors due to non-precise characterization is evaluated by modifying the pixel geometry in the computation of the ISA matrix while keeping the right geometry for the construction of the self-apodized spectrum. The remaining relative errors are presented in Figure 31 for the cases

where the corner pixel has been shifted (left panel) or shrunk (right panel), with radiometric relative errors of 0.1% approximately.

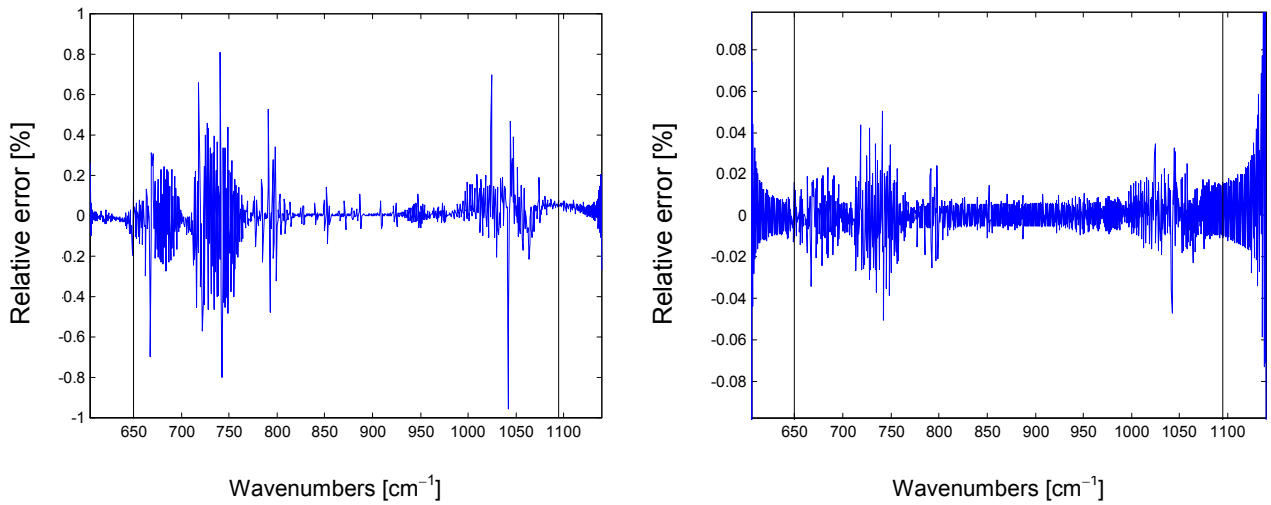

Figure 31: Errors due to non-precise characterization

Finally, as for the noise amplification effects, they have been extensively studied and no signal deterioration is expected following self-apodization removal.

Summary

The self-apodization effect (or FOV effect) introduced by beam divergence within the interferometer is corrected via a matrix multiply operation within the SDR algorithm. The matrix is derived from knowledge of the FOV size, shape, geometry and off-axis angles for each FOV obtained from instrument design and/or when characterizing the instrument on the ground. The operation corrects the spectral distortion resulting from this geometrical relationship and transforms the ILS into an ideal sinc response for all FOV's without significant error. The accuracy of this process is summarized in Table 11. Initial errors varying between 0.02% and 2% are reduced by a factor of more than 25 using this method and resulted in a residual error of less than 0.05%. This yields negligible radiometric bias errors of less than 0.1%.

Table 11: Summary of standard deviation error [%]

SA Not Corrected / *SA Corrected*	Central Pixel	Edge Pixel	Corner Pixel
LW Band	3.7×10^{-2}	4.2×10^{-1}	7.7×10^{-1}
	2.6×10^{-4}	4.0×10^{-3}	6.8×10^{-3}
MW Band	1.0×10^{-1}	1.15	2.15
	2.6×10^{-3}	4.3×10^{-2}	8.5×10^{-2}
SW Band	2.1×10^{-2}	2.4×10^{-1}	4.6×10^{-1}
	9.0×10^{-5}	7.6×10^{-4}	9.0×10^{-4}

3.6.4 Residual Term

Since effects other than FOV self apodization might be significant, then the correction of the ILS field of view effect discussed in the previous may not be sufficient. For example, the interferometer modulation efficiency may vary with the optical path difference. Phenomenon like residual diffraction, DA tilt versus OPD or other mechanical imperfection may be responsible for this effect. In order to consider those effects, a modulation efficiency term $M_{b,p}[m]$ over the interferogram is introduced. This term is derived after the geometric self apodization ILS effect has been removed (see Section 3.6.3). The modulation efficiency versus OPD is defined uniquely for FOV p, band b and interferogram sample m. It is modeled using a fourth order polynomial.

$$M_{b,p}[m] = C0_{b,p} + C1_{b,p} \cdot x[m] + C2_{b,p} \cdot x^2[m] + C3_{b,p} \cdot x^3[m] + C4_{b,p} \cdot x^4[m] \tag{44}$$

The coefficients C0, C1, C2, C3 and C4 are constants associated with each FOV and IR band which were derived during ILS characterization of the sensor. $x[m]$ is the OPD position in units of cm at each sample point m of the interferogram. Typically, $x[m]$ spans a +/-0.8 cm range in the LWIR band (i.e. x = 0 at ZPD). The OPD position is related to the metrology sampling interval and sample number of the interferogram. Thus, values for $x[m]$ can be computed as follows

$$x[m] = \lambda_S^{b-CMO} \cdot DF_b \cdot \left(m - \frac{N_b}{2} \right) \tag{44a}$$

where N_b is the number of m samples in band b, DF_b is the decimation factor applied to the interferogram samples within the CrIS sensor and λ_S^{b-CMO} is the metrology sampling interval in cm for band b. Typically, C0 = 1 and C1 = C3 = C4 = 0. C2 is tailored during CrIS system level ILS testing.

Removal of this nonideal modulation versus OPD effect requires multiplying the interferogram at each sample point m by the inverse of this function yielding,

$$M_{b,p}^{-1}[m] = \frac{1}{C0_{b,p} + C1_{b,p} \cdot x[m] + C2_{b,p} \cdot x^2[m] + C3_{b,p} \cdot x^3[m] + C4_{b,p} \cdot x^4[m]} \tag{44b}$$

Thus, $M_{b,p}^{-1}[m]$ is the inverse of this residual modulation efficiency at interferogram sample index m. The residual ILS effect due to this nonuniform modulation efficiency versus OPD is not wave number dependent and the spectrum of this correction term can be computed by taking the Fourier transform

$$M_{b,p}^{-1}[m'] = fftshift\left\{M_{b,p}^{-1}[m]\right\} \tag{45}$$

$$\widetilde{R}_{b,p}^{-1}[n] = FFT\left\{M_{b,p}^{-1}[m']\right\} \tag{45a}$$

Where $\widetilde{R}_{b,p}^{-1}[n]$ is the complex correction for the nth spectral channel in band b and FOV p. The $fftshift\{\ \}$ function swaps the first half of samples with last half of samples prior to execution of the FFT in order to make the resultant FFT spectrum phase symmetric about ZPD.

The correction when applied in spectral space is a convolution. Since the application of this residual correction term is done via a convolution, we can easily express it in matrix form in order to include it into the CMO operator. In matrix form, the residual term can be expressed as,

$$\widetilde{R}_{b,p}^{-1}[k',k] = \frac{1}{N_b}\sum_{n=0}^{N_b-1}\widetilde{R}_{b,p}^{-1}[n]\,\mathrm{e}^{2\pi i n(k'+k)/N_b} \tag{46}$$

where k' and k are row and column indexes associated with the CMO matrix correction.

3.6.5 Guard Band Damping

The results for the ILS correction shown previously were done using spectra damped in the guard band. The digital filter within the CrIS instrument performs two functions. It limits the band in order to decimate the signal, and it damps the signal in the guard band in order to prevent aliasing. But the digital filter is removed after the radiometric calibration, and the guard bands are no longer damped. Aliasing thus occurs since the self–apodization correction operator supposes a periodic signal. In order to correct the ILS properly, another filter is required to prevent the energy in the guard band to contaminate the precious information within the band. Also, it is important that this new filter be constant inside the band, since the correction operator is non-local. This non-locality will amplify the amplitude variation of the filter, and introduce an undesired bias into the spectra.

We have chosen to combine two Fermi steps for the simplicity and ease of use. The filter is defined by the following equation,

$$f_b[k] = \left[\frac{1}{\mathrm{e}^{a_2(k_0-a_1-k)}+1}\right]\left[\frac{1}{\mathrm{e}^{a_4(k-k_1-a_3)}+1}\right] \tag{47}$$

Table 12 shows the different values used for the three bands:

Table 12: Parameters for the post calibration filter $f_b[k]$

	LW	MW	SW
k	[1-864]	[1-528]	[1-200]
k_0	77	49	22
k_1	789	481	180
a_1	15	22	8
a_2	0.5	1.0	2.0
a_3	15	22	8
a_4	0.5	1.0	2.0

To be independent of wave number, equation (47) is expressed in bins. It must be remarked that the bin number range begin at 1, and not at zero. In case the range starts at 0, the three k's in Table 12 need to be reduced by 1.

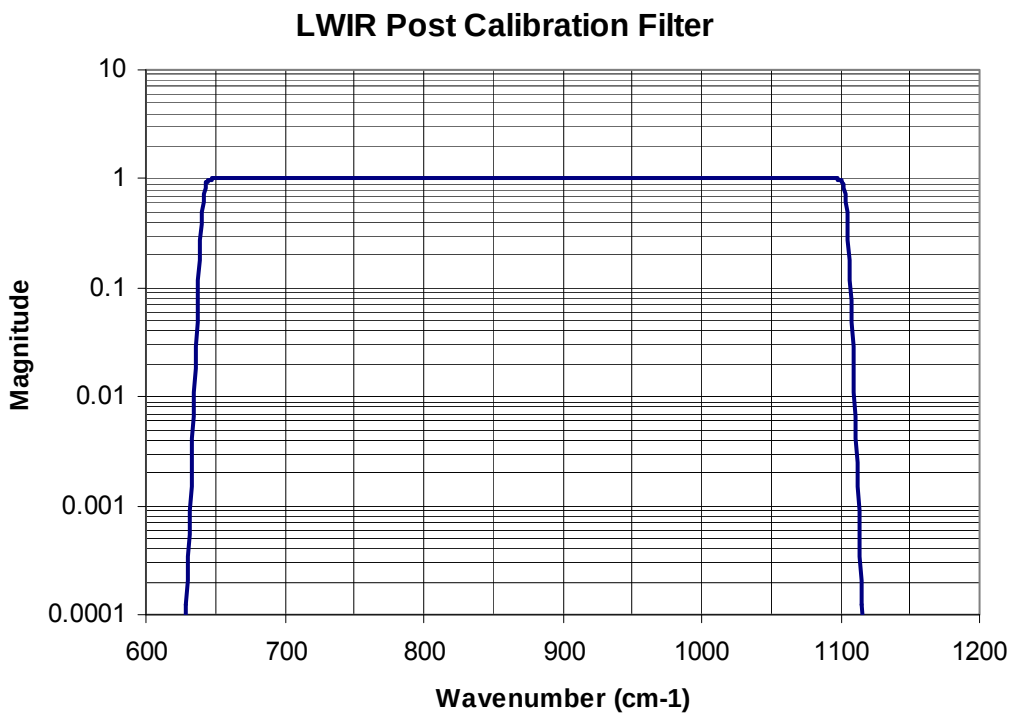

Figure 32: Post calibration filter for the LW band

3.6.6 ILS Retrieval

The spectral calibration of the instrument is impacted by optical alignments and FOV geometry. The ILS retrieval process has been designed to eliminate the spectral shifts and FWHM errors through an iterative tuning process of 109 ILS parameters associated with 27 detector channels as depicted in Figure 33. A more detailed treatment of this topic is covered in [RD 39] and [RD 40].

A CO_2 laser operating at 950 cm^{-1} floods the instrument aperture and is used to produce interferogram data in the LWIR band. Data is collected in the thermally stabilized environment, after adjusting for the laser intensity and electrical gain to avoid bit trim mask clipping. CO_2 laser wavelength knowledge of 0.05 ppm is used to calibrate the internal CrIS neon standard and to permit iterative adjustment of ILS parameters with SDR algorithm in the loop, Key ILS parameters include:

- Effective neon wavelength
- FOR centering to interferometer boresight,
- FOV angular offsets
- FOV size
- Residual modulation efficiency versus OPD

Four data sets consisting of 600 interferograms each are collected in this process. This includes 1) cold BB target data, 2) warm BB target data, 3) laser ON data and 4) laser OFF data. The laser data is radiometrically and spectrally calibrated using cal target data and default ILS parameters. Test set background is removed by differencing laser ON and laser OFF data. The resulting spectrum is averaged and sinc interpolated to produce highly over sampled spectra permitting accurate line

center and FWHM determination. Errors are used to adjust ILS parameters in order to better remove the errors in the next iteration. Co registration data is used to make ILS adjustments in MWIR & SWIR.

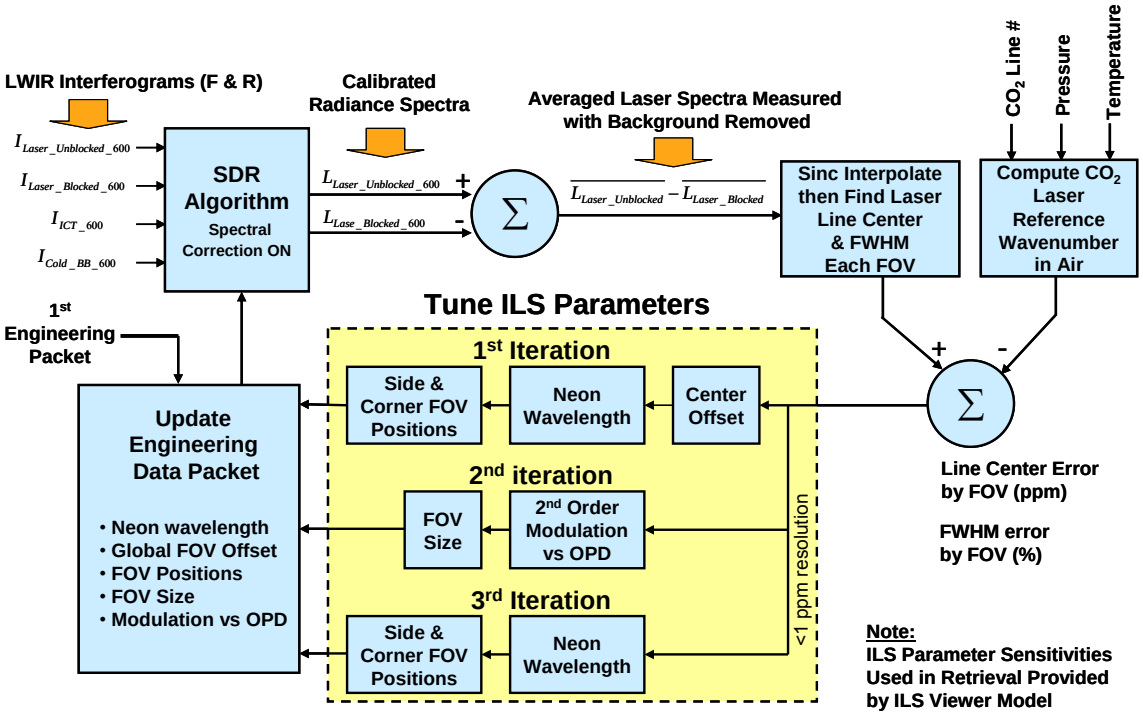

Figure 33: ILS Retrieval Procedure

ILS parameter sensitivities (derivatives) used in the iterative retrieval are provided by ILS viewer model [RD 49] and [RD 50]. These sensitivities are only computed once and remain static throughout the iterative ILS retrieval process. Synthesis of MW & SW ILS parameters require use of bench slit scan data to make minor adjustments to the FOV geometry retrieved for the LWIR band. After ILS testing is complete on the bench, then the "Effective Neon Wavelength" loaded into the engineering packet is properly adjusted for vacuum.

FM1 bench testing has shown that the ILS retrieval process works very well. The retrieval process produces identical ILS in all FOVs. The FM1 test results also show excellent match of absolute spectral calibration using neon reference to CO2 laser reference.

During thermal vacuum testing, gas cell ILS tests are conducted to further tune ILS parameters to optimal values. This is necessary because the attachment of the bench cooler to the CrIS sensor causes some slight optical misalignment in the aft optics which can alter the ILS. In addition, the wavelength in air versus vacuum is different for the neon and metrology laser. The vacuum tests assure that the best adjustments to neon wavelength and FOV positions have been made.

3.7 SIGNAL APODIZATION

Both spectral characteristics and signal-to-noise are critical to retrieval accuracy of advanced IR sounders. For an unapodized (boxcar apodized) interferometer, the channel response function, given by the cosine transform of the apodization function, is a $sinc(\sigma)$ function, where σ is proportional to the frequency separation from the channel center. This function has large side-lobes that alternate in sign and fall off slowly with increasing frequency separation. Typically, interferograms are apodized (the interferogram is multiplied by a function which, in effect, smoothes the spectrum) to produce a channel response function that is localized and has small side-lobes.

When the Hamming apodization function is compared to other apodization functions found in the literature, it is found that it is a reasonable function to use for remote sensing purposes if the instrumental signal-to-noise is on the order of 1000. [RD 10] discusses the effects of apodization as it relates to sounding applications and shows that apodization should have no effect on retrieval results in the absence of band edges effect. [RD 31] examines the use of Hamming and Blackman-Harris apodization to reduce radiometric bias and random errors caused by edges effects when processing band limited signals such is the case for CrIS. Guard band damping also accomplishes this need to suppress edge effects while maintaining as close to ideal sinc(σ) spectral response as possible.

In conclusion, Hamming, Blackman-Harris and unapodized ILS are well accommodated in the SDR algorithm as a user defined option. Guard band damping is applied in all cases. The Hamming FWHM is a reasonable value to use when describing the effective spectral resolution of the proposed IR interferometric sounders. At the opposite, when sidelobe suppression is more important than spectral resolution, the Blackman-Harris apodization is a much better choice.

3.7.1 Unapodized Channel Response Function

The raw data product from an interferometer is a cosine transform of the incoming radiance (interferogram). The instrument has a finite maximum optical path difference, MPD. One obtains the radiance spectrum, convolved with a channel response function, by taking the cosine transform of the product of the interferogram, $I(x)$, with an apodization function, $A(x)$. The channel response function is the cosine transform of the apodization function. In the interferogram domain, the unapodized (or boxcar) apodization function is defined as:

$$A(x) = \begin{cases} 1 & \text{for } |x| \le MPD \\ 0 & \text{for } |x| > MPD \end{cases} \tag{48}$$

where x is the optical path difference. The channel response function for an unapodized interferometer is equal to

$$\frac{\sin(2\pi MPD\sigma)}{\pi\sigma} \equiv 2MPD\ \mathrm{sinc}(2MPD\sigma) \tag{49}$$

where σ is the wavenumber frequency. The unapodized channel radiance $S(\sigma)$ is given by a convolution of the channel response function with the monochromatic radiance at the entrance to the interferometer:

$$S(\sigma) = S_0(\sigma) \otimes 2MPD\mathrm{sinc}(2MPD\sigma) \tag{50}$$

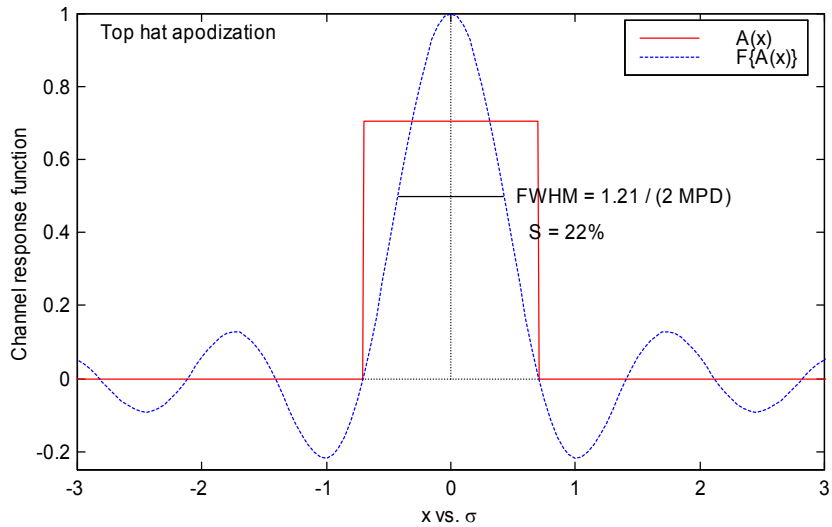

Figure 34: Boxcar apodization function and its sinc Fourier transform

The Nyquist sampling theorem states that if a spectrum is band-limited, i.e. $S(\sigma)=0$ for $|\sigma| \geq \sigma_{\max}$, then no additional information is gained by sampling the interferogram at a rate higher than $1/(2\sigma_{\max})$, although information is lost if the interferogram is sampled at a lower rate [RD 11]. The resulting unapodized spectrum is given as an array of radiance values, $S(\sigma)$ (or $S[n]$ where *n* is the channel index number).

The sinc function has large side-lobes which alternate between negative and positive values about the zeroes of the function spaced at $\sigma = \pm n/(2\,MPD)$. The first four side-lobes have heights of –21.7%, +12.8%, –9.1%, and +7.1% with respect to the central lobe (see Figure 34). The full-width-half-maximum (FWHM) of the sinc function is equal to:

$$FWHM = \frac{0.603355}{MPD} = \frac{1.20671}{2\,MPD} \tag{51}$$

Equation (51) is used to describe the effective spectral resolution of an interferometer. Such a definition can be used to compare the resolution achievable from one interferometer to another, with different values of *MPD.* This definition is misleading, however, if one attempts to compare the spectral resolution of an interferometer to that of an instrument in which the channel response function does not have side-lobes. In typical bandpasses, only 45% of the unapodized spectral radiance comes from the central lobe. The remainder of the radiance comes primarily from the first few side-lobes, but non-negligible contributions arise from very distant frequencies within the band pass, as the heights of the unapodized channel response function side-lobes are still above 1% at 30 zeroes from the central lobe.

In addition to not having a well defined resolution, the use of non-localized unapodized radiances produces complications in the retrieval of geophysical parameters. For multispectral retrievals (e.g., combining microwave and infrared radiances) it is convenient, but not necessary, to represent radiances in brightness temperature (i.e., the temperature of a blackbody with the same radiance). For unapodized spectra, brightness temperature is a meaningless concept due to the distortion, caused by the negative side-lobes which can produce negative channel radiances. The unapodized channel response function also produces complications in the development of efficient and accurate methods to compute channel radiances, such as the use of channel averaged transmittance functions.

3.7.2 Hamming's Filter Function

Many apodization functions can be applied to an interferogram which will localize the channel response function for the purpose of generation of rapid and accurate radiances. It is desirable to use an apodization function which satisfies retrieval models and also allows returning from apodized radiances into unapodized radiances, if this is required.

The apodization of an interferogram can be shown to be a linear transformation in spectral space between apodized and unapodized spectra [RD 10]. The Hamming apodization function is a reasonable and efficient function to use in atmospheric remote sensing applications with high signal-to-noise instruments, both because its channel response function has side-lobes less than 1% of the central lobe and because it has a well behaved analytic inverse transformation. The inverse transformation can be used to readily convert computed Hamming apodized spectra to spectra computed for other apodization functions (including unapodized) which may have poorer characteristics with regard to calculating channel transmittance parameters or radiances.

The Hamming cosine apodization function is given by:

$$A(x) = \begin{cases} (1-2a) + 2a\cos\left(\pi \dfrac{x}{MPD}\right) & \text{for } |x| \le MPD \\ 0 & \text{for } |x| > MPD \end{cases} \tag{52}$$

which has values of $A(x=0)=1$ and $A(x=MPD)=1-4a$.

The channel response function is given by the cosine transform of Equation (52) and is equal to:

$$H(\sigma) = 2MPD \cdot \mathrm{sinc}(2MPD\,\sigma)\left[(1-2a) + 2a\frac{(2MPD\,\sigma)^2}{1-(2MPD\,\sigma)^2}\right] \tag{53}$$

Apodized spectra can be shown to be equal to a 3-point running mean of unapodized spectra if the Nyquist channel spacing of $\Delta\sigma = 1/(2\,MPD)$ is used:

$$L[n] = (1-2a)\cdot L[n] + a\big(L[n-1] + L[n+1]\big) \qquad 0 < n < N-1 \tag{54}$$

Special case corresponds to both ends of the spectra, where we have:

$$\begin{aligned} L[0] &= (1-2a)\cdot L[0] + a\cdot L[1] \\ L[N-1] &= (1-2a)\cdot L[N-1] + a\cdot L[N-2] \end{aligned} \tag{55}$$

The matrix representation is similarly given by:

$$H[k,k'] = \begin{cases} a & \text{if } k = k'-1 \text{ or } k = k'+1 \\ 1-2a & \text{if } k = k' \\ 0 & \text{elsewhere} \end{cases} \tag{56}$$

The apodization operation is then simply performed by a simple matrix multiplication:

$$L'_{b,p} = \mathbf{H}\cdot L_{b,p} \tag{57}$$

The fact that the five spectral operators (post calibration filter, spectral resampling, self-apodization removal, residual ILS removal and Hamming apodization) are all matrix operators permits their combination into a single matrix to speed up subsequent computation:

$$\begin{aligned} L^{es}_{b,p}[n'] &= (\mathbf{H}_b \cdot \mathrm{R}^{-1}_{\mathrm{b,p}} \cdot \mathbf{SA}^{-1}_{b,p} \cdot \mathbf{F}_b \cdot \mathbf{f}_{\mathrm{b}}) \cdot L^{es}_{b,p}[n] \\ L^{es}_{b,p}[n'] &= \mathbf{CMO}_{b,p} \cdot L^{es}_{b,p}[n] \\ L^{es}_{b,p}[n''] &= \mathrm{T}_{\mathrm{b}} \cdot L^{es}_{b,p}[n'] \end{aligned} \tag{58}$$

where $\mathbf{CMO}_{b,p}$ stands for Correction Matrix Operator and T_{b} is the truncation operator that selects the user's grid according to Tables 5 to 7 (n'' is a subset of n').

Hamming found an optimum value of a which minimizes the first side-lobe of the channel response function. He also showed that the optimum value of a was a function of the number of points in the spectrum; however, the optimum value of a converged to $a = 0.23$ for more than 100 points. With this value for a, the FWHM is equal to $1.8152/(2\,MPD)$, which is 50.4% larger than FWHM of the sinc.

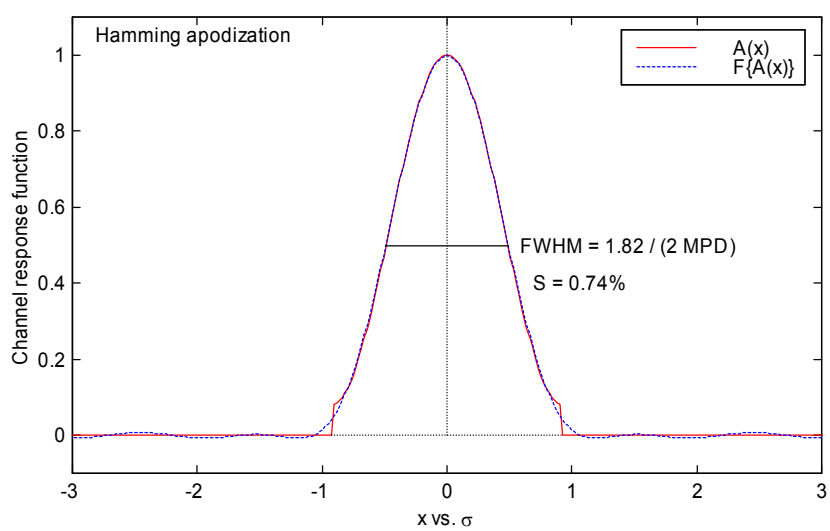

Figure 35: Hamming apodization function and its Fourier transform

The Hamming function has small side-lobes which heights for the first two equal to –0.74%, +0.27% with respect to the central lobe (see Figure 35).

One result of apodization is that the noise and signal become correlated between neighboring channels. For $a = 0.23$, the 3-point running filter reduces the noise in a given channel by a factor of 1.6; noise in adjacent channels is correlated by 62.5% and noise in channels separated by $\Delta\sigma = 1/(2\,MPD)$ is correlated by 13.3%.

In the case of the Hamming channel response function, the residuals are considerably less than the expected instrument noise levels for advanced sounders, which are on the order of 0.1°C.

The information content only depends on the value of MPD, not on the apodization function. The Gaussian apodization function has similar qualities to the Hamming function but has significant values extending to larger MPD. This implies that more information content exists in the Gaussian response function and that the small side-lobes of the Hamming channel response function actually degrade

the resolution compared to the Gaussian function, so that the effective resolution of the interferometer is actually slightly poorer than $1.8/(2\ MPD)$.

The inverse transformation can be expressed as

$$L[n] = \frac{c_0}{(1-2a)}\left(L[n] + \sum_{i=1}^{N} r^i \cdot \left(L[n+i] + L[n-i]\right)\right) \tag{59}$$

With $c_0 = 1.909188309204$, and $r = -0.5590375815769$ for the Hamming case (a = 0.23).

Equations (59) and (54) express the set of unapodized radiances and cosine apodized radiances as linear combinations of each other. Hence, the information content of the complete set of radiances, including noise effects, is identical. This implies that retrieval using unapodized radiances, or cosine apodized radiances with $0 < a < 0.25$, should produce identical results provided all the channels are used. Furthermore, it implies that while the width of the central response function of an apodized function is larger than that of the unapodized function, there is no loss in "resolution" as both sets of functions contain equivalent information.

The Hamming function is a good function to use as a basis for calculating radiances and also reasonable to use in analysis of data because:

It gives a good tradeoff between spectral purity and apparent spectral resolution,

The channel noise correlation is localized,

And a simple analytic inverse exists.

In addition, radiance calculations need only to be done for the subset of channels being used in the retrieval process.

In cases where the SNR is about 1000, the Hamming side-lobes contribute less than the noise value to the radiance calculation and the Hamming radiances are indistinguishable from those radiances calculated from localized channel response functions. The inverse Hamming matrix utilizes all the Hamming channel radiances and, therefore, can be used to create radiances for apodization functions with smaller side-lobes.

3.7.3 Blackman-Harris's Apodization Function

The solution to the problem of leakage is to truncate the signal to be transformed less abruptly than with the rectangular cutoff. This is equivalent to finding a cutoff or apodization function with a Fourier transform which shows fewer side lobed than the sinc function. Numerous such functions exist, as the Hamming function presented in the previous section for example. An extensive overview of their individual properties can be found in the reviews by Harris [RD 12].

The width of the resulting function defines the best resolution achievable with a given apodization function. This is because if two spectral lines are to appear resolved from one another, they must be separated by at least the distance of their HWHM, otherwise no "dip" will occur between them. A sidelobe suppression always causes main lobe broadening; leakage reduction is only possible at the cost of resolution.

The choice of a particular apodization function depends therefore on what one is aiming at. If the optimum resolution of $1.21\ /\ (2\ MPD)$ is mandatory, boxcar truncation (= no apodization) should be chosen (Section 3.7.1). The Hamming function has shown to have a resolution of $1.82\ /\ (2\ MPD)$.

Now if a resolution loss of 100% compared to the boxcar can be tolerated, the 3-term Blackman-Harris apodization is recommended. It produces one of the highest lobe suppression and can be considered among the top performers in commonly used FTIR apodization filters. The three- and four-term Blackman-Harris apodization function is defined as follows:

$$A(p) = a_0 + a_1 \cos(\pi\, p) + a_2 \cos(2\pi\, p) + \left[\, a_3 \cos(3\pi\, p) \,\right] \tag{60}$$

This set of windows is a generation of the Happ-Genzel function. The coefficients given in Table 13 have been optimized numerically to trade main lobe width for sidelobe suppression. The Blackman function has very small side-lobes with heights smaller than 0.03% with respect to the central lobe, as shown in Figure 36 presenting the apodization function and its Fourier transform.

Table 13: Blackman-Harris coefficients

	a_0	a_1	a_2	a_3
3-term BH	0.42323	0.49755	0.07922	0.0
4-term BH	0.35875	0.48829	0.14128	0.01168

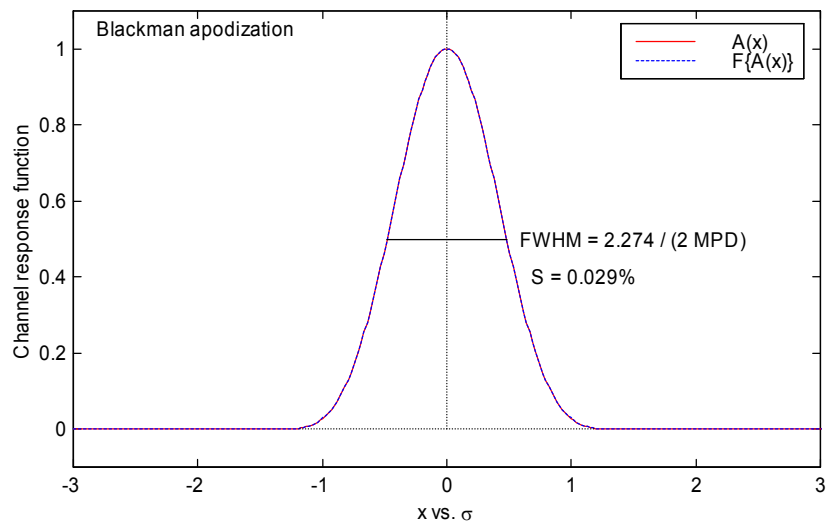

Figure 36: Blackman-Harris 3-terms apodization function and its Fourier transform

Summary

The Hamming apodization function is a reasonable function to use for analysis of interferometric data in remote sensing applications because it is suitable for rapid and accurate calculation of channel radiances. In addition, it produces a good trade-off between apparent spectral resolution and spectral purity. When comparing an interferometer to other instruments with localized channel response functions, the spectral resolution of the Hamming apodized interferogram, $FWHM = 1.8/\,(2\ MPD)$, is a reasonable value to use for the effective resolution of the instrument because radiances computed using only the central lobe of the Hamming channel response function agree to within the instrument noise to those using the entire Hamming response function. In addition, it offers the ability to transform from Hamming back to unapodized whereas other apodizations such as Blackman once applied do not allow the unapodized to be fully recoverable.

However, stronger apodizations such as Blackman allows for best retrieval code execution speed since it localizes the spectrum more, allowing the development of a faster forward model. Moreover, Blackman apodization has better sidelobe suppression to isolate modeling errors and band edge effects. It is intended to offer multiple apodization options (including unapodized) as a user selectable

feature in the scientific code. The choice of apodization impacts both SDR and EDR algorithms. Whatever apodization is chosen by the user, the code applies it to all three bands.

3.8 CMO UPDATES

The Correction Matrix Operator (CMO) is a two dimensional matrix that operates on the calibrated radiance vector produced in each IR band of the CrIS sensor. The CMO has many functions that include:

1. Post Calibration Digital filter to suppress out-of-band noise and artifacts
2. Spectral re-sampling from instrument FFT channel centers to a fixed set of user grid channel centers
3. Removal of the ILS self apodization effect
4. Removal of residual modulation efficiency distortion versus OPD not related to self apodization
5. Application of a user defined spectral response function (unapodized, Hamming or Blackman Harris)

Mathematically, the CMO is a matrix produced from the product of 5 separate matrices as previously described in equation 58 and reproduced below in equation 60a.

$$\begin{aligned} L^{es}_{b,p}[n'] &= (\mathbf{H}_b \cdot \mathrm{R}^{-1}_{\mathrm{b,p}} \cdot \mathbf{SA}^{-1}_{b,p} \cdot \mathbf{F}_b \cdot \mathbf{f}_{\mathrm{b}}) \cdot L^{es}_{b,p}[n] \\ L^{es}_{b,p}[n'] &= \mathbf{CMO}_{b,p} \cdot L^{es}_{b,p}[n] \\ L^{es}_{b,p}[n''] &= \mathrm{T}_{\mathrm{b}} \cdot L^{es}_{b,p}[n'] \end{aligned} \tag{60a}$$

Where

$\boldsymbol{H_b}$ = User defined spectral response function in band "b" (item #5 above)

$\boldsymbol{R^{-1}}_{b,p}$ = Residual ILS removal operator (item #4 above)

$\mathbf{SA^{-1}_{b,p}}$ = Self apodization removal operator (item #3 above)

$\mathbf{F_b}$ = Spectral resampling operator (item #2 above)

$\mathbf{f_b}$= Post calibration digital filter (item #1 above)

$L^{es}_{b,p}[n]$ = Input radiance for n^{th} channel on sensor wavenumber grid for FOV "p" in band "b"

$L^{es}_{b,p}[n']$ = Output radiance for n^{th} channel on SDR expanded user grid for FOV "p" in band "b"

$L^{es}_{b,p}[n'']$ = Output radiance for n^{th} channel on SDR output user grid for FOV "p" in band "b"

$\mathbf{CMO_{b,p}}$ = Correction Matrix Operator for FOV "p" in band "b"

$\mathrm{T_b}$ = Truncation operator in band "b"

The order of matrix multiplication when operating on $L^{es}_{b,p}[n]$ is important and must be maintained as described in equation 60a (right to left) with $\mathbf{f_b}$ operating first on $L^{es}_{b,p}[n]$ and $\boldsymbol{H_b}$ operating last. The formation of the CMO is also in this same order. There are 27 unique CMOs that must be maintained which correspond to the 9 FOVs in each of 3 IR bands.

The parameters needed to compute each of these 5 matrices are contained either in an SDR Algorithm configuration file read when the application is launched or in the CrIS engineering packet RDRs. Static parameters that do not change from one CrIS sensor to the next and which also do not change over the entire CrIS mission are contained in the SDR Algorithm configuration file. $\boldsymbol{H_b}$ and $\mathbf{f_b}$ are examples of matrices computed only once from SDR Algorithm configuration files at application startup. The remaining matrices $\boldsymbol{R}^{-1}_{b,p,}$ $\mathbf{SA}^{-1}_{\mathbf{b,p}}$ and $\mathbf{F_b}$ must be re-computed whenever data from the CrIS engineering packet used to formulate these matrices change. Figure 37 illustrates the process used to update CMO contents based upon the changes of data seen in the CrIS engineering packet.

The CMO will not be updated unless the interferometer metrology wavelength changes by more than a predetermined threshold (i.e. 2 ppm) or unless the FOV dependent ILS parameters in the engineering packet are changed by ground command. ILS parameter updates for a specific CrIS sensor are not expected to change during the operational mission. The metrology laser wavelength that impacts matrix $\mathbf{F}$ can change once per orbit when a neon re-calibrations of this wavelength is scheduled. An accumulated drift of 2 ppm is not expected to occur during only one orbit. Thus, the CMO updates are expected to be infrequent. The 2 ppm trigger threshold can be changed to some larger or smaller tolerance by changing this parameter in the engineering data packet.

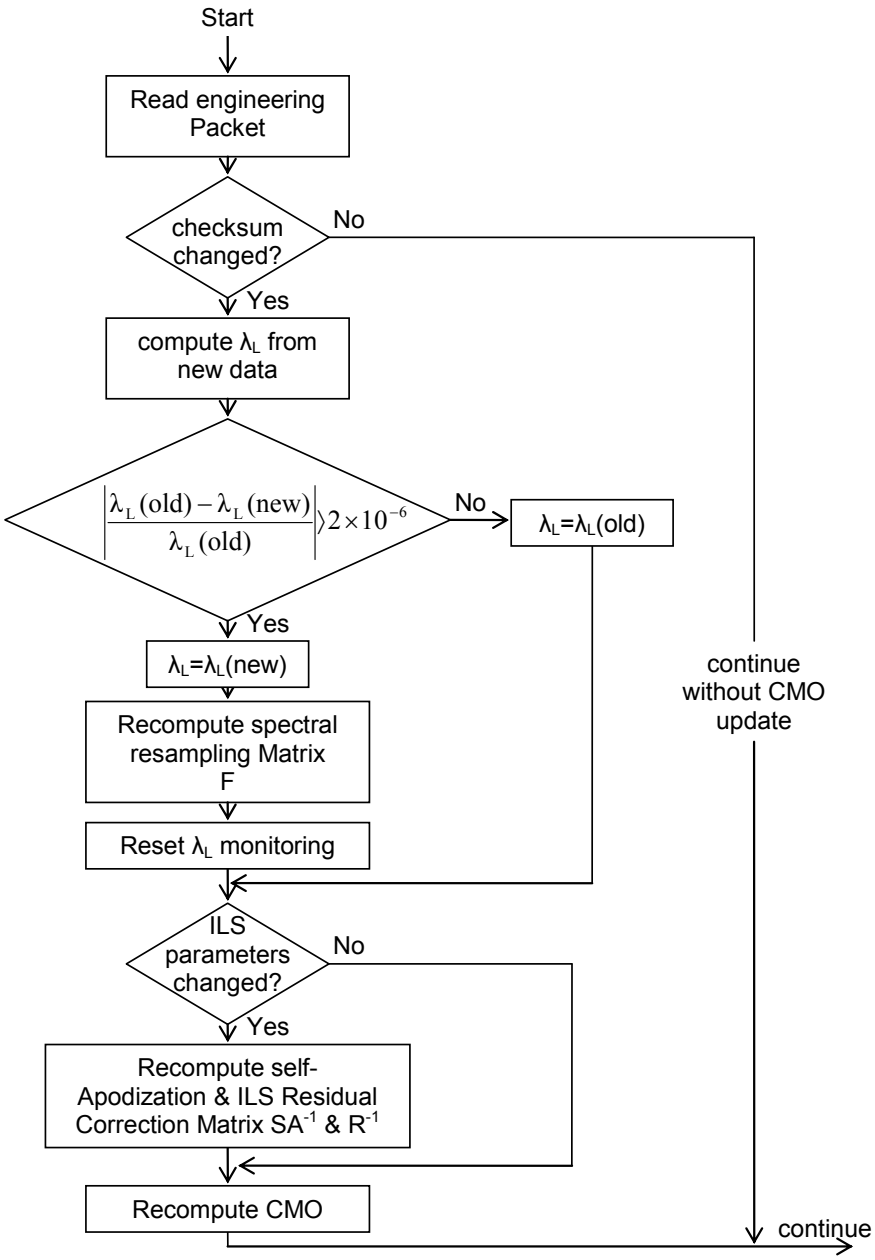

Figure 37: Flow Diagram for Updating CMO

4. SPECTRAL CALIBRATION

This section defines suitable algorithms for spectral calibration. Spectral calibration is the process of assigning absolute values to the wavenumber axis (x-axis spectral bins). This process shall be done for each CrIS channel with a specified accuracy of 5 ppm for all FOVs. This is a necessary step mainly because of possible variations in the metrology system, and other effects listed in Figure 38. The laser diode is prone to wavelength shifts due to junction temperature variations, injection current variations, and aging.

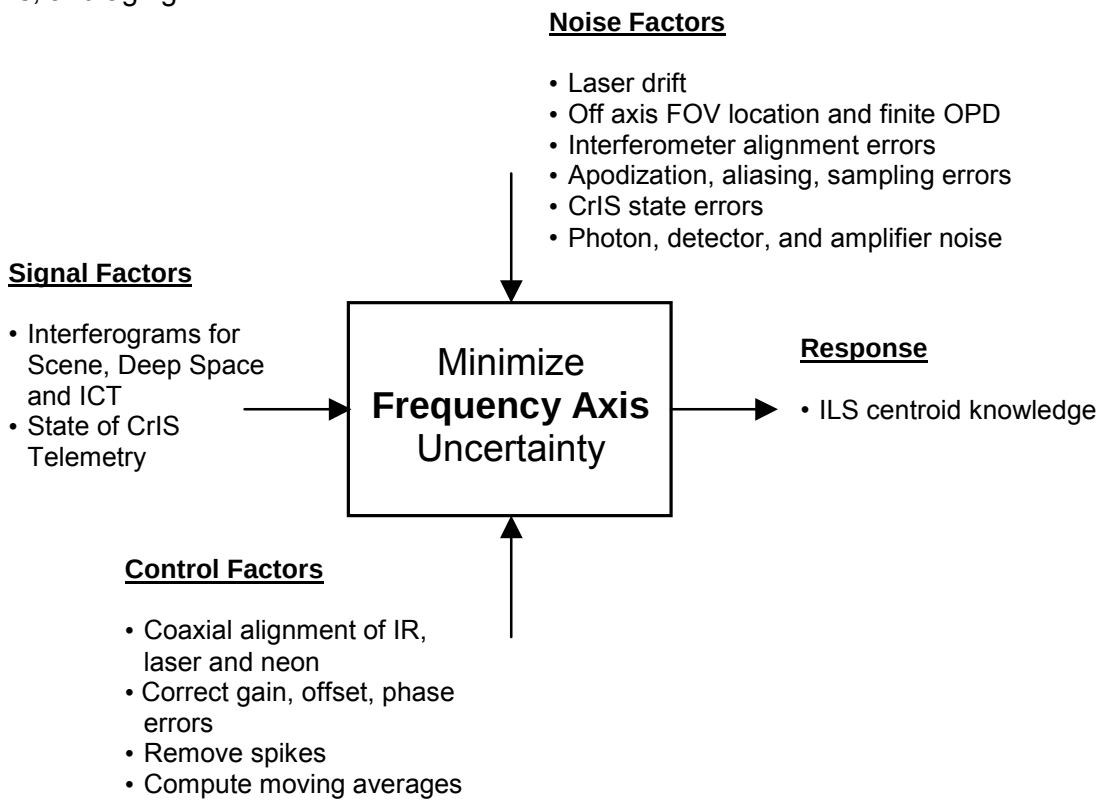

Figure 38: Spectral Calibration Parameter diagram

Before going any further, it is necessary to note that Spectral Calibration is related to the three following operations:

1– **Relabeling of the spectral axis**

The first operation is to assign correct wavenumbers to each measured bin throughout a spectral band, not taking into account other spectral effects like self-apodization. It is a simple relabeling of the spectral axis, using a neon measurement as a spectral calibration reference. See sections 4.1 and 9.2.

2– **Spectral resampling to common user's grid**

The second operation is to resample the spectral scale on a predefined common spectral axis definition and to fix the unapodized resolution (underlying sinc width). This is done via a spectral matrix multiplication, as described in Section 3.5

3– **ILS correction**

The third operation brings bins to their correct positions, based on the initial positions assigned by the previous modules. The ILS correction procedure is described in Section 3.

4.1 NEON-LAMP AS A SPECTRAL REFERENCE

The wavelength measurement system provides a laser wavelength measurement based on the comparison of the wavelength of the metrology laser and a filtered neon lamp [RD 13]. The filtered neon lamp is injected in the interferometer with the same optical path as the metrology laser. Metrology detectors convert the optical signal in an electrical signal. During a sweep measurement, counters are used to determine the number of fringes from both sources. The relative accuracy of the wavelength measurement depends on the interferogram length and the counting mechanism. Relative accuracy is improved by implementing interpolation at the beginning and at the end of a sweep measurement. Moreover, relative accuracy can also be improved by averaging measurements thus reducing the relative uncertainties.

These neon measurements are in the CrIS engineering data packet so that the precise laser metrology wavelength can be computed for use in SDR algorithm processing. Co-alignment of the neon, laser and IR beams through the interferometer is also important for this calibration process to be accurate. These alignments are maintained through the mission life so as to achieve the overall 10 ppm wavelength calibration accuracy of the CrIS sensor.

4.1.1 Wavelength Calculation

Figure 39 illustrates the process of counting and interpolating neon fringes during a single sweep of the CrIS interferometer. With a CrIS interferometer OPD sweep rate of 10 cm/sec ±1%, the interferometer's 1550 nm laser metrology produces a post detected electronic signal frequency of 64.4 kHz ±1%. The 703.24 nm neon line emission produces a 142.2 kHz ± 1% frequency. The ratio of these two frequencies remains the same regardless of the exact interferometer OPD sweep rate. This property can be used to measure the relative wavelength of the laser emission to that of the neon.

Each sweep of the interferometer produces exactly 21,294 sampling pulses for use by the IR channels. Only the last 75% of the available sampling window is used to count neon fringes (A/D convert pulse 5,324 to 21,294). This will result in roughly 17,600 neon fringes counted per sweep.

Since 17,600 neon counts are insufficient in number to achieve the desired <1 ppm wavelength resolution from calibration, interpolation of the neon fringe count by at least a factor of 57 is necessary. A high speed 33 MHz clock on-board the CrIS sensor is used to perform interpolation by a factor of 232.

Figure 39 illustrates how five parameters are measured for each neon calibration sweep in order to compute the ratio of neon to laser metrology wavelength with the required 2 ppm accuracy. These parameters are transmitted to the ground via the CrIS Engineering data packet which is rebroadcast once every 4 minutes. The measured parameters are defined as:

N_{Ne}: Neon cal fringe count, 17,600 ±180 counts nominal per sweep

T_{begin}: Neon cal starting count (full period), 232 ± 3 counts (using 33 MHz interpolation clock)

T_{end}: Neon cal ending count (full period), 232 ± 3 counts (using 33 MHz interpolation clock)

ΔT_{begin}: Neon cal starting partial count, 0 to 235 counts (using 33 MHz interpolation clock)

ΔT_{end}: Neon cal ending partial count, 0 to 235 counts (using 33 MHz interpolation clock)

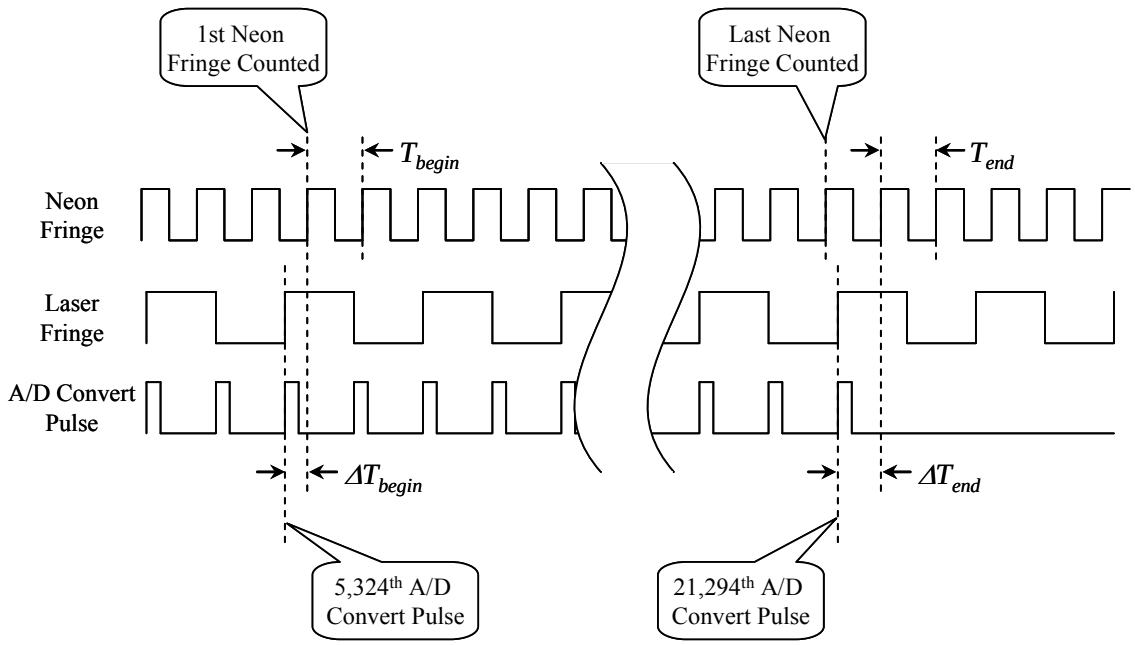

Figure 39: Neon calibration scheme using fringe count interpolation approach

A neon fringe counter is enabled whenever the 5,324th A/D convert pulse occurs in an interferometer sweep. The output of this counter is latched whenever the 21,294th A/D convert pulse occurs. This latched value is the integer neon fringe count N_{Ne} for that sweep. A 33 MHz clock is counted to determine the duration of the other 4 parameters shown in Figure 39.

4.1.2 Calculation of Laser Metrology Wavelength

The ground based SDR algorithm will compute laser metrology wavelength from neon calibration data. The interpolated neon fringe count for one sweep of the interferometer is given by:

$$N_{Ne,Int} = N_{Ne} + \frac{\Delta T_{begin}}{T_{begin}} - \frac{\Delta T_{end}}{T_{end}} \tag{61}$$

and the interferometer laser metrology wavelength can then be computed from

$$\lambda_L = \frac{\lambda_{Ne} \cdot N_{Ne,Int}}{(21{,}294 - 5{,}324)/2} = \frac{\lambda_{Ne} \cdot N_{Ne,Int}}{7{,}985} \tag{62}$$

Normalizing the calculation in equation (61) by use of T_{begin} and T_{end} allows the fractional neon fringe on each end of the sweep to be accurately measured by a high speed clock and counter regardless of the exact OPD rate experienced at beginning and end of sweep.

A unique λ_L is computed for each neon calibration sweep. There can be from 1 to 127 sweeps comprising a neon calibration data set. The number of sweeps used to collect data is configured via a table upload command to the CrIS instrument. The default number of data collection sweeps is 30. The actual number of neon calibration sweeps performed is reported in the CrIS engineering data packet. Version 2.17 and later of SDR code support band specific laser wavelength calculation when a MWIR and SWIR neon wavelength offset is entered into the CrIS engineering packet. Engineering packet version 10 or later is needed to support this function.

4.1.3 Rejecting Bad Neon Count Measurements (Quality Control)

The ground based SDR algorithm will detect and reject neon calibration data containing a neon fringe count error. This type of corruption will be rare. It can be caused by a radiation induced single event upset (SEU) in the space environment or due to an isolated EMI event that corrupts the neon channel S/N ratio below acceptable limits.

Normally, 5 parameters on each of 30 neon calibration sweeps shall compose a set of measured data for a complete laser wavelength calibration. Thus, λ_L will be computed 30 times in this example. Prior to averaging these 30 separate calculations to arrive at the final wavelength estimate, the SDR Algorithm will check for any "out of family" single sweep measurements and reject these from being included in the average. Rejecting a bad data sweep is based upon a determination that there has been a neon fringe count error. Since a neon fringe count error will result in a +/-56.8 ppm error or more (when a single measurement is compared to the ensemble average), then a +/-28 ppm threshold can be set to detect these single measurement errors.

SDR Algorithm rejects neon calibration data for i^{th} sweep if

$$\left| \frac{\lambda_L[i] - \langle \lambda_L \rangle}{\langle \lambda_L \rangle} \right| \geq 28 \times 10^{-6} \tag{63}$$

where $\langle \lambda_L \rangle$ is the average of all λ_L's computed (set of 30 in the baseline example). Whenever a single $\lambda_L[i]$ calculation is rejected, then $\overline{\lambda}_L$ is recomputed using only the remaining good quality $\lambda_L[i]$'s in the set.

Whenever less than 75% of the data set is accepted (< 22 of 30 measurements), the SDR Algorithm will not use the new laser calibration and retain the previous wavelength calibration for use in processing CrIS RDRs.

4.2 METROLOGY WAVELENGTH MONITORING

The SDR Science Code also monitors the drift in LWIR laser diode wavelength between each neon lamp calibration as a quality control measure. A parametric model accomplishes this monitoring by using laser diode temperature and bias current reported in telemetry. The model is characterized on the ground prior to launch. The laser diode temperature and current used in the parametric model are averaged across the 4 minute moving window to reduce the telemetry noise contribution. Every 8 seconds a new "monitored" LWIR metrology wavelength is computed.

Monitoring of laser wavelength drift is performed relative to the LWIR metrology wavelength that was last used to reformulate the CMO. **This monitored laser wavelength is not used by the SDR algorithm to trigger any CMO updates (code version 2.18 and above)**. Prior versions of SDR code performed corrections on the CMO based upon laser diode drift as reported in telemetry. This feature is no longer necessary and is no longer supported by ITT. Updates of CMO can now only be triggered by a neon calibration of the metrology laser or a change of ILS parameters in the engineering packet via ground command.

The monitored LWIR metrology wavelength is still reported in the LWIR, MWIR and SWIR SDR packets. MWIR & SWIR metrology wavelength is not monitored or reported (the LWIR value is reported instead).

5. RADIOMETRIC CALIBRATION

Radiometric calibration is the process of assigning absolute values in physical units (usually radiance) to the intensity axis (ordinate y-axis) with a specified accuracy. For this purpose, deep space and internal calibration target (ICT - blackbody) are used as standard reference spectral radiance.

The calibration algorithm removes phase dispersion of the sensor over each IR band. Once removed, the complex spectral data is thus remapped into a cosine transform where the imaginary portion of the spectra can be discarded for a 1.41 noise factor improvement. Only the cosine transform data (real part of the calibrated spectrum) is delivered to the EDR algorithm. The sin transform data (imaginary part of the calibrated spectrum) can also be used to estimate noise.

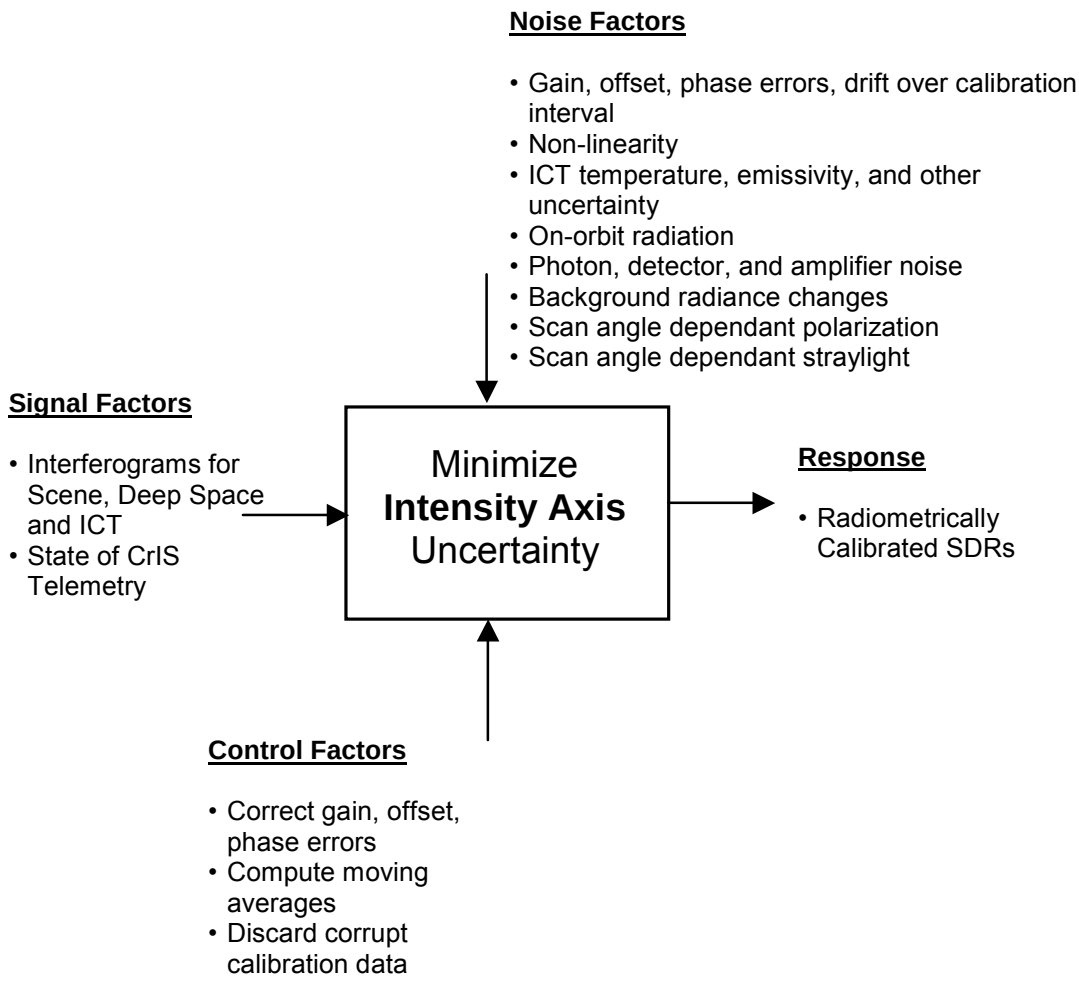

Figure 40: Radiometric Calibration Parameter Diagram

The generic term “radiometric calibration” refers to the following operations performed over each IR band:

Removal of offset and multiplication by the gain of a scene spectrum:

- Implement calibration Equation with point-by-point complex multiplication
- Use emissivity and temperature telemetry of the ICT to calculate the calibration BB radiance
- Measure the calibration references at each scan
- Perform a moving average of the warm target data and cold target data.

Removal of sensor induced phase dispersion:

- Remove detector non-linearity (if present)
- Correct for fringe count errors
- Correct for off-axis self-apodization on each FOV
- Correct for polarization errors
- Remove orthogonal noise components (delivers real component)

5.1 BASIC RADIOMETRIC RELATIONS

The basic mathematical relation between interferograms and spectra is the Fourier transform. The general relationship between an interferogram and its equivalent spectrum can be expressed as:

$$\widetilde{S}(\sigma) = \mathsf{F}\{I(x)\} \tag{64}$$

where the left side of the equation (spectral domain) denotes the spectrum as a function of wavenumber (σ), and the right side (spatial domain) denotes the Fourier transform of the interferogram as a function of the optical path (x). As the measured interferogram is not symmetrical (because of dispersions effects in the beamsplitter and electronics, among other contributors), the resulting spectrum will be complex (represented here by the over-tilde (~) notation). The thermal emission of the beamsplitter can cause contributions having repercussions in the imaginary part [RD 14] (complex filtering sends components in the real part). Thus the resulting observed phase becomes dependent on the incident photon flux, i.e. the phase of deep space, scene, and calibration blackbody spectra may vary substantially.

The computer implementation of the discrete Fourier transform uses the standard Fast Fourier Transform (FFT) algorithms. The transformation is represented as:

$$\widetilde{S}[n] = FFT\{I[m]\} \tag{65}$$

When using numerical Fourier transforms, special care must be taken about special particularities of the numerical implementation (see Appendix 9.1 for more details). Also, when dealing with decimated interferograms, *alias unfolding* (also called Spectrum Unscrambling or Spectrum Re-ordering) must be performed in order to remove the down conversion to a zero IF (Intermediate Frequency) introduced at the satellite level (See Appendix 9.2 for more details).

5.2 GENERAL CALIBRATION EQUATION

The basic approach for determining absolute radiance measured by a FTIR spectrometer is the same as that used for filter radiometers and has been used successfully for other interferometric applications [RD 3]. The detectors and electronics are designed to yield in principle an output which is linear with respect to the incident radiance for all wavenumbers in the optical pass band of the instrument, and two reference sources are viewed to determine the slope and offset which define the linear instrument response at each wavenumber.

The measurement obtained by the system is proportional to the spectral power distribution at the detector. The latter is composed of the emission coming from each input port, along with thermal emission of the spectrometer. Using the notation given in Section 1.6, the measurement can be expressed by the linear relation:

$$\widetilde{S}^{S}(\sigma) = \widetilde{G}(\sigma)\left(F_{INT}(L(\sigma) + \widetilde{O}(\sigma)) + \varepsilon\right) \tag{66}$$

where $\widetilde{S}^{S}(\sigma)$ is the calculated complex spectrum from an *earth scene measurement* (arbitrary units, commonly referred to as digital units [d.u.]),

$L(\sigma)$ is the true incident spectral radiance from the *scene* (in [r.u.]),

$\widetilde{G}(\sigma)$ is the overall spectral responsivity of the instrument, referred to as *gain*, it is a complex function to include interferogram phase dispersion/delays, (d.u./r.u.)

$\widetilde{O}(\sigma)$ is the instrument emission, referred to as *offset,* it is the stray radiance, including all modulated radiance that does not come from the scene (in [r.u.]),

F_{INT} is the instrument operator due to the ILS effects, which includes all effects that the instrument might introduce such as self-apodization, IGM modulation, etc. The notation $F_{INT}L(\sigma)$ implies that the radiance $L(\sigma)$ has been affected by the instrument, (unitless)

ε is the noise, with zero mean $\bar{\varepsilon} = 0$, and standard deviation equal to *NEdN*, (in [r.u.]).

Equation (66) expresses the linear relationship between the true spectral radiance L and the measured, uncalibrated spectrum $\widetilde{S}^{S}$. Two non-equivalent calibration observations are required in order to determine the two unknowns, that are the gain $\widetilde{G}$ and the offset radiance $\widetilde{O}$ as defined in Equation (66). The offset is the radiance, which, if introduced at the input of the instrument, would give the same contribution as the actual emission from various parts of the optical train.

Equation (66) can be solved to yield:

$$\widetilde{G} = \frac{\widetilde{S}^{H} - \widetilde{S}^{C}}{F_{\mathrm{INT}}L^{H} - F_{\mathrm{INT}}L^{C}} \quad \text{[d.u./r.u.]} \tag{67}$$

and
$$\widetilde{O} = \frac{\widetilde{S}^C F_{\mathrm{INT}} L^H - \widetilde{S}^H F_{\mathrm{INT}} L^C}{\widetilde{S}^H - \widetilde{S}^C} \quad \text{[r.u.]} \tag{68}$$

where L^C and L^H are the calculated radiances, modeled by the theoretical spectral radiance of the corresponding observed uncalibrated radiances $\widetilde{S}^C$ and $\widetilde{S}^H$. Those 2 references could be a hot and a cold blackbody modeled by the Planck function (Equation 3) multiplied by the emissivity of the blackbody.

By inverting Equation (66), one can derive the calibration equation used to convert a spectrum from an unknown scene into calibrated data:

$$L' = F_{\mathrm{INT}} L = \frac{\widetilde{S}^S}{\widetilde{G}} - \widetilde{O} \tag{69}$$

For ideal spectra with no noise, this expression for the calibrated radiance would be purely real, since the phases of the ratioed difference spectra are the same. This cancellation of the phases avoids the square root of two (1.4142) noise amplification, which is obtained by taking the magnitude of spectra with nonzero phase. Because the phase of the ratio of difference spectra is zero to within the noise, the calibrated spectrum can equally well be defined in terms of the real part of the ratio (as shown) or in terms of the magnitude of the ratio [RD 3]. When non-linearity is present, a special correction must be applied on different interferograms coming from affected detectors.

5.3 CrIS SPECIFIC CALIBRATION EQUATION

Using equations (67), (68) and (69) yields,

$$F_{\mathrm{INT}} L^S = \frac{\widetilde{S}^S}{\dfrac{\widetilde{S}^H - \widetilde{S}^C}{F_{\mathrm{INT}} L^H - F_{\mathrm{INT}} L^C}} - \frac{\widetilde{S}^C F_{\mathrm{INT}} L^H - \widetilde{S}^H F_{\mathrm{INT}} L^C}{\widetilde{S}^H - \widetilde{S}^C}, \tag{70}$$

Rearranging terms one then obtains,

$$F_{\mathrm{INT}} L^S = \frac{\widetilde{S}^S \left(F_{\mathrm{INT}} L^H - F_{\mathrm{INT}} L^C\right) - \left(\widetilde{S}^C F_{\mathrm{INT}} L^H - \widetilde{S}^H F_{\mathrm{INT}} L^C\right)}{\widetilde{S}^H - \widetilde{S}^C} \tag{71}$$

Further algebraic simplification along with inclusion of the averaging operator <> for hot and cold calibration spectrum results in equation (72):

$$L^S = F_{INT}^{-1} \left[\frac{\widetilde{S}^S - \langle \widetilde{S}^C \rangle}{\langle \widetilde{S}^H \rangle - \langle \widetilde{S}^C \rangle} \right] \cdot F_{INT} L^H + F_{INT}^{-1} \left[\frac{\langle \widetilde{S}^H \rangle - \widetilde{S}^S}{\langle \widetilde{S}^H \rangle - \langle \widetilde{S}^C \rangle} \right] \cdot F_{INT} L^C \tag{72}$$

This calibration equation accounts for the effects of both cold and hot calibration target radiance. During normal on-orbit operation the cold reference radiance L^C = 0 so that the second term in equation (72) can be ignored resulting in a further simplification. Of course, during ground testing with cold calibration targets having elevated temperature, this form of equation is more useful.

In the CrIS algorithm software implementation, the F_{INT}^{-1} term in equation (72) is combined into the CMO matrix. Most of the effects of instrument operator F_{INT} on the hot and cold calibration target radiances is shifting the radiance spectra toward the smaller wavenumber. It can be shown that the shifted spectral grid is related to the un-shifted spectral grid by equation (73):

$$\sigma_{FOV} = \sigma * (1 + \delta_{FOV}) \tag{73}$$

where σ_{FOV} is the wavenumber after spectral shift caused by instrument operator and δ_{FOV} is the spectral shift factor, respectively, for each of the FOV positions. Therefore, instead of computing the complex instrument operator and apply it to the calibration radiances, the SDR algorithm calculates the physical radiances of the calibration targets on the shifted spectral grid to account for the instrument operator effects. Tests based on CrIS sensor thermo-vacuum test data have shown this approximation is very accurate and results in small, negligible errors.

5.4 ICT RADIOMETRIC MODEL

The radiometric model used to generate the theoretical ICT radiance must be as accurate as possible in order to accurately predict the amount of radiance reflected from the ICT that originates from the external environment. The radiometric model takes into account the emissivity, transmissions and temperatures of the various elements seen by the ICT.

The components of the model are sketched in Figure 41. The external environment is to be understood to have blackbody contributors to the total radiance as seen by the instrument when looking at the ICT. Here, the environment surfaces represent a collection of many components modeled as a blackbody and at some temperature different than the ICT. Figure 41 illustrates the approximate half angle views to the various external environment surfaces.

Mechanical modeling combined with ray trace is used to more accurately compute the true view factors that the ICT has to each external surface. The environment outside the ICT radiates energy into the ICT, some of which is reflected back out.

The total ICT radiance emitted is the sum of the direct ICT emission and the reflected ICT radiance originating from each of the external surfaces. The external environmental is made up of the SSM baffle, OMA housing, instrument frame, reflected ICT radiance from the cold view of the IFM beamsplitter, ICT baffle and earth views.

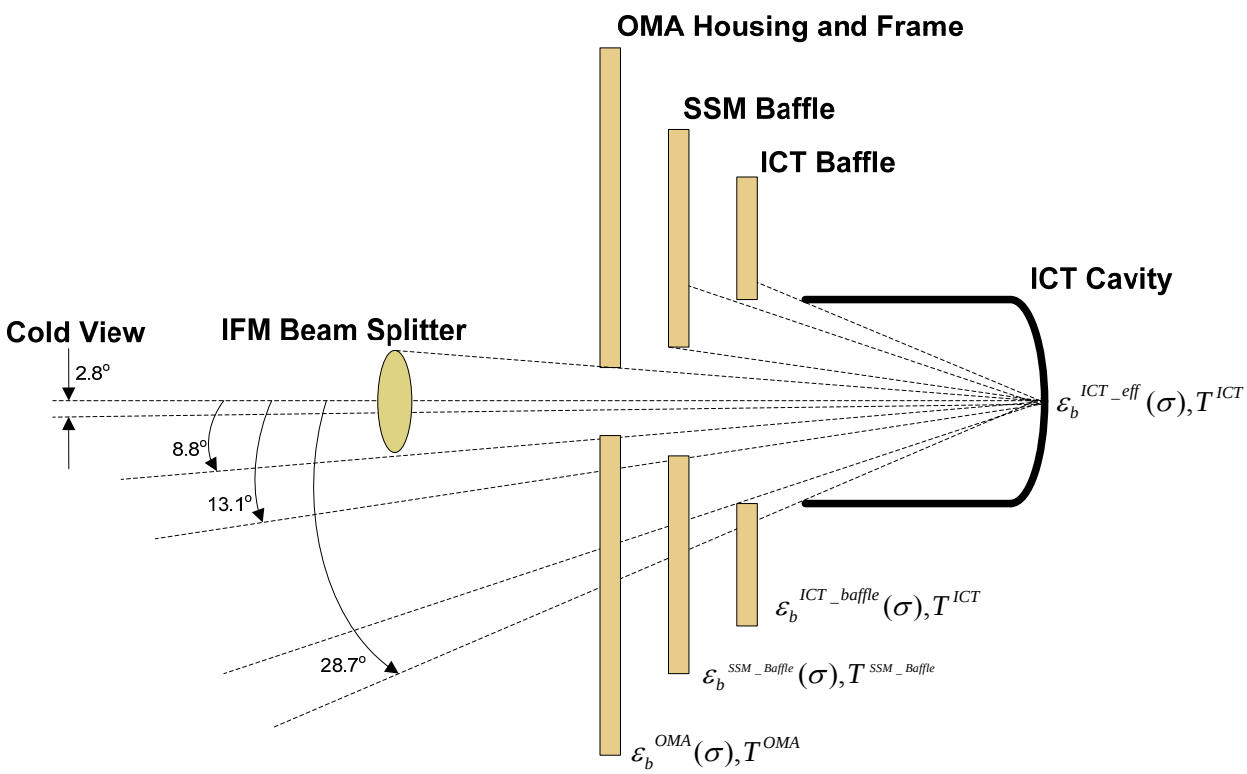

Figure 41: Radiometric model when the scene is the ICT

5.4.1 Radiometric Error

Deleted. This section originally written in 2003 is superseded by more recent analysis. See ITT document 8231508 for a detailed treatment of radiometric error sources.

5.4.2 Radiometric Model Formulation

The radiance seen by the CrIS instrument when viewing the ICT is a combination of a direct emission from the ICT and reflected radiance originating from various external environment surfaces that the ICT views. Mathematically, the relationship is as follows:

$$L_b^{ict}[n] = C_b^{ICT}[n] + C_b^{SSM_baffle}[n] + C_b^{OMA}[n] + C_b^{ICT_baffle}[n] + C_b^{ICT_ref}[n] + C_b^{Space}[n] \tag{74a}$$

Where:

$$C_b^{ICT}[n] = \varepsilon_b^{ICT_eff}[n] \cdot B\left(\sigma_b[n], \left\langle T^{ICT} \right\rangle\right) \tag{75}$$

$$C_b^{SSM_baffle}[n] = \left(1 - \varepsilon_b^{ICT_eff}[n]\right) \cdot \varepsilon_b^{SSM_baffle} \cdot A^{SSM_baffle} \cdot B\left(\sigma_b[n], \left\langle T^{SSM_baffle} + T^{offset} \right\rangle\right) \tag{76}$$

$$C_b^{OMA}[n] = \left(1 - \varepsilon_b^{ICT_eff}[n]\right) \cdot \varepsilon_{OMA} \cdot (1 - \varepsilon_b^{SSM}) \cdot (A^{OMA} + A^{Frame} + A^{BS_warm}) \cdot B(\sigma_b[n], \left\langle T^{OMA} \right\rangle) \tag{77}$$

$$C_b^{ICT_baffle}[n] = \left(1 - \varepsilon_b^{ICT_eff}[n]\right) \cdot \varepsilon_b^{ICT_baffle} \cdot A^{ICT_baffle} \cdot B\left(\sigma_b[n], \left\langle T^{ICT} \right\rangle\right) \tag{78a}$$

$$C_b^{ICT_ref}[n] = \left(1 - \varepsilon_b^{ICT_eff}[n]\right) \cdot (1 - \varepsilon_b^{SSM})^2 \cdot A^{BS_cold} \cdot \frac{B\left(\sigma_b[n], \left\langle T^{ICT} \right\rangle\right)}{2} \tag{78b}$$

$$C_b^{Space}[n] = \left(1 - \varepsilon_b^{ICT_eff}[n]\right) \cdot \varepsilon_b^{Avg_Earth} \cdot A^{Space} \cdot B\left(\sigma_b[n], \left\langle T^{Avg_Earth} \right\rangle\right) \tag{78c}$$

Each symbol in equations 74a through 78c is defined in Table 14.

Table 14: Symbols description for the ICT radiometric model

Symbol	Description	Comment
$\varepsilon_b^{ICT_eff}[n]$	ICT effective emissivity for n^{th} channel in band "b" on the sensor wavenumber grid.	Quantified in engineering packet. Emissivity for wavenumber channels in guard band are set equal to the band edge emissivity value.
$\varepsilon_b^{\mathrm{SSM_Baffle}}$	SSM baffle surface emissivity in band "b"	Quantified in engineering packet, one value per IR band
$\varepsilon_b^{\mathrm{ICT_Baffle}}$	ICT baffle surface emissivity in band "b"	Quantified in engineering packet, one value per IR band
$\varepsilon_b^{\mathrm{OMA}}$	OMA surface emissivity in band "b"	Quantified in engineering packet, one value per IR band
$\varepsilon_b^{Avg_Earth}$	average Earth emissivity in band "b" for on-orbit operations (SSM target emissivity for ground testing)	Quantified in engineering packet, one value per IR band
$\varepsilon_b^{\mathrm{SSM}}$	scene selection module mirror emissivity in band "b"	Quantified in engineering packet, one value per IR band
$\langle T^{\mathrm{ICT}} \rangle$	average ICT temperature [K]	average of PRT1 & PRT2 ICT temperatures over the moving window, TLM measurement
$\langle T^{\mathrm{SSM_Baffle}} \rangle$	average baffle temperature [K]	average over the moving window, TLM measurement. Section 5.4.2.1 SSM baffle temperature corrections
$\langle T^{\mathrm{offset}} \rangle$	Average offset correction to SSM baffle temperature [K]	Accounts for baffle temperature gradient. Function of orbit position. Values for 21 orbit positions are in engineering packet. Interpolation used to get correction for all orbit positions
T^{Avg_Earth}	average Earth temperature for on-orbit operations (SSM Target used for ground testing)	Quantified in engineering packet, Single average earth surface temperature used
A^{Frame}	ICT view of Frame	Quantified in engineering packet, obtained from ray trace model
$A^{\mathrm{SSM_Baffle}}$	ICT view of SSM baffle	Quantified in engineering packet, obtained from ray trace model
$A^{\mathrm{ICT_Baffle}}$	ICT view of ICT baffle	Quantified in engineering packet, obtained from ray trace model
$A^{\mathrm{BS_warm}}$	ICT view of warm portion of the interferometer beamsplitter	Quantified in engineering packet, obtained from ray trace model
$A^{\mathrm{BS_cold}}$	ICT view of cold portion of the interferometer beamsplitter	Quantified in engineering packet, obtained from ray trace model
A^{Space}	ICT view of earth	Quantified in engineering packet, obtained from ray trace model
A^{OMA}	ICT view of OMA housing	Quantified in engineering packet, obtained from ray trace model

Table 15 summarizes view factors from the ICT bottom surface to all the external environmental surfaces that the ICT can see. These view factors were obtained using a detailed mechanical model of the CrIS sensor in combination with ray trace software. A 95% ICT surface emissivity was assumed along with multiple bounces and reflections to the external environment during the modeling process. A surface emissivity of 1.00 is used for scan baffle, frame, OMA, space and ICT baffle during this view factor modeling. The SSM mirror reflectance is 1 - emissivity. The mirror front surface emissivity used was 0.01. The energy reflected off the SSM mirror was assumed to be 100% specular.

Table 15: Fraction of View from ICT Bottom Surface to Each Environment Surface (notional)

View From	To	Fractional View to Environment
ICT Base	ICT Walls	-
ICT Base	ICT Base	-
ICT Base	ICT Baffle	0.175
ICT Base	Scan Baffle	0.508
ICT Base	Scan Mirror	
ICT Base	Frame	0.214
ICT Base	Opto-Mechanical Assembly (OMA)	
ICT Base	Warm Beamsplitter	0.086
ICT Base	Cold Beamsplitter	0.008
ICT Base	Space	0.009

5.4.2.1 SSM Baffle Temperature Correction

Accurate knowledge of the SSM scan baffle temperature is needed in order for the ICT environmental corrections model to more accurately represent the true sensor environment. The temperature sensor which monitors the scan baffle temperature is located on the opposite end of the scan baffle viewed by the ICT. Therefore, the temperature gradient from one end of the baffle to the other needs to be predicted. A detailed thermal model was used to predict changes of the SSM scan baffle temperature gradient with orbit position for the NPP mission.

Table 16 displays the temperature gradient between the SSM baffle temperature sensor and the end of the SSM baffle, as viewed by the ICT base. The delta T in Kelvin is shown versus orbit time in seconds. Time zero corresponds to the orbit time when spacecraft is at the North Pole.

Table 16: SSM Baffle Temperature Offset Correction versus Orbit Position (notional)

Orbit Time after North Pole (sec)	SSM Baffle Temperature Correction (K)
0	-1.67
288.6	-1.36
577.1	-1.82
865.7	-3.26
1154.3	-3.47
1442.9	-3.57
1731.4	-3.59
2020.0	-3.26
2308.6	-3.1
2597.1	-1.33
2885.7	-2.5
3174.3	-2.2
3462.9	-0.94
3751.4	-0.07
4040.0	0.49
4328.6	1.22
4617.1	1.47
4905.7	1.28
5194.3	1.02
5482.9	0.47
5771.4	-0.58

The temperature corrections are cubic spline interpolated in order to produce an SSM Baffle temperature correction for each second of one orbit. The orbital period, in seconds, is a parameter found in the four-minute engineering packet along with the time stamp corresponding to a neon calibration and the 21 unique temperature correction points of Table 16. The default orbital period is set at 6060 seconds. The neon calibration time stamp will correspond to the spacecraft position over the North Pole. Figure 42 shows the spline interpolated fit to the 21 points from Table 16.

If the orbital period is 6060 seconds, then there will be 6060 correction points computed. Indexing of these temperature corrections is accomplished by differencing the current RDR time stamp with the last neon calibration time stamp (rounding the difference to 1 second increments). If the difference is more than the orbital period, then the difference is modulo corrected by 6060 seconds (or alternate orbit period as defined in the engineering packet).

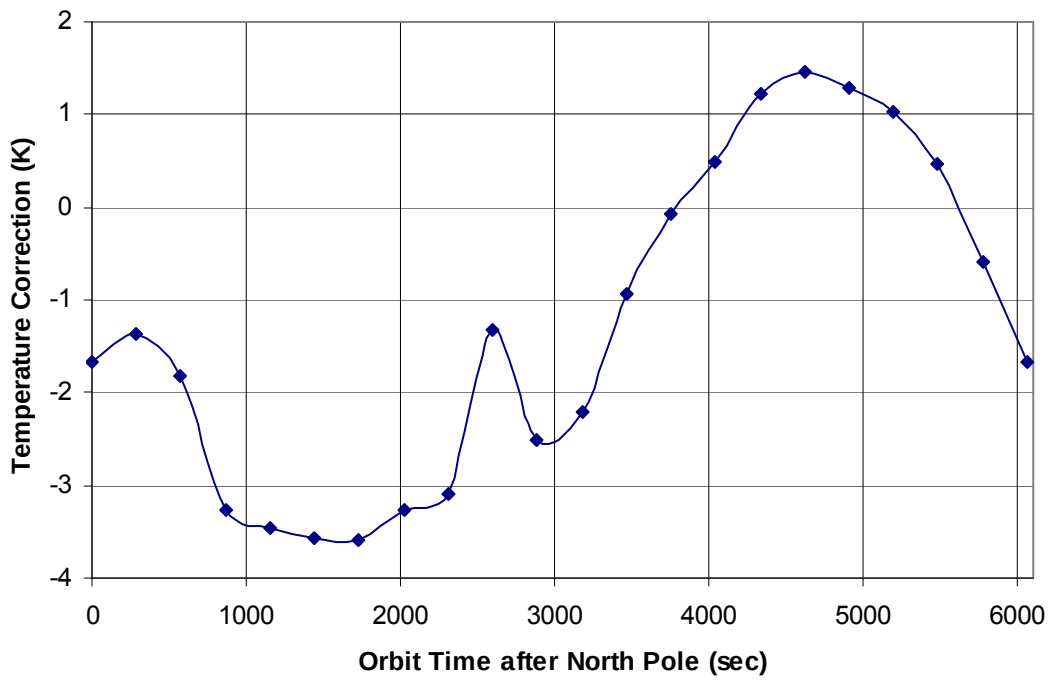

Figure 42: Interpolated Temperature Corrections for SSM Baffle (notional)

5.5 ICT TEMPERATURE COMPUTATION

Temperature readings of the CrIS ICT are derived from transfer curves with parameters coming from engineering data packets and ADC counts coming from science TLM packets.

The ICT temperature is the average of two PRT temperature sensors which are read every 200 msec from the CrIS sensor. The telemetry circuitry that digitizes this information also digitizes the resistance of two very stable calibration resistors that are used for reference. These auxiliary telemetry readings allow virtually all of the electronic readout error to be cancelled by using a 2 point resistance calibration of the telemetry circuitry. Thus, a more accurate ICT temperature reading results with less than 15 mK readout error [RD 36].

Measured quantities transmitted in science telemetry:

ICT_LOW_CAL = TLM reading of 200 ohm calibration resistor
ICT_HIGH_CAL = TLM reading of 240 ohm calibration resistor
ICT_#1 = TLM reading of PRT#1
ICT_#2 = TLM reading of PRT#2
ICT_CAL_RTD = TLM reading of temperature sensor attached to Cal resistors

Constants transmitted in engineering packet:

R_{0_PRT1} = Resistance of PRT1 @0^0C (ohm)
α_{PRT1} = PRT1 temperature coefficient, 1st order term (ohm/ohm/^{0}C)
β_{PRT1} = PRT1 temperature coefficient, 2nd order term (ohm/ohm/$^0C^2$)

R_{0_PRT2} = Resistance of PRT2 @0^0C (ohm)
α_{PRT2} = PRT2 temperature coefficient, 1st order term (ohm/ohm/^{0}C)
β_{PRT2} = PRT2 temperature coefficient, 2nd order term (ohm/ohm/$^0C^2$)
$R_{0_LOW_CAL}$ = Low value calibration resistance @0^0C (ohm)
α_{LOW_CAL} = Low value calibration resistance temperature coefficient (ohm/ohm/^{0}C)
$R_{0_HIGH_CAL}$ = High value calibration resistance @0^0C (ohm)
α_{HIGH_CAL} = High value calibration resistance temperature coefficient (ohm/ohm/^{0}C)
R_{0_RTD} = Resistance @0^0C of RTD that measures temp of Cal resistors (ohm)
α_{RTD} = RTD temperature coefficient (ohm/ohm/^{0}C)

ICT Temperature Readout Equations

There are five steps in the computation of ICT temperature

1. Calculate the temperature of the calibration resistors used in CrIS telemetry electronic circuits which is given by T_{RTD},

$$T_{RTD} = \frac{\left[\left(R_{0_LOW_CAL}\right)-\left(R_{0_RTD}\right)\right]+\left[\left(R_{0_HIGH_CAL}\right)-\left(R_{0_LOW_CAL}\right)\right]\cdot\left[\frac{\left(ICT_{CAL_RTD}\right)-\left(ICT_{LOW_CAL}\right)}{\left(ICT_{HIGH_CAL}\right)-\left(ICT_{LOW_CAL}\right)}\right]}{R_{0_RTD}\cdot\alpha_{RTD}} \quad (79a)$$

2. Adjust calibration resistor value based upon the temperature of the calibration resistors,

$$R_{LOW_CAL} = R_{0_LOW_CAL}\cdot\left[1+\alpha_{LOW_CAL}\cdot T_{RTD}\right]$$

$$R_{HIGH_CAL} = R_{0_HIGH_CAL}\cdot\left[1+\alpha_{HIGH_CAL}\cdot T_{RTD}\right] \quad (79b)$$

3. Compute ICT PRT resistances (both PRTs) using digitized telemetry and two point resistor calibration.

$$R_{PRT1} = R_{LOW_CAL}+\left[\left(R_{HIGH_CAL}\right)-\left(R_{LOW_CAL}\right)\right]\cdot\left[\frac{\left(ICT_\#1\right)-\left(ICT_{LOW_CAL}\right)}{\left(ICT_{HIGH_CAL}\right)-\left(ICT_{LOW_CAL}\right)}\right]$$

$$R_{PRT2} = R_{LOW_CAL}+\left[\left(R_{HIGH_CAL}\right)-\left(R_{LOW_CAL}\right)\right]\cdot\left[\frac{\left(ICT_\#2\right)-\left(ICT_{LOW_CAL}\right)}{\left(ICT_{HIGH_CAL}\right)-\left(ICT_{LOW_CAL}\right)}\right] \quad (79c)$$

4. The known second order dependence of the PRT resistance with temperature is used to calculate the PRT temperatures by solving quadratic equations,

$$\mathrm{R}_{PRT1} = \mathrm{R}_{0_PRT1}\cdot\left(1+\alpha_{PRT1}\cdot \mathrm{T}_{PRT1}+\beta_{PRT1}\cdot \mathrm{T}^2_{PRT1}\right)$$

$$\mathrm{R}_{PRT2} = \mathrm{R}_{0_PRT2}\cdot\left(1+\alpha_{PRT2}\cdot \mathrm{T}_{PRT2}+\beta_{PRT2}\cdot \mathrm{T}^2_{PRT2}\right) \quad (79d)$$

5. The above quadratic equations for very linear PRTs are solved using Taylor series expansion to produce two ICT temperatures (T_{PRT1} and T_{PRT2}),

$$T_{PRT1} = -\left[\frac{R_{0_PRT1} - R_{PRT1}}{R_{0_PRT1} \cdot \alpha_{PRT1}}\right] \cdot \left(1 + w_1 + 2w_1^2 + 5w_1^3 + ...\right) \qquad w_1 = \left[\frac{R_{0_PRT1} \cdot \beta_{PRT1} \cdot \left(R_{0_PRT1} - R_{PRT1}\right)}{\left(R_{0_PRT1} \cdot \alpha_{PRT1}\right)^2}\right]$$

$$T_{PRT2} = -\left[\frac{R_{0_PRT2} - R_{PRT2}}{R_{0_PRT2} \cdot \alpha_{PRT2}}\right] \cdot \left(1 + w_2 + 2w_2^2 + 5w_2^3 + ...\right) \qquad w_2 = \left[\frac{R_{0_PRT2} \cdot \beta_{PRT2} \cdot \left(R_{0_PRT2} - R_{PRT2}\right)}{\left(R_{0_PRT2} \cdot \alpha_{PRT2}\right)^2}\right] \quad (79e)$$

Only the first 4 terms of the Taylor series expansion are used in the calculation. The temperatures from both PRT sensors are then averaged by the SDR Algorithm. Temporal averaging is also performed using a moving window spanning 4 minutes. Since readings are made every 200 msec, this results in a moving average of ICT temperature having 2400 samples. Half these samples are in the 2 minutes preceding the current earth scene measurement and half are in the 2 minutes following the current earth scene measurement.

5.6 SIGNAL COADDITION

The common practice of co addition of interferograms is valid for the reduction of true noise (short-term random fluctuations). However, it is not valid for dealing with instability and drift, as it produces a range of interferometric modulation analogous to optical pseudo-coherence effects [RD 15, RD 16]. This also jeopardizes the multiplex advantage of FTS. The quantitative structure of the modulus spectrum of a shifted interferogram is unchanged. A better practice is to average spectra. Hence spectra can be averaged validly. This and the fact that FCE detection is easier to perform in the spectral domain have favored SDR Algorithms design to opt for this approach on raw spectra.

In order to achieve the requested radiometric accuracy, 30 cold DS calibration measurements must be co added together and 30 ICT calibration measurements must be co added together in order to increase the SNR. The chosen method is a moving average that co adds the N^{ma} (= 30) closest in time equivalent measurements in order to estimate background radiance and gain.

5.6.1 Moving Average

The moving average is defined as follows:

$$\left\langle T_j \right\rangle = \frac{1}{N^{ma}} \sum_{i=j-N^{ma}/2}^{j+N^{ma}/2-1} T_i \ , \qquad (80)$$

that is, a simple averaging inside a small moving window.

Before the co addition is performed, individual interferograms of a sequence need to have a common fringe count alignment. This is why a FCE detection/correction is applied to each spectrum before being inserted into the moving average.

The moving average concept can be summarized as follows:

Keep in memory N^{ma} (= 30 as a baseline) different sweeps, and sequentially update each one of these window elements,

Recompute the mean of all window elements when requested.

The complete re-updating of the calibration moving window takes 4 minutes.

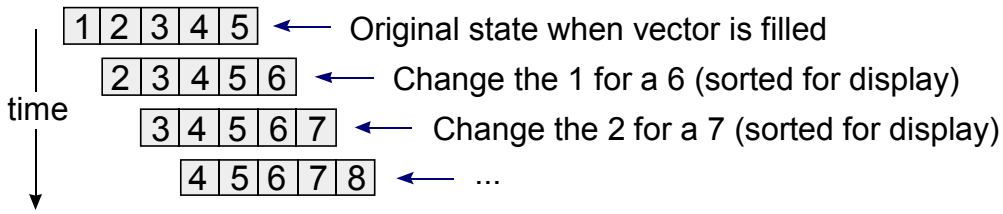

Figure 43: Moving average window updating (example case N^{ma} = 5)

Moving windows are considered un-weighted (each element has an equal importance) in order to maintain an equal signal to noise ratio.

The spectral co addition is a simple point-by-point addition and is expressed by:

$$\left\langle \underline{\tilde{S}}^{X}[n] \right\rangle = \frac{1}{N^{ma}} \sum_{i=0}^{N^{ma}-1} \underline{\tilde{S}}^{X}[i,n] \tag{81}$$

where the various terms are described in Section 7.3.1.

The co addition should also take into account the moving average of the temperature parameters. This is done as follows:

$$T^{Y} = \frac{1}{N^{ma}} \sum_{i=0}^{N^{ma}-1} T^{Y}[i] \tag{82}$$

What should be averaged is in reality the blackbody radiance corresponding to each ICT measurement. But, for simplicity of the processing, we make the following linearity hypothesis:

$$\frac{1}{N} \sum_{i=0}^{N-1} B(T_i) \approx B\left(\frac{1}{N} \sum_{i=0}^{N-1} T_i \right) \tag{83}$$

which is valid in the case of a monotonic function like the Planck distribution for a narrow range of temperatures and wave-numbers. The SDR Algorithms therefore average temperatures, computed from raw instrument readings as described in Section 5.4.1.

5.6.2 Impact of Temperature Drift

In the CrIS instrument, the ICT is not thermally stabilized. Temperature variations will be present in the moving average window, introducing deviation from the real expected values for the averaged ICT. In order to estimate the error, we computed the difference between the average of blackbodies and a blackbody at the average temperature of those blackbodies, i.e.

$$\varepsilon[\sigma] = 100 \frac{\frac{1}{N} \sum_{i=1}^{N} B[\sigma, T_i] - B[\sigma, \langle T \rangle]}{B[\sigma, 287]} . \tag{84}$$

We compute also the error on the radiance using the following equation,

$$\mathrm{e} = 100 \frac{\sum_{\sigma} \left(\frac{1}{N} \sum_{i=1}^{N} B[\sigma, T_i] - B[\sigma, \langle T \rangle] \right)}{\sum_{\sigma} B[\sigma, 287]} . \tag{85}$$

Considering a drift of 0.08 K/min, maximal temperature of 310 K, and a number of samples between 8 and 30, we compute the error caused by the temperature drift. We have assumed a linear temperature drift. It must be remarked that for ICT temperatures lower than 310 K, the error will be even smaller. The maximal temperature difference encounter inside the moving window is 0.32 K.

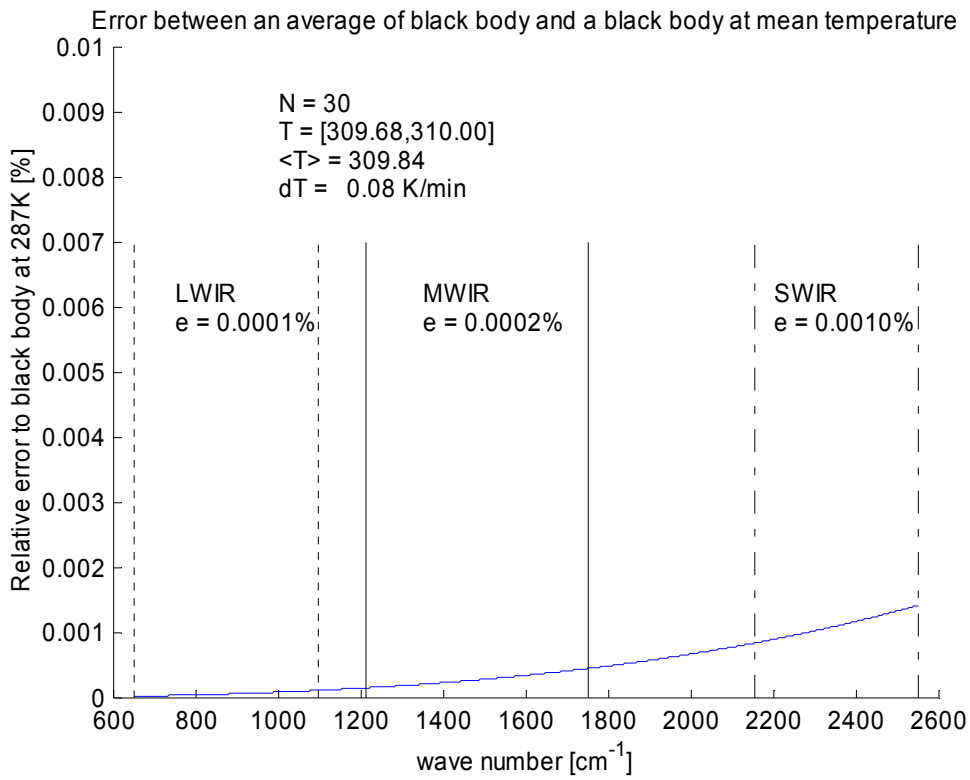

Figure 44: Relative error causes by combining many blackbodies (N=30)

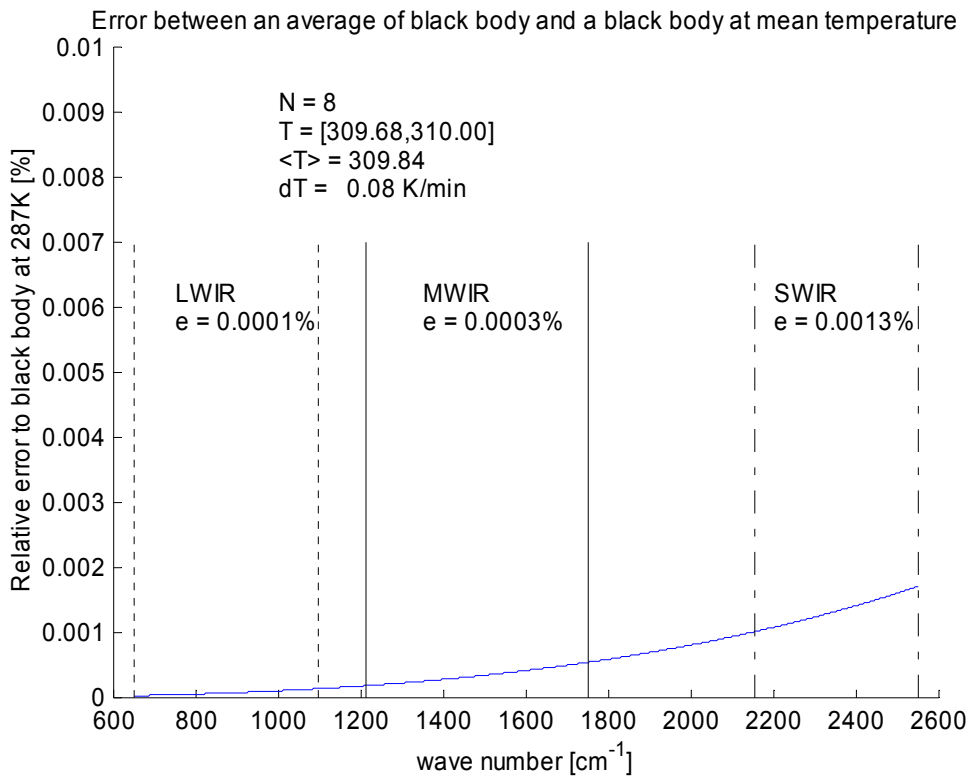

Figure 45: Relative error caused by combining many blackbodies (N=8)

Few remarks must be made about the impact of the temperature drift:

The number of samples has negligible impact on the error,

The error depends primarily on the temperature variation (min/max) inside the moving window,

The error has a quadratic dependency over the temperature differences, when the temperature drift is constant.

The quadratic dependency of the error over the temperature differences comes from the second order term in the Taylor expansion. In our temperature range, only the linear term dominates. As the temperature differences increase, the quadratic term in the Taylor expansion becomes more important, increasing the error of the linear approximation.

Figure 44 and Figure 45 show clearly the negligible impact of the temperature drift in the radiometric calibration. The worst case is in the SW band, in which the error over the radiance is 13 ppm. We can see that the error is almost the same with 8 or 30 samples.

5.6.3 Throughput Delay

The present concept is to pipeline the processing so that SDRs and EDRs are processed in parallel, thus allowing a near full 20 minutes to be allocated to each function. A “throughput delay” of one minute maximum has been defined for the SDR Algorithms and one minute maximum for the EDR algorithms. Throughput delay is the maximum latency occurring by processing an earth scene through the algorithm from input to output. These latencies can be caused by the need to process four minutes worth of on-orbit data that encompass calibration measurements and apply all of these measurements to the single earth scene being processed. Allowing for a one minute throughput delay

in SDR Algorithms and a one minute throughput delay in EDR algorithms leaves 18 minutes of time left for processing the entire block of 1.25 orbits of data.

According to current acquisition plan (see Section 0) the CrIS collects 34 Fields of Regard (FOR) during each 8-second scan sweep. Four of these are calibration data, while 30 are earth scenes. Each FOR contains 9 Fields of View (FOV). 1.25 orbits of data will thus result in 290 000 FOVs to be processed by the SDR Algorithms within 18 minutes. This then computes to a faster than real-time processing speed of 3.7 ms per FOV for the SDR Algorithms.

The 1.25 × 101 minutes of orbit data (946 scans) will be transmitted down in 10 minutes, corresponding to a factor 10 faster than real-time processing constant. The N^{ma} moving average window elements need to be filled completely before the computation of the earth scenes calibration begins, in order to reach the proper SNR threshold. Waiting for 30 scans in real-time would take 4 minutes, at 8 sec/scan. But in the faster than real-time processing scheme, this takes 24 seconds. In order to account for the process and loading, this throughput delay is rounded up to 1 minute.

During this waiting time, no SDR outputs are generated. After the pipeline is filled, the SDR Algorithms will hand out calibrated spectra at the requested interval.

REF _Ref446469644 \h Figure 46 summarized the throughput delay in measurement sequence. The mean calibration spectra and associated ICT mean temperatures are computed from a mean of $N^{ma}/2$ before and $N^{ma}/2$ after the requested time, where the middle is the most representative of the true status of the calibration target.

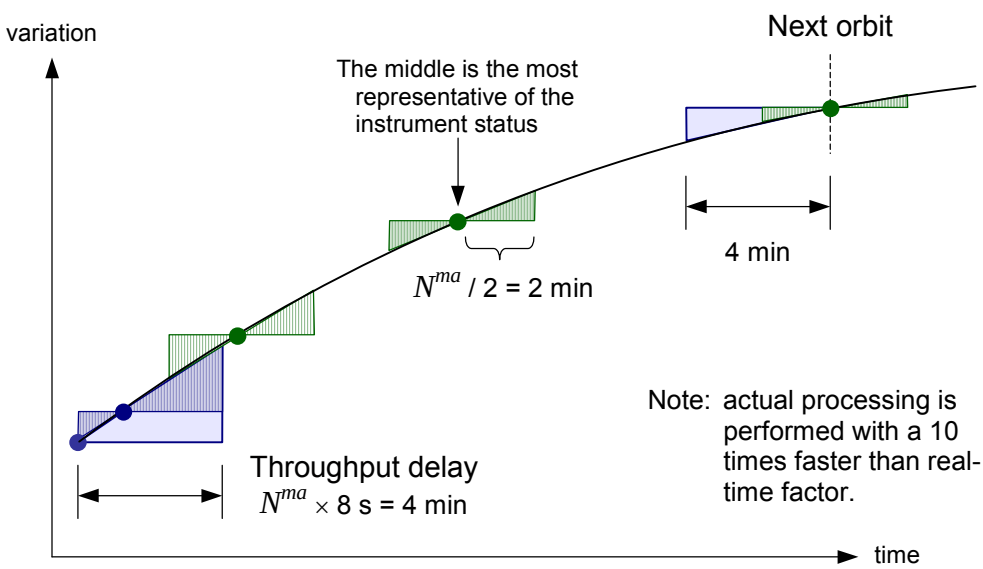

Figure 46: Throughput delay in measurement sequence with $N^{ma}=30$

The moving average of N^{ma} = 30 deep space looks and 30 Internal Calibration Target (ICT) averages are performed 15 samples prior to the earth scene and 15 samples after earth scene. This centering of the calibration averaging is most representative of the instrument background around the time of earth scene measurement. At the beginning of the processing, a special mode should be implemented for the filling of all the moving average window elements by reading ahead the calibration measurements scans of the orbit.

With a moving window size of $N^{ma}=30$, it takes approximately four minutes of on-orbit data collection to span this ±15 samples of calibration information to support this computation. The present CrIS baseline instrument design is being engineered to maintain better than 0.1% change in instrument radiometric background radiance over four minute intervals such as this. Should this stabilization of the instrument background prove impractical from a cost standpoint, then mathematical interpolation techniques will be added to the averaging algorithms to account for changes in the instrument thermal conditions and/or detector responsivities. The opposite is more likely to happen, where a high stability enables the moving average window to be of a larger size (to increase the SNR).

All valid calibration data (ICT/DS) that fit within the ±2 minutes around ES data are used to perform calibration. At the beginning and the end of this temporal sequence, ES data are calibrated using less calibration data.

6. GEOMETRIC CALIBRATION

The goal of the geometric calibration is to map CrIS line-of-sight pointing vectors to geodetic longitude and latitude. This is illustrated in Figure 47. To accomplish this task, several coordinate systems are defined (Section 6.1) and generic coordinate system transformations are reviewed (Section 6.2). The geometric calibration algorithm itself is partitioned (Section 6.3) into a sensor specific algorithm (Figure 48 and Section 6.4), where the line-of-sight vectors are expressed in the S/C body frame, and a spacecraft generic algorithm (Section 6.5) where the intersection of the line-of-sight vectors with the Earth ellipsoid is evaluated to give the geodetic longitude and latitude. Finally, timing conventions are discussed (Section 6.6).

The exact spacecraft level geometric calibration algorithm definition is the responsibility of the SSPR and should be used for all NPP/NPOESS instrument payloads. This algorithm, and the coordinate systems it uses, is liberally outlined here to provide some overview of the end-to-end process.

This section thus focuses on sensor level geometric calibration up to the spacecraft reference frame.

The overall geometric calibration process is summarized by the P-diagram shown on Figure 49.

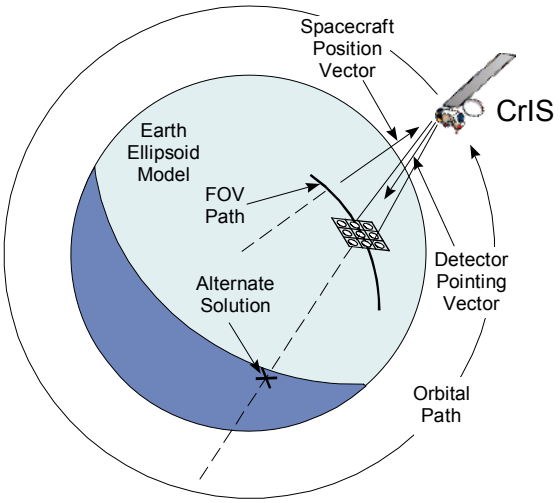

Figure 47: Geometry of the detector field of view and Earth ellipsoid intersection

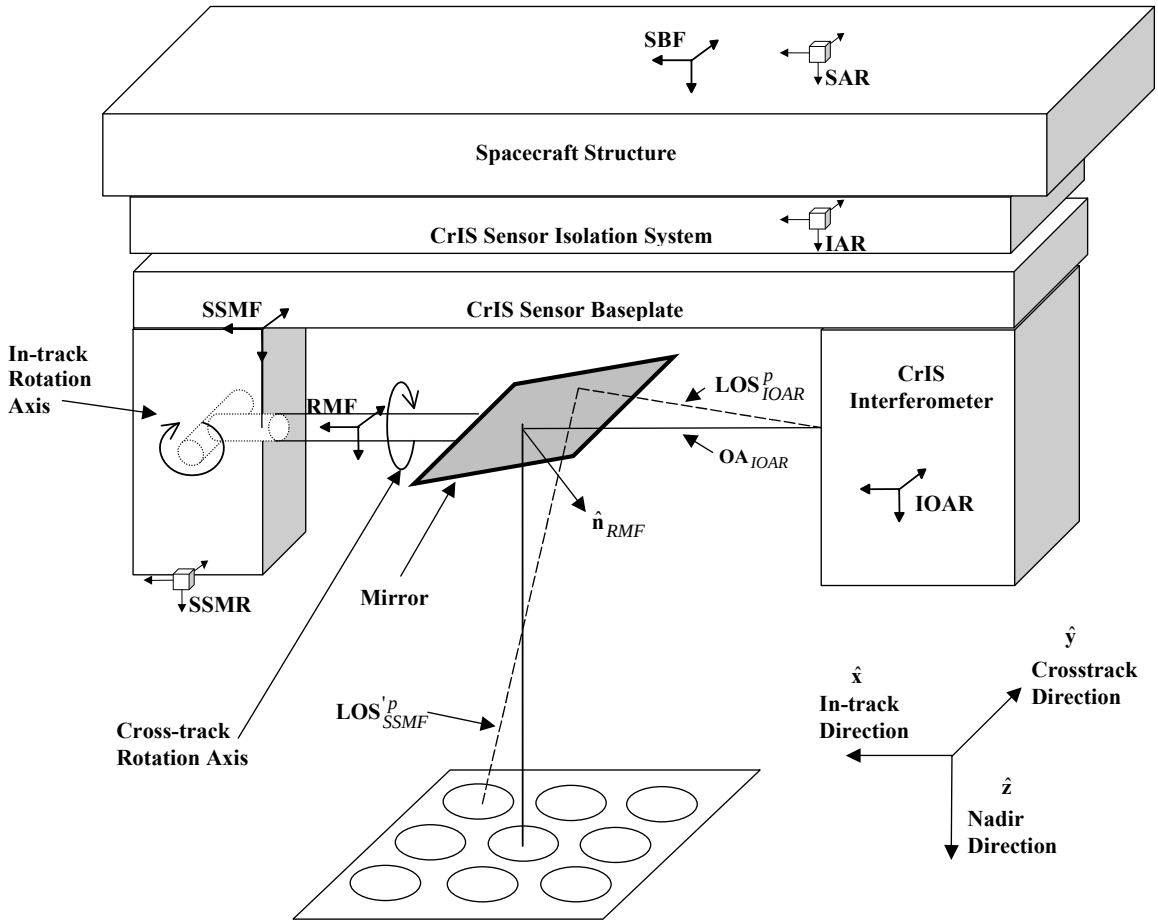

Figure 48: Sensor Algorithm Level Coordinate Systems

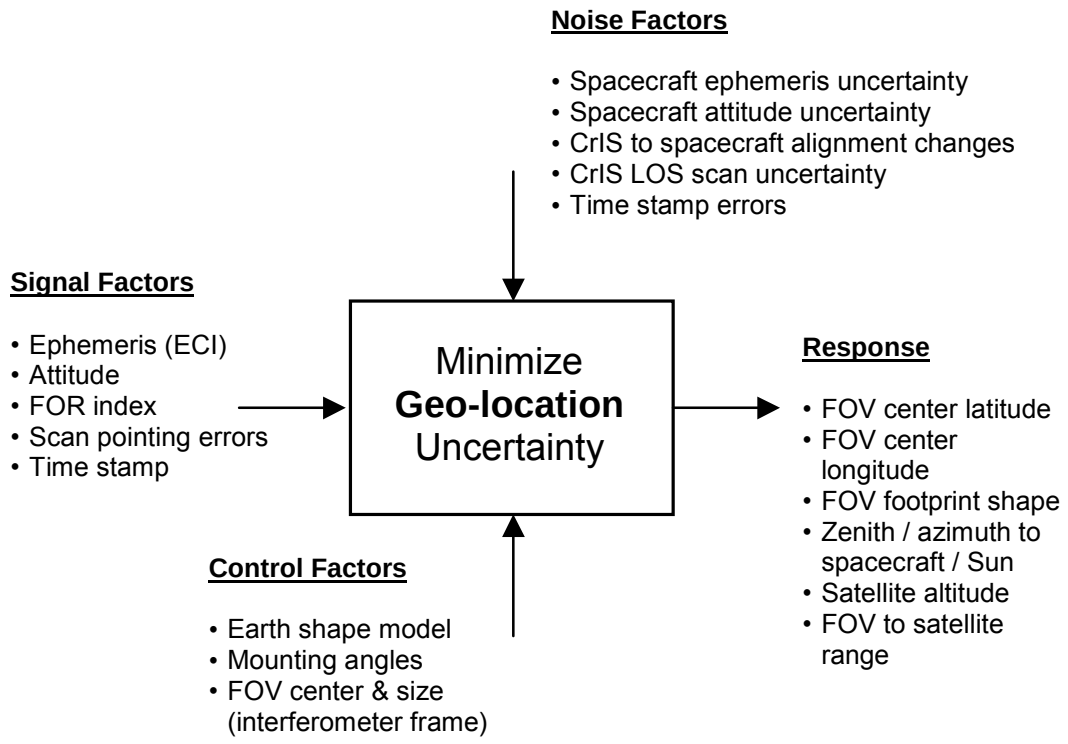

Figure 49: Geometric Calibration Parameter Diagram

6.1 COORDINATE SYSTEMS

This section describes coordinate systems that must be defined in order to achieve geometric calibration. A generic definition of coordinate systems is first given. A description of all required coordinates systems is presented in separate sub-sections, that is:

Sensor level algorithm coordinate systems:

Interferometer Optical Axis Reference (IOAR)

Rotating Mirror Frame (RMF)

Scene Selection Mirror mounting feet Frame (SSMF)

Scene Selection Module Reference (SSMR)

Instrument Alignment Reference (IAR)

Spacecraft Body Frame (SBF) defined by the Spacecraft Alignment Reference (SAR)

Spacecraft level algorithm coordinate systems:

Orbital Coordinate System (OCS)

Earth Centered Inertial (ECI)

Earth Centered Earth Fixed (ECEF) or Earth Centered Rotating (ECR)

World Geodetic System 1984 (WGS84)

Topocentric-Horizon Coordinate System (THCS)

6.1.1 Coordinate System Definition

All coordinate systems are XYZ orthogonal reference frames. One way of specifying these three reference axes is to define them with vectors perpendicular to surfaces of a reference cube (Figure 50). The XYZ labeling of the axes follows the right-handed convention; the X and Y axes are perpendicular and define a plane, the Z axis is given by the cross-product of the X and Y axes.

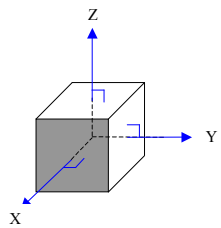

Figure 50: Coordinate System Defined By Reference Cube

6.1.2 Interferometer Optical Axis Reference (IOAR)

The IOAR coordinate system is defined by two mutually orthogonal vectors that define the plane perpendicular to the interferometer optical axis (OA). To ease the conversion to the other coordinate systems, the optical axis is defined along the +X axis (instead of the more standard +Z axis). This reference frame is used to define the line-of-sight vectors relative to the interferometer optical axis (see Figure 48). This frame is slightly misaligned with respect to the SSMF (see Section 6.1.4).

6.1.3 Rotating Mirror Frame (RMF)

The RMF coordinate system is defined by the X axis being along the SSM cross-track rotation axis, and by the Y axis being along the in-track rotation axis when the cross-track angle is zero. The third axis Z is given by the cross product of the X and Y axes. The SSM mirror orientation is fixed in this coordinate system and rotates with it. This reference frame is introduced to account for mounting errors of the 45 degree inclined mirror relative to the cross-track rotational axis. By definition, this frame coincides with the SSMF (see Section 6.1.4) when in-track and cross-track rotation angles are both zero (see Figure 48).

6.1.4 Scene Selection Mirror Mounting Feet Frame (SSMF)

The SSMF coordinate system contains the rotation mechanisms. By definition, the in-track rotation axis is fixed along the Y axis of this coordinate system, while the cross-track rotation axis is along its X axis when the in-track rotation angle is zero. The third axis Z is given by the cross-product of the X and Y axes (see Figure 48). This reference frame is fixed with respect to SSMR (see Section 6.1.5) and is used to perform all calculations that account for the motion of the SSM mirror.

6.1.5 Scene Selection Module Reference (SSMR)

The SSMR coordinate system is defined by a reference optical cube mounted on the CrIS SSM. This cube is used to measure the orientation of the SSM relative to the CrIS IAR (see Section 6.1.6 and Figure 48).

6.1.6 Instrument Alignment Reference (IAR)

The IAR is defined by a reference optical cube mounted on the CrIS instrument optical bench. This cube is used to measure the orientation of the CrIS instrument relative to S/C body frame (SBF) (see Section 6.1.7 and Figure 48). The calibration of this orientation is performed after the CrIS sensor is mounted to the satellite frame.

6.1.7 Spacecraft Body Frame (SBF)

The SBF is located at the spacecraft center of mass. It is defined by the spacecraft alignment reference (SAR) optical cube mounted on the spacecraft body frame (see Figure 48).

6.1.8 Orbital Coordinate System (OCS)

In the orbital coordinate system, the X and Z axes define orbital plane. The +Z axis always points towards geocentric Earth center. The +X axis is normal to Z and in nominal velocity direction. The Y axis complete the right-handed coordinate system ($Y = Z \times X$).

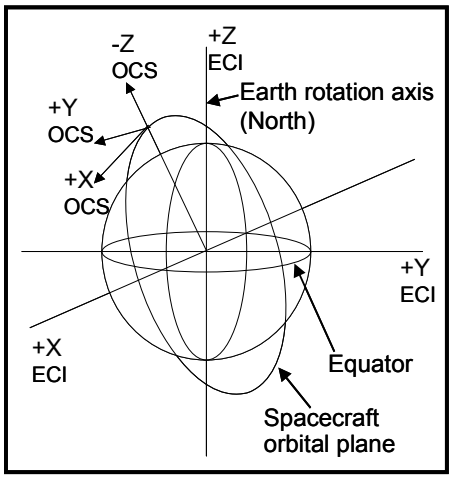

Figure 51: Orbital Coordinate System (OCS)

6.1.9 Earth Centered Inertial (ECI)

In the Earth centered inertial coordinate system the origin is at the earth center of mass, the +X axis passes through the Sun center during vernal equinox (first day of spring).

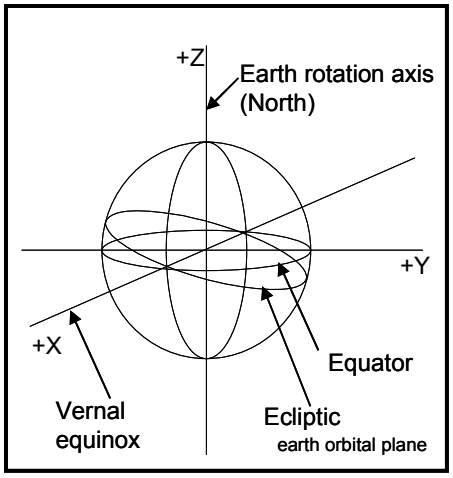

Figure 52: Earth Centered Inertial (ECI)

6.1.10 Earth Centered Earth Fixed (ECEF) or Earth Centered Rotating (ECR)

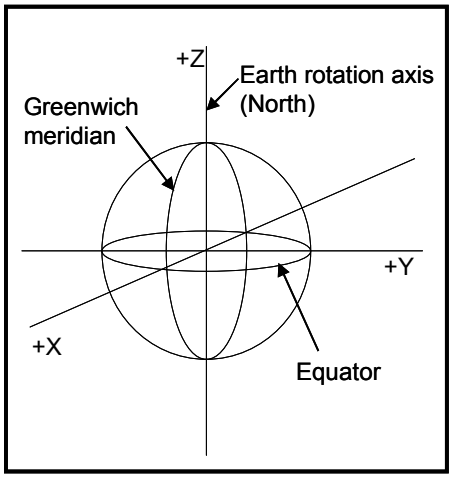

Figure 53: Earth Centered Earth Fixed (ECEF) or Earth Centered Rotating (ECR)

The ECR coordinate system rotates with the Earth. Angles in this coordinate system are computed relative to Earth center and do not exactly correspond to latitude and longitude.

6.1.11 World Geodetic System 1984 (WGS84)

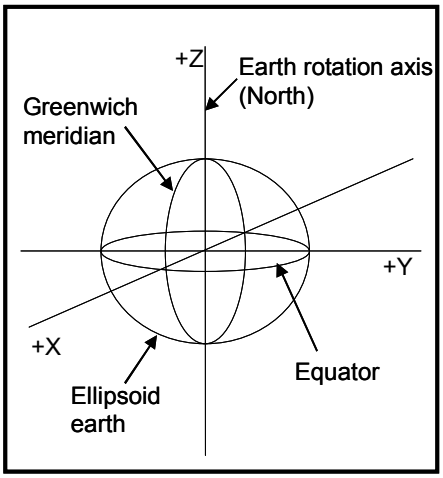

Figure 54: World Geodetic System 1984 (WGS84)

The WGS84 coordinate system accounts for the non-circular Earth shape at sea level. Angles intersecting the Earth surface in this model correspond to geodetic latitude and longitude.

6.1.12 Topocentric-Horizon Coordinate System (THCS)

In the topocentric-horizon coordinate system, the geodetic latitude and longitude defines the observer position. The azimuth is measured clockwise from North (-X) about the Z axis. The zenith is measured relative to +Z axis.

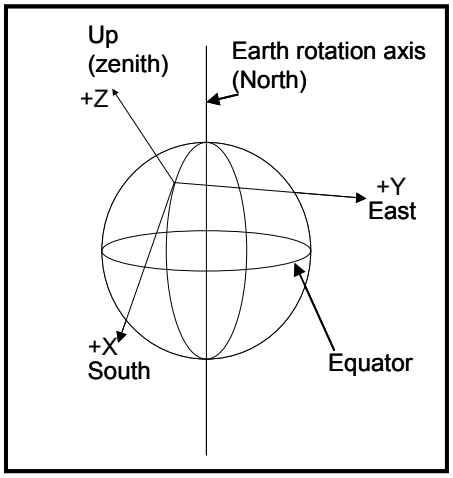

Figure 55: Topocentric-Horizon Coordinate System (THCS)

6.2 COORDINATE SYSTEM TRANSFORMATIONS

Given a coordinate system (X_1, Y_1, Z_1) we can align its axes on a second coordinate system (X_2, Y_2, Z_2) by defining three transformations (Euler's theorem). In 3D Cartesian space, orthogonal matrices expressing rotations about the three axes can represent these transformations. Adopting a terminology used to describe the spatial orientation (or attitude) of a given moving vehicle, we will refer to rotations about the (X, Y, Z) axes as (Roll, Pitch, Yaw)[2] respectively. Here, the right-hand convention is adopted (see Figure 56).

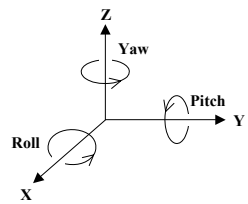

Figure 56: Roll, Pitch and Yaw Rotations

Therefore, the alignment of a coordinate system (X_1, Y_1, Z_1) on a second coordinate system (X_2, Y_2, Z_2) can be generally expressed as (xyz convention in Goldstein [RD 33]):

$$\mathbf{T}_{X_2Y_2Z_2/X_1Y_1Z_1} = \mathbf{R}_X(\psi)\mathbf{P}_Y(\theta)\mathbf{Y}_Z(\phi). \tag{86}$$

where $\mathbf{T}_{X_2Y_2Z_2/X_1Y_1Z_1}$ is the resulting transformation operator and the rotation matrices are given by:

$$\mathbf{R}_X(\psi) = \begin{bmatrix} 1 & 0 & 0 \\ 0 & \cos(\psi) & -\sin(\psi) \\ 0 & \sin(\psi) & \cos(\psi) \end{bmatrix}, \tag{87}$$

$$\mathbf{P}_Y(\theta) = \begin{bmatrix} \cos(\theta) & 0 & \sin(\theta) \\ 0 & 1 & 0 \\ -\sin(\theta) & 0 & \cos(\theta) \end{bmatrix}, \tag{88}$$

$$\mathbf{Y}_Z(\phi) = \begin{bmatrix} \cos(\phi) & -\sin(\phi) & 0 \\ \sin(\phi) & \cos(\phi) & 0 \\ 0 & 0 & 1 \end{bmatrix}. \tag{89}$$

The rotations can be interpreted in two complementary ways: a rotation of a vector in the directions defined (*active*) or a rotation of the coordinate axes in the opposite direction (*passive*). From equation (83), adopting the *passive* interpretation, note that the first rotation ($\mathbf{Y}_Z(\phi)$) is performed around the

[2] These are sometimes referred to as the Tait-Bryand angles.

original coordinate system, but the two other rotations $\mathbf{R}_X(\psi)\mathbf{P}_Y(\theta)$ are performed around the transformed coordinate systems.

6.3 ALGORITHM PARTITIONING

As illustrated in Figure 57 below, the geometric calibration algorithm is divided in two parts. The sensor specific algorithm computes CrIS LOS vectors in SBF at given UTC time. The spacecraft level algorithm computes the intersection of those LOS vectors with the Earth ellipsoid to give geodetic longitude and latitude at given UTC time.

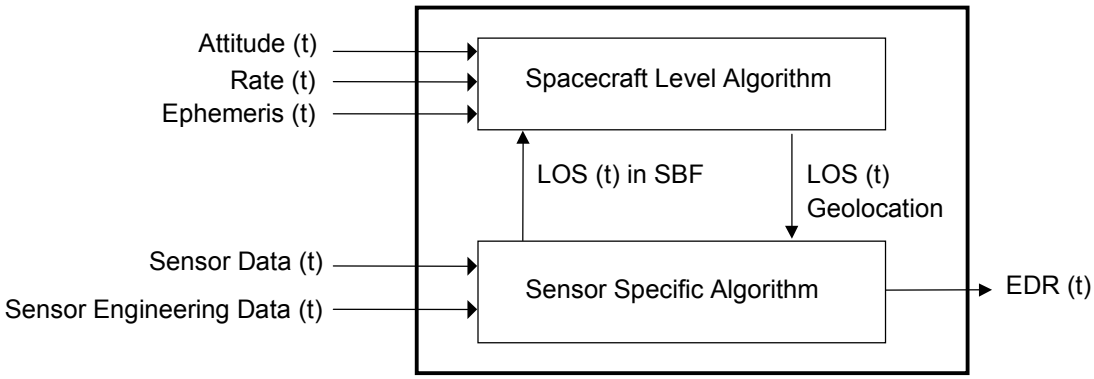

Figure 57: Geometric Calibration Algorithm Partitioning

Here is a detailed description of the required Sensor and Engineering data:

Sensor Data:

SSM in-track and cross-track servo errors (2 angles from Science TLM packet)

UTC time stamp (from IGM packet)

FOR and FOV indexes (from IGM packet)

Engineering Data:

Time stamp bias (Time that must be added to the time stamp in interferogram packet data in order to get time that the SSM in-track is pointing at null position).

– FOR index to in-track (pitch) and cross-track (roll) angles relative to nadir (SSMF) look up table (SSMF, 30x2 angles)

SSM Scan Plane, Optical Reference, and Static Optical Measurement test (TP8195887) provides alignment measurements of the SSM optical line of sight for <u>seven scan positions</u> and also LOS position corresponding to the “In-track torque null” offset of the mechanism.

The seven calibrated positions are interpolated to the 30 earth positions. The cross-track and in-track position errors are calculated.

The in-track offsets due to nodding for the 30 earth positions are calculated for the nodding motion centered about the “torque null”

A tool has been developed to perform the above calculations and to provide the high quality LOS data for 30 earth locations (30 in-track values and 30 cross-track values) by combining positional errors and in-track offsets derived above from test data

LW FOV offset angles (pitch and yaw) relative to LW FOV 5 LOS (IOAR, 9x2 angles)

LW FOV5 LOS offset angles (pitch and yaw) relative to interferometer bore sight (IOAR, 2 angles)

Pitch and yaw misalignments of interferometer optical axis (IOAR) relative to scan mechanism (SSMF, 2 angles)

Scene selection mirror mounting feet frame (SSMF) to SSMR optical cube offset angles (SSMR, 3 angles)

SSM optical cube to IAR optical cube offset angles (IAR, 3 angles)

IAR optical cube to SBF (SAR optical cube) offset angles (SBF, 3 angles)

Pitch and yaw misalignments of interferometer optical axis (IOAR) relative to scan mechanism, SSMF angles θ_{RMF} *and* ϕ_{RMF} :

When in-track (pitch) and cross-track (roll) angles are derived from test data, they include the effects of scan mirror misalignments with respect to its shaft and the yaw misalignments of the shaft with respect to the SSMMF. CrIS SDR geo-location algorithm has been re-designed based on the cross-track and in-track angles derived from test measurements. Therefore, RMF rotation angles θ_{RMF} *and* ϕ_{RMF} are zero and are no longer included in the engineering packet.

6.4 SENSOR SPECIFIC ALGORITHM

The goal of the sensor specific algorithm is to compute CrIS line-of-sight vectors in the S/C body frame at any given time. The algorithm steps are as follows (see Figure 48 for reference):

1. Compute CrIS FOV LOS in SSMF coordinate system

   Get current FOR (i) and FOV (p) indexes

   Express normal to SSM mirror in RMF coordinate system ($\hat{\mathbf{n}}_{RMF}$)

   Compute normal to SSM mirror in SSMF (fixed coordinate system) by applying rotations from actual LOS positions with respect to SSMF and servo errors (in-track and cross-track) The cross-track servo error count is linearly transformed into microradians which is added to the commanded angle.

   Express FOV LOS in IOAR (Apply rotations on IOA to get FOV LOS for pixel p)

   Apply IOAR-SSMF transformation to account for pitch and yaw misalignments between interferometer and scan mechanism

   Compute reflected FOV LOS using mirror normal in SSMF

2. Compute SSMF to SBF transformation operator
3. Compute CrIS FOV LOS in SBF coordinate system

6.4.1 CrIS FOV LOS in SSMF Coordinate System

The CrIS line-of-sight angles must be derived from FOV offset angles measurements, the alignment of SSM to interferometer bore sight and cross-track angle for a given FOR index in engineering packet. In-track and cross-track servo errors, reported in science telemetry packet, must also be taken into account.

1. Express normal to SSM mirror in RMF coordinate system, assuming that the mirror is perfectly mounted at 45 degrees:

$$\hat{\mathbf{n}}_{RMF} = \frac{1}{\sqrt{2}}\begin{bmatrix} -1 \\ 0 \\ 1 \end{bmatrix}. \tag{90}$$

2. Because RMF rotational angles θ_{RMF} and ϕ_{RMF} are zero,

$$\hat{\mathbf{n}}'_{RMF} = \mathbf{P}(\theta_{RMF})\mathbf{Y}(\phi_{RMF})\hat{\mathbf{n}}_{RMF} = \hat{\mathbf{n}}_{RMF}. \tag{91}$$

3. Compute normal to SSM mirror in SSMF (fixed coordinate system) by applying rotations from actual cross-track angle, actual in-track bias angle and servo errors (in-track and cross-track). The cross-track servo error count is linearly transformed into microradians which is then added to the commanded angle. This gives:

$$\hat{\mathbf{n}}^{i}_{SSMF} = \mathbf{P}(\psi^{i}_{SSMF})\mathbf{R}(\phi^{i}_{SSMF})\hat{\mathbf{n}}'_{RMF}. \tag{92}$$

where i is the FOR index, ψ^{i}_{SSMF} is the sum of the actual in-track bias and in-track servo error angles, ϕ^{i}_{SSMF} is the sum of the actual cross-track and cross-track servo error angles and $\hat{\mathbf{n}}^{i}_{SSMF}$ the mirror normal in SSMF coordinate system. The FOVs rotation angle offsets are consistent with those used for computing the self-apodization function of section 3.6.

Express FOV LOS in IOAR (apply rotations on optical axis to get FOV LOS for pixel p):

$$\mathbf{LOS}^{p}_{IOAR} = \mathbf{P}(\theta^{LW,p}_{IOAR})\mathbf{Y}(\phi^{LW,p}_{IOAR})\mathbf{OA}_{IOAR} \tag{93}$$

where $\mathbf{OA}_{IOAR}$ is the optical axis vector (from the interferometer bore sight), $\theta^{LW,p}_{IOAR}$ and $\phi^{LW,p}_{IOAR}$ are the sum of the FOV5 offset and pixel p angle relative to the optical axis (in-track and cross-track angles after reflection respectively) and $\mathbf{LOS}^{p}_{IOAR}$ the line-of-sight vector for pixel p.

4. Apply IOAR-SSMF transformation to account for pitch and yaw misalignments between interferometer and scan mechanism:

$$\mathbf{LOS}^{p}_{SSMF} = \mathbf{P}(\theta_{SSMF})\mathbf{Y}(\phi_{SSMF})\mathbf{LOS}^{p}_{IOAR}. \tag{94}$$

5. Compute reflected FOV LOS using mirror normal in SSMF

$$\mathbf{LOS}'^{p,i}_{SSMF} = \mathbf{LOS}^{p}_{SSMF} - 2(\mathbf{LOS}^{p}_{SSMF} \bullet \hat{\mathbf{n}}^{i}_{SSMF})\hat{\mathbf{n}}^{i}_{SSMF}. \tag{95}$$

6.4.2 SSMF to SBF Transformation Operator

The Scene Selection Mirror mounting feet Frame to S/C body frame transformation can be expressed as follows:

$$\mathbf{T}_{SBF/SSMF} = \mathbf{T}_{SBF/IAR}\mathbf{T}_{IAR/SSMR}\mathbf{T}_{SSMR/SSMF}. \tag{96}$$

where the transformation operators on the right hand side of equation (96) are constructed according the generic coordinate system transformation given in equation (86), using the adequate set of offset angles.

6.4.3 CrIS FOV LOS in SBF Coordinate System

In SBF, a CrIS FOV LOS of a given FOR location can be obtained using:

$$\mathbf{LOS}'^{p,i}_{SBF} = \mathbf{T}_{SBF/SSMF}\mathbf{LOS}'^{p,i}_{SSMF} \tag{97}$$

The line-of-sight vectors can also be expressed in terms of a pitch and a roll with respect to the SBF nadir unit vector[3], that is:

$$\mathbf{LOS}'^{p,i}_{SBF} = \mathbf{R}(\psi^{p,i}_{SBF})\mathbf{P}(\theta^{p,i}_{SBF})\hat{\mathbf{z}}_{SBF}\ . \tag{98}$$

Solving for the pitch and roll angles we get:

$$\begin{aligned} \theta^{p,i}_{SBF} &= -\sin^{-1}(x), \\ \psi^{p,i}_{SBF} &= \tan^{-1}(y/z), \end{aligned} \tag{99}$$

where x, y and z are the rectangular coordinates of the line-of-sight vectors $\mathbf{LOS}'^{p,i}_{SBF}$.

The Figure 58 shows the CrIS FOVs at nadir (FOR position #33 used during tests on the ground) and at cross-track scan position FOR #1 when projected on a plane at an altitude of 833 km.

Note: Although the SDR Algorithm can compute the CrIS LOS relative to the spacecraft body frame, this feature is not currently in use. Instead, the CrIS LOS is reported relative to the CrIS instrument frame defined by the orthogonal cube surfaces of the optical cube mounted to the CrIS optical bench. Zero data entered into the CrIS engineering packet for the SBF to IAR frame transformation causes no coordinate transformation to be performed relative to the spacecraft body frame even though the matrix calculation is performed.

[3] Note that the SBF will not exactly point at nadir. But this will be taken into account by the offset angles between the SAR optical cube and the spacecraft attitude determination reference frame and the spacecraft attitude itself.

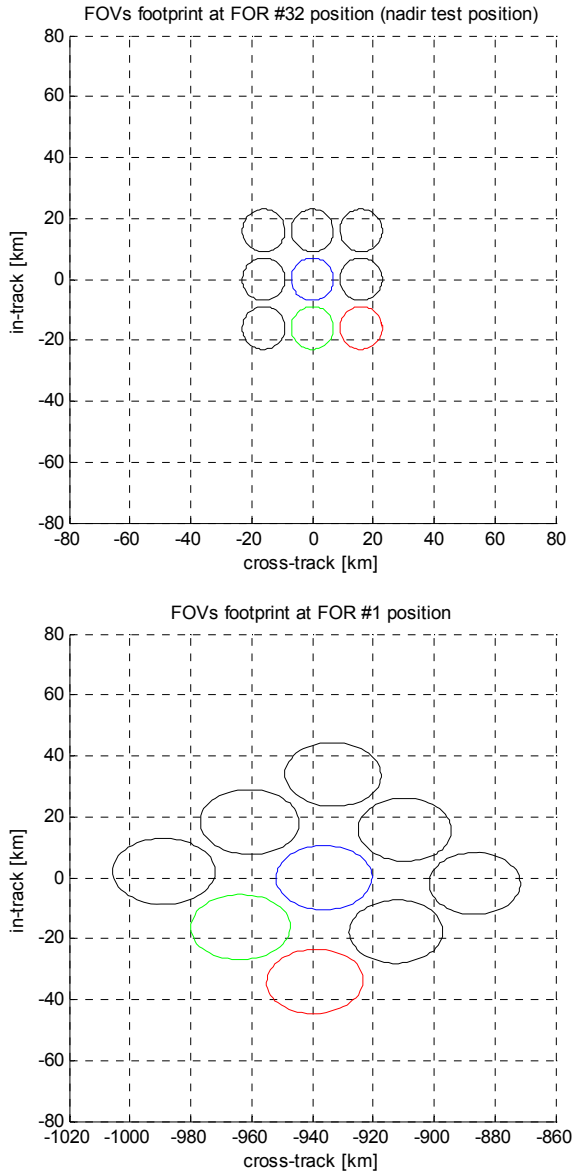

Figure 58: Sample of CrIS FOVs Footprint on a Perfect Plane

6.5 SPACECRAFT LEVEL ALGORITHM

The goal of the spacecraft level algorithm is to compute the intersection of the CrIS line-of-sight vectors referenced to the instrument frame with the Earth ellipsoid to give the geodetic longitude and latitude in each FOV. This algorithm is the responsibility of the spacecraft integrator as agreed to in [RD 52].

6.6 TIMING CONVENTIONS

A time stamp is inserted into the secondary header of every CrIS RDR data packet. This time stamp corresponds to the 200 msec sync immediately following every interferogram data collection. For purposes of geolocation, this time stamp must be adjusted to correspond to the actual orbit time when the CrIS in-track FOV footprint points to null position. Typically, this occurs approximately 84 msec prior to the time stamp value transmitted in the RDR. The precise value of this time stamp bias adjustment is placed into the CrIS engineering packet.

When interferograms are processed through the SDR algorithm, the same time stamp appearing in the RDR is also placed into the SDR secondary header. The time stamp for geolocation purposes is computed separately and placed into a special field in the body of the SDR output.

7. MODULES DEFINITION

This section summarizes the key processing steps necessary to transform RDRs into SDRs. The overall processing chain can be partitioned into modules listed below. More details about the architectural design necessary to fully implement SDR algorithms are presented elsewhere [RD 30].

1. Initialization
   - Software initialization, the algorithm needs a one-time initialization
2. Input Data Handling
   - Low level and configuration data handling for software
   - Calibration and science data handling
3. Preprocessing
   - Interferogram to spectrum transformation
   - Moving average handling
   - Non-Linearity Correction
4. Spectral Calibration
   - Laser wavelength calibration from neon lamp data
   - Laser wavelength drift monitoring
   - Spectral axis labeling and alias unfolding
5. Radiometric Calibration
   - ICT radiance calculation
   - Complex calibration (removes instrument induced offset and phase)
   - Polarization correction (if necessary)
   - Spectrum correction (applies the correction matrix operator (CMO) to remove ILS errors, to apply user selectable apodization, and to map channels to fixed wavenumber grid)
6. Geolocation
   - FOV LOS calculation relative to spacecraft body frame
7. Quality Control
   - NEdN estimation
   - Metrology wavelength monitoring
   - Temperatures monitoring
   - FCE handling
8. Post-processing
   - User required spectral bins selection
   - SDR data formatting
9. Output Data Handling

The conventions used for the flowcharts shown in this section are described below:

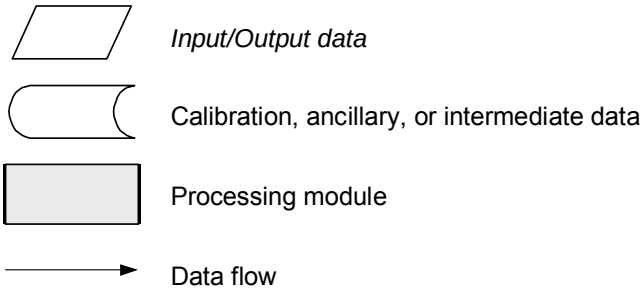

Shown on Figure 59 is the overall data processing chain necessary to transform raw interferograms into spectrally and radiometrically calibrated and corrected spectra. A more detailed description of the key processing steps is given in the following sections.

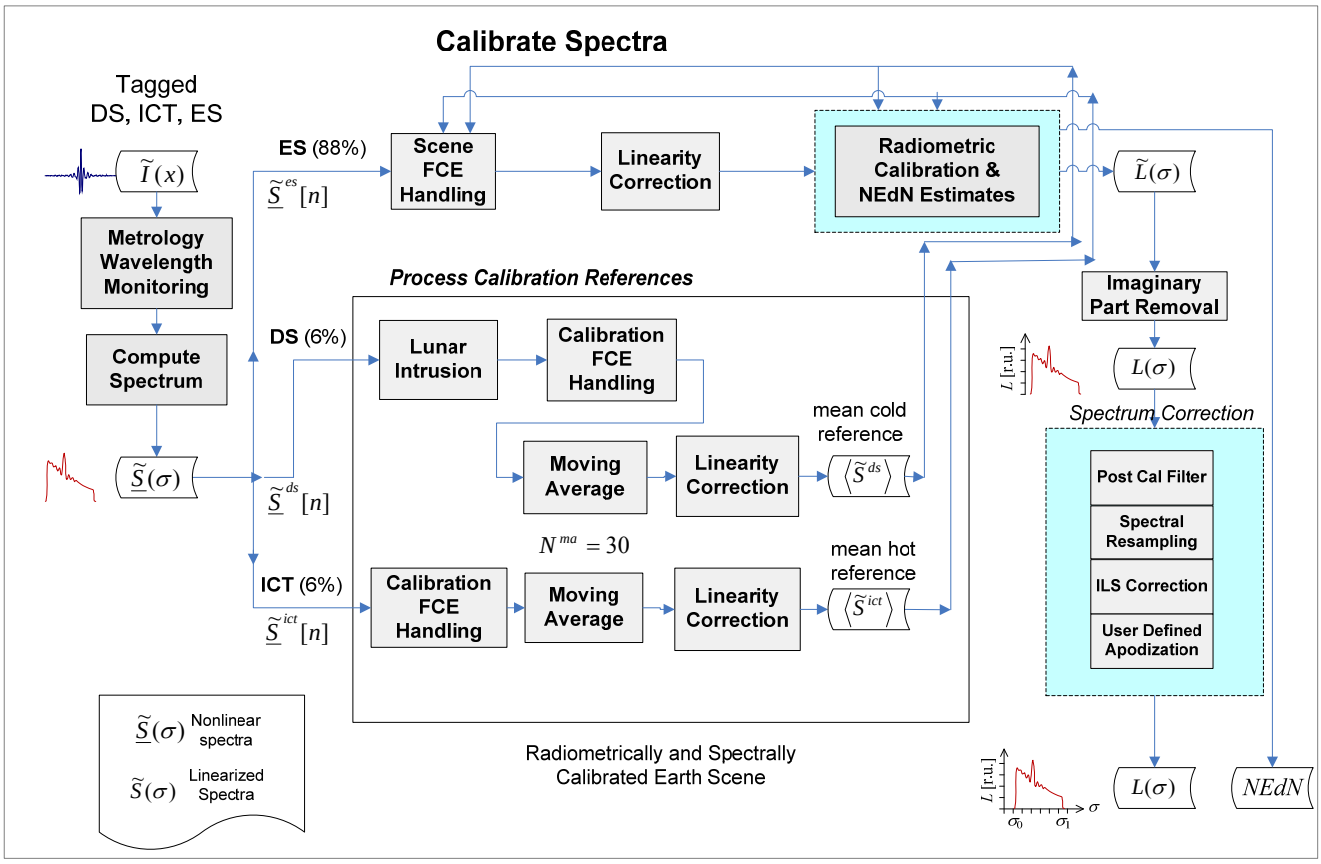

Figure 59: General flow diagram for the radiometric and spectral calibration

7.1 INITIALIZATION

This module is intended for software initialization. The algorithm needs a one time initialization. Data used by the SDR algorithm is initialized by means of a configuration file and receipt of an engineering packet from the CrIS sensor. The content of these files is described in the tables below. A more detailed listing of engineering data packet parameter formats can be found in the CrIS Command and Data Packet Dictionary (ITT Document 8196185).

Table 17: Tunable Parameters Reported via the Four Minute Engineering Telemetry RDR

Parameter	Comments
Effective Neon Bulb Wavelength for LWIR	Used in the computation of the laser frequency using Neon calibration data.
Effective Neon Bulb Wavelength Offsets for MWIR and SWIR	ppm offsets from LWIR value for MWIR and SWIR bands.
ILS curve fit parameters	Used to correct for modulation efficiency variation with OPD
ILS FOV offset and size parameters	Use to correct of off-axis pixel self apodization effects
Nonlinearity Correction Parameters	V_{inst}, $a_{2,}$, interferometer modulation efficiency, PGA Gains and PGA conversion factors for each detector channel. FIR Filter Gains in each band relative to FM1 sensor
LW ICT Emissivity table	Wavenumber specific effective emissivities (650 – 1095 cm-1) end point emissivity values are extended into guard band
MW ICT Emissivity table	Wavenumber specific effective emissivities (1210 – 1750 cm-1) end point emissivity values are extended into guard band
SW ICT Emissivity table	Wavenumber specific effective emissivities (2155 – 2550 cm-1) end point emissivity values are extended into guard band
Polarization Calibration	% Polarization difference relative to ICT at a specific wavenumber
Polarization Wave Numbers	Wavenumbers at which polarization calibration information is provided
ICT environment model	Surface emissivities and view factors of instrument surfaces viewed by ICT & included in the ICT radiance calculation. Scan baffle temperature gradient information versus orbit time from North Pole
Orbit Period	Duration in seconds of one orbit
Science TLM conversion coefficients	Engineering unit conversion coefficients associated with parameters monitored in eight second science/calibration telemetry RDR

Parameter	Comments
Science TLM Limits	Limits associated with parameters monitored in eight second science/calibration telemetry RDR
Mapping Parameters	
SSM cross track positions	Angles relative to SSM mounting feet
SSM mirror misalignment	Mirror mount pitch and yaw errors
SSM in-track position	In-track commanded null offset
SSMR, SSMF, IAR , IFM bore sight & SBF alignments	Alignment angles
Time stamp bias	Bias added to interferogram time stamp to account for in-track motion compensation. SDR packet time stamp plus bias offset is the orbit time that defines FOV geolocation
CrIS Bit Trim Mask LW	Used to reverse the bit trimming of interferogram packets
CrIS Bit Trim Mask MW	Used to reverse the bit trimming of interferogram packets
CrIS Bit Trim Mask SW	Used to reverse the bit trimming of interferogram packets
LW Data Extraction Information	
Number of A/D samples	Used to reverse the bit trimming of interferogram packets
Decimation & number of filter taps	Used to reverse the bit trimming of interferogram packets
MW Data Extraction Information	
Number of A/D samples	Used to reverse the bit trimming of interferogram packets
Decimation & number of filter taps	Used to reverse the bit trimming of interferogram packets
SW Data Extraction Information	
Number of A/D samples	Used to reverse the bit trimming of interferogram packets
Decimation & number of filter taps	Used to reverse the bit trimming of interferogram packets

In addition to the parameters provided through the instrument RDRs, there are many configuration options that modify the processing performed by the SDR Algorithm. These values are modified via the configuration files provided by DMS. Table 18 summarizes the SDR Algorithm operating parameters that are defined in a configuration file at application startup.

Table 18: Tunable Parameters Provided via Configuration Files

Configuration file Mnemonic	Description
allowCalibrationTargetDataMissing	**Allows for missing ICT/DS reference measurements**
allowEngineeringDataPacketsMissing	**Allows for missing engineering packets**
allowScienceTlmDataMissing	**Allows for missing 8-second science packets**
allowSpaceTargetTemperatureDataMissing	**Allows for missing space target data**
calibrationTargetDataValidityDuration	**Absolute temporal displacement to ES under calibration**
calibrationTargetDataValidityDurationTolerance	**Max temporal displacement of FOR under calibration**
disableTimeStampBasedMovingWindow	Adds additional constraints to packet timing
dsTemperatureOrigin	Specifies origin for file
elapsedTimeForValidScienceTlmData	Absolute temporal displacement to ES under calibration
elapsedTimeForValidSpaceTargetTemperature	Max temporal displacement of FOR under calibration
ictEmissivityOrigin	Specifies emissivities are used from main config file
instrumentTemperatureOrigin	Specifies source of value
maximumNumberOfFceTriesDuringIctDsSynchronization	Max fringe counts to try in both directions
maximumNumberOfIctDsSynchronizationTries	Max ES window depth to seek valid measurement
scienceTlmTimeDifferenceTolerance	Absolute temporal displacement
skipIctDsPhaseSynchronization	Phase aligns initial ICT/DS reference windows
spaceTargetTemperatureTimeDifferenceTolerance	Max temporal displacement for temperature correlation
useDeepSpaceRadiance	Specifies calibration equation to consider cold target radiance contribution
useIctEnvironmentalCorrectionModel	Sets ICT temp to include component contributions
suppressSsmBaffleProfile	Turns SSM baffle temp correction ON/OFF
useWavenumberDependentDsEmissivity	Specifies emissivities are used from main config file
useWavenumberDependentIctEmissivity	Specifies emissivities are used from main config file
monitorLunarIntrusion	Discards DS measurements above a threshold
maxLunarRadianceRatio	Discards DS measurements above this threshold
referenceSceneWindowSize	number of reference scenes to average
earthSceneWindowSize	minimum number of earth scenes
validWindowSize	minimum number of valid references needed in window to declare valid data
apodizationType	Apodization (none, Hamming, Blackman-Harris)
applyIlsFovEffectsCorrection	Specifies the application of ILS corrections
applyIlsResidualEffectCorrection	Specifies the application of ILS residual corrections
applyPolarizationCorrections	Specifies the application of scene specific corrections
applyPostCalibrationFilterMatrixCorrection	Specifies the application of matrix correction
applyResamplingMatrix	Specifies the application of resampling corrections
disableLaserMonitoring	Specifies the monitoring for laser drift
edrLwDeltaSigma	Specifies wavenumber spacing for Resampling for LW
edrLwMaximumWavenumber	Specifies the high clipping range for LW See Note
edrLwMinimumWavenumber	Specifies the low clipping range for LW See Note
edrLwNumberOfPoints	Specifies the number of points in range for LW See Note

Configuration file Mnemonic	Description
edrMwDeltaSigma	Specifies wavenumber spacing for Resampling for MW
edrMwMaximumWavenumber	Specifies the high clipping range for MW See Note
edrMwMinimumWavenumber	Specifies the low clipping range for MW See Note
edrMwNumberOfPoints	Specifies the number of points in range for MW See Note
edrSwDeltaSigma	Specifies wavenumber spacing for Resampling for SW
edrSwMaximumWavenumber	Specifies the high clipping range for SW See Note
edrSwMinimumWavenumber	Specifies the low clipping range for SW See Note
edrSwNumberOfPoints	Specifies the number of points in range for SW See Note
impulseNoiseCountThreshold	Specifies limit to flag
laserDiodeWavelengthOrigin	Identifies the source for measurement (telemetry or config)
performFringeCountErrorHandling	Enables FCE Handling
useSavedMatrices	Allows for use of saved matrices
clipGuardBands	Set to clip guard bands
forIdentifierDs	Specifies the FOR of the DS reference measurement
forIdentifierIct	Specifies the FOR of the ICT reference measurement
forwardSweepDirectionLabel	“F” for Forward by convention
forwardSweepDirectionIdentifier	“0” by convention
laserDiodeWavelength	Laser wavelength used in place of TLM (LWIR)
laserDiodeWavelengthOffsetMW	ppm offset used to compute MWIR laser wavelength in place of TLM
laserDiodeWavelengthOffsetSW	ppm offset used to compute SWIR laser wavelength in place of TLM
lwBandLabel	“LW”
lwBenchMeanIctEmissivity	LW ICT Emissivity (Instrument Location = Bench)
lwChamberMeanIctEmissivity	LW ICT Emissivity (Instrument Location = Chamber)
lwDataPointsDecimatedInterferogram	LW data points decimated
lwDataPointsUndecimatedInterferogram	LW data points undecimated
lwDecimationFactor	LW decimation factor
mwBandLabel	“MW”
mwBenchMeanIctEmissivity	MW ICT Emissivity (Instrument Location = Bench)
mwChamberMeanIctEmissivity	MW ICT Emissivity (Instrument Location = Chamber)
mwDataPointsDecimatedInterferogram	MW data points decimated
mwDataPointsUndecimatedInterferogram	MW data points undecimated
mwDecimationFactor	MW decimation factor
numberFOR	Number of FOR
numberFOV	Number of FOV
numberSamplesPerLaserWavelength	Number of samples per wavelength
numberSpectralBands	Number of spectral bands
reverseSweepDirectionIdentifier	“1” by convention
reverseSweepDirectionLabel	“R” for reverse
spaceTargetTemperatureDriftLimit	Specifies limit to flag
swBandLabel	“SW”
swBenchMeanIctEmissivity	SW ICT Emissivity (Instrument Location = Bench)
swChamberMeanIctEmissivity	SW ICT Emissivity (Instrument Location = Chamber)
swDataPointsDecimatedInterferogram	SW data points decimated
swDataPointsUndecimatedInterferogram	SW data points undecimated
swDecimationFactor	SW decimation factor
engineeringCalibrationFrameType	The frame type of the CCSDS Engineering packet

Configuration file Mnemonic	Description
scienceCalibrationFrameType	The frame type of the CCSDS Science packet
surfaceEmissivityCoeff_C0	No longer used
surfaceEmissivityCoeff_C1	No longer used
surfaceEmissivityCoeff_C2	No longer used
surfaceEmissivityCoeff_C3	No longer used
LinErr_a2_LW1	Nonlinearity correction coefficient used in place of engineering TLM
LinErr_a2_LW2	Nonlinearity correction coefficient used in place of engineering TLM
LinErr_a2_LW3	Nonlinearity correction coefficient used in place of engineering TLM
LinErr_a2_LW4	Nonlinearity correction coefficient used in place of engineering TLM
LinErr_a2_LW5	Nonlinearity correction coefficient used in place of engineering TLM
LinErr_a2_LW6	Nonlinearity correction coefficient used in place of engineering TLM
LinErr_a2_LW7	Nonlinearity correction coefficient used in place of engineering TLM
LinErr_a2_LW8	Nonlinearity correction coefficient used in place of engineering TLM
LinErr_a2_LW9	Nonlinearity correction coefficient used in place of engineering TLM
LinErr_a2_MW1	Nonlinearity correction coefficient used in place of engineering TLM
LinErr_a2_MW2	Nonlinearity correction coefficient used in place of engineering TLM
LinErr_a2_MW3	Nonlinearity correction coefficient used in place of engineering TLM
LinErr_a2_MW4	Nonlinearity correction coefficient used in place of engineering TLM
LinErr_a2_MW5	Nonlinearity correction coefficient used in place of engineering TLM
LinErr_a2_MW6	Nonlinearity correction coefficient used in place of engineering TLM
LinErr_a2_MW7	Nonlinearity correction coefficient used in place of engineering TLM
LinErr_a2_MW8	Nonlinearity correction coefficient used in place of engineering TLM
LinErr_a2_MW9	Nonlinearity correction coefficient used in place of engineering TLM
LinErr_a2_SW1	Nonlinearity correction coefficient used in place of engineering TLM
LinErr_a2_SW2	Nonlinearity correction coefficient used in place of engineering TLM
LinErr_a2_SW3	Nonlinearity correction coefficient used in place of engineering TLM
LinErr_a2_SW4	Nonlinearity correction coefficient used in place of engineering TLM
LinErr_a2_SW5	Nonlinearity correction coefficient used in place of engineering TLM
LinErr_a2_SW6	Nonlinearity correction coefficient used in place of engineering TLM
LinErr_a2_SW7	Nonlinearity correction coefficient used in place of engineering TLM
LinErr_a2_SW8	Nonlinearity correction coefficient used in place of engineering TLM
LinErr_a2_SW9	Nonlinearity correction coefficient used in place of engineering TLM
LinErr_Vinst_LW1	Nonlinearity correction coefficient used in place of engineering TLM
LinErr_Vinst_LW2	Nonlinearity correction coefficient used in place of engineering TLM
LinErr_Vinst_LW3	Nonlinearity correction coefficient used in place of engineering TLM
LinErr_Vinst_LW4	Nonlinearity correction coefficient used in place of engineering TLM
LinErr_Vinst_LW5	Nonlinearity correction coefficient used in place of engineering TLM
LinErr_Vinst_LW6	Nonlinearity correction coefficient used in place of engineering TLM
LinErr_Vinst_LW7	Nonlinearity correction coefficient used in place of engineering TLM
LinErr_Vinst_LW8	Nonlinearity correction coefficient used in place of engineering TLM
LinErr_Vinst_LW9	Nonlinearity correction coefficient used in place of engineering TLM
LinErr_Vinst_MW1	Nonlinearity correction coefficient used in place of engineering TLM
LinErr_Vinst_MW2	Nonlinearity correction coefficient used in place of engineering TLM
LinErr_Vinst_MW3	Nonlinearity correction coefficient used in place of engineering TLM
LinErr_Vinst_MW4	Nonlinearity correction coefficient used in place of engineering TLM
LinErr_Vinst_MW5	Nonlinearity correction coefficient used in place of engineering TLM
LinErr_Vinst_MW6	Nonlinearity correction coefficient used in place of engineering TLM
LinErr_Vinst_MW7	Nonlinearity correction coefficient used in place of engineering TLM

Configuration file Mnemonic	Description
LinErr_Vinst_MW8	Nonlinearity correction coefficient used in place of engineering TLM
LinErr_Vinst_MW9	Nonlinearity correction coefficient used in place of engineering TLM
LinErr_Vinst_SW1	Nonlinearity correction coefficient used in place of engineering TLM
LinErr_Vinst_SW2	Nonlinearity correction coefficient used in place of engineering TLM
LinErr_Vinst_SW3	Nonlinearity correction coefficient used in place of engineering TLM
LinErr_Vinst_SW4	Nonlinearity correction coefficient used in place of engineering TLM
LinErr_Vinst_SW5	Nonlinearity correction coefficient used in place of engineering TLM
LinErr_Vinst_SW6	Nonlinearity correction coefficient used in place of engineering TLM
LinErr_Vinst_SW7	Nonlinearity correction coefficient used in place of engineering TLM
LinErr_Vinst_SW8	Nonlinearity correction coefficient used in place of engineering TLM
LinErr_Vinst_SW9	Nonlinearity correction coefficient used in place of engineering TLM
LinErr_ModEff_LW1	Nonlinearity correction coefficient used in place of engineering TLM
LinErr_ModEff_LW2	Nonlinearity correction coefficient used in place of engineering TLM
LinErr_ModEff_LW3	Nonlinearity correction coefficient used in place of engineering TLM
LinErr_ModEff_LW4	Nonlinearity correction coefficient used in place of engineering TLM
LinErr_ModEff_LW5	Nonlinearity correction coefficient used in place of engineering TLM
LinErr_ModEff_LW6	Nonlinearity correction coefficient used in place of engineering TLM
LinErr_ModEff_LW7	Nonlinearity correction coefficient used in place of engineering TLM
LinErr_ModEff_LW8	Nonlinearity correction coefficient used in place of engineering TLM
LinErr_ModEff_LW9	Nonlinearity correction coefficient used in place of engineering TLM
LinErr_ModEff_MW1	Nonlinearity correction coefficient used in place of engineering TLM
LinErr_ModEff_MW2	Nonlinearity correction coefficient used in place of engineering TLM
LinErr_ModEff_MW3	Nonlinearity correction coefficient used in place of engineering TLM
LinErr_ModEff_MW4	Nonlinearity correction coefficient used in place of engineering TLM
LinErr_ModEff_MW5	Nonlinearity correction coefficient used in place of engineering TLM
LinErr_ModEff_MW6	Nonlinearity correction coefficient used in place of engineering TLM
LinErr_ModEff_MW7	Nonlinearity correction coefficient used in place of engineering TLM
LinErr_ModEff_MW8	Nonlinearity correction coefficient used in place of engineering TLM
LinErr_ModEff_MW9	Nonlinearity correction coefficient used in place of engineering TLM
LinErr_ModEff_SW1	Nonlinearity correction coefficient used in place of engineering TLM
LinErr_ModEff_SW2	Nonlinearity correction coefficient used in place of engineering TLM
LinErr_ModEff_SW3	Nonlinearity correction coefficient used in place of engineering TLM
LinErr_ModEff_SW4	Nonlinearity correction coefficient used in place of engineering TLM
LinErr_ModEff_SW5	Nonlinearity correction coefficient used in place of engineering TLM
LinErr_ModEff_SW6	Nonlinearity correction coefficient used in place of engineering TLM
LinErr_ModEff_SW7	Nonlinearity correction coefficient used in place of engineering TLM
LinErr_ModEff_SW8	Nonlinearity correction coefficient used in place of engineering TLM
LinErr_ModEff_SW9	Nonlinearity correction coefficient used in place of engineering TLM
lwPGAGainSetting_FOV1	PGA Gainsetting used in place of engineeringTLM for non-linearity cor
lwPGAGainSetting_FOV2	PGA Gainsetting used in place of engineeringTLM for non
lwPGAGainSetting_FOV3	PGA Gainsetting used in place of engineeringTLM for non
lwPGAGainSetting_FOV4	PGA Gainsetting used in place of engineeringTLM for non
lwPGAGainSetting_FOV5	PGA Gainsetting used in place of engineeringTLM for non
lwPGAGainSetting_FOV6	PGA Gainsetting used in place of engineeringTLM for non
lwPGAGainSetting_FOV7	PGA Gainsetting used in place of engineeringTLM for non
lwPGAGainSetting_FOV8	PGA Gainsetting used in place of engineeringTLM for non
lwPGAGainSetting_FOV9	PGA Gainsetting used in place of engineeringTLM for non
mwPGAGainSetting_FOV1	PGA Gainsetting used in place of engineeringTLM for non

Configuration file Mnemonic	Description
mwPGAGainSetting_FOV2	PGA Gainsetting used in place of engineeringTLM for non
mwPGAGainSetting_FOV3	PGA Gainsetting used in place of engineeringTLM for non
mwPGAGainSetting_FOV4	PGA Gainsetting used in place of engineeringTLM for non
mwPGAGainSetting_FOV5	PGA Gainsetting used in place of engineeringTLM for non
mwPGAGainSetting_FOV6	PGA Gainsetting used in place of engineeringTLM for non
mwPGAGainSetting_FOV7	PGA Gainsetting used in place of engineeringTLM for non
mwPGAGainSetting_FOV8	PGA Gainsetting used in place of engineeringTLM for non
mwPGAGainSetting_FOV9	PGA Gainsetting used in place of engineeringTLM for non
swPGAGainSetting_FOV1	PGA Gainsetting used in place of engineeringTLM for non
swPGAGainSetting_FOV2	PGA Gainsetting used in place of engineeringTLM for non
swPGAGainSetting_FOV3	PGA Gainsetting used in place of engineeringTLM for non
swPGAGainSetting_FOV4	PGA Gainsetting used in place of engineeringTLM for non
swPGAGainSetting_FOV5	PGA Gainsetting used in place of engineeringTLM for non
swPGAGainSetting_FOV6	PGA Gainsetting used in place of engineeringTLM for non
swPGAGainSetting_FOV7	PGA Gainsetting used in place of engineeringTLM for non
swPGAGainSetting_FOV8	PGA Gainsetting used in place of engineeringTLM for non
swPGAGainSetting_FOV9	PGA Gainsetting used in place of engineeringTLM for non
lwLinearityCorrectionControlParam	Allows correction parameter origin from telemetry or config
mwLinearityCorrectionControlParam	Allows correction parameter origin from telemetry or config
swLinearityCorrectionControlParam	Allows correction parameter origin from telemetry or config
performLWLinearityCorrectionControl	Turns correction ON or OFF
performMWLinearityCorrectionControl	Turns correction ON or OFF
performSWLinearityCorrectionControl	Turns correction ON or OFF
lwFirAccumulatorStartBit	Nonlinearity correction coefficient used in place of engineering packet value
mwFirAccumulatorStartBit	Nonlinearity correction coefficient used in place of engineering packet value
swFirAccumulatorStartBit	Nonlinearity correction coefficient used in place of engineering packet value
lwFirFilterScale	Nonlinearity correction coefficient used in place of engineering packet value
mwFirFilterScale	Nonlinearity correction coefficient used in place of engineering packet value
swFirFilterScale	Nonlinearity correction coefficient used in place of engineering packet value
lwPassBandStart	Used for nonlinearity correction
mwPassBandStart	Used for nonlinearity correction
swPassBandStart	Used for nonlinearity correction
lwPassBandStop	Used for nonlinearity correction
mwPassBandStop	Used for nonlinearity correction
swPassBandStop	Used for nonlinearity correction
firFilter_LWBin1_Real to firFilter_LWBin255_Real	Used for nonlinearity correction
firFilter_LWBin1_Imag to firFilter_LWBin255_Imag	Used for nonlinearity correction

Configuration file Mnemonic	Description
firFilter_MWBin1_Real to firFilter_MWBin255_Real	Used for nonlinearity correction
firFilter_MWBin1_Imag to firFilter_MWBin255_Imag	Used for nonlinearity correction
firFilter_SWBin1_Real to firFilter_SWBin255_Real	Used for nonlinearity correction
firFilter_SWBin1_Imag to firFilter_SWBin255_Imag	Used for nonlinearity correction
blackmanHarrisParamA0	Used to compute user apodization
blackmanHarrisParamA1	Used to compute user apodization
blackmanHarrisParamA2	Used to compute user apodization
blackmanHarrisParamA3	Used to compute user apodization
computedWavelengthRejectionThreshold	neon calibration quality control parameter
fceParamLwAmpThreshRejectLimit	Fringe Count validation parameter
fceParamLwDimensionThresholdLimit	Fringe Count validation parameter
fceParamLwFractionalFceThresholdLimit	Fringe Count validation parameter
fceParamLwGoodLinearFittingThreshLimit	Fringe Count validation parameter
fceParamLwMaxFceThreshLimit	Fringe Count validation parameter
fceParamLwMaxIndex	Max index used in FCE detection
fceParamLwMinIndex	Min index used in FCE detection
fceParamRefThreshold	Fringe Count validation parameter
fceParamCalThreshold	Fringe Count validation parameter
hammingParameter	Parameter used for Hamming apodization
ictPrt1Bias	Parameters use to calculate ICT Temperature (default is zero). Not used operationally
ictPrt2Bias	Parameters use to calculate ICT Temperature (default is zero). Not used operationally
laserWavelengthDriftTolerance	Used to determine if calculated laser wavelength should replace existing laser wavelength
maximumFractionRejections	Fringe Count validation parameter
numberOpdOverscanSamples	Number of samples to trim from each end of the interferogram.
polarizationCorrectionFitOrder	Order of Polynomial fit used to calculate Polarization Curve
postCalibrationLwA1	LW Parameters used to calculate Post Calibration filter
postCalibrationLwA2	
postCalibrationLwA3	
postCalibrationLwA4	
postCalibrationLwK	LW Parameters used to calculate Post Calibration filter
postCalibrationLwK0	
postCalibrationLwK1	
postCalibrationMwA1	MW Parameters used to calculate Post Calibration filter
postCalibrationMwA2	
postCalibrationMwA3	
postCalibrationMwA4	

Configuration file Mnemonic	Description
postCalibrationMwK	MW Parameters used to calculate Post Calibration filter
postCalibrationMwK0	
postCalibrationMwK1	
postCalibrationSwA1	SW Parameters used to calculate Post Calibration filter
postCalibrationSwA2	
postCalibrationSwA3	
postCalibrationSwA4	
postCalibrationSwK	SW Parameters used to calculate Post Calibration filter
postCalibrationSwK0	
postCalibrationSwK1	
plankConstantC1	Used in radiance calculation
plankConstantC2	Used in radiance calculation
beamsplitterTempBench	Used in place of TLM when designated
beamsplitterTempChamber	Used in place of TLM when designated
LWBin1 through LWBin864	864 Space Target wavenumber dependant emissivity values used in place of TLM
MWBin1 through MWBin528	528 Space Target wavenumber dependant emissivity values used in place of TLM
SWBin1 through SWBin200	200 Space Target wavenumber dependant emissivity values used in place of TLM
dsTempBench	used in place of bench TLM (optional)
dsTempChamber	used in place of chamberTLM (optional)
ictTempBench	used in place of bench TLM (optional)
ictTempChamber	used in place of chamber TLM (optional)
meanDsEmissivityBench	Used only for bench test
meanDsEmissivityChamber	used only for TVAC testing
omaTempBench	used in place of science packet TLM (optional)
omaTempChamber	used in place of science packet TLM (optional)
scanBaffleTempBench	used in place of science packet TLM (optional)
scanBaffleTempChamber	used in place of science packet TLM (optional)
lwIctBaffleEmissivity	used in place of engineering packet TLM (optional)
mwIctBaffleEmissivity	used in place of engineering packet TLM (optional)
swIctBaffleEmissivity	used in place of engineering packet TLM (optional)
ictBaffleViewFactor	used in place of engineering packet TLM (optional)
lwScanBaffleEmissivity	used in place of engineering packet TLM (optional)
mwScanBaffleEmissivity	used in place of engineering packet TLM (optional)
swScanBaffleEmissivity	used in place of engineering packet TLM (optional)
scanBaffleViewFactor	used in place of engineering packet TLM (optional)
lwOmaFrameEmissivity	used in place of engineering packet TLM (optional)
mwOmaFrameEmissivity	used in place of engineering packet TLM (optional)
swOmaFrameEmissivity	used in place of engineering packet TLM (optional)
omaFrameViewFactor	used in place of engineering packet TLM (optional)
warmBeamsplitterViewFactor	used in place of engineering packet TLM (optional)
coldBeamsplitterViewFactor	used in place of engineering packet TLM (optional)
lwEarthTargetEmissivity	used in place of engineering packet TLM (optional)
mwEarthTargetEmissivity	used in place of engineering packet TLM (optional)
swEarthTargetEmissivity	used in place of engineering packet TLM (optional)
earthTargetViewFactor	used in place of engineering packet TLM (optional)
earthTargetTempBench	used in place of engineering packet TLM (optional)
earthTargetTempChamber	used in place of engineering packet TLM (optional)

Configuration file Mnemonic	Description
Offset1	Decimated Scan Baffle Compensation Profile points used in place of engineering packet TLM
Offset2	Decimated Scan Baffle Compensation Profile points used in place of engineering packet TLM
Offset3	Decimated Scan Baffle Compensation Profile points used in place of engineering packet TLM
Offset4	Decimated Scan Baffle Compensation Profile points used in place of engineering packet TLM
Offset5	Decimated Scan Baffle Compensation Profile points used in place of engineering packet TLM
Offset6	Decimated Scan Baffle Compensation Profile points used in place of engineering packet TLM
Offset7	Decimated Scan Baffle Compensation Profile points used in place of engineering packet TLM
Offset8	Decimated Scan Baffle Compensation Profile points used in place of engineering packet TLM
Offset9	Decimated Scan Baffle Compensation Profile points used in place of engineering packet TLM
Offset10	Decimated Scan Baffle Compensation Profile points used in place of engineering packet TLM
Offset11	Decimated Scan Baffle Compensation Profile points used in place of engineering packet TLM
Offset12	Decimated Scan Baffle Compensation Profile points used in place of engineering packet TLM
Offset13	Decimated Scan Baffle Compensation Profile points used in place of engineering packet TLM
Offset14	Decimated Scan Baffle Compensation Profile points used in place of engineering packet TLM
Offset15	Decimated Scan Baffle Compensation Profile points used in place of engineering packet TLM
Offset16	Decimated Scan Baffle Compensation Profile points used in place of engineering packet TLM
Offset17	Decimated Scan Baffle Compensation Profile points used in place of engineering packet TLM
Offset18	Decimated Scan Baffle Compensation Profile points used in place of engineering packet TLM
Offset19	Decimated Scan Baffle Compensation Profile points used in place of engineering packet TLM
Offset20	Decimated Scan Baffle Compensation Profile points used in place of engineering packet TLM
Offset21	Decimated Scan Baffle Compensation Profile points used in place of engineering packet TLM
overrideEarthTargetTemp	instructs the algorithm to ignore the Earth Temp engineering packet TLM value.
durationOfOrbit	Orbit Duration used to override engineering packet value from TLM (optional)
detectorSelectionLWFOV1	process FOV ON/OFF
detectorSelectionLWFOV2	process FOV ON/OFF
detectorSelectionLWFOV3	process FOV ON/OFF
detectorSelectionLWFOV4	process FOV ON/OFF
detectorSelectionLWFOV5	process FOV ON/OFF
detectorSelectionLWFOV6	process FOV ON/OFF
detectorSelectionLWFOV7	process FOV ON/OFF
detectorSelectionLWFOV8	process FOV ON/OFF
detectorSelectionLWFOV9	process FOV ON/OFF
detectorSelectionMWFOV1	process FOV ON/OFF
detectorSelectionMWFOV2	process FOV ON/OFF
detectorSelectionMWFOV3	process FOV ON/OFF
detectorSelectionMWFOV4	process FOV ON/OFF
detectorSelectionMWFOV5	process FOV ON/OFF
detectorSelectionMWFOV6	process FOV ON/OFF

Configuration file Mnemonic	Description
detectorSelectionMWFOV7	process FOV ON/OFF
detectorSelectionMWFOV8	process FOV ON/OFF
detectorSelectionMWFOV9	process FOV ON/OFF
detectorSelectionSWFOV1	process FOV ON/OFF
detectorSelectionSWFOV2	process FOV ON/OFF
detectorSelectionSWFOV3	process FOV ON/OFF
detectorSelectionSWFOV4	process FOV ON/OFF
detectorSelectionSWFOV5	process FOV ON/OFF
detectorSelectionSWFOV6	process FOV ON/OFF
detectorSelectionSWFOV7	process FOV ON/OFF
detectorSelectionSWFOV8	process FOV ON/OFF
detectorSelectionSWFOV9	process FOV ON/OFF
sceneSelectionICT	process scene data ON/OFF
sceneSelectionES1	process scene data ON/OFF
sceneSelectionES2	process scene data ON/OFF
sceneSelectionES3	process scene data ON/OFF
sceneSelectionES4	process scene data ON/OFF
sceneSelectionES5	process scene data ON/OFF
sceneSelectionES6	process scene data ON/OFF
sceneSelectionES7	process scene data ON/OFF
sceneSelectionES8	process scene data ON/OFF
sceneSelectionES9	process scene data ON/OFF
sceneSelectionES10	process scene data ON/OFF
sceneSelectionES11	process scene data ON/OFF
sceneSelectionES12	process scene data ON/OFF
sceneSelectionES13	process scene data ON/OFF
sceneSelectionES14	process scene data ON/OFF
sceneSelectionES15	process scene data ON/OFF
sceneSelectionES16	process scene data ON/OFF
sceneSelectionES17	process scene data ON/OFF
sceneSelectionES18	process scene data ON/OFF
sceneSelectionES19	process scene data ON/OFF
sceneSelectionES20	process scene data ON/OFF
sceneSelectionES21	process scene data ON/OFF
sceneSelectionES22	process scene data ON/OFF
sceneSelectionES23	process scene data ON/OFF
sceneSelectionES24	process scene data ON/OFF
sceneSelectionES25	process scene data ON/OFF
sceneSelectionES26	process scene data ON/OFF
sceneSelectionES27	process scene data ON/OFF
sceneSelectionES28	process scene data ON/OFF
sceneSelectionES29	process scene data ON/OFF
sceneSelectionES30	process scene data ON/OFF
sceneSelectionDS	process scene data ON/OFF
sceneSelectionNSD	process scene data ON/OFF
sceneSelectionNadir	process scene data ON/OFF
maxBufferDepth	performance setting to restrict the algorithm's "read-ahead-buffers" for PC with limited RAM.

Configuration file Mnemonic	Description
calibrationType	Turns Calibration On/Off
outputStyle	control flag to generate SDR files
exportReferenceSpectra	Includes DS & ICT spectra SDR output
discardInvalidSpectra	discard invalid spectra in SDR output when set
baseDirectory	Specifies output directory of SDR output files
instrumentLocation	used for bench or chamber ground testing
calculateNEdN	Enable/disable NEdN estimate calculation
boxCarWidth	Window size of spectral smoothing for NEdN estimate
windowManagementStyle	Used to specify processing of contiguous data sets

Note: Grayed entries in table are historical reference only and no longer configurable

7.2 INPUT DATA HANDLING

The purpose of this module is to read and decode data packets before they can be further processed. Within an operational implementation of the algorithms, this module should also be responsible to call the appropriate data processing sequence according to the type of data ingested. For example, an engineering data packet could trigger the initialization of the correction matrix operator (see Radiometric Calibration section below), or the calibration of the laser diode wavelength, from laser diode and neon fringe counts (see Spectral Calibration section below). From the software implementation point of view, other functions contained in this module are responsible to ingest parameters that are needed to configure the software and define ancillary data. Low-level data input functions (implementation dependant) are also foreseen.

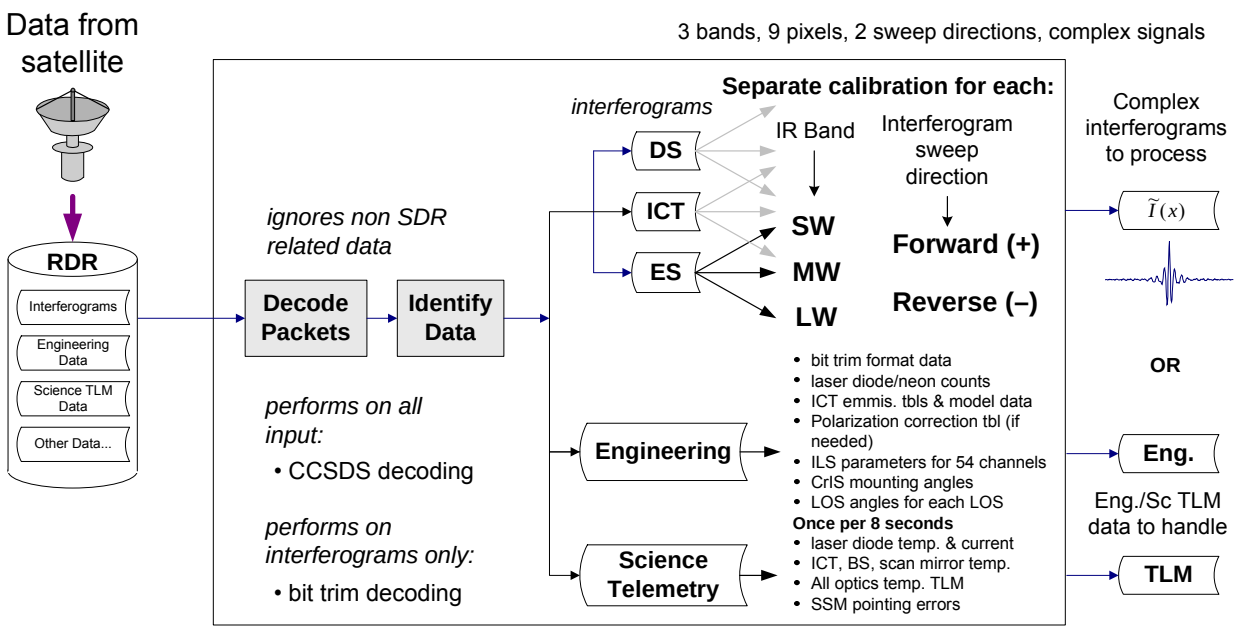

Figure 60: Input Data Handling Flow Chart

Table 19: Parameters Monitored via the Eight Second Science Telemetry RDR

Parameter	Comments
IE CCA Calibration Resistor Temperature (epoch 1..40) - (refers to 200 msec epoch)	40 Readings
Low Range Calibration Resistor (epoch 1..40)	40 Readings
High Range Calibration Resistor (epoch 1..40)	40 Readings
ICT Temperature #1 (epoch 1..40)	40 Readings
ICT Temperature #2 (epoch1..40)	40 Readings
Cross Track Servo Error (sample 21, epoch 4..33)	30 Readings
In Track Servo Error (sample 21, epoch 4..33)	30 Readings
Laser Diode Current (epoch 39)	Single Reading
Laser Diode Temperature (epoch 39)	Single Reading
Beamsplitter Temperature #1 (epoch 39)	Single Reading
OMA Structure Input Temperature #1 (epoch 39)	Single Reading
OMA Structure Input Temperature #2 (epoch 39)	Single Reading
SSM Scan Mirror Temperature (epoch 39)	Single Reading
SSM Scan Mirror Baffle Temperature (epoch 39)	Single Reading
Stage 2 Cooler Temperature (epoch 39)	Single Reading
Stage 4 Cooler Temperature (epoch 39)	Single Reading
Stage 1 Cooler Temperature (epoch 39)	Single Reading
Stage 3 Cooler Temperature (epoch 39)	Single Reading
Telescope Temperature #1 (epoch 39)	Single Reading

Table 20: Parameters Continuously Monitored via the Four Minute Engineering Packet RDR

Parameter	Comments
CRC of Four Minute Engineering Telemetry RDR	Used to trigger check of tunable parameters
Spectral Calibration Parameters	Used to calculate metrology laser frequency
Laser Pulses Counted Per Sweep	
Number Of Neon Calibration Sweeps	
Effective Neon Wavelength	
Neon Calibration Time Stamp	
Repeat Neon Calibration Interval	
Neon Calibration Data	One sample per Number Of Neon Calibration Sweeps
Starting Count (Sample 1..128)	
Starting Partial Count (Sample 1..128)	
Fringe Count (Sample 1..128)	
Ending Partial Count (Sample 1..128)	
Ending Count (Sample 1..128)	

7.3 PREPROCESSING

This module is responsible to process interferograms (IGMs) according to their type (ES, DS, or ICT). It makes the appropriate calls to transform the IGMs into spectra, to perform the moving window update if data are calibration target IGMs (DS or ICT), and makes sure that all data are synchronized with respect to fringe count errors before any further processing. See section about Fringe Count Error Handling within Quality Control section below.

7.3.1 Interferogram to Spectrum Transformation

This function is responsible to transform the interferograms into raw spectra. Before performing the FFT (a prime factor based algorithm (PFBA) is used), 2 extra decimated interferogram samples are discarded, one on each side of the interferogram. Those 2 extra points in RDR output interferograms were originally intended as spare samples to accommodate a slight interferogram offset from ZPD center. However, the CrIS instrument hardware design maintains ZPD centering to within a fraction of one sample and these extra interferogram samples can always be discarded. The number of samples discarded (0, 2, 4, 6, etc) is a configuration file parameter. This parameter should always be set to equal to 2 samples in the SDR configuration file without exception.

Next, an FFT shift is performed on the trimmed interferogram vector which swaps the first half of points in the array with the second half of points. This shifting of points prior to execution of the FFT makes the output points of the FFT come out in the desired order. Lastly, the FFT is performed and then the magnitude scaled by λ_s and DF in order to complete the discrete Fourier transform as described by equation 1. Figure 61 shows a summary of these processing steps.

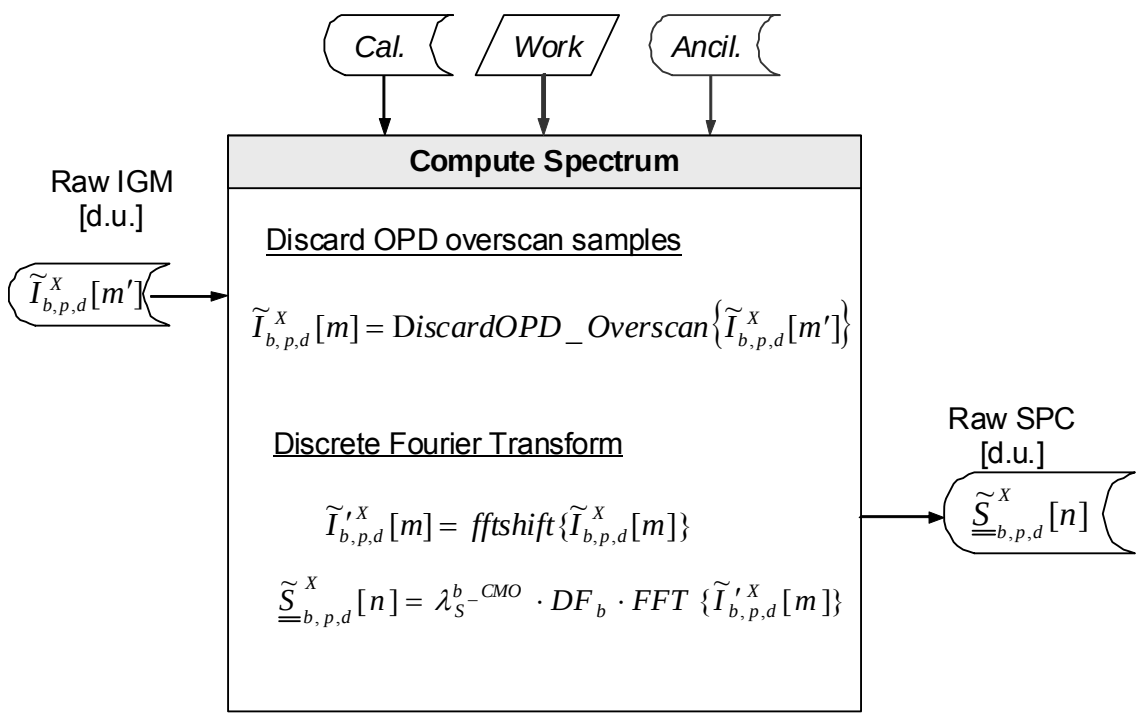

Figure 61: Compute Spectrum Flowchart

7.3.1.1 Definition of variables

Input variables

$\widetilde{I}^{X}_{b,p,d}[m']$ raw complex interferogram in [d.u.] for band b, FOV "p" and sweep direction "d" prior to discarding 2 overscan samples and corresponding either to X = DS, ICT, or ES. (0 ≤ m' ≤ N_b-1+2)

$\underline{\underline{\widetilde{S}}}^{X}_{b,p,d}[n]$ raw complex uncalibrated spectrum prior to linearity correction & alias unfolding

$\lambda^{b_CMO}_{S}$ interferogram sampling interval for band "b"(cm)

DF_b Decimation factor used in band "b

N_b Number of points in output spectrum (calculated from bit trim removal process and with overscan samples removed)

Calibration data

None.

Ancillary data

None.

Local variables

$\widetilde{I}^{X}_{b,p,d}[m]$ raw complex interferogram in d.u. for band "b", FOV "p" and sweep direction "d" with 2 overscan samples discarded (0 ≤ m ≤ N_b-1)

$\widetilde{I}'^{X}_{b,p,d}[m]$ raw complex interferogram in d.u. for band "b", FOV "p" and sweep direction "d" with points reordered according to fftshift function and with 2 overscan samples discarded (0 ≤ m ≤ N_b-1)

Output variables

$\underline{\underline{\widetilde{S}}}^{X}_{b,p,d}[n]$ raw complex spectrum in [d.u.] for band "b", FOV "p" and sweep direction "d" prior to linearity correction and prior to alias unfolding, corresponding either to X = DS, ICT, or ES

Operators

$\mathrm{DiscardOPD_Overscan}\{\}$ discards the 2 extra interferogram samples, one on each end.

$fftshift\ \{\}$ produces new vector with 1st half & 2nd half of points swapped

$FFT\{\widetilde{I}[m]\} = \sum_{m=0}^{N_b-1} \widetilde{I}[m] \cdot e^{\frac{-2\pi imn}{N_b}} = \widetilde{S}[n]$ Definition of standard FFT function in MATLAB or C++ which produces complex output vector from complex input vector where 0 ≤ n ≤ N_b-1 and where 0 ≤ m ≤ N_b-1

7.3.1.2 Exception handling

Output spectrum not created if I or Q bit trim failure flag set or invalid data flag set in RDR data.

7.3.2 Moving Average Handling

This module handles the moving average of calibration target measurements (DS, ICT) and the global shifting of data sets to accomplish this. Thirty DS and ICT measurements spanning 4 minutes of instrument operation are averaged per the default SDR configuration file setting. However, selection of a moving average from 0 to at least 512 is also supported. The moving window averages for DS and ICT are maintained on the uncalibrated spectrum prior to non-linearity correction.

The moving window average is maintained by using a First-In-First-Out (FIFO) memory array. The FIFO maintains each individual contributor of the average as well as the running average. Updates to the running average are made by adding the newest contributor and subtracting the oldest contributor. Averaging of science telemetry within the moving window is also performed. Any ICT spectra, DS spectra or telemetry in the FIFO tagged as invalid are not included in the averaging.

In the event that a FCE has been detected and validated for the current DS or ICT spectrum, then the phase of the current ICT or DS spectrum is corrected to match the phase of all prior ICT or DS spectrum contained in the moving window.

In the event that a FCE has been detected and validated for the earth scene spectrum (corresponding to the earth scene spectrum in the middle of the DS/ICT moving window average), then the phase of all ICT & DS data in the moving average is corrected to match the phase of the earth scene spectrum.

A general description of the moving window average process is given in Section 5.6.1. The processing sequence is shown in Figure 62.

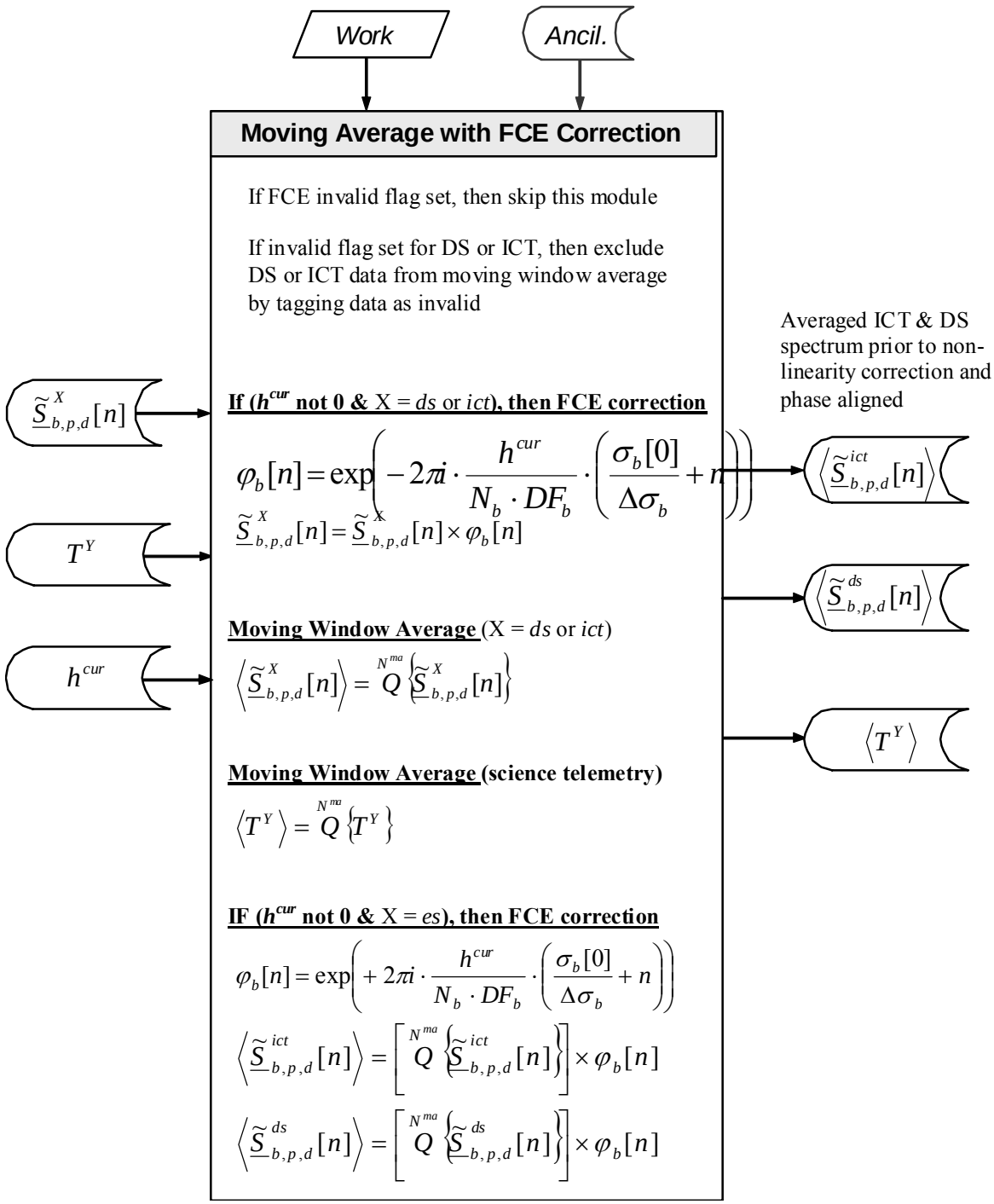

Figure 62: Moving Average Flowchart

Note: Operations on telemetry variables (T^{Y}) are performed only if incoming science telemetry packet is present. Y refers to each telemetry element (Y = ICT, BS, etc.). Definition of variables

Input variables

$\underline{\tilde{S}}^{X}_{b,p,d}[n]$ When *(X = ict)*, raw complex ICT spectrum in [d.u.] prior to linearity correction and prior to FCE correction for band *"b"*, FOV *"p"*, sweep direction *"d"* and spectral channel *"n"*.

When *(X =ds))*, raw complex DS spectrum in [d.u.] prior to linearity correction and prior to FCE correction for band *"b"*, FOV *"p"*, sweep direction *"d"* and spectral channel *"n"*.

T^{Y} science telemetry data in engineering units prior to averaging (Y = SSM baffle temp, ICT PRT1 temp, ICT PRT2 temp, cooler temps 1, 2, 3 & 4, telescope temp, laser diode temp, laser diode current, OMA1 temp, OMA2 temp, beamsplitter temp and preamp voltages for linearity correction for each FOV in each band)

H^{cur} integer fringe count error estimate *(cur = ict, ds or es)*.

Calibration data

None required for this function.

Ancillary data

N^{ma} moving average window size (baseline is 30) from SDR configuration file

N_b Number of spectral points in band "b" (derived from engineering packet entry after subtracting overscan samples)

Work variables (global nature)

$\sigma_b[0]$ wavenumber corresponding to first channel center in band *"b"* on instrument grid [cm^{-1}]

$\Delta\sigma_b$ channel spacing in band "b" on instrument grid [cm^{-1}]

DF_b decimation factor used in band *"b"*

Local variables

$\varphi[n]$ term used to correct phase shift in channel "n" due to FCE.

Output variable

$\left\langle \underline{\tilde{S}}^{ict}_{b,p,d}[n] \right\rangle$ average of N^{ma} raw complex ICT spectrum in channel *"n"* [d.u.] prior to non-linearity correction and after FCE correction for band *"b"*, FOV *"p"* and sweep direction *"d"*.

$\left\langle \underline{\tilde{S}}^{ds}_{b,p,d}[n] \right\rangle$ average of N^{ma} raw complex DS spectrum in channel *"n"* [d.u.] prior to non-linearity correction and after FCE correction for band *"b"*, FOV *"p"* and sweep direction *"d"*.

$\left\langle T^{Y} \right\rangle$ mean calculated for telemetry component Y (Y = SSM baffle temp, ICT PRT1 temp, ICT PRT2 temp, cooler temps 1, 2, 3 & 4, telescope temp, laser diode temp, laser diode current, OMA1 temp, OMA2 temp, beamsplitter temp). Only telemetry marked as valid within the moving window is included in this average.

Operators

$\overset{N^{ma}}{Q}\left\{\underline{\tilde{S}}^{X}_{b,p,d}[n]\right\}$ Updates FIFO queue of size N^{ma} with $\underline{\tilde{S}}^{X}_{b,p,d}[n]$ and computes the average of FIFO contents in each spectral channel *"n"* by using only the N^{ma} FIFO content that is marked valid. The FIFO update is performed independently for band *"b"*, FOV *"p"*, sweep direction *"d"*. *(X = ict or ds)*

$\overset{N^{ma}}{Q}\left\{T^{Y}\right\}$ Updates FIFO queue of size N^{ma} containing a collection of T^{Y} elements and computes the average of FIFO contents using only the N^{ma} elements that are marked valid for each telemetry parameter "Y".

7.3.2.1 Exception handling

Computed temperatures exceed expected values.

Note: If FCE Detection module (see Quality Control/Fringe Count Error Detection section below) identifies an abnormal FCE in a calibration measurement (which can be caused for example by an in-interferogram FCE) then this signal is tagged as invalid and is discarded in order to avoid corruption of the moving average window.

If any ICT or DS spectrum is declared invalid by CrIS sensor, lunar intrusion test or other QC measure, then the corresponding spectrum is excluded from the moving window average.

If the number of valid spectra in the moving window drops below 50% of the designated moving window size (or other config file designated fraction), then the "Invalid Radiometric Calibration" flag is set.

If science telemetry packet is missing for a given 8 second sweep, then those telemetry values shall be excluded from the moving window average.

7.4 SPECTRAL CALIBRATION

7.4.1 Laser Wavelength Calibration from Neon Lamp Data

This function computes the interferometer's laser metrology wavelength by using a neon bulb line emission as a reference. The neon calibration data is updated once per orbit and then placed into the CrIS engineering packet for ground processing.

Calibration of the interferometer laser metrology wavelength is achieved by counting the number of neon lamp fringes during an OPD sweep interval metered by 7985 laser metrology fringes. Any fractional neon fringe at the beginning and end of the OPD interval is interpolated using a high speed clock. An update of laser wavelength and CMO is performed only if the wavelength correction

exceeds a specified tolerance (i.e. 2 ppm). The specified tolerance is a configurable value carried in the engineering packet. If the correction is less than this amount, then the prior wavelength calibration is retained without update and without a corresponding update to the CMO. Slight offset of MWIR and SWIR relative to LWIR is accommodated by the calibration process. The wavelength offset in ppm relative to LWIR is a parameter in the engineering packet.

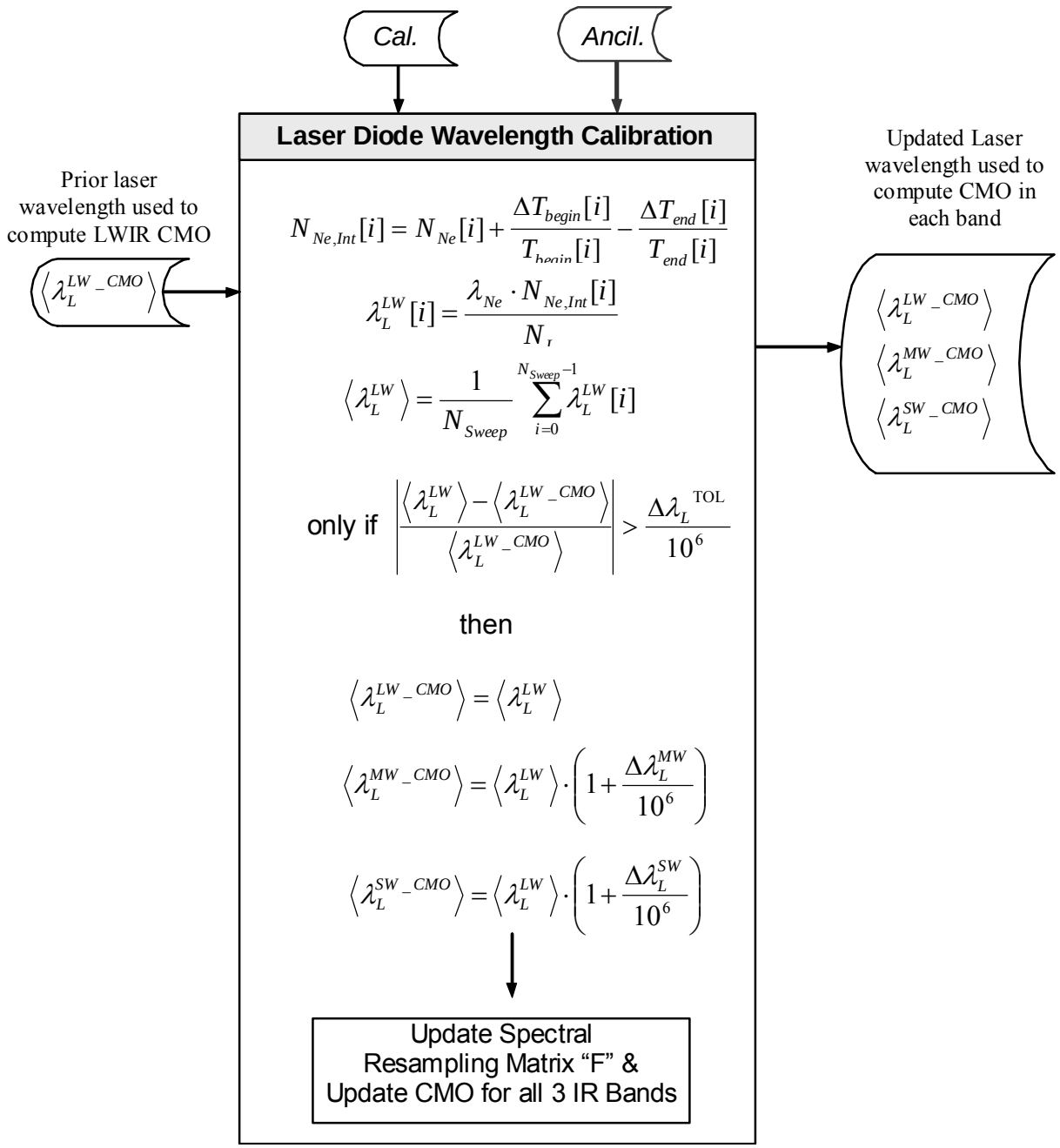

Figure 63: Laser Diode Wavelength Calibration Flowchart

7.4.1.1 Definition of variables

Input variables

$\left\langle \lambda_L^{LW_CMO} \right\rangle$ Average LWIR laser metrology wavelength [cm] computed by processing and averaging neon calibration data found in engineering data packet. CMO superscript indicates value was used in computing previous CMO matrix.

Calibration data from engineering packet

$N_{Ne}[i]$ integer neon fringe count from ith sweep …….(0 ≤ i ≤ N_{Sweep}-1)

$T_{begin}[i]$ integer neon fringe count parameter from ith sweep used for interpolation

$T_{end}[i]$ integer neon fringe count parameter from ith sweep used for interpolation

$\Delta T_{begin}[i]$ integer neon fringe count parameter from ith sweep used for interpolation

$\Delta T_{end}[i]$ integer neon fringe count parameter from ith sweep used for interpolation

N_{Sweep} Number of neon calibration sweeps collected & reported in engineering packet (1 ≤ N_{Sweep} ≤ 128)

N_L number of laser metrology wavelengths used to meter OPD during neon calibration sweep (N_L = 7985 always)

Ancillary data from engineering packet

λ_{Ne} reference neon wavelength [i.e. 703.4524 nm]

$\Delta\lambda_L^{TOL}$ change in laser wavelength needed to trigger a CMO update [e.g. 2 PPM].

$\Delta\lambda_{Ne}^{MW}$ neon wavelength offset for MWIR band [ppm]

$\Delta\lambda_{Ne}^{SW}$ neon wavelength offset for SWIR band [ppm]

Local variables

$N_{Ne,int}[i]$ neon wavelengths counted during ith calibration sweep (non integer, interpolated)

$\left\langle \lambda_L^{LW} \right\rangle$ Average LWIR laser metrology wavelength [cm] computed from current engineering packet neon calibration data

Output variables

$\left\langle \lambda_L^{LW_CMO} \right\rangle$ Averaged LWIR laser metrology wavelength [cm] used in formation of new CMO

$\left\langle \lambda_L^{MW_CMO} \right\rangle$ Averaged MWIR laser metrology wavelength [cm] used in formation of new CMO

$\left\langle \lambda_L^{SW_CMO} \right\rangle$ Averaged SWIR laser metrology wavelength [cm] used in formation of new CMO

7.4.1.2 Exception handling

If engineering packet checksum is unchanged from prior engineering packet that was processed, then this module is skipped.

The averaged LWIR laser diode wavelength is computed from many neon calibration sweeps (30 is the default). Outliers as defined by equation 63 are removed before the average is re-computed and reported. The tolerance on outliers is defined in the SDR config file. See section 4.1.3.

At least 75% of the neon calibration data in the engineering packet must pass the quality control measure defined by equation 63 in Section 4.1. If less than 75% of the calibration data is good, then the old laser metrology wavelength calibration is retained and no update is made. Fractions other than 75% can be specified in the SDR config file.

7.4.2 Laser Wavelength Drift Monitoring

This function calculates the current LWIR metrology laser wavelength drift from prior neon calibration by using laser diode temperature and electrical bias telemetry data. The wavelength drift is then added to the prior laser wavelength that was determined when the last neon calibration was last performed and accepted as an update in the CMO. If the engineering packet indicates that a ppm offset in laser wavelength for LW, MW and SW are to be used, then the laser monitoring will calculate a monitored wavelength for each IR band. In order to improve the accuracy of this estimate, the telemetry data (laser diode temperature and current) is averaged across the 4 minute moving window and used in the wavelength drift estimation. This laser monitoring is provided as a quality control check only. Results of the laser monitoring are **not used to update the CMO (software versions 2.18 and beyond).**

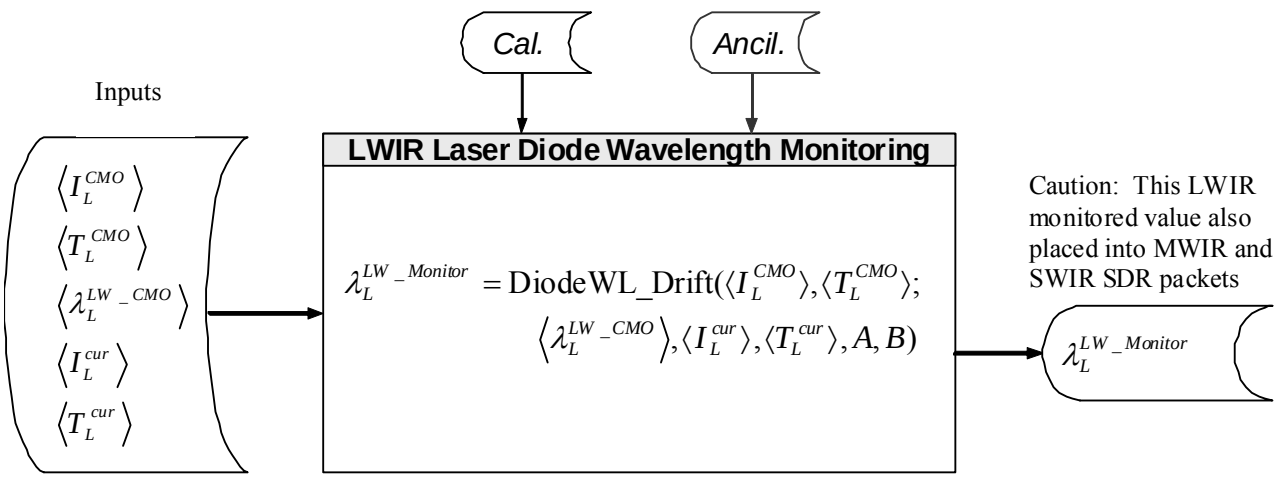

Figure 64: LWIR Laser Diode Wavelength Monitoring Flowchart

7.4.2.1 Definition of variables

Input variables

$\langle I_L^{CMO} \rangle$ average laser diode bias current when CMO was last updated

$\langle T_L^{CMO} \rangle$ average laser diode temperature when CMO was last updated

$\langle \lambda_L^{LW_CMO} \rangle$ average LWIR laser diode wavelength used when CMO was last updated (cm)

$\langle I_L^{cur} \rangle$ average laser diode bias current (from current moving window average)

$\langle T_L^{cur} \rangle$ average laser diode temperature (from current moving window average)

Calibration data

None

Ancillary data from engineering packet

A coefficient used to convert a change in temperature into a change in wavelength (e.g. ppm/cm, from latest engineering data packet).

B coefficient used to convert a change in bias current into a change in wavelength (e.g. ppm/cm, from latest engineering data packet).

Local variables

None

Output variables

$\left\langle \lambda_L^{LW_Monitor} \right\rangle$ Monitored LWIR laser diode wavelength.

Functions

$\mathrm{DiodeWL_Drift}\{\}$ Calculates monitored laser diode wavelength that accounts for laser diode wavelength drift since last time CMO was updated. The laser wavelength drift is assumed to be a linear function of diode bias current and temperature changes since last CMO update.

7.4.2.2 Exception handling

Caution: In version 2.17 and later of SDR code $\lambda_L^{LW_CMO}, \lambda_L^{MW_CMO}$ and $\lambda_L^{SW_CMO}$ may differ slightly due to band specific neon wavelength offset in the CrIS engineering packet. However, the MWIR and SWIR monitored laser wavelength is set equal to the LWIR value when reported in SDRs ($\lambda_L^{LW_Monitor} = \lambda_L^{MW_Monitor} = \lambda_L^{SW_Monitor}$) and does not include the effect of band specific neon wavelength offsets. Only the LWIR monitored laser wavelength reported in SDR packets should be used for quality control purposes to flag any excess laser wavelength drift since last CMO update.

Caution: If a data set processed by SDR algorithm does not contain the engineering packet and science telemetry packet that corresponds to the time of neon calibration, then the LWIR monitored laser wavelength is calculated relative to the laser diode temperature and current corresponding to 1st engineering packet and science telemetry that was actually processed. This does not yield the wavelength drift since last neon calibration.

7.4.3 Spectral Axis Labeling and Alias Unfolding

The spectral calibration module defines the spectral grid associated to each spectrum. Based on the latest laser diode wavelength estimate, the spectral grid spacing and the minimum wavenumber of the band are computed. The raw spectrum is then rotated the desired number of points to unfold the spectral alias that was introduced by filtering and decimation on-board the CrIS sensor. The unfolding is performed symmetrically about the band center. This yields a continuous spectrum free of alias fold points and with channel centers defined by the metrology sampling interval λ_s, decimation factor DF_b and the number of complex interferogram points processed N_b.

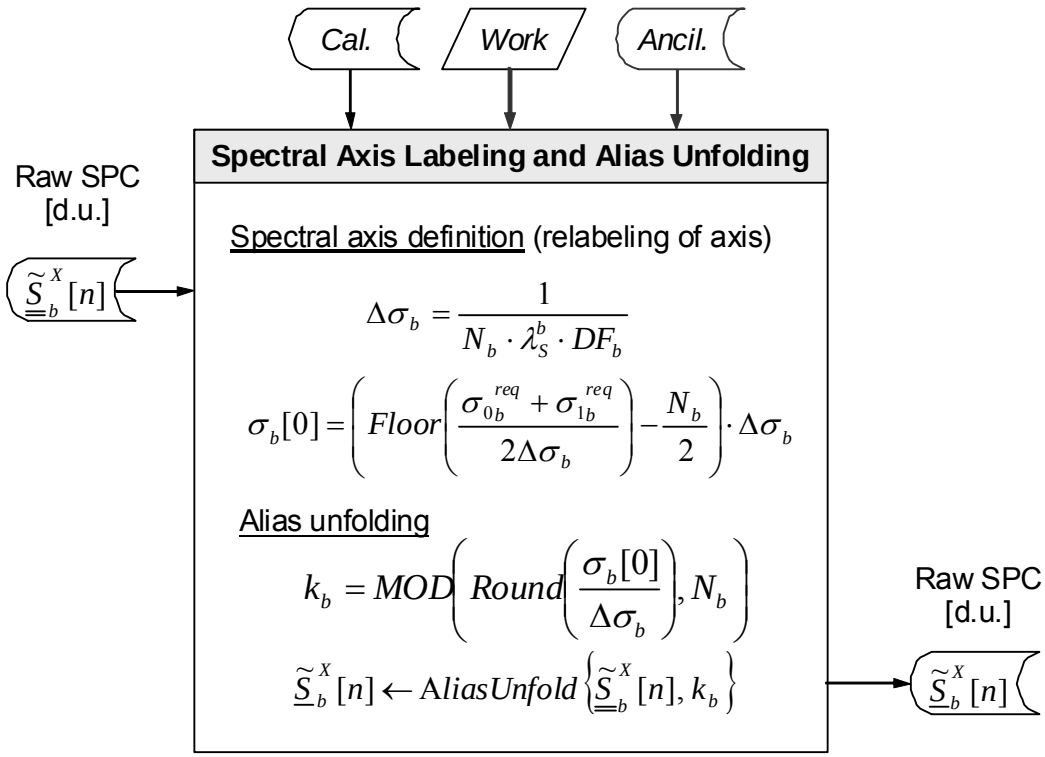

Figure 65: Spectral Axis Labeling and Alias Unfolding Flowchart

7.4.3.1 Definition of variables

Input variables

$\underline{\underline{\tilde{S}}}_b^X[n]$ raw complex spectrum in [d.u.] <u>prior</u> to alias unfolding, corresponding either to X = DS, ICT, or ES. These spectra have not yet been through non-linearity correction.

Calibration data

λ_S^b metrology sampling interval in band "b" [cm] ($\lambda_S^b = \lambda_L^b / 2 \approx 775 \times 10^{-7}\, cm$).
The sampling interval is half the laser metrology wavelength defined for each band

Ancillary data

σ_{0b}^{req} required minimum wavenumber channel center of 1st channel located in the pass band of band "b" for SDR output grid [cm^{-1}].
(i.e. LWIR = 650.000 cm^{-1}, MWIR = 1210.000 cm^{-1} & SWIR = 2155.000 cm^{-1})

σ_{1b}^{req} required maximum wavenumber channel center of last channel located in the pass band of band "b" for SDR output grid [cm^{-1}]
(i.e. LWIR = 1095.000 cm^{-1}, MWIR = 1750.000 cm^{-1} & SWIR = 2550.000 cm^{-1})

DF_b decimation factor used in band "b".

Local variables

k_b origin point of alias for band "b" used as an index to unfold spectrum and remove alias effect introduced by CrIS sensor signal processing

Output variables

$\underline{\tilde{S}}_b^X[n]$ raw complex spectrum in [d.u.] for band "b" <u>after</u> alias unfolding, corresponding to X = DS, ICT, or ES. These spectra have not yet been through non-linearity correction.

$\sigma_b[0]$ wavenumber corresponding to 1st channel center in band "b" on sensor wavenumber grid [cm^{-1}]. This is the wavenumber corresponding to the first channel center in the <u>guard band</u> prior to ILS correction. Also this is the first channel center in the IR spectrum after alias unfolding.

$\Delta\sigma_b$ channel spacing in band "b" for sensor wavenumber grid prior to ILS correction [cm^{-1}]. This will depend upon laser metrology wavelength.

Operators

$AliasUnfold\{V, k\}$ shifts a complex numerical vector V according to a given fold point k to eliminate the alias folding that was introduced on CrIS sensor.

7.4.3.2 Exception handling

None

7.5 RADIOMETRIC CALIBRATION

7.5.1 Radiometric Complex Calibration

Radiometric calibration transforms the digital count into radiance unit. The complex calibration process also permits the cancellation of the instrument phase. Polarization correction can also be applied if required.

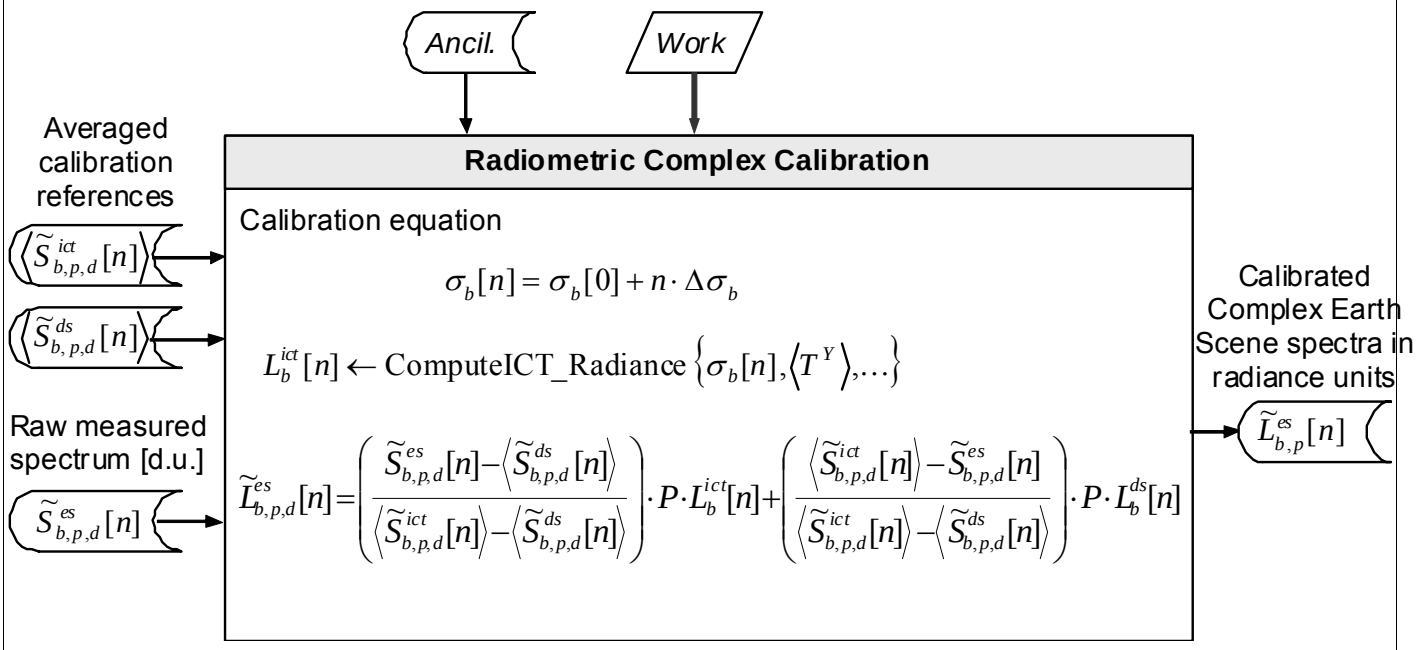

Figure 66: Radiometric Complex Calibration Flowchart

Radiometric complex calibration is essentially the computation of Equation (69), corresponding to a subtraction of the offset and a multiplication by the overall gain, as described in Section 5.3. The radiometric calibration is a point-by-point complex operation. All spectral arrays processed are complex, thus accounting for both magnitude and phase effects when performing this type of calibration. The data arrays used as input to this process have all undergone non-linearity correction in a prior step.

7.5.1.1 Definition of variables

Input variables

$\langle \widetilde{S}_{b,p,d}^{ds}[n] \rangle$ raw complex spectrum of deep space (DS) averaged over N^{ma} measurements, expressed in [d.u.] at channel center "n". This spectra has been corrected for non-linearity. Corresponds to band "b", FOV "p" and sweep direction "d"

$\langle \widetilde{S}_{b,p,d}^{ict}[n] \rangle$ raw complex spectrum of internal calibration target (ICT) averaged over N^{ma} measurements, expressed in [d.u.] at channel center "n". This spectra has been corrected for non-linearity. Corresponds to band "b", FOV "p" and sweep direction "d"

$\widetilde{S}^{es}_{b,p,d}[n]$ raw complex earth scene (ES) atmospheric spectrum measurement, expressed in [d.u.] at channel center "n". This spectra has been corrected for non-linearity. Corresponds to band "b", FOV "p" and sweep direction "d"

Calibration data

(see parameters in Section 7.5.2 for ICT radiance calculation).

Ancillary data (known from instrument characterization)

see description of ICT radiance parameters and calculation in Section 7.5.2

Work variables (from Moving Average module)

$\left\langle T^{Y} \right\rangle$ mean calculated for telemetry component Y [Kelvin]

(Y = SSM baffle temp, ICT PRT1 temp, ICT PRT2 temp, OMA1 temp, OMA2 temp).

Local variables

$\sigma_b[0]$ wavenumber of channel having n = 0 [cm^{-1}]

$\Delta\sigma_b$ channel spacing [cm^{-1}]

$\sigma_b[n]$ wavenumber of nth channel center (sensor wavenumber grid) in band "b" [cm^{-1}]

$L^{ict}_b[n]$ ICT radiance calculated from ICT model for n^{th} channel (sensor wavenumber grid) in band "b" [r.u.] …….(see section 7.5.2).

$L^{ds}_b[n]$ deep space target radiance calculated for n^{th} channel (sensor wavenumber grid) for band "b" [r.u.]. This term is not used for on-orbit operation per SDR config file setting. During TVAC operation, radiance is calculated using the DS target temperature & emissivity.

Output variables

$\widetilde{L}^{es}_{b,p}[n]$ calibrated complex (real and imaginary) earth scene radiance in the nth channel (sensor wavenumber grid) of FOV "p" in band "b" [r.u.]

flags → transfer FCE flags from DS, ICT, ES to SDR output.

Operators

P polarization of current earth scene view relative to ICT view. Each of 30 earth scene positions and space can have a different P. .Polarization correction is also segmented into 9 wavenumber regions spanning the 3 IR bands (9 table entries for each of the 30 earth positions plus deep space position). P values = 1.0 nominally. Values entered into engineering packet are (1 – P) in percent. This calibration feature not required on CrIS and is turned OFF via an SDR config file setting. There is no polarization calibration performed on the CrIS sensor during ground test.

ComputeICT_Radiance{} Function that computes ICT radiance from model inputs (see Section 5.4 & Section 7.5.2 for more details about this calculation)

7.5.1.2 Exception handling

The sweep direction "*d*" of the ICT and DS calibration spectra must be selected to match the sweep direction "*d*" of the earth scene when performing this calibration operation.

Incompatible sizes of signals: (i.e. number of points does not match between DS, ICT, and ES). This should not happen and is only an internal check.

Earth scene spectra tagged with an invalid flag are not processed (skipped) and do not generate a corresponding SDR output packet.

7.5.2 ICT Radiance Calculation

The radiometric model is used to calculate total ICT radiance due to direct emission from the ICT as well as reflection of radiance originating from the ICT external environment. The model uses an emissivity table for the ICT, emissivities of external surfaces, view factors to those surfaces and temperatures of the four most important contributors of radiance.

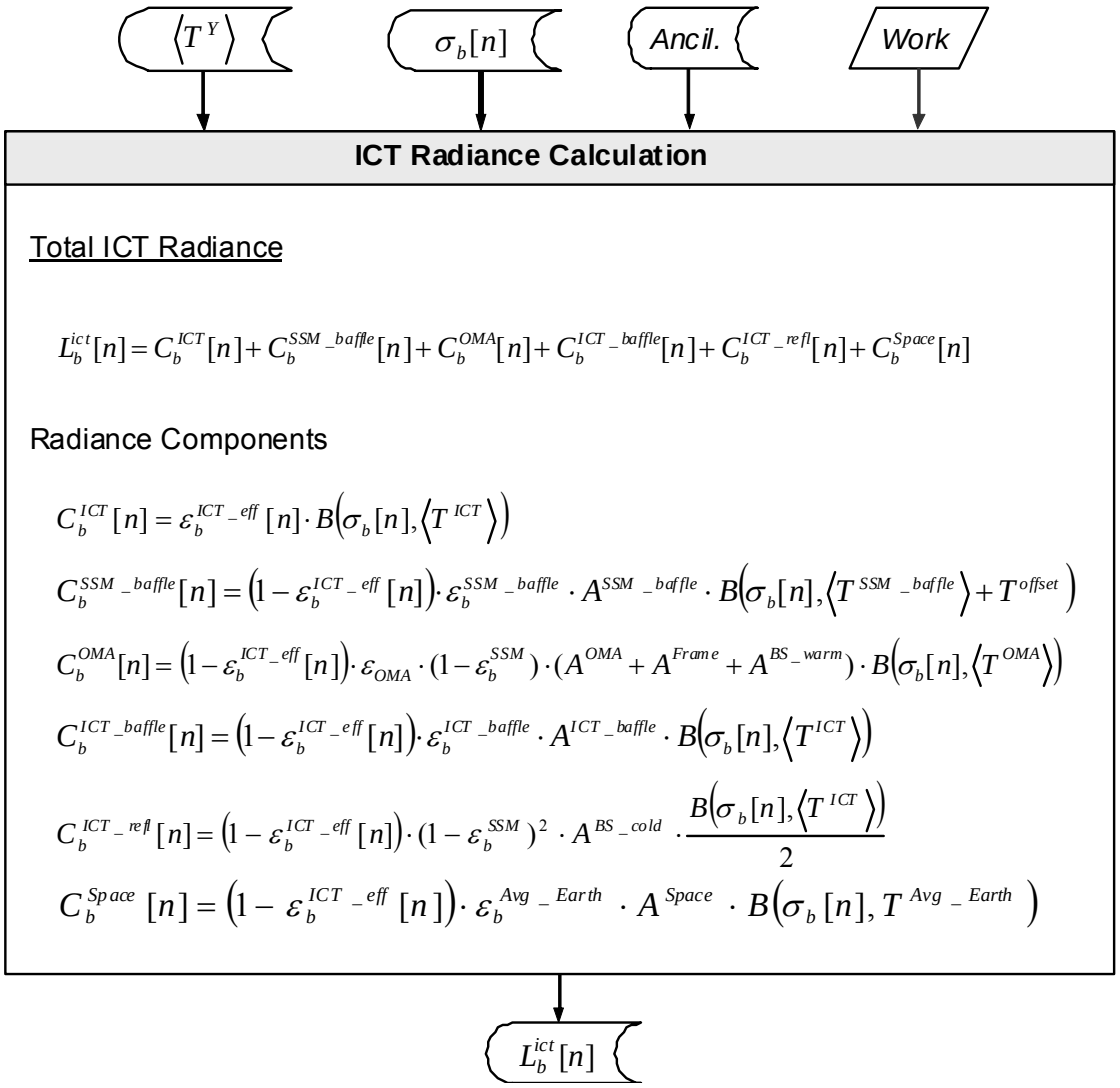

Figure 67: ICT Radiance Calculation

7.5.2.1 Definition of variables

Input variables

$\langle T^Y \rangle$ Mean calculated for telemetry component Y [Kelvin]
(Y = SSM baffle temp, ICT temp, OMA temp).

$\sigma_b[n]$ Wavenumber corresponding to n^{th} channel center in band "b" on sensor grid (cm^{-1}).

Calibration data from engineering packet

T^{offset}	The SSM baffle temperature will be corrected by this offset in Kelvin to account for differences between SSM baffle temperature sensor and temperature seen by the ICT bottom surface. This offset temperature is modeled as a function of orbit position and stored for reference in the CrIS engineering packet. See section 5.4.2.1 for details.
T^{Avg_earth}	Temperature of the earth (or SSM target for TVAC testing) expressed in Kelvin.
$\varepsilon_b^{ICT_eff}[n]$	ICT effective emissivity in n^{th} channel of band "b" on sensor wavenumber grid.
$\varepsilon_b^{SSM_baffl}$	Surface emissivity of the SSM baffle in band "b".
$\varepsilon_b^{ICT_baffle}$	Surface emissivity of the ICT baffle in band "b".
$\varepsilon_b^{Avg_Earth}$	Surface emissivity of the earth (or SSM target for ground testing) in band "b".
$\varepsilon_b^{\mathrm{SSM}}$	SSM scan mirror emissivity in band "b".
$\varepsilon_b^{\mathrm{OMA}}$	Opto-Mechanical Assembly surface emissivity in band "b".
A^{SSM_baffle}	View factor of ICT to SSM baffle & SSM mirror (fraction relative to total external environment)
A^{ICT_baffle}	View factor of ICT to ICT baffle (fraction relative to total external environment)
A^{Space}	View factor of ICT to earth (or SSM target during TVAC) (fraction relative to total external environment)
$A^{\mathrm{OMA}} + A^{Frame}$	View factor of ICT to OMA & frame (fraction relative to total external environment)
A^{BS_warm}	View factor of ICT to warm beamsplitter (fraction relative to total external environment)
$A^{\mathrm{BS_cold}}$	View factor of ICT to Cold Beamsplitter (fraction relative to total external environment)

Ancillary data

None required for this function

Work variables

None required for this function.

Local variables

$C_b^{ICT}[n]$	Direct ICT radiance emitted in n^{th} channel of band "b" [mW/m^2/sr/cm^{-1}]
$C_b^{SSM_baffle}[n]$	SSM baffle contribution to radiance in n^{th} channel of band "b" [mW/m^2/sr/cm^{-1}]
$C_b^{ICT_baffle}[n]$	ICT baffle contribution to radiance in n^{th} channel of band "b" [mW/m^2/sr/cm^{-1}]
$C_b^{OMA}[n]$	OMA, frame & warm beamsplitter contribution to radiance in n^{th} channel of band "b" [mW/m^2/sr/cm^{-1}]
$C_b^{ICT_refl}[n]$	Reflected ICT radiance from cold beamsplitter view in n^{th} channel of band "b" [mW/m^2/sr/cm^{-1}]
$C_b^{Space}[n]$	Earth radiance contribution (or SSM target during TVAC) in n^{th} channel of band "b" [mW/m^2/sr/cm^{-1}]

Output variables

$L_b^{ict}[n]$ Total ICT radiance in n^{th} channel on sensor wavenumber grid in band "b" [mW/m^2/sr/cm^{-1}]

Operators

$$B(\sigma, T) = \frac{c_1 \sigma^3}{e^{(c_2 \sigma / T)} - 1}$$

Planck function having the radiation constants:

$$c_1 = 1.1910427 \times 10^{-5} \ \mathrm{cm^3 m}W/(\mathrm{m^2 cm^{-1}})$$

$$c_2 = 1.4387752 \quad K\,\mathrm{cm}$$

7.5.3 Spectrum Correction

This is a sub module of the radiometric calibration module. It combines in one operation the post calibration filter, resampling to the user grid, correction for off-axis self apodization, correction for residual ILS error due to modulation efficiency versus OPD and applies user selected apodization. The spectral correction takes the form of a matrix, which is applied to each spectra following radiometric calibration.

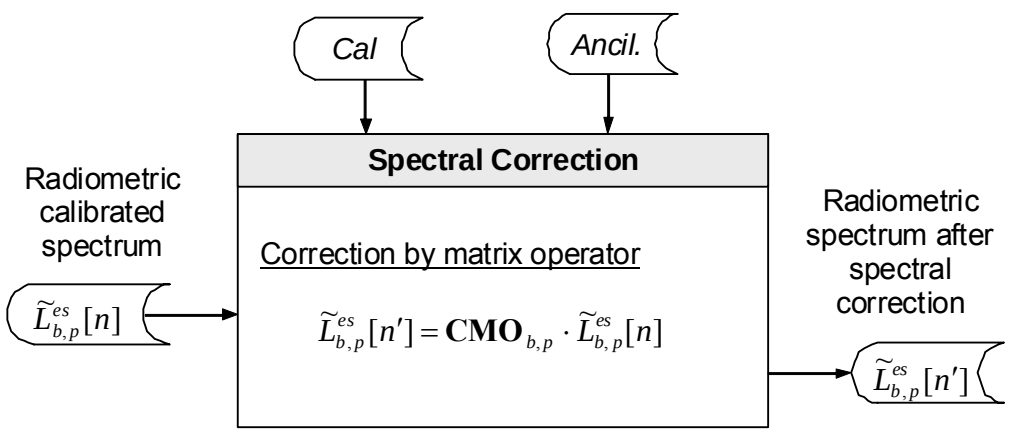

Figure 68: Spectral Correction Flowchart

7.5.3.1 Definition of variables

Input variables

$\widetilde{L}_{b,p}^{es}[n]$ Complex (real and imaginary) calibrated radiance of earth scene in n^{th} channel on sensor spectral grid for FOV "p" in band "b". This complex input spectrum has already undergone non-linearity correction and FCE correction.

Calibration data

$\mathbf{CMO}_{b,p}$ real spectral correction matrix operator for FOV "p" in band "b" (see Section 3.8, Section 7.5.3.2 and Figure 69)

Ancillary data

None required for this function

Output variables

$\widetilde{L}^{es}_{b,p}[n']$ Complex calibrated radiance of earth scene in n^{th} channel on SDR expanded user grid for FOV "p" in band "b". The last operation consists in truncating to the defined EDR user's grid (not shown here).The resulting output spectrum has undergone radiometric calibration, non-linearity correction, FCE correction and all spectral corrections. Only the real part of this spectrum should contain valid science data and the imaginary part can be discarded later by the user if desired.

7.5.3.2 CMO computation

This subsection describes the computation of the correction matrix operator $\mathbf{CMO}_{b,p}$.

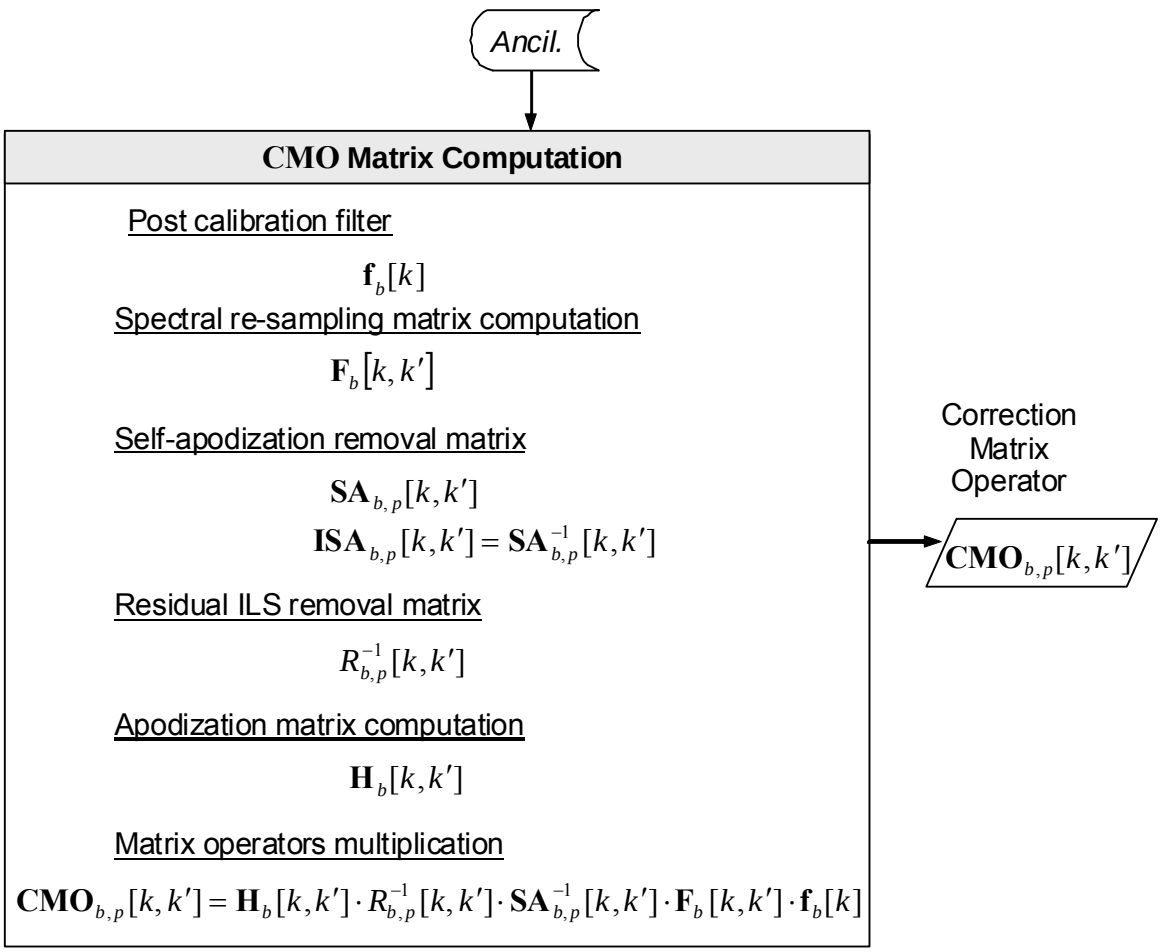

Figure 69: Self-Apodization Matrix Operator Computation

Definition of variables

Input variables

$\lambda_L^{b_CMO}$ Laser metrology wavelength in band "b" calculated from neon calibration data in engineering packet (see Section 7.4.1)

Calibration data from engineering packet (ILS parameters)

27 in-track FOV offsets relative to FOV 5 [urad]
27 cross-track FOV offsets relative to FOV 5 [urad]
3 in-track FOV 5 offsets [urad]
3 cross-track FOV 5 offsets [urad]
27 FOV widths [urad]
27 sets of residual ILS parameters with 5 values (C0, C1, C2, C3, C4) in each set

Ancillary data

N_b Number of output spectral bins for each band (from configuration file)

$a_0, a_1, a_2, a_3,$ Blackman-Harris apodization parameters (from SDR configuration file)

a ,Hamming apodization parameters (from SDR configuration file)

$\lambda_S^b(opt)$ Effective sampling interval in band "b" needed to produce user grid.
$\lambda_S^b(opt) = 2 \cdot MPD_b^{req} / N_b$

Local variables

k Row index for matrix

k' Column index for matrix

$f_b[k]$ Post calibration filter defined for each band (see section 3.6.5)

$F_b[k,k']$ Spectral resampling/interpolator matrix operator (see section 3.5)

$SA_{b,p}^{-1}[k,k']$ Self-apodization removal matrix operator (see Section 3.6.2)

$R_{b,p}^{-1}[k,k']$ Residual ILS matrix removal operator (see section 3.6.4)

$H_b[k,k']$ Hamming or Blackman-Harris apodization matrix operator (see Section 3.7)

$\lambda_S^{b_CMO}$ Interferogram sampling interval in band "b" used in $F_b[k,k']$ matrix formulation and defined by $\lambda_S^{b_CMO} = \dfrac{\lambda_L^{b_CMO}}{2}$

Output of Process

$\mathbf{CMO}_{b,p}[k,k']$ Correction Matrix Operator for FOV "p" in band "b".

7.5.3.3 Exception handling

See Section 3.8 for exceptions and rules when to update CMO.

7.5.4 Non-linearity Correction

Non-linearity correction scales the raw uncalibrated spectra for the Earth scene, deep space, and ICT views prior to the complex calibration to correct for the detector's non-linearity.

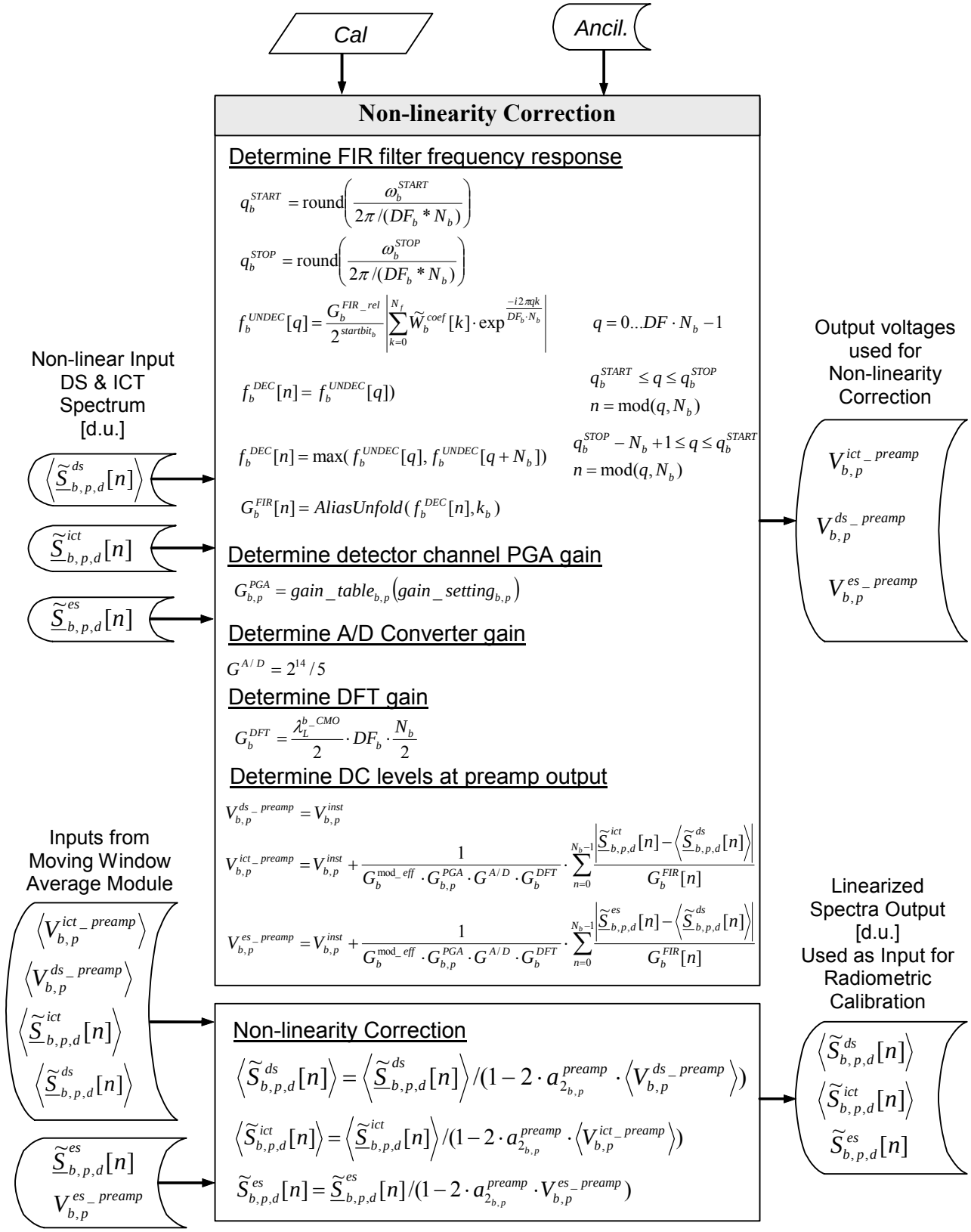

Figure 70: Non-linearity Correction Flowchart

7.5.4.1 Definition of variables

Input variables

$\left\langle \underline{\widetilde{S}}^{ds}_{b,p,d}[n] \right\rangle$ Uncalibrated complex deep space (DS) spectrum for FOV "p" in band "b" and sweep direction "d" prior to nonlinearity correction [d.u.]. N^{ma} measurements averaged.

$\left\langle \underline{\widetilde{S}}^{ict}_{b,p,d}[n] \right\rangle$ Uncalibrated complex (ICT) spectrum for FOV "p" in band "b" and sweep direction "d" prior to nonlinearity correction [d.u.]. N^{ma} measurements averaged.

$\underline{\widetilde{S}}^{es}_{b,p,d}[n]$ Uncalibrated complex earth scene (ES) spectrum for FOV "p" in band "b" and sweep direction "d" prior to nonlinearity correction [d.u.]. No averaging.

$\left\langle V^{ict_preamp}_{b,p} \right\rangle$ Average preamp DC voltage from photo flux and dark current when viewing ICT in FOV "p" of band "b". Computed from AC interferogram. Averaged in moving window average module.

$\left\langle V^{ds_preamp}_{b,p} \right\rangle$ Average preamp DC voltage from photo flux and dark current when viewing DS in FOV "p" of band "b". Obtained from V^{inst} parameter in engineering packet. Averaged by moving window average module.

Calibration data from engineering packet

$a^{preamp}_{2_{b,p}}$ Non-linearity correction parameter at preamp output for FOV "p" in band "b" [Volt^{-1}]

$V^{inst}_{b,p}$ Non-linearity correction parameter – preamp DC output voltage due to background and dark current for FOV "p" in band "b" [Volt]

$G^{FIR_rel}_{b}$ FIR filter coefficient gain relative to $\widetilde{W}^{FIR}_{b}[k]$ coefficients stored in SDR configuration file. This parameter = 1.0 for FM1. May change for subsequent instrument

$G^{\mathrm{mod}_eff}_{b,p}$ Interferometer modulation efficiency for FOV "p" in band "b"

$startbit_b$ Number of unneeded lower order bits discarded during bit trim in band "b"

$gain_table_{b,p}$ PGA conversion coefficients for FOV "p" in band "b"

$gain_setting_{b,p}$ PGA settings for FOV "p" in band "b"

N_b Number of decimated interferogram or spectral points for band "b". Calculated from information in bit trim parameter list in engineering packet.

DF_b Decimation factor for band "b"

Ancillary data from SDR configuration file

$\widetilde{W}^{FIR}_{b}[k]$ Complex FIR filter coefficients for band "b", $0 \le k \le 254$

ω^{START}_{b} Normalized frequency (0 to 2π) at lower band edge for band "b" at which the FIR filter meets the passband ripple design specification

ω_b^{STOP} Normalized frequency (0 to 2π) at upper band edge for band "b" at which the FIR filter meets the passband ripple design specification

Work variables

k_b Value of FIR filter bin index in band "b" used as rotation point to unfold the FIR filter decimation boundary. As computed in Section 7.4.3, & Figure 65.

$\lambda_L^{b_CMO}$ Laser metrology wavelength in band "b" calculated from neon calibration data in engineering packet (see Section 7.4.1)

Local variables

$G_b^{FIR}[n]$ FIR filter magnitude response in band "b" for DFT index [n]. [counts/ count]

$G_{b,p}^{PGA}$ PGA gain for band "b", FOV "p", [volts/volt]

$G^{A/D}$ A/D Converter conversion constant, [counts/volt]

G_b^{DFT} DFT gain for band "b", [counts/count]

$V_{b,p}^{es_preamp}$ DC output of preamp from detector current while viewing Earth Scene in band "b", FOV "p", [volts]

$V_{b,p}^{ict_preamp}$ DC output of preamp from detector current while viewing ICT in band "b", FOV "p", [volts]

$V_{b,p}^{ds_preamp}$ DC output of preamp from detector current while viewing deep space in band "b", FOV "p", [volts]. This value is constant and is stored in engineering packet.

Output variables

$\left\langle \widetilde{S}_{b,p,d}^{ds}[n] \right\rangle$ Complex deep space (DS) spectrum after linearity correction, averaged over N^{ma} measurements for band "b", FOV "p" and sweep direction "d" [d.u.].

$\left\langle \widetilde{S}_{b,p,d}^{ict}[n] \right\rangle$ Complex ICT spectrum after linearity correction, averaged over N^{ma} measurements for band "b", FOV "p" and sweep direction "d" [d.u.].

$\widetilde{S}_{b,p,d}^{es}[n]$ Complex Earth Scene spectrum after linearity correction for band "b", FOV "p" and sweep direction "d" [d.u.].

Operators

$gain_table_{b,p}(gain_setting_{b,p})$ Function that converts a HEX PGA gain setting into electrical gain for band "b", FOV "p" in units of volt per volt (Four-minute Engineering Packet).

$\max(f_b^{UNDEC}[q], f_b^{UNDEC}[q+N_b])$ Used to form the maximum of every element from two vectors having same dimension. In this case, used to form the maximum FIR filter

frequency response in the FIR filter stop band due to aliased FIR filter response overlapping in that region.

$AliaUnfold\ (f_b^{DEC}[n], k_b)$ Used to unfold the decimated FIR filter response to match the unfolding that was performed on the CrIS signal spectrum. k_b is the index where folding occurs.

7.5.4.2 Exception handling

This module shall provide one status flag bit, NL_correction_requested, indicating that non-linearity correction has been enabled and successfully executed. (If moving window data insufficient, then flag is set low).

7.6 QUALITY CONTROL

7.6.1 NEdN Estimation

Estimating NEdN is part of the Quality Control module as depicted in Figure 71. The NEdN estimate is based on ICT measurements which have been collected within the moving window averaging interval (CrIS uses a 4 minute window yielding 30 ICT measurements). The calibrated ICT measurements provide ability to calculate "actual" NEdN based on the stable ICT target temperature. A "smoothing" function is employed in the spectral domain to further average the NEdN estimate over 17 adjacent spectral bins. The number of bins used to smooth the estimate can be set in the SDR Algorithm configuration file. The NEdN estimate is calculated on the sensor wavenumber grid and then interpolated to the output SDR wavenumber grid.

The NEdN calculation is similar to the radiance calculation done for earth scenes as previously depicted in Figure 66. However, the NEdN calculation uses ICT spectra in place of earth scene spectra and spectra that have not yet been corrected for nonlinearity. The deep space radiance is also accounted for in this calculation in order to produce acurrate NEdN estimates during ground test.

When the NEdN estimate function is turned ON, the NEdN estimate is calculated based upon calibration target views. Therefore, the estimate is only updated once every 8 seconds when a new set of calibration data is collected. The result is reported in all SDR packets including earth scenes. This calculation can be disabled if desired. If disabled, then the reported NEdN is zero in SDRs.

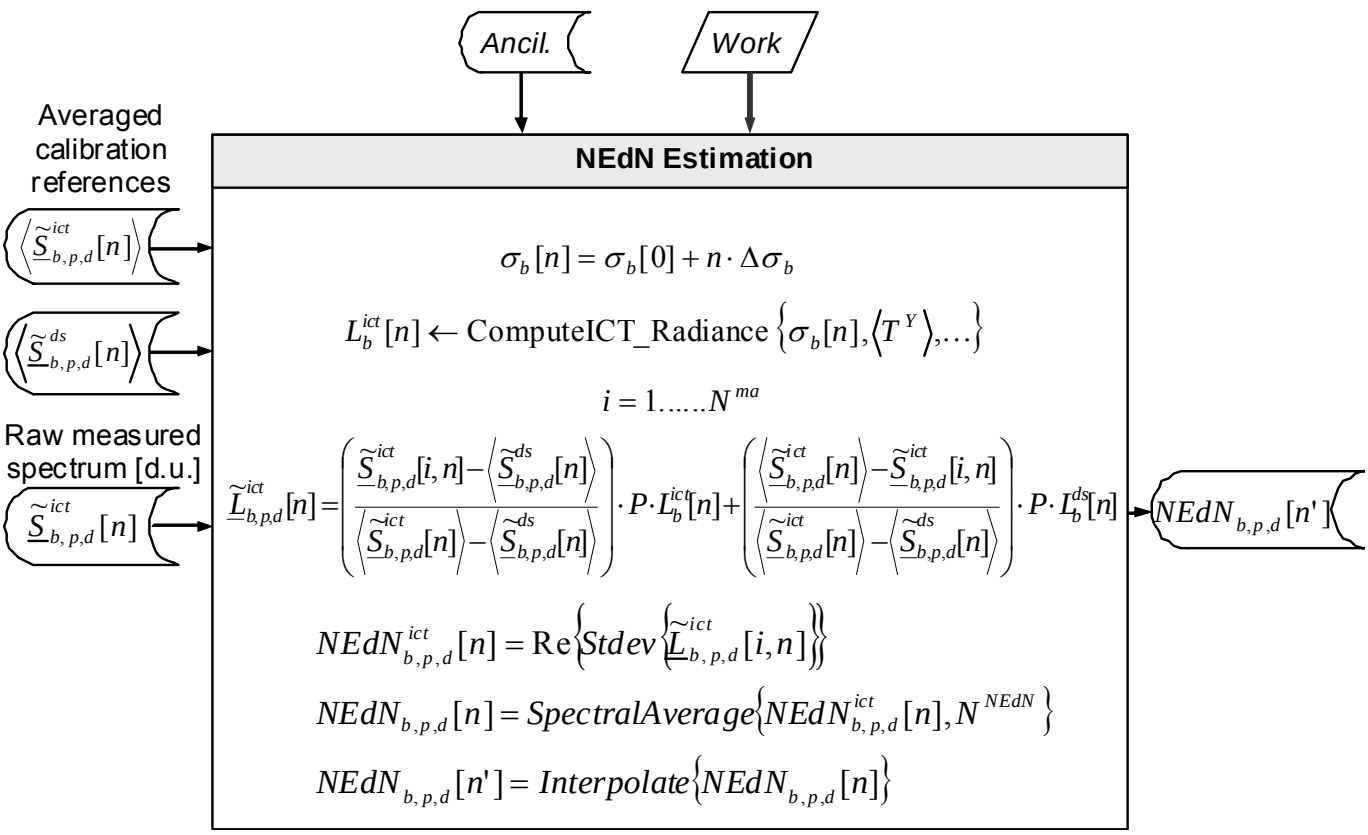

Figure 71: NEdN Estimation Flowchart

7.6.1.1 Definition of variables

Input variables

$\left\langle \underline{\widetilde{S}}^{ds}_{b,p,d}[n] \right\rangle$ Raw complex spectrum of deep space (DS) averaged over N^{ma} measurements expressed in [d.u.] at channel center "n". This spectrum has not been corrected for non-linearity. Corresponds to band "b", FOV "p" and sweep direction "d"

$\left\langle \underline{\widetilde{S}}^{ict}_{b,p,d}[n] \right\rangle$ Raw complex spectrum of internal calibration target (ICT) averaged over N^{ma} measurements expressed in [d.u.] at channel center "n". This spectrum has not been corrected for non-linearity. Corresponds to band "b", FOV "p" and sweep direction "d"

$\underline{\widetilde{S}}^{ict}_{b,p,d}[i,n]$ Raw complex spectrum of internal calibration target (ICT) expressed in [d.u.] at channel center "n". This spectra has not been corrected for non-linearity. Corresponds to band "b", FOV "p" and sweep direction "d" for i^{th} element in moving window.

Calibration data from engineering packet

See parameters in Section 7.5.2 for ICT radiance calculation.

Ancillary data (from SDR configuration file)

N^{NEdN} Number of spectral bins used to perform NEdN spectral smoothing (default = 17). This parameter must be an odd number in config file.
Also see description of ICT radiance parameters and calculation in Section 7.5.2

Work variables (from Moving Average module)

$\left\langle T^{Y} \right\rangle$ mean calculated for telemetry component Y [Kelvin]
(Y = SSM baffle temp, ICT PRT1 temp, ICT PRT2 temp, OMA1 temp, OMA2 temp).

Local variables

$\sigma_b[0]$ Wavenumber of channel having n = 0 [cm^{-1}]

$\Delta\sigma_b$ Channel spacing on sensor wavenumber grid [cm^{-1}]

$\sigma_b[n]$ Wavenumber of nth channel center (sensor wavenumber grid) in band "b" [cm^{-1}]

$L^{ict}_b[n]$ ICT radiance calculated from ICT model for n^{th} channel (sensor wavenumber grid) in band "b" [mW/m^2/sr/cm^{-1}]. …….(see section 7.5.2).

$\underline{\widetilde{L}}^{ict}_{b,p,d}[i,n]$ Complex calibrated ICT radiance for i^{th} sample in moving window [mW/m^2/sr/cm^{-1}]. The calibrated radiance corresponds to FOV "p" and sweep direction "d" for n^{th} channel center in band "b". This ICT radiance has not been corrected for non-linearity.

$NEdN^{ict}_{b,p,d}[n]$ NEdN in n^{th} channel of band "b" for FOV "p" and sweep direction "d". This NEdN estimate is based upon the standard deviation of the real part of the complex ICT

radiance for spectra within the moving window. No spectral averaging. This value is calculated on channel centers associated with the sensor wavenumber grid.

Output variables

$NEdN_{b,p,d}[n']$ NEdN estimate for n^{th} channel on SDR wavenumber output grid. A NEdN estimate is provided for band "b", FOV "p" and sweep direction "d". This NEdN estimate is based upon the standard deviation of the ICT radiance for spectra within the moving window and then spectrally smoothed by using an averaging boxcar window of length N^{NEDN} symmetric about the channel center (default, N^{NEDN} =17). The spectral channels reported are clipped to match the number of earth scene channels reported.

Operators

$Interpolate\{\ \}$ DIAG mode cubic spline interpolation method. Interpolates NEdN result from sensor wavenumber grid "n" to SDR output wavenumber grid n'

7.6.2 Fringe Count Error Handling

This module detects and corrects FCE in raw spectrum measurements. If the input is a calibration measurement (ICT, DS), then the ratio is taken between this spectrum and the corresponding current mean. In the case of an earth scene (ES) measurement, a slightly different, but equivalent, approach is taken.

In the case of a detected FCE mismatch, the current means are shifted back to the present measure, which defines the current FCE alignment. If a slope error is flagged in a calibration measurement, indicating a mismatch of some sort, no corrective approach is taken. This is done in order to avoid contaminating the moving average with a single erroneous event.

A general description of the process is given in Section 3.3.4. Fringe count error detection and correction are explained in more details in following 2 sections.

7.6.3 Fringe Count Error Detection

The Fringe Count Error Handling module analyzes incoming raw spectra to ensure their phase compatibility before the computation of radiometric calibration. It is necessary to detect fringe count errors before the co addition of equivalent signals, and before the combination of calibration measurements to the scene measurement. Thus, the detection procedure interacts with the moving average procedure. In the case where a fringe count error is detected, previous signals are shifted to the current signal. This way, all the following interferograms will have the same fringe count ordering. With its validity checks, this robust method is independent of the inherent signal decimation, and works for any pixel

The FCE detection is performed in LW band, starts in FOV1 and progresses from FOV to FOV in the band until there is a successful detection. The calculated correction is applied to all FOVs and bands of that field of regard for the Porch Swing Direction (PSD). The order of detection tries are as follows LW1, LW2, …LW9. The FOVs with no data are skipped. MW and SW data are not used for FCE detection.

The variable h^{cur} is the fringe count alignment reference for the calibration measurements. It is used to keep the alignment deficiency between the current instrumental FCE and the moving window elements. After the resetting of the moving window elements for a given calibration category, this variable is reset to zero. This correction scheme is devised in order to minimize the re-shifting of the moving average windows, which need to be aligned only during the moving average updates. Note: The three kinds of scenes will be on the same grid, following the assumption that the sampling wavenumber remains stable within the 2 ppm requirement.

The FCE detection module analyzes the phase of raw spectra to establish if there was a fringe count error. It performs the low level computation of linear phase extraction from a complex input function $\widetilde{R}_{LW}[n]$. A general description of the process is given in Section 3.3.3. This algorithm is function of $\widetilde{R}_{LW}[n]$ as well as the current laser metrology sampling length $\lambda_S^{LW_CMO}$.

For the LWIR band, the input spectral function $\widetilde{R}_{LW}[n]$ is defined as follows (see Section 3.3):

For *Calibration Measurements* with X = ICT or DS and b = LW

$$\underline{\widetilde{R}}_{b,p,d}^{X}[n] = \frac{\underline{\widetilde{S}}_{b,p,d}^{X}[n]}{\left\langle \underline{\widetilde{S}}_{b,p,d}^{X}[n] \right\rangle} \tag{100}$$

For *Earth Scenes* with X = ES and b = LW

$$\underline{\widetilde{P}}_{b,p,d}^{es}[n] = \frac{\underline{\widetilde{S}}_{b,p,d}^{es}[n]}{\left\langle \underline{\widetilde{S}}_{b,p,d}^{ict}[n] \right\rangle - \left\langle \underline{\widetilde{S}}_{b,p,d}^{ds}[n] \right\rangle} \tag{101}$$

$$\underline{\widetilde{Q}}_{b,p,d}^{ds}[n] = \frac{\left\langle \underline{\widetilde{S}}_{b,p,d}^{ds}[n] \right\rangle}{\left\langle \underline{\widetilde{S}}_{b,p,d}^{ict}[n] \right\rangle - \left\langle \underline{\widetilde{S}}_{b,p,d}^{ds}[n] \right\rangle} \tag{102}$$

$$\underline{\widetilde{R}}_{b,p,d}^{es}[n] = \frac{\underline{\widetilde{P}}_{b,p,d}^{es}[n]}{\pm\sqrt{\left|\underline{\widetilde{P}}_{b,p,d}^{es}[n]\right|^2 - \left(\mathrm{Im}\left\{\underline{\widetilde{Q}}_{b,p,d}^{ds}[n]\right\}\right)^2} + i\ \mathrm{Im}\left\{\underline{\widetilde{Q}}_{b,p,d}^{ds}[n]\right\}} \tag{103}$$

The SDR algorithm uses only the positive square root term to implement the phase extraction function equation (103).

For this last computation, it is assumed that the calibration measurements are aligned on the same ZPD count. This wouldn't be the case in the very unlikely case where a fringe count error would occur between the first two calibration measurements. Even if this would occur, the health monitoring module will detect the non-linear result and problematic calibrated scenes will be flagged accordingly.

In order to improve the accuracy of the linear fitting, data points with a too low SNR for ICT and DS spectra must be rejected. The present method selects points with a pre-defined amplitude reference threshold $A^{\mathrm{Re}f_thres}$ parameter. A typical value for the Amplitude Threshold Rejection Limit $A^{\mathrm{Re}f_thres}$ is 0.25.

In order to improve the accuracy of the linear fitting for earth scene spectra the present method requires the earth scene spectral magnitude in each FFT bin to be larger than the magnitude of the instrument background when viewing deep space. A pre-defined amplitude reference threshold A^{Cal_thres} parameter is used to establish this minimum value relative to deep space. A typical value for the Amplitude Calibration Rejection Limit A^{Cal_thres} is 1.05.

Ancil. *Work*

FCE Detection

Average calibration spectra

$\left\langle \underline{\tilde{S}}^{ict}_{b,p,d}[n] \right\rangle$

$\left\langle \underline{\tilde{S}}^{ds}_{b,p,d}[n] \right\rangle$

Unaveraged Spectra

$\underline{\tilde{S}}^{ds}_{b,p,d}[n]$

$\underline{\tilde{S}}^{ict}_{b,p,d}[n]$

$\underline{\tilde{S}}^{es}_{b,p,d}[n]$

Compute phase (for b = LW only)

$$\underline{\tilde{R}}^{X}_{b,p,d}[n] \leftarrow \text{PixelFCE_Preparation}\left\{\underline{\tilde{S}}^{es}_{b,p,d}[n], \left\langle \underline{\tilde{S}}^{ict}_{b,p,d}[n] \right\rangle, \left\langle \underline{\tilde{S}}^{ds}_{b,p,d}[n] \right\rangle, \ldots\right\}$$

$$\varphi^{X}_{b,p,d}[n] \leftarrow \text{atan2}\left\{\text{Im}\left\{\underline{\tilde{R}}^{X}_{b,p,d}[n]\right\}, \text{Re}\left\{\underline{\tilde{R}}^{X}_{b,p,d}[n]\right\}\right\}$$

$$\varphi^{X}_{b,p,d}[n] \leftarrow \text{PhaseUnwrap}\left\{\varphi^{X}_{b,p,d}[n]\right\}$$

Extract phase versus channel (b = LW only)

$$p = \text{Index}\left\{\frac{\left|\underline{\tilde{R}}^{X}_{b,p,d}[n]\right|}{\text{Max}\left(\left|\underline{\tilde{R}}^{X}_{b,p,d}[n]\right|\right)} > A^{\text{Ref_thres}}\right\} \quad \text{When X = DS or ICT}$$

$$p = \text{Index}\left\{\frac{\left|\underline{\tilde{S}}^{es}_{b,p,d}[n]\right|}{\left|\left\langle \underline{\tilde{S}}^{ds}_{b,p,d}[n] \right\rangle\right|} > A^{Cal_thres}\right\} \quad \text{When X = ES}$$

$$\sigma_b[p] = \sigma_b[0] + p \cdot \Delta\sigma_b$$

$$\varphi^{X}_{b,p,d}\Big|_{\sigma=0}, \Delta\varphi^{X}_{b,p,d} \leftarrow \text{LinearFit}\left\{\varphi^{X}_{b,p,d}[p], \sigma_b[p]\right\}$$

Compute Fringe Count

$$h^{X}_{b,p,d} = \frac{\Delta\varphi^{X}_{b,p,d}}{2\pi\,\lambda_S^{b_CMO}}$$

$$h^{cur} = \text{floor}\left\{h^{X}_{b,p,d} + 0.5\right\}$$

Validity check (X = DS, ICT, ES and b = LW)

if $\left|h^{X}_{b,p,d} - h^{cur}\right| > h^{thres}$ flag fractional FCE

if $\left|h^{cur}\right| > h^{\max}$ flag excess FCE

$$\left\langle s^2 \right\rangle = Ave\left(\varphi^{X}_{b,p,d}[p] - \left(\Delta\varphi^{X}_{b,p,d} \cdot \sigma_b[p] + \varphi^{X}_{b,p,d}\Big|_{\sigma=0}\right)\right)^2\Bigg|_{\text{Valid [p]}}$$

if $\left\langle s^2 \right\rangle > s^{thres}$ flag goodness of fit error

if $\text{Length}\{p\}/N_b < N^{thres}$ flag dimension error

Current FCE

h^{cur}

Flags

Correction Failed
FCE Detect
FCE Corrected
FCE > threshold

Figure 72: Fringe Count Error Computation Flowchart

7.6.3.1 Definition of variables

Input variables

$\underline{\widetilde{S}}^{es}_{b,p,d}[n]$ Complex earth scene spectrum with a potential FCE prior to non-linearity correction. Uncalibrated instrument counts for n^{th} channel on sensor wavenumber grid for FOV "p", sweep direction "d" and LWIR band (b = LWIR)

$\underline{\widetilde{S}}^{ict}_{b,p,d}[n]$ Complex ICT spectrum with a potential FCE prior to non-linearity correction. Uncalibrated instrument counts for n^{th} channel on sensor wavenumber grid for FOV "p", sweep direction "d" and LWIR band (b = LWIR)

$\underline{\widetilde{S}}^{ds}_{b,p,d}[n]$ Complex DS spectrum with a potential FCE prior to non-linearity correction. Uncalibrated instrument counts for n^{th} channel on sensor wavenumber grid for FOV "p", sweep direction "d" and LWIR band (b = LWIR)

Calibration data from engineering packet

None

Ancillary data from SDR configuration file

$A^{\mathrm{Re}f_thres}$ Amplitude threshold rejection limit for DS or ICT (typically 0.25).

A^{Cal_thres} Amplitude threshold rejection limit for earth scene relative to DS (typically 1.05).

h^{thres} Fractional FCE threshold limit (typically 0.1).

$h^{\max}$ Maximum expected FCE (typically 18).

s^{thres} Goodness of linear fitting threshold limit (typically 0.004).

N^{thres} Relative number of points to fit inferior limit (typically 0.2).

Work variables (from Compute Spectrum module)

$\widetilde{R}^{X}_{b,p,d}[n]$ Phase extraction function from which linear phase dependency is computed. Phase in n^{th} channel for FOV "p", sweep direction "d" in LWIR band (b = LWIR). X = DS, ICT & ES.

$\lambda_S^{LW_CMO}$ Sampling interval used in the construction of CMO for LWIR band

Local variables

$\varphi^{X}_{b,p,d}[n]$ phase of the $\underline{\widetilde{R}}^{X}_{b,p,d}[n]$ function after 2π unwrap at each channel center "n" in band "b", FOV "p" and sweep direction "d" [radian]. X = DS, ICT or ES. b = LWIR

p Vector containing indexes used to perform linear fit. Channel centers having insufficient signal magnitude are thereby rejected and not included in the fitting process.

$\varphi^{X}_{b,p,d}\Big|_{\sigma=0}$ Linear fit y-intercept . Phase in radians at zero wavenumber. Value corresponds to band "b", FOV "p" in sweep direction "d". X = DS, ICT or ES.

$\Delta\varphi^{X}_{b,p,d}$ Linear fit slope. Change of phase versus wavenumber. [radian/cm^{-1}] Value corresponds to band "b", FOV "p" in sweep direction "d". X = DS, ICT or ES.

s^2 Square of standard deviation for the goodness of fit indicator.

Output variables

h^{cur} Integer fringe count error of current input signal

Output flags

Correction Failed	Set if none of the 9 LWIR FOVs validated If DS & ICT scene, then marked invalid If earth scene, then processed without FCE correction
FCE detect	Set if FCE ≠ 0 or FCE = 0 & any of the four validations failed
FCE corrected	Set if FCE ≠ 0 and phase correction applied to spectrum
FCE > threshold	Set if detected FCE too large (i.e. > 18 counts)

Operators

$\mathrm{Index}\{n\}$ Builds vector "p" of index values from "n" that satisfy inequality

$\mathrm{PixelFCE_Preparation}\{\}$ Computes the phase extraction function $\underline{\tilde{R}}^{X}_{b,p,d}[n]$ according to equations 100 through 103.

$\mathrm{PhaseUnwrap}\{\ \}$ Removes phase jumps in signal in case it exceeds the range [$-\pi$,$+\pi$]. Compensations of $\pm 2\pi$ are added to the phase where discontinuities (absolute difference greater than 2π) are noticed between two consecutive points.

$\mathrm{LinearFit}\{\mathrm{y, x}\}$ Computes a linear fit on data points of array y, given together with its associated abscissa wavenumber values x (not uniformly distributed). See Appendix 9.3. Returns a y-intercept and slope

7.6.3.2 Exception handling

See explanation of status flags in Table 22.

7.6.4 Fringe Count Error Correction

Application of FCE correction is discussed in Section 7.3.2 and Figure 62.

7.6.5 Data Quality Indicators

The SDR Algorithm compiles data contamination error flags and various types of exception sets by each of the data processing modules. Quality Control is assured by the gathering of all various processing quality checks corresponding to output data. Table 21 and Table 22 summarize the data quality control performed or handled by the SDR Algorithm.

Table 21: RDR Quality Flags in RDR Status Word

RDR Quality Flag	Bit	Value	Description and Handling
	11-15		Spare bits (unused)
Bit Trim Failed	10		If set at least one sample in the interferogram was clipped during the bit trimming process; the interferogram is excluded from processing.
Fringe Count Error Detect	9		If set a significant number of fringes have been missed shifting the interferogram ZPD outside of a window monitored by the instrument; the interferogram is excluded from processing.
Invalid Data	8		If set the instrument has invalid data, the interferogram is excluded from processing.
Impulse Noise Count	0-7		Represents the number of samples in the interferogram that exceeded the impulse noise mask and were set to zero; if > 1 the resultant spectrum is flagged as having excess noise (NEdN). This tolerance is configurable.

Table 22: SDR Quality Flags

SDR Quality Flag	Value	Description and Handling
Linearity correction	0-1	0 = no correction 1 = non-linearity correction was applied
Lunar Intrusion	0-1	If set, then at least one spectrum in the Deep Space moving average was invalidated due to a lunar intrusion. This flag is specific to each detector by FOV and band
User Apodization selected	0-2	0 = Blackman_Harris 1 = Hamming 2 = None
Invalid Geolocation	0-1	If set the geolocation information included in the SDR is invalid.
Calibration Type	0-1	0= not calibrated 1= complex calibration
Invalid Radiometric Cal	0-1	This flag not supported (inactive)
Excess NEdN	0-1	If set, the Impulse Noise Count in the RDR was greater than the configurable tolerance.
Excess Thermal Drift	0-1	Set if any of the monitored instrument temperatures drifted more than the allowed value specified in engineering packet.
Suspect Neon Spectral Cal	0-1	Set if the Neon calibration data reported in the 4 minute engineering packet did not yield a valid laser wavelength. CMO was not updated at last neon cal.
FCE Exceeds Threshold	0-1	Set if the calculated number of fringe losses exceeds the maximum allowed as defined in SDR config file.
FCE Correction Failed	0-1	Set if the phase of the spectrum could not be corrected. Unable to validate the FCE detection that was made.
FCE Corrected	0-1	Set if a fringe count error was detected and the phase of the spectrum was corrected.
FCE Detect	0-1	Set if a fringe count error was detected.
Invalid Data	0-1	Set if bit trim failed or RDR invalid (ZPD saturation) or FCE correction failed, DS with lunar intrusion, DS or ICT moving window below min moving window tolerance, RDR time stamp fails validation
DS Window Size	UInt16	The number of DS spectra used to calibrate the earth scene.

ICT Window Size	UInt16	The number of ICT spectra used to calibrate the earth scene.
Calculated detector Vdc	UInt16	100 uV/LSB Range [0.0000 – 6.5535 Volt] (LSB = Least Significant Bit)

7.7 POST-PROCESSING

This module is intended to be responsible for final data preparation prior to output.

7.7.1 User Required Spectral Bins Selection

This processing step retains final selection of bins of the resampled spectral grid to be distributed in SDRs.

7.7.2 SDR Data Formatting

This processing step collects the data and fills the fields that define SDRs.

7.8 OUTPUT DATA HANDLING

This module is responsible for output and archive of SDRs formatted by the post-processing module. This formatting of data in SDR output is defined in the AOD. Also see [RD 35].

8. CONCLUSION

Summary of ATBD Document

The present Algorithm Theoretical Basis Document defines the Level 1B algorithms needed on the ground in order to produce meaningful data meeting all the requirements of the CrIS instrument. This ATBD exposes the scientific basis, the mathematical description, and documentation of these algorithms required to generate as output geolocated, radiometrically and spectrally calibrated spectra in which instrument distortions are efficiently removed. Different algorithms are exposed and tradeoffs are given to substantiate the choice of the most appropriate algorithms for the task. The ATBD shows the functional partition and the internal data flow inside the SDR Algorithms, identifying data structures, and the transforms between them. The major features of the planned on-orbit and ground calibration processes are described and discussions are conducted over what is to be done in order to minimize output errors.

The SDR Algorithms successfully transform input RDR into SDR delivered as output, producing calibrated spectra meeting the specifications and requirements of the CrIS instrument. The algorithm performance is meeting all assigned top-level system performance and is compatible with the sensor's design.

Key algorithm characteristics

All essential concepts exposed in Section 2.1 have been covered in the remaining parts of the document. The effects of phase dispersion, fringe count errors, signal self-apodization, polarization, spectral shifts, are included.

The SDR Algorithms remove design particularities and attributes of the CrIS sensor, contained in RDRs, from the SDR user. SDR Algorithms convert data from real CrIS hardware into data that appears to originate from an ideal CrIS sensor. The SDRs are handed out with a pixel-invariant, sampling wavelength-invariant properties, and uniform (common) spectral grid outputs. The SDR Algorithms thus relieve EDR algorithms from any sensor specific perturbations.

The pixel-invariant property is done through off-axis self-apodization removal. All pixels at the SDR to EDR interface have the same characteristics: a standard geolocated grid, a standard wavenumber grid, a standard instrument line shape and wavenumber values. Stability of ILS is assured by the CrIS dynamical alignment. Proper ILS correction is a key element of the SDR algorithm, allowing a sensor with multiple FOVs to be used to process measured radiances by contrasting channels that have already undergone spectral correction. Without such correction, the implementation of the “Cloud Clearing” algorithm or any other pixel-to-pixel comparison at the EDR level may be compromised.

The SDR Algorithms rely on a set of data that is independent from any external instrument sources; all required inputs are taken from the CrIS sensor raw data records.

The SDR Algorithms are fault-tolerant: features have been incorporated into the algorithm and software designs to accommodate operational environment errors, including potential errors induced by anomalous conditions (impulse noise, FCE, sampling wavenumber drifts, etc.). The developed algorithms are strong and robust: they will work even in the presence of single unrecoverable error: for example, in the presence of a totally wasted calibration signal, this signal is discarded by the process in order to avoid corrupting the moving average, and the process then resumes its normal operations.

The current version of the SDR Algorithms represents the most up-to-date trade for the design. It has the modular flexibility of its inherent design in terms of its ability to accommodate requirement changes, performance enhancement, and technology insertions. An effort was made to create an adaptable and flexible design that can withstand adjustments and refinements to meet unexpected

future changes. The SDR Algorithms follow a simple structure, allowing similar processing for most of the measurements (DS, ICT, and ES).

Moreover, much of the present SDR Algorithms have heritage in other space programs, like the Engineering Model and Flight Model development and testing of MIPAS [RD 26], where Bomem has applied its expertise and developed solutions that helped the functional definition of practical interferometer calibration algorithms, like with the IASI program [RD 27] for example. The CrIS Engineering and Demonstration Model (EDM) [RD 7] is another example where Bomem has validated its models and algorithms, reaching a radiometric accuracy of better than 0.2%.The original science grade code was developed by ABB using MATLAB. ITT re-implemented this code in C++. The C++ implementation enhanced the science algorithm in terms of functional flexibility to support system level testing and in processing speed.

Scientific Code

The SDR Scientific Code is a prototype of what the operational software will do. It is used to demonstrate the validity of all the SDR Algorithms in a working environment. The CrIS SDR Science Code demonstrates all performance related requirements as well as special features needed for CrIS test activities.

Final Word

The SDR science code in MATLAB developed by ABB Bomem (CDR 1/22/02) has been fully documented (ATBD, ADD, IODD, user manual, and test plan). ABB performed the science code tests, validated and delivered the code to ITT and NGST (10/20/03). ITT implemented the C++ version of the code and provided additional testing flexibility with improved FCE detection, lunar intrusion, nonlinearity correction, and improved ICT environmental corrections. The C++ version, which can perform with 40 times better execution speed, can process real time CrIS RDRs to SDR. The full end to end implementation of C++ code has been validated using original ABB test plan test scenes plus ITT enhancement of verification tests. The code was extensively used for EDU3 and FM1 testing. NGST was last supplied with SDR C++ code and documentation in January 2009 (software version ct_sdr2.18.0). NGST code testing of the code re-confirmed ITT and Bomem code verification. NGST confirmed that the CrIS SDR algorithm outputs contain all the input data required by the CrIMSS EDR algorithm.

SDR updates to resolve all known issues since the last code delivery have been incorporated into ITT SDR code. The updated software has been used to reprocess EDU3 and FM1 data and to verify the changes to the science algorithm. The current version of ATBD (-CrIS-0067 E SDR ATBD) incorporates all the algorithm changes. Re-validation of updated SDR C++ code version 2.18 is complete.

9. APPENDICES

9.1 FAST FOURIER TRANSFORMS

Data acquisition yields the digitized interferogram $I(x)$, which must be converted into a spectrum by means of a mathematical operator called Fourier transformation (FT). Generally, the FT determines the frequency components making up a continuous waveform. However, if the waveform (the interferogram) is sampled and consists of N discrete, equidistant points, one has to use the discrete version of the FT, i.e. the discrete FT (DFT). The used conventions for the discrete direct and inverse numerical Fourier transforms are, as expressed in the interferogram and the spectrum domains:

$$S[n] = \Delta x \sum_{m=0}^{N-1} I[m]\, e^{-2\pi i\, m\, n/N} \tag{107}$$

$$I[m] = \Delta \sigma \sum_{n=0}^{N-1} S[n]\, e^{+2\pi i\, m\, n/N} \tag{108}$$

The equivalent function calls for the Fast Fourier Transform implementation are given by:

$$S_{b,p,d}[n] = \mathrm{FFT}\left\{ I_{b,p,d}[m] \right\} \tag{109}$$

$$I_{b,p,d}[m] = \mathrm{I\,FFT}\left\{ S_{b,p,d}[n] \right\} \tag{110}$$

with the following notation:

N is the total number of points in numerical arrays

n the interferogram index data points: $0, \ldots, N-1$

m the spectral index data points: $0, \ldots, N-1$

and Δx the sampling of the interferogram: $$\Delta x = \frac{2\,MPD}{N} = \lambda_S = \frac{1}{\sigma_s} \quad [\mathrm{cm}] \tag{111}$$

and $\Delta \sigma$ the sampling of the spectrum: $$\Delta \sigma = \frac{1}{2\,MPD} = \frac{\sigma_s}{N} \quad [\mathrm{cm}^{-1}] \tag{112}$$

The relation coupling the two spaces is: $$\Delta x \cdot \Delta \sigma = \frac{1}{N} \tag{113}$$

Results are expressed in term of unit of amplitude per sampling interval (Δx or $\Delta \sigma$), i.e., when integrating, the amplitude value must be multiplied by this sampling.

9.1.1 Comments on Various Algorithms

The Fast Fourier Transform algorithm is perhaps the one algorithmic discovery that has had the greatest practical impact in history. Fourier transforms are of fundamental importance in such

disparate applications as optics, acoustics, quantum physics, telecommunications, system theory, and signal processing including speech recognition. For years, progress in these areas was limited by the fact that the known algorithms for calculating Fourier transforms all took far too long.

The discovery by Cooley and Tukey in 1965 of a fast algorithm revolutionized the situation: problems previously considered infeasible could now at last be tackled. In one early test for the “new” algorithm, the Fourier transform was used to analyze data from an earthquake that had taken place in Alaska in 1964. While the classic algorithm took more than 26 minutes of computation, the “new” algorithm was able to perform the same task in less than two and half seconds. Ironically it turned out that an efficient algorithm had already been published in 1942 by Danielson and Lanczos, and all the necessary theoretical groundwork for Danielson and Lanczos's algorithm had been published by Runge and Konig in 1924. And if that were not sufficient, Gauss describes a similar algorithm in a paper written around 1805 and published posthumously in 1866!

The “Fast Fourier Transform” (FFT) is an algorithm implementing the Fourier transform in a very efficient manner, with a much less complexity than a direct implementation as the one expressed in Equation (107).

There are different algorithms for performing numerical Fourier transforms. There are prime-factor algorithms, which only works on sizes that are products of relatively prime factors. There is also the Winograd algorithm. There is Bruun's algorithm (and related methods). And, there are various methods to change an FFT into a convolution, which can then be performed using one of a variety of fast convolution algorithms. Also, you can express the FFT in terms of fast Hartley transforms. That's all the major methods, but there are probably a few other obscure (and thoroughly impractical) algorithms.

These methods, however, tend to be either difficult to implement (and thus slow in practice) or limited to a small set of sizes. It is not clear if they offer any general advantage in practice. However, each of them tends to be useful in particular cases.

The choice of the right (fastest) FFT for a given application is a good question. No single implementation FFT can claim to be the “best" or the "fastest". A given implementation can behave differently on various machines and environments. It depends on many factors, among which a few are listed below:

- type of processor available (architecture, registers, etc.)
- size of memory available (main memory and cache memory)
- can the number of points be rounded to a power of two?
- size of transforms to be computed (up to 1024 points, or 1 M points?)
- use or not of intermediate temporary vectors
- use or not pre-computed trigonometric tables
- acceptable complexity of implementation
- type of complex data representation
- etc.

For example, some assembler Radix 4 routines outperform Radix 8 routines, while other optimized compiled in C language are faster on other machines with larger number of registers and local cache. The complexity of a given FFT routine is also an important factor to consider: some very fast routines are so complicated that their implementation in a DSP for example would be out of the question, while other almost as fast routines are much simpler and can be coded in a small number of lines.

Some implementations use the complex data structure, while others use double precision data type to store complex numbers. This is not really a problem as data storage structure can always be interchanged by modifying the source code.

For some applications, the precomputation of trigonometric tables has no effect on the overall performance, while in other applications this could be detrimental. Double precision computation is preferable for adequate numerical accuracy. This is especially true if a trigonometric recurrence algorithm is chosen, where the last points may be totally corrupted due to "rounding effect" in single precision. On modern computers, double precision algorithms require almost the same computing time as the single precision algorithms, so there should be no penalty using maximum precision.

In summary, one has to check various FFT routines and his practical requirements to choose the right tool for the job. The choice of the FFT algorithm is an important issue for SDR Algorithms accuracy. From an accuracy point of view, no specific FFT algorithm is imposed and different algorithms are possible that use different optimization techniques. Care must be taken when considering the exponent sign ($\pm$) and the normalization constant ($1/N$ or $1/\sqrt{N}$ employed in the direct or inverse transform particular implementation. Consult [RD 18] for a thorough study and various implementations of discrete FFTs.

9.1.2 Data translation and centering

Signal swapping is required for bit reverse vectors data storage, where zero frequency is at the middle point of the signal. An alternative way to avoid this operation is to introduce a linear phase shift into the input data to change the position of the transform. In one dimension, we have the following translation relationship:

$$\mathsf{F}\left\{ f(x)\, e^{\pm 2\pi i\, x\, \sigma_0 / N} \right\} = F(\sigma \mp \sigma_0) \tag{114}$$

If we want to center the FFT result in the data array, we let $\sigma_0 = N/2$ in the previous equation:

$$\mathsf{F}\left\{ f(x_i)\,(-1)^i \right\} = F(\sigma - N/2) \tag{115}$$

This shows that to store the data with the origin at the center of the array, it is necessary to multiply the array by a phase factor of $(-1)^i$ to end up with a centered function after the transform is taken. For phase shifted, centered data, we have:

$$S(\sigma_i - N/2)\cdot(-1)^i = \mathsf{F}\left\{ I(x_i - N/2)\cdot(-1)^i \right\} \tag{116}$$

Therefore to obtain the correct result, the transform must also be multiplied by a $(-1)^i$ phase factor. For more information, consult [RD 11].

9.1.3 Prime Factor Algorithm Fast Fourier Transform

The Prime Factor Algorithm Fast Fourier Transform is a very effective self-sorting in-place complex FFT. It uses the Prime Factor Algorithm as described by Temperton [RD 5 and RD 6]. The implementation given by Dave Hale at the Center for Wave Phenomena at the Colorado School of Mines [RD 18] can rival most of all other existing algorithms when limited to a given set of dimensions (239 different values).

Other algorithms exist for array dimensions factor of any small prime numbers. Among these there are variants of the Cooley-Tukey algorithm (1965), as the one developed by P. Swarztrauber at the National Center for Atmospheric Research (FFTPACK), or others based on the subroutine FOURG by N. M. Brenner (1969) IBM Contributed Program Library, taken from the NAASA public library, Leonard J. Harding, April 1976 University of Michigan Computer Control, Ann Arbor. There is also machine-optimized versions by FFTW which can be competitive.

The execution times given in Table 8 correspond to the three fastest FFT routines available, coded in C with CodeWarrior Pro 3 and optimized executables on a Pentium II at 350 MHz. The first is the PFA FFT, as implemented by the Center for Wave Phenomena at the Colorado School of Mines, and a FFT by Ooura. The two others are described below, while the fourth is the one available in Matlab 6 which is FFTW from www.fftw.org. The execution times shall only be considered relative with respect to one another. These times are representative of the complexity of the algorithms, and can be viewed as estimates of the number of floating point operations required. Timings are given for the dimensions closest to the expected dimensions given in the present CrIS instrument specifications.

1: **Prime Factor Algorithm (PFA) in-place FFT**

The fastest of the fastest.
+ extremely fast for selected values of N
– only works for a few limited values of N (see conditions), N must be factorable into mutually prime factors taken from the set $\{2, 3, 4, 5, 7, 8, 9, 11, 13, 16\}$. In other words,

$$n = 2^p \cdot 3^q \cdot 5^r \cdot 7^s \cdot 11^t \cdot 13^u \text{ where } 0 \le p \le 4,\ 0 \le q \le 2,\ 0 \le r,s,t,u \le 1$$

2: **Mixed-Radix** (2-3-4-5-n) based on a variant of the Cooley-Tukey algorithm.

Developed by P. Swarztrauber at the National Center for Atmospheric Research (FFTPACK). Code inspired from IMSL library.
Good for N not powers of 2.
+ Optimized for small prime factors 2, 3, 4, 5.
(faster than Brenner when only these factors are present)
+ reasonably fast when not powers of 2.
– medium size implementation (880 lines of code).

3: **Modified Cooley-Tukey FFT**

Based on code by N. M. Brenner, adapted by Leonard J. Harding, NAASA library.
Good for N not power of 2.
+ faster than IMSL when N composed of large prime factors.
+ very small size implementation (190 lines of code).

9.2 ALIAS UNFOLDING

After the operation of decimation on an interferogram, the spectral range of the corresponding spectrum changes and must be precisely determined. To assign correct spectral axis one must perform *alias unfolding* (also called spectrum unscrambling or spectrum re-ordering).

Let us suppose an original spectrum of N points with frequencies ranging from 0 to σ_s, where σ_s is the sampling frequency of the reference laser. We decimate the IGM using a decimation frequency DF_b

(b for channel/band index), and keeping only N_b points. Then, the apparent frequencies range from 0 to σ_S/DF_b. The spectral range determination implies the reordering of the spectrum and a shift to the original band.

The reordering point k is determined with the following:

Defining

$$\Delta\sigma_{\mathrm{dec}\,b} = \frac{1}{N_b \cdot \lambda_S \cdot DF_b} \tag{117}$$

the alias width is given by

$$W_b = N_b \cdot \Delta\sigma_{\mathrm{dec}b} = \frac{1}{\lambda_S \cdot DF_b} \tag{118}$$

We want to position one alias window right over the spectral range of the numerical filter. Finding the integer number of $\Delta\sigma_{\mathrm{dec}\,b}$ closest to the center of the numerical filter range determines the position of the lower limit of this alias window which is

$$\sigma_{\min b} = k\ \Delta\sigma_{\mathrm{dec}\,b} \tag{119}$$

with

$$k = \mathrm{Floor}\left\{\frac{\left(\sigma_{\min b}^{req} + \sigma_{\max b}^{req}\right) - W_b}{2 \cdot \Delta\sigma_{\mathrm{dec}\,b}}\right\} \tag{120}$$

where $\sigma_{\min b}^{req}$ and $\sigma_{\max b}^{req}$ correspond to the numerical filter limits.

Equation 120 provides the pivot which reorders the spectrum to cover the band of interest. One just has to rotate the spectrum k points to the left:

$$S[n] = \mathrm{A}liasUnfold\left\{S[n],\ k \bmod N_b\right\} \tag{121}$$

An example of the effect aliasing of decimation after complex numerical filtering is provided in Figure 73.

The numerical operation of unscrambling must be executed after each Fourier transform on decimated signals.

Decimation and alias unfolding
(data compression scheme)

As seen in the spectrum domain $S(\sigma)$

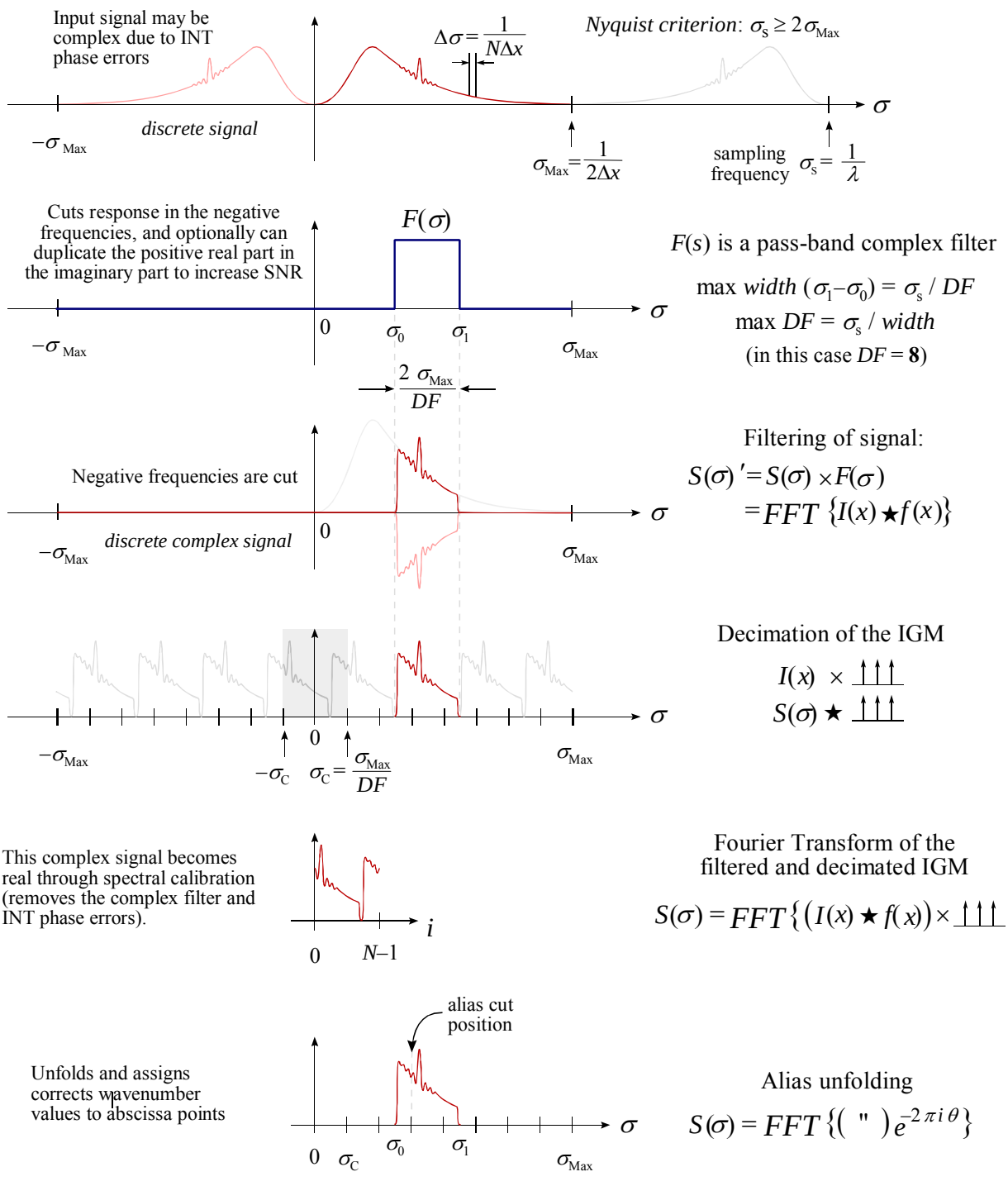

Figure 73: Interferogram decimation and alias unfolding

9.3 LINEAR FITTING

Description:

This sub function is used for the determination of the slope and the ordinate of a straight line through a set of data points. It is used for the determination of the slope for the fringe count error detection.

We give here a general description for the implementation of the algorithm that is independent of the type of data used as input.

Processing:

Variable	Descriptive Name	I/O	Type	Ranges / References / Remarks
N	Dimension of vectors to fit	i	i	No restriction on the size of *N*
x_i	Abscissa data values	i	r	could also be specified by: $x_i = x_0 + i\Delta x = \Delta x(-N/2+i)$
y_j	Ordinate data values	i	r	
m	Computed slope of the fitted line	o	r	
b	Computed ordinate at origin of the fitted line	o	r	

One of the simplest implementation of the linear fitting is defined as follows:

$$y = mx + b \tag{122}$$

$$t = N \times \sum_{i=0}^{N-1} x_i^2 - \left(\sum_{i=0}^{N-1} x_i \right)^2 \tag{123}$$

$$m = \frac{1}{t}\left[N \times \sum_{i=0}^{N-1} x_i y_i - \sum_{i=0}^{N-1} x_i \times \sum_{i=0}^{N-1} y_i \right] \tag{124}$$

$$b = \frac{1}{t}\left[\sum_{i=0}^{N-1} y_i \times \sum_{i=0}^{N-1} x_i^2 - \sum_{i=0}^{N-1} x_i \times \sum_{i=0}^{N-1} x_i y_i \right] \tag{125}$$

When the abscissa data is uniformly distributed at Δx intervals, the previous expression can be further simplified:

$$y = mx + b$$

$$\begin{aligned} x &= x_0,\ x_0 + \Delta x,\ x_0 + 2\Delta x,\ \ldots,\ x_0 + (N-1)\Delta x \\ &= x_0 + [0, 1, 2, \ldots (N-1)]\ \Delta x \end{aligned} \tag{126}$$

$$t_1 = \frac{6}{\Delta x N(N+1)}, \tag{127}$$

$$t_2 = t_1 \sum_{i=0}^{N-1} y_i , \tag{128}$$

$$t_3 = \frac{2t_1}{N-1} \sum_{i=0}^{N-1} i y_i \tag{129}$$

$$m = t_3 - t_2 , \tag{130}$$

$$b = t_2\left(x_0 + \Delta x \frac{2N-1}{3} \right) - t_3\left(x_0 + \Delta x \frac{N-1}{2} \right), \tag{131}$$

9.3.1 Implementation of the linear interpolation

The following function call defined throughout the present document:

$$m, b = \text{LinearInterpolate}\left\{ S[n];\ \Delta\sigma, \sigma^{\min}, N,\ \sigma_{fit}^{\min}, \sigma_{fit}^{\max} \right\} \tag{132}$$

OR

$$m / \Delta\sigma, b = \text{LinearInterpolate}\left\{ S[n];\ N, n_0, n_1 \right\} \tag{133}$$

where $S[n]$ is the input function defined on N points, with numerical spectral axis values starting from $\sigma^{\min}$ and separated by $\Delta\sigma$. The $\sigma_{fit}^{\min}$ and $\sigma_{fit}^{\min}$ values define the spectral range limits in which the fit has to be computed.

Numerical interpolation shall be implemented as given in the previous section describing linear fitting when abscissa data is uniformly distributed.

9.4 NUMERICAL INTEGRATION

When we talk about numerical integration (which is also called "quadrature") we immediately think about "Simpson's rule" or "Trapezoidal rule". The classical formulas for integrating a function whose values are known at equally spaced steps have a certain elegance about them, and they are redolent with historical association. But computing methods evolve and times change; with the exception of two of the most modest formulas ("extended trapezoidal rule" and "extended midpoint rule", see [RD 19]), the classical formulas are almost entirely useless. They are museum pieces, but beautiful ones.

Integration with Gaussian Quadratures

Gaussian quadratures are among the most beautiful and the most powerful methods for numerical integration [RD 20]. The theory behind these methods goes back to Karl F. Gauss (1777–1885), who used in 1814 continued fractions to develop the subject. In 1826, Karl G. Jacobi (1804–1851) rederived Gauss's results by means of orthogonal polynomials. The systematic treatment of arbitrary weight functions $W(x)$ using orthogonal polynomials is largely due to Elwin B. Christoffel (1829–1900) in 1877.

The basic idea of Gaussian quadratures is to give ourselves one more degree of freedom with respect to traditional methods by an enlightened choice of the location of the abscissa points at which the function is to be evaluated: these points will no longer be equally spaced.

Instead of studying the habitual class of integrals of simple polynomial functions, we now study the class of integrands "polynomial times some known function $W(x)$". The function $W(x)$ can then be chosen to remove integrable singularities from the desired integral. Given $W(x)$, in other words, and given an integer N, we can find a set of weights w_i and abscissas x_i such that the following approximation becomes exact if $f(x)$ is a polynomial:

$$\int_a^b W(x)\, f(x)\, dx \;\approx\; \sum_{i=0}^{N-1} w_i\, f(x_i) \tag{134}$$

The fundamental theorem behind N-points Gaussian quadratures comes from the fact that the abscissas of Equation (134) together with the weighting function $W(x)$ in the interval $(a,\ b)$ are precisely the roots of an orthogonal polynomial $p_N(x)$ for the same interval and weighting function. Without going into more mathematical details, lets mention that many known quadratures exist for different forms of the $W(x)$ function. The most general case where $W(x) = 1$ and with $-1 < x < 1$, implying Legendre polynomials P_N: these specific integrals are called *Gauss-Legendre quadratures*. This category is well suited for boundary conditioned physical problems like wave guides or resonators.

$$W(x) = 1 \quad \text{and} \quad -1 < x < 1$$

$$w_i = \frac{2}{(1 - x_i^2)\left[P_N'(x_i)\right]^2}$$

Legendre polynomial recurrence relation:

$$(n+1)\, P_{n+1} = (2n+1)\, x\, P_n - n\, P_{n-1}$$

9.5 DETERMINATION OF THE GOODNESS OF FIT

After a given fit has been computed, the standard deviation can be computed to evaluate the dispersion of the fit. The standard deviation is the root mean square of the deviations, and is associated with the *second moment* of the data about the mean [RD 21].

A goodness of fit indicator can also be computed between the reference points and the fit to determine with which validity they are similar. A useful operator used to evaluate the goodness of fit criteria is mathematically derived as follows:

$$r = \frac{\sum_{i=0}^{N-1}(f_i - \bar{f})(y_i - \bar{y})}{\sqrt{\sum_{i=0}^{N-1}(f_i - \bar{f})^2}\sqrt{\sum_{i=0}^{N-1}(y_i - \bar{y})^2}} \quad [-1\ldots1] \tag{135}$$

where f_i is the fitted data, or the experimental spectrum

y_i is the model data, or the reference spectrum

and $\bar{f}$ and $\bar{y}$ are the means of the vectors f and y.

Correlation coefficient *r*

r is the *linear-correlation coefficient,* also called the *product-moment correlation coefficient*, or *Pearson's* r. It indicates the strength of the association between the dependent and independent variables. The magnitude of the coefficient is not easy to interpret (see definition of coefficient of determination), but the sign (+ or –) indicates the direction of the relationship. The coefficient of correlation varies from -1 to $+1$, with -1, for example, indicating a reversed relationship (as one grows larger, the other grows smaller).

Coefficient of determination r^2

Measures the proportion of the variation of the dependent variable about its mean that is explained by the independent or predictor variable(s). The coefficient r^2 can vary between 0 and 1, inclusive. If the regression model is properly applied and estimated, the higher the value of r^2, the greater the explanatory power of the regression equation, and therefore the better the prediction of the criterion variable [RD 22]. It takes a value of 1, termed “complete correlation”, when the model and the experimental points match one-by-one.

r^2 has the following properties:

$r^2 = 1$ when input functions (the model and the experimental points) match perfectly.

$r^2 = 0$ when input functions are completely uncorrelated.

When a correlation is known to be significant, r^2 is one conventional way of summarizing its strength. In fact, the value of r^2 can be translated into a statement about what residuals (root mean square

deviations) are to be expected if the data are fitted to a straight line by the least-squares method. This value is always bounded, but it does not indicate when a fit departs linearly from the reference.

Another similar determination coefficient is R^2 which closely relates to the χ^2 criteria, and is defined as:

$$R^2 = 1 - \frac{\sum_{i=0}^{N-1}(f_i - y_i)^2}{\sum_{i=0}^{N-1}(y_i - \bar{y})^2} \tag{136}$$

$$R^2 = 1 - \frac{\text{unexplained variation}}{\text{total variation about the mean}} \quad [-\infty \ldots 1]$$

R^2 has the following properties:

$R^2 = 1$ when input functions (the model and the experimental points) match perfectly.

$R^2 = 0$ when input functions are completely uncorrelated.

$R^2 = -\infty$ when input functions are completely anti-correlated.

An ill conditioned case occurs when the model *y* is distributed around zero in a horizontal line: this causes both correlation factors to take small values even in the presence of good fits.

In summary, r and R are the correlation coefficients, while r^2 and R^2 are the determination factors. It is on the last two values that the present analysis is based. The squared values are used to simplify the understanding, and both r^2 and R^2 are used to get as much information as possible for the goodness of the fit. At the end of the study, maybe it will be judged that only one identifier is sufficient for a correct identification.

Further details regarding the correlation/determination coefficient can be found at the following references: [RD 19, Chap. 15], [RD 21, Chap. 11], [RD 22, Chap. 11], [RD 23, Sect. 24.12].

<u>Processing</u>:

Variable	Descriptive Name	I/O	Type	Ranges / References / Remarks
N	Dimension of input vectors	i	i	$i = 0..N-1$
y_i	Ordinate values of reference data points	i	r	
f_i	Ordinate values of fitted data	i	r	
s	Standard deviation	o	r	
r^2	Determination factor	o	r	$-1 \le r^2 \le 1$
R^2	Determination factor	o	r	$-\infty < R^2 \le 1$

9.6 DEFINITIONS

In this appendix, we review some of the basic terms used in the document. For each term, we provide (in *italics*) the definition established by the mission prime contractor, if such a definition exists. Then, if necessary, we present an interpretation of the definition for the CrIS instrument SDR Algorithms.

9.6.1 Sensor Calibration

Sensor calibration is the procedure for converting instrument measurement data into data with the required physical units while correcting systematic errors.

Three types of calibration for CrIS can be identified:

Radiometric Calibration: The process of assigning absolute values in radiance units, (noted [r.u.] expressed in $\mathrm{m}W / (\mathrm{m}^2\ \mathrm{sr}\ \mathrm{cm}^{-1})$) to the intensity axis (y-axis) with a specified accuracy. This calibration equation remodulates the data to real components. The radiometric calibration implies the knowledge of a certain spectral calibration.

Spectral Calibration: The process of assigning absolute values in cm^{-1} to the wavenumber axis (x-axis) with a specified accuracy. Also the process of removing systematic errors from the Instrument Line Shape (ILS) with a specified accuracy.

Geometric Calibration: The process of assigning an absolute earth surface location in geodetic latitude and longitude to a given atmospheric spectrum with a specified accuracy.

9.6.2 Raw Data Record (RDR)

Raw data records are full resolution, unprocessed digital sensor data, time-referenced and earth located (or orbit-located for in-situ measurements), with radiometric and geometric calibration coefficients appended (but not applied) to the data. Aggregates (sum or weighted averages) of detector samples are considered to be full resolution data if the aggregation is normally performed to meet resolution and other requirements. Sensor data are unprocessed with the exceptions of lossless data compression (decimation and bit trimming) which is allowed [RD 24].

All calibration data will also be retained and communicated to the ground without lossy compression.

The CrIS contractor shall be responsible or generating operational RDRs ([**RD 25**] 3.2.1.1.3.1).

9.6.3 Sensor Data Record (SDR)

Sensor data records are full resolution sensor data that are time referenced, earth located (or orbit-located for in-situ measurements), and calibrated by applying the calibration information including radiometric and geometric calibration coefficients and georeferencing parameters such as platform ephemeris. These data are processed to engineering units (radiance). Calibration, ephemeris, and any other ancillary data used for the conversion are either included directly in the SDR product or otherwise referenced as external files.

9.6.4 Environmental Data Record (EDR)

Environmental data (also termed "mission data") refers to all data, atmospheric, oceanographic, terrestrial, space environmental and climatic, being sensed and collected by the satellite or derived, at least in part, from these measurements.

9.6.5 Data product Levels

The following table summarizes the various levels of data distribution for the CrIS products:

Table 23: CrIS Product Levels Classification

Level	Description
Level 0 (RDR's)	Raw Data Records (RDR)s from CrIS sensor formatted to CCSDS transmission standards. Unprocessed raw data packages of instrument data at original resolution, are time ordered (no overlap), with duplicate packets removed. Contents of data record include sensor raw science data, housekeeping and calibration data merged with spacecraft orbit information (ephemeris, attitude, and time data). The data granule is assumed to be 1.25 orbits maximum. → RDR sensor output
Level 1A (interme-diate level)	Level 0 data (including reconstructed interferograms) which may have been reformatted or transformed reversibly, located to a coordinate system, and packaged with needed calibration characterization data needed to begin calibration procedure.
Level 1B (SDR's)	Radiometrically, spectrally (frequency), and geolocated calibrated spectra mapped onto EDR channel sets with specific ILS and apodization, with annotated quality indicators.
Level 2 (EDR's)	Environmental variables retrieved from Level 1 data. Geolocated profiles of pressure, temperature, and humidity of the atmosphere. Land and ocean skin temperature, and total column ozone.

The present document refers to the computation of Level 1B data.

9.6.6 Measured Data

Measured data is all raw sensor data acquired by the instrument after digitization.

By this is meant the data points from the source signal. In the case of CrIS, the source signal can be a raw unprocessed interferogram sampled at full resolution from any of the nine FOVs and from any of the three IR spectral bands covered by a FOV.

The following separates the different measurements taken by the instrument according to the physical meaning and content of the observational data acquired.

<u>Scene Measurements</u>

CrIS will take measurements of the atmosphere at different angles. The surface of the earth is scanned in discrete steps using the pointing mirror. A single scene measurement is taken at each pointing value.

Deep Space Measurements

The instrument itself is contributing to the observed spectrum. In order to remove this contribution, it is necessary to take a measurement of a “cold” scene, i.e. a scene with negligible radiance. Since the instrument contribution is varying, mainly because of temperature orbital variations, this offset measurement shall be repeated regularly.

Blackbody Measurements

Measurements of an internal calibration source, a well-characterized blackbody source, are performed to characterize the instrument responsivity (or gain). These measurements are also repeated regularly because of the expected responsivity variations. A complete determination of the instrument gain is composed of several blackbody measurements combined with an equivalent number of deep space measurements combined in a moving average.

Of all the measurement types listed previously, only the scene measurements contain the desired scientific information, i.e. spectra of the atmosphere. All other measurements are characterization measurements for calibration. Using the results from these characterization measurements, the calibration procedure is applied to the scene measurements.

Deep space and blackbody measurements are used for the radiometric calibration. Deep space measurements are taken for the subtraction of the instrument contribution (self-emission) from the scene measurements and blackbody measurements.

9.6.7 Auxiliary Data

Auxiliary data are defined as all the additional data sent by the instrument, apart from the observational data, required by the ground processing to allow full interpretation of its observational data for the delivery of ground segment data products.

From the instrument point of view, auxiliary data are those data used in the processing which come from a CrIS measurement data stream (instrument data packets from the signal processor electronics), since interpretation and evaluation of the observational data is done on ground.

Science TLM Data

These auxiliary data, that include calibration information, like ICT temperatures, optical temperatures, laser diode temperature and bias current, scan position errors, etc., are referred to Science TLM Data and are transmitted to the ground at each cross-track scan (8 seconds).

Although neon calibration data falls in the category, this particular data is transmitted less frequently in Engineering Data packets (see below).

Engineering Data

These auxiliary data, that include instrument characterization data, transfer curves coefficients, physical constants and also neon calibration data, are referred to Engineering Data and are transmitted to the ground after many cross-track scans (30, equivalent to 4 minutes).

9.6.8 Ancillary Data

Ancillary data are all data to be provided by external source to allow full interpretation and evaluation of its observational data.

Ancillary data are defined as all additional data required by the ground processing for the generation and delivery of ground segment data products, coming neither from the space segment nor from the ground segment itself. These data are intended to be rarely changed. They include constant definitions, templates for data validation, look-up tables for data conversion, etc...

The CrIS SDR algorithm requires no ancillary data, this kind of data being transmitted to the ground within Engineering Data packets (see Auxiliary Data section above).

9.6.9 Other Instrument Specific Terms and Definitions

Accuracy

A measure of correctness to a true value. Under most reasonable conditions accuracy may have a probabilistic distribution function, i.e. normally or Gaussian distributed. If symmetrically distributed the standard deviation, 1σ or some other interval 2σ or 3σ should be identified. If a measurement has small systematic errors, the measurement is considered to have high accuracy.

Apodization

Apodization (originating from the Greek work $\alpha\pi o\delta$, which means “removal of the feet”) consists of the multiplication of an interferogram by a decaying function. It is the process which attenuates the spurious “feet” in the spectral domain.

It is a mathematical transformation carried out on data received from an interferometer to alter the instrument’s response function before the Fourier transformation is calculated to obtain the spectrum.

Calibration data

Data calculated by the ground segment from specific periodical observational data (IGM) and used to calibrate subsequent scene spectra.

Decimation

Operation consisting of taking one out of a predetermined number of points in a sampled signal. It is also called “undersampling”. When a signal has been properly filtered, the decimation permits a decrease in the number of points required to represent the signal with the same resolution.

Field of Regard

The Field Of Regard (FOR) has 9 Fields Of Views (FOV) forming a 3 by 3 matrix. In each band, a separate detector is associated with each FOV.

Input data

In the present document, the term input refers to the origin with respect to the ground processor. It also implicitly means data that is continuously produced. Thus, input data will contain either the primary data coming from the Space Segment or additional data coming from the Flight Operation Segment.

Instrument Line Shape (ILS) and Resolution

The ILS is the response of the spectrometer to a monochromatic spectral stimulus. A distinct ILS exists for each wavenumber and for each FOV. In general, the ILS corresponds to a small deviation from an ideal sinc response.

The resolution of the instrument is defined as the FWHM of the ILS. For the sinc function definition we have:

$$\text{FWHM} = \frac{1.2}{2\,MPD} \quad \text{(unapodized)}$$

$$\text{FWHM} = \frac{2}{2\,MPD} \quad \text{(Hanning apodized)}$$

Interferogram

The intensity $I(x)$ of the combined IR beams, measured by the detector of an interferometer as a function of the moving mirror displacement x.

Interferometer Sweep

An interferometer sweep is the data recording for a single measurement resulting in a complete interferogram. A sweep can be in either direction, reverse or forward.

Measurement Scan Sequence

A measurement scan sequence comprises a sequence of interferometer sweeps within a fixed time interval and at variable cross track scan angles with respect to the CrIS nadir view. See [RD 29] for more details.

Scanning occurs in the cross track direction using a scan mirror angled at 45° to the interferometer optical axis. The resulting scan pattern for this scan configuration is shown in Figure 16. Although image rotation results, this scan provides adequate performance while minimizing scan mirror size and complexity. The scan mirror assembly is designed to keep the field of view on a fixed location on the ground during integration; this process is termed Image Motion Compensation (IMC).

Noise

The noise performance requirements are defined at the aperture of the system by the noise-equivalent radiance difference (NEdN) arriving from the top of the atmosphere (TOA). The noise-equivalent temperature difference (NEdT) at a given wavenumber is defined by dividing the NEdN at that wavenumber by the derivative with respect to the Planck black body radiance function, evaluated at 250 degrees K at the same wavenumber.

Optical Frequency

As commonly used, optical frequency, σ is the reciprocal of the radiation wavelength λ and has the modern-day units of cm^{-1} and are called wavenumbers.

Optical Path Difference

When two optical waves are separated temporally by the equivalent of one wavelength, recombination leads to constructive interference or consonance. When the separation is a half wave, destructive interference or dissonance occurs. The above separations are referred to as optical path difference (OPD) denoted Δ, and may vary from zero to many waves. Related to OPD is the term

phase difference, $\delta = k(x_2 - x_1) = k\Delta$ where $k = 2\pi / \lambda$ and is referred to as the propagation number. The physical meaning of k is that it may be interpreted as the number of wave per $2n$ centimeters.

Precision

Precision is a measure of repeatability, either short term or long term, in performing a measurement. Under most reasonable conditions precision may have a probabilistic distribution function, e.g. normally or Gaussian distributed. If symmetrically distributed, the standard deviation 1σ, or some other interval 2σ or 3σ, should be identified.

Radiation Terms

Radiance and spectral radiance are field quantities, as in Maxwellian electromagnetic theory and correspond to the radiant power per unit solid angle per unit area from a source and additionally per unit wavelength, $\Delta\lambda$ or unit optical frequency $\Delta\sigma$. The chosen radiance units [r.u.] for the CrIS are mW/(m^2 sr cm^{-1}). The unit cm^{-1} denotes wavenumbers. Radiance and spectral radiance are denoted by the symbol $L(\sigma)$. The term $B(\sigma)$ appears in much of the FTIR literature and denote spectral radiance when referring to a blackbody.

Repeatability

The closeness of the agreement between the results of successive measurements of the same measure and carried out under the same conditions of measurements.

Scene

Atmosphere observational data; defined in contrast with blackbody and deep space observation.

Spectral Bands

A spectral band is defined as the radiometric pass band of the scene radiance for a single detector or group of detectors where the edge of the band is defined by the 50% response point relative to the peak response in that band.

Spectral Bin Size

The spectral bin size is defined as $1/(2\ MPD)$, where MPD is the optical path difference from Zero Path Difference (ZPD) in the sampled interferogram. The spectral bin size is a function of off axis field angle.

Spectrum

A display or plot of radiation intensity as a function of wavelength or frequency.

Unapodized Spectral Resolution

The unapodized spectral resolution is defined as $1/(2\ MPD)$, where MPD is the maximum on-axis optical path difference from Zero Path Difference (ZPD) in the sampled interferogram.

Zero padding

The process of adding zeroes at the extremities of interferograms in order to bring their length to a number of points corresponding to the smallest power of 2 greater than the initial number of points. Zero-padding (sometimes wrongly called “zero-filling”) is usually performed to speed-up the computation process by bringing the number of points of the interferogram vector compatible with standard fast Fourier transform algorithms. But special FFTs like mixed radix routines also exist for dimensions that are factor of small prime factors that can circumvent the necessity of doing zero

padding. Care must be taken to the edge effects: in order to avoid discontinuities, the interferogram must first be moved to a zero DC level by a proper DC offset removal procedure.

— End of document —